

**Christoph
Richter**

**Liner impedance modeling in
the time domain
with flow**

ISBN 978-3-7983-2186-1 (Druckausgabe)
ISBN 978-3-7983-2185-4 (Online-Version)

∞ Gedruckt auf säurefreiem alterungsbeständigem Papier

Druck/ druckmuck@digital e.K.
Printing: Großbeerenstr. 2-10, Geb. 2 links, 12107 Berlin

Vertrieb/ Universitätsverlag der TU Berlin
Publisher: Universitätsbibliothek
Fasanenstr. 88 (im VOLKSWAGEN-Haus), D-10623 Berlin
Tel.: (030)314-76131; Fax.: (030)314-76133
E-Mail: publikationen@ub.tu-berlin.de
<http://www.univerlag.tu-berlin.de>

Liner impedance modeling in the time domain with flow

vorgelegt von
Diplom-Ingenieur
Christoph Richter
aus Berlin

Von der Fakultät V – Verkehrs- und Maschinensysteme
der Technischen Universität Berlin
zur Erlangung des akademischen Grades

Doktor der Ingenieurwissenschaften
– Dr.-Ing. –

genehmigte Dissertation

Promotionsausschuss:

Vorsitzender:	Prof. Dr.-Ing. Dieter Peitsch
Berichter:	Prof. Dr.-Ing. Frank Thiele
	Prof. Dr.-Ing. Jan Delfs

Tag der wissenschaftlichen Aussprache: 23. September 2009

Berlin 2009

D 83

To Herta Jöchen

Preface

This work principally represents the research on time-domain impedance modeling that was carried out over a period of almost four years within the recent DFG project LIMiT. Further contributions also arose within the CombustionNoise DFG research initiative, which began in 2003. More generally, the current work forms a part of the continued development of the applied CAA method, to which I have contributed since 2001. The first steps were taken in collaboration with Xiaodong Li, whose earlier work in Berlin laid the foundation for the development of the current CAA method. Later on, Norbert Schönwald and Łukasz Panek, Daniel Morgenweck, Verina Krause and Junis Abdel Hay also became actively involved in this development.

This work would not have been possible without the direct or indirect contribution of many others: Mei Zhuang, with her course on Computational Aeroacoustics held in Berlin and Klaus Ehrenfried, with his excellent lecture „Strömungsakustik“ have provided much theoretical input. Klaus contributed the idea of the source location based on the acoustic intensity to this work. I would also like to thank him for the highly insightful scientific discussions. Chao Yu and Mei Zhuang kindly allowed the application of their AIBM as a far-field method for some of the presented results. I would also like to acknowledge the excellent scientist Ulf Michel for multiple contributions, ranging from the development of project ideas to the placement of international collaborations. He provided the idea of a modal-axisymmetric approach, which was developed within the framework of the European Community funded project TurboNoiseCFD and the DFG project SWING+. In particular I want to acknowledge the assistance of Clemens Buske, who did an excellent job in simulating the radiation from lined ducts. Furthermore, I would like to acknowledge the assistance of Alessandro Bassetti and Kingsley Lawrence Iroba for proofreading and commenting the work.

A special thanks goes to my supervisor Frank Thiele for providing the excellent creative environment, continuous funding, international contacts and a strategic project planning that has enabled to me to carry out this work. I especially want to thank him for allowing me to continue the lecture course on Computational Aeroacoustics and to contribute to the course „Strömungsakustik“.

I would like to thank Sjoerd W. Rienstra and Walter Eversman for the great analytical and numerical works and for the permission to use their figures for benchmarking. A numerical method cannot be developed without high quality experiments supporting their validation. These experiments were contributed by Michael Jones, Toni Parrott and Willie Watson at NASA Langley; Stefan Busse, Claus Heuwinkel, Nancy Kings, Friedrich Bake, Ingo Röhle and Lars Enghardt at DLR Berlin; Paul Murray, Piergiorgio Ferrante and Antonio Scofano from the company AleniaAermacchi and Christian Bender, Horst Büchner and Henning Bockhorn from the University of Karlsruhe. Additional flow data for the GCN5 configuration has been provided by Feichi Zhang and Peter Habisreuter from the University of Karlsruhe. The airfield noise barrier problem was brought to my attention by Christophe Barlieb of CDMB Architects.

Last but not least I want to thank my family, my daughters Leya and Sarah, my beloved wife Jeannette and my parents Helga and Hartmut Schemel for providing the support and freedom, which finally made this work possible.

Zusammenfassung

Diese Arbeit gibt eine Einführung in die Modellierung von lokal reagierenden Wänden, sogenannten Linern. Ein Impedanzmodell zur Beschreibung eines Liners im Zeitbereich und dessen praktische Anwendung mit einem numerischen Verfahren für die Beschreibung der Schallausbreitung werden präsentiert. Besonderes Augenmerk wird auf die Modellierung von Strömungseinflüssen auf die resultierende Impedanz einer überströmten akustischen Auskleidung und die Vermeidung der mit dem Modell in Verbindung gebrachten Instabilität gelegt. Das numerische Verfahren wird zunächst detailliert beschrieben. Dabei wird auch auf die verschiedenen zur Anwendung gebrachten Modellgleichungen eingegangen. Des Weiteren werden Randbedingungen und numerische Herangehensweisen für die Verwendung von beliebigen mittleren Strömungszuständen und krummlinigen Koordinatensystemen aufgezeigt. Eine Methode zur direkten Überprüfung der numerischen Lösung mittels der akustischen Intensität, die ohne die Kenntnis einer analytischen Lösung auskommt, wird ebenfalls vorgestellt. Zur Überprüfung werden zahlreiche veröffentlichte Lösungen für Fragestellungen zur Schallausbreitung in akustisch ausgekleideten Strömungskanälen und die Abstrahlung von solchen Kanälen herangezogen. Die nahezu perfekte Übereinstimmung für viele der Beispiele verifiziert das Impedanzmodell und die numerischen Methode. Es werden modal axialsymmetrische, zwei- und dreidimensionale Problemstellungen von den Beispielen abgedeckt. Der Einfluss der verschiedenen Ansätze zur Unterdrückung der Strömungsinstabilität wird ebenfalls an diesen Beispielen untersucht. Es wird eine Methode zur Berechnung der Impedanz aus Messungen mit überströmten Dämpfern vorgestellt. Sie basiert auf einer Optimierung der Modellparameter des Impedanzmodells im Zeitbereich. Das Verfahren liefert den gesamten Frequenzgang der Impedanz mit einer Optimierung. Vier verschiedene akustische Auskleidungen werden untersucht. Bei allen wird der Frequenzgang sehr gut durch das verwendete, erweiterte Helmholtz-Resonator-Modell wiedergegeben. Bei einer Untersuchung der notwendigen Modellgenauigkeit für die Berechnung der Impedanz, wird ein relativ großer Einfluss von kleinen Reflexionen auf das Ergebnis bei der Verwendung von Druckamplituden als Vorgabe vom Experiment nachgewiesen. Daher werden in den folgenden Beispielen energetische Reflexions- und Transmissionsfaktoren, welche unabhängig von Reflexionen an den Rohrenden sind, zur Definition der Zielfunktion verwendet. Es werden Verbindungen zwischen den Modellparametern des Impedanzmodells und den spezifischen Abmessungen der akustischen Auskleidung hergestellt. Diese werden verwendet, um einer Messung zugängliche Parameter der Auskleidung aus den optimierten Modellparametern zu berechnen. Diese liegen für die vier Beispiele mit Ausnahme einiger Fälle, bei denen die Resonanzfrequenz des Helmholtz-Resonators nicht innerhalb des vermessenen Frequenzbereichs liegt, im erwarteten Bereich. Zuletzt werden noch Beispiele für die Anwendung der Impedanzmodellierung im Zeitbereich gegeben. Dabei wird Gebrauch von der Verknüpfung der Modellparameter zur Geometrie der Resonatoren gemacht. Das Impedanzmodell verringert die numerische Problemgröße dabei wesentlich.

Abstract

This work gives an introduction to the numerical modeling of locally reacting acoustic treatments. A time-domain impedance model and its implementation with a numerical method for Computational Aeroacoustics are presented. A special emphasis is put on the modeling of the flow effect on the impedance and the treatment of the related flow instability. First, the numerical method is described in detail including a variety of mathematical model equations, which are used in the present work. Boundary conditions and numerical approaches for the handling of arbitrary base flow fields and curvilinear meshes are presented as well. A method for the direct validation of a numerical solution by using the acoustic intensity is developed. It does not require an analytical solution. In a first validation, several benchmark problems from the literature, concerning the sound propagation in lined flow ducts and the radiation from such ducts, are considered. The almost perfect agreement of the current method for a large number of different problems verifies the correct implementation of the impedance model and the numerical method. Modal-axisymmetric, two- and three-dimensional examples are covered. The effect of removing the flow instability is studied with these examples. An impedance eduction method is applied, using an optimization to obtain the model parameters of the extended Helmholtz resonator model from *in-situ* measurements with four different liner samples. All are found to be well described by the extended Helmholtz resonator model. The time-domain impedance eduction provides the whole frequency response of the impedance by one optimization. The impact of the numerical modeling on the resulting impedance is also studied. The results indicate a significant influence of reflections in the experiment on the resulting impedance, when using pressure amplitude data as input for the impedance eduction. Thereafter, reflection independent energy transmission and reflection coefficients are used as input for the impedance eduction. The link between the educed model parameters and the geometry of the liner is pointed out. The connection is used to calculate measurable parameters of the liner from known geometry parameters and the eduction result. The educed geometry is found to be in a reasonable range for most of the examples. An exception is found with few cases, where the resonant frequency of the liner is not covered by the range of frequencies that is considered in the experiment. Finally, the link between geometry and impedance model is used in three different applications. The application of a time-domain impedance model significantly reduces the problem size in these cases.

Contents

Preface	I
Zusammenfassung	III
Abstract	IV
Nomenclature	IX
1. Introduction	1
1.1. Background	1
1.2. State of the art in Computational Aeroacoustics (CAA)	3
1.2.1. Zonal approaches	6
1.2.2. High-order CAA schemes	8
1.2.3. Non-reflective boundary conditions	8
1.2.4. Impedance modeling in the time domain	9
1.3. Relevant experiments	10
1.3.1. Measurement of the normal incidence impedance	10
1.3.2. <i>In-situ</i> measurement of the impedance	11
1.4. Structure of this work	13
2. Mathematical modeling	15
2.1. Governing equations	15
2.1.1. Mass conservation of a fluid element	16
2.1.2. Momentum balance over a fluid element	16
2.1.3. Energy balance over a fluid element	17
2.2. Nondimensional mathematical model	17
2.3. Perturbation approach	19
2.4. Nonlinear perturbed nonconservative nonlinear Euler model (PENNE)	19
2.5. Linearized Euler equations	20
2.6. Isentropic pressure–density relation	21
2.7. Modal axisymmetric approach	21
3. CAA method	25
3.1. Discretization schemes	25
3.1.1. Spatial discretization	25
3.1.2. Time stepping	27
3.1.3. Low-pass filtering of the solution	27
3.2. Base-flow field	30

3.3.	Handling of curvilinear meshes	31
3.3.1.	Metric	31
3.3.2.	Normal vector of a domain boundary	32
3.4.	Wall modeling for CAA methods	34
3.5.	Non-reflective boundary conditions	36
3.5.1.	Radiation/outflow boundary condition	36
3.5.2.	Sponge layer	40
3.5.3.	Perfectly matched layer (PML)	41
3.6.	Sound source	42
3.6.1.	Plane waves	43
3.6.2.	Generalization of the filtering approach for the interpolation of the source	43
3.6.3.	Modes in a cylindrical duct	44
4.	Time-domain impedance modeling	47
4.1.	The concept of acoustic impedance	47
4.2.	The Helmholtz resonator in frequency domain	48
4.2.1.	Helmholtz resonator panels for acoustic lining	49
4.2.2.	Neck correction	50
4.3.	Extension to high frequencies	50
4.3.1.	The broadband $\lambda/4$ -resonator	50
4.3.2.	Ko's broadband impedance model	51
4.3.3.	The extended Helmholtz resonator model (EHR)	53
4.3.4.	Comparison of the impedance models	54
4.4.	Models for a grazing flow on the impedance surface	56
4.4.1.	A resolved boundary layer at the impedance wall	57
4.4.2.	The Ingard/Myers boundary condition	57
4.4.3.	Hydrodynamic surface waves and the instability	58
4.5.	Development of a time domain representation	62
4.5.1.	Impedance models based on the mass-spring-damper analogy	62
4.5.2.	Implementation of the extended Helmholtz resonator (EHR) with flow	63
4.5.3.	Outlook: Generalization of time-domain impedance modeling	66
5.	Analysis and assessment of the numerical results	69
5.1.	Motivation	69
5.2.	Source location	69
5.2.1.	Introduction of the QPL scale for the source power level	70
5.3.	Intensity definitions	70
5.4.	Solution validation based on a global conservation of acoustic energy	71
5.5.	Comparison of the intensity definitions	73

6.	Impedance eduction from measurements	75
6.1.	Overview of the impedance eduction process	75
6.2.	Objective function	75
6.2.1.	Impedance eduction based on raw sound pressure level data	76
6.2.2.	Impedance eduction based on energy transmission and reflection	76
6.3.	Flow effects	77
6.4.	Optimization algorithm	78
7.	Results and Discussion	79
7.1.	Validation and verification of the impedance models	79
7.1.1.	Verification of the impedance boundary condition with the analytical solution	79
7.1.2.	Validation of the impedance models and the CAA method with a generic fully lined inlet duct	89
7.1.3.	Sound radiation from lined ducts	102
7.1.4.	Investigations using the benchmark data from the NASA grazing flow impedance tube (GIT) experiment	114
7.1.5.	Conclusions to the validation and code benchmark	118
7.2.	Impedance eduction	119
7.2.1.	NASA impedance flow tube experiment	120
7.2.2.	Plane liner samples at the DLR flow impedance test facility	130
7.2.3.	Single axisymmetric resonator	138
7.2.4.	Conclusions to the eduction results	143
7.3.	Applications of the EHR	144
7.3.1.	Modeling of the plenum impedance in an experiment for entropy noise	145
7.3.2.	Modeling of the plenum impedance in a combustion chamber	150
7.3.3.	Effect of large Helmholtz resonators on the propagation of low frequency noise	153
7.3.4.	Conclusions to the application examples	158
8.	Conclusions and Outlook	159
	Appendix	161
A.	Supplemental material for the mathematical models	163
A.1.	Derivations	163
A.1.1.	Manipulation of the energy equation	163
A.1.2.	Nondimensional form of the equations	164
A.1.3.	Transformation to the nonlinear PENNE equations	165
A.1.4.	Relation of the linearized Euler equations to the wave equation and concluding remarks	166
A.2.	Matrix–Vector form of the mathematical models for implementation	166
A.2.1.	Gradient and divergence for the specific coordinate systems	167

A.2.2. Nonlinear equations	167
A.2.3. Linearized model equations	169
B. Supplemental material for the CAA method	171
B.1. Discretization schemes	171
B.1.1. Spatial discretization	171
B.1.2. Temporal discretization	173
B.1.3. Filtering stencils	174
C. The effective impedance with flow	177
D. Detailed resources for the impedance eduction	179
D.1. SPL and phase data comparison for the NASA-GIT experiment	180
D.1.1. Uniform flow and anechoic terminations	180
D.1.2. Uniform flow and measured termination impedance	185
D.1.3. Measured flow profile and termination impedance	190
D.2. Comparison of energy transmission, reflection and dissipation coefficients	195
D.2.1. Perforate SDOF liner (AA-1)	195
D.2.2. SDOF liner with wire mesh (AA-2)	196
D.2.3. Axisymmetric samples with large cavity volume (DLR-1C)	197
Bibliography	201

Nomenclature

Latin symbols

A	Source amplitude
a	coefficients of the spatial discretization
B	Radial source amplitude function
c	speed of sound
d	damping rate per surface area for the mechanical analog
e	specific energy per volume
f	frequency
f_0	resonant frequency
f_f	characteristic frequency of Ko's impedance model
g	component of the metric tensor
H	cavity depth of a prismatic cavity volume
i	imaginary unit ($e^{i\omega t}$ -convention)
I	intensity vector
I	component of the intensity vector
J_m	Bessel function of the order m
K	volumetric force
k	free field wave number ($k = \frac{\omega}{c}$)
K_m	spring rate for the mechanical analog
k_m	spring rate per surface area for the mechanical analog
L	face sheet thickness and typical length dimension (L_∞)
l	cavity depth of a $\lambda/4$ -resonator
M	number of points forward involved to the discretization
m	azimuthal mode number
m_f	face reactance parameter (EHR)
N	number of points backward involved to the discretization
M_m	mass for the mechanical analog
m_m	mass per surface area for the mechanical analog
n	wall normal vector
n	radial mode number
P	power (energy per time)
p	pressure
q	heat conduction
Q	ratio of the Bessel and Neumann functions at the source
q_s	acoustic source strength
r	radial coordinate in cylindrical coordinates and energy reflection coefficient

R_f	face resistance parameter (EHR)
S	surface
s	specific entropy
s_p	curvature and convective terms (Ingard/Myers boundary condition)
S_0	open area of a liner panel or resonator
S_V	face area of a prismatic cavity volume
T_l	time constant/time delay (EHR)
T	temperature
t	time and energy transmission coefficient respectively
\mathbf{u}	velocity vector
u'	axial velocity perturbation
V	Volume of a cavity
v'	radial velocity perturbation
v_{gr}	group velocity
w	coefficients of the filter
w'	azimuthal velocity perturbation
\mathbf{x}	position vector in Cartesian coordinates
x	axial coordinate in cylindrical coordinates and component of the coordinate vector
Y_m	Neumann function of the order m
Z	complex impedance
z	inverse Fourier-transform of Z
Z'	effective impedance with flow

Dimensionless quantities

He	Helmholtz number, $He = L\omega/c$
Ma	Mach number, $Ma = u/c$
Re	Reynolds number, $Re = cL/\nu$
Sr	Strouhal number, $Sr = Lf/u_0$

Greek symbols

β	scaling factor of the cotangent term/cavity reactance parameter (EHR)
Δx	step size of the spatial discretization
Δ	energy dissipation coefficient
Δ_L	neck length correction
ε	cavity resistance parameter (EHR)
γ	ratio of the specific heats
λ	wavelength
μ	pressure in the fluid layer at rest (Ingard/Myers boundary condition)
$\mu_{m,n}$	eigenvalue of the Bessel function for the source
ν	kinematic viscosity

ω	angular frequency
ω_f	characteristic angular frequency of Ko's impedance model
ϕ	acoustic potential
φ	azimuthal angle in cylindrical coordinates
Φ	perturbation vector
Ψ	transfer function of a filter
ψ	stream function
ϱ	density
σ	filtering and damping factor and open area ratio
σ	open area ratio of a liner
τ	component of the stress tensor and time (for integration)
τ	stress tensor
ξ	coordinate vector in the computational domain
Ξ	Objective function
ζ	dimensionless impedance

Operators

∇_n	normal derivative $n \cdot \nabla$
$\langle \cdot \rangle_t$	time average
δ_{ij}	Kronecker delta function
$\frac{D}{Dt}$	material derivative
\mathcal{F}	Fourier transform
Im	imaginary part of a complex number
Re	real part of a complex number

Superscripts

'	perturbation about the average flow state or spatial derivative
*	complex conjugate or numerical approximation to an expression
^	complex amplitude
~	dimensional quantity and fluid at rest at the surface

Subscripts

0	average flow state/base flow quantity
∞	unit quantity for nondimensional description
n	normal component
a	acoustic perturbation
x	axial component

Acronyms

AIBM	Acoustic Intensity based Method
CAA	Computational Aero-Acoustics
CDS	Central differencing scheme
CFD	Computational Fluid Dynamics

CFL	Courant–Friedrichs–Lewy ¹ number
CPU	central processing unit
DFG	Deutsche Forschungsgemeinschaft
DG	Discontinuous Galerkin method [98]
DRP	Dispersion Relation Preserving scheme [127]
EHR	Extended Helmholtz Resonator [108]
FEM	Finite Element Method
GIT	NASA grazing flow impedance tube
LDDRK	Low-Dissipation Low-Dispersion Runge-Kutta scheme [50]
LEE	linearized Euler equations
LES	Large Eddy Simulation
MPI	Message passing interface [130]
MS	Multiple Scales
PDE	partial differential equation
PENNE	Perturbed Nonconservative Nonlinear Euler Equations
PML	perfectly matched layer
PPW	points per wavelength
RANS	Reynolds averaged Navier-Stokes
SDOF	single degree of freedom
SPL	sound pressure level
WKB	Wetzel, Kramers and Brillouin

¹R. Courant, K. Friedrichs and H. Lewy, Über die partiellen Differenzengleichungen der mathematischen Physik, *Mathematische Annalen*, vol. 100, no. 1, pages 32–74, 1928.

1. Introduction

1.1. Background

The sustained development of today's air traffic is connected to a complex interaction of the airports as economical hot spots and the surrounding infrastructure. This usually results in attracting people to live in the structurally and economically well established areas in the vicinity of airports. To serve the objective of an airport, airplanes have to pass its surrounding at low altitude for take-off and approach maneuvers. Due to the exposed radiation from an aircraft flying low overground in urban areas the air-traffic noise affects a large number of people. The European Community estimates, [26], that over 40 million people were affected by aircraft noise in Europe in the year 2001. For comparison only 24 million were affected by road noise and about three million by railway noise according to the same study [26]. The economical growth of an airport is found to be limited mainly by the public acceptance of the air traffic with respect to the noise emission [26] and consequently the noise emission of each single flight maneuver. Due to the effects of noise on economy, environment, well being and health, aircraft noise reduction is an important objective of the union and national European funding for research activities defined for instance in the ACARE 2010 and 2020 goals [27], and the noise radiation from an aircraft at take-off and approach is a critical design condition for all aircraft components.

In addition to the community noise requirements the cabin noise has become a major comfort criterion and marketing argument for aircraft manufacturers. With increasing application of composite materials in aircraft construction, the noise reception into the cabin has become even more critical. Acoustic design of all aircraft components is usually a compromise between noise reception and lightweight construction. The requirement of additional damping of the cabin and nacelle for noise reduction in the worst case cancels the weight reduction achieved by the application of modern composite materials. A noise reduction at the source of noise is a major objective to exploit the potential of modern materials and lightweight construction.

On the noise emission side, all devices in the outer flow (wings, flaps, landing gear etc.) are potential sources of airframe noise. This is the major source of aircraft noise besides the noise generation by the aeroengines. Modern high-bypass ratio turbofan-engines are characterized by a large reduction of the jet noise. It is still the major source of noise at approach. However, a continued reduction of the jet noise makes the latent internal noise sources become dominant at approach conditions for certain observation angles today. Such sources are for instance the main fan, engine core and internal-flow noise. The compressor, turbine and combustion system are abstracted as the core, which features further different acoustic source mechanisms.

Fan, compressor and turbine consist of rotating and fixed blades, which produce the necessary momentum for the main fan and at the same time radiate rotor-alone and rotor-stator-interaction noise. Future turbofan engine designs will probably feature geared fans. This would result in additional fan noise and mechanical noise from the lightweight gear box, together with a further reduction of jet noise. Noise radiation and thrust generation are inseparably connected to a certain extent [35], such that the possible emission reduction is limited for these components. However, the ducted-fan design allows for further noise reduction on the internal path of noise by using acoustic lining.

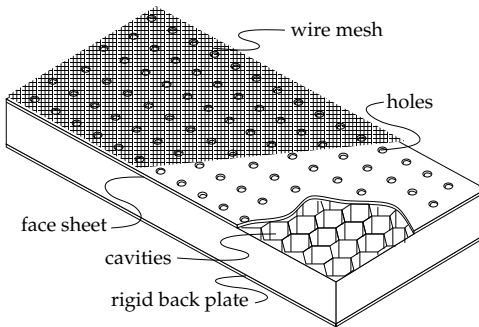


Figure 1.1.: Honeycomb-type liner panel

Today, the passive acoustic treatment of the internal path of noise in aeroengines is a standard technique. The best ratio of weight and noise reduction is currently achieved by generalized Helmholtz resonator panels as the one sketched in Fig. 1.1. The third generation of such panels still features the basic design consisting of rigid back plate, cavities and perforated face sheet. However, a wire mesh has been added to obtain stable damping properties for all flow speeds. The description as Helmholtz resonator or coupled system

of such resonators still applies rather well for these linings. New aeroengine liner concepts involve a septum inside the cavity to produce multiple degrees of freedom. In this way the broadband damping behavior of the liner can be improved. Future developments may involve ceramic foams and even active or adaptive liner concepts, which require a generalized theory for their description.

Numerical methods have successfully gained acceptance in all fields of industrial research and development. While the industrial application of computational fluid dynamics (CFD), which mainly concerns the averaged flow characteristics, has been left behind for the research, the focus at the Universities has been towards the development of accurate and cost-efficient numerical methods for the description of unsteady flow phenomena. Numerical methods for the computation of specific aeroacoustic phenomena have been greatly developed over the last two decades. These methods can exhibit important achievements for all the issues that are relevant to the aeroacoustics of an aeroengine. The turbo-machinery noise generation is well described by advanced CFD methods based on unsteady RANS or DES approaches [87]. The combustion system is covered by unsteady RANS or LES approaches e. g. [13, 70, 140]; the jet noise is well predictable using a combination of classical DES, LES or DNS as well as newly developed high-order methods and an acoustic analogy to obtain the far-field radiation, e. g. [5]. Finally the sound propagation inside

the engine ducts and to the moderate far field is efficiently predicted by high-order schemes for computational aeroacoustic problems [74, 115, 135, 141, 142].

The description of the whole engine by a single optimally efficient method is still out of reach for the next few years. This means that zonal approaches, combining different methods for different physics, form the state of the art up to now. The concept of this zonal description of the problem will be addressed in more detail below. Even though the modeling of the noise generation and propagation has made significant advances in the past, there are still two essential modeling problems remaining insufficiently solved. One concerns the non-reflective boundary condition at the open ends of the computational domain. The related numerical boundary conditions are usually based on the idea to allow no reflections at such points, which is then more or less realized for the numerical solution of a specific problem. The other is the efficient description of an acoustic lining under flow conditions in the time domain, which is still insufficient in terms of stability and the coverage of relevant liner designs. A time-domain impedance boundary condition, which is able to model a variety of different acoustic impedances would be a solution for both of the above problems. It could be applied as a replacement for the non-reflective boundary conditions modeling the reflections from connected duct systems outside the computational domain, as well as for its original purpose of describing an acoustic treatment.

The current work contributes to the development of impedance boundary conditions. It concerns the extension of a numerical method for computational aeroacoustics (CAA) by a time-domain impedance boundary condition, which allows grazing flow conditions. An optimized computational aeroacoustics (CAA) method is chosen as platform for the implementation of the impedance boundary condition. The field currently undergoes a rapid development, such that this work must address the enhancement of the CAA method and boundary conditions, as well as its generalization to three-dimensional problems. However, the time-domain impedance boundary condition is not limited to the current numerical method and the application with an aeroengine problem. Rather, the current work is intended to provide a general insight to time-domain impedance modeling. The validation and verification of the method with the analytical solution and experiments is an important aspect of the current work. In addition, a method for the validation of a specific numerical solution, which is based on the conservation of the acoustic energy, is presented.

1.2. State of the art in Computational Aeroacoustics (CAA)

An attempt of a definition of CAA: While the origin of the discipline of Aeroacoustics can be precisely tracked back to a publication of Sir James Lighthill [75] in 1952, the origin of Computational Aeroacoustics can only approximately be defined; it can be dated back to the early 1980's. The first occurrence of the term "computational aeroacoustics" is probably in a visionary publication of Hardin and Lamkin

[42], who claimed and showed that with the ongoing development of computing resources, computational aeroacoustics has become possible with one of the first aeroacoustic simulations of a cylinder-wake flow. In a second publication, [43], Hardin and Lamkin introduced the acronym CAA for computational aeroacoustics. Unlike the numerical method which is described in this work, Hardin and Lamkin used a non-optimized “classical” CFD method in their early works.

In their sense, the term CAA was originally defined as a numerical simulation of the aerodynamic noise generation with standard CFD methods in combination to a simulation of the noise propagation with an acoustic far-field prediction method. Later the term CAA method was applied to describe the large variety of new high-order methods [50, 67, 93, 127], which were developed specialized for the simulation of aeroacoustic phenomena. The growing CAA community adopted and extensively applied the term CAA method for any computational method that was developed to describe the aerodynamic noise generation and/or propagation. This definition still covers the application of an acoustic analogy as CAA method. However, today the term is commonly used, other than it was originally defined, in the sense of an optimized method for solving the governing equations of the acoustic wave propagation in an arbitrary flow. In order to give to the CAA method which is used in this thesis a more definite form, the state of the art in CAA methods, is described following in this section.

Problem size for acoustic applications:

To understand the requirement of a special numerical method for the computation of aeroacoustic phenomena, one may consider the following task. The sound propagation in a cube with a side length of 1 m is to be calculated without flow. The medium is considered to be air with a speed of sound of approximately $c = 340$ m/s. The upper frequency limit to be resolved is set to 10 kHz. The resulting minimum wave length is $\lambda = 0.034$ m. Now consider a numerical method, which uses an equidistant mesh to solve a wave equation numerically. The numerical accuracy of the method depends on the spatial resolution. Therefore, the minimum number of points per wavelength (PPW) is given by the highest wave number and the accuracy requirement of the scheme. The free-field wave number $k = \omega/c$ is considered as the upper limit; higher duct modes and waves propagating transverse to the

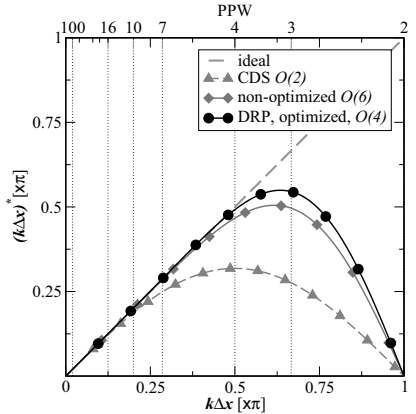


Figure 1.2.: Computed relative wave number over physical relative wave number.

mesh have a lower projected wave number. An example of the functional dependence of the relative wavenumber $(k \Delta x)^*$ of several central differencing schemes on $(k \Delta x)$, which defines the accuracy limit of the scheme, is given in Fig. 1.2. One can see from the figure, that a low-order scheme requires a higher resolution for the same accuracy. The exact accuracy limit is, however, not visible from the mode of presentation in the figure. The number of points per wavelength is connected to $(k \Delta x)$ by $n_{PPW} = \lambda / \Delta x = 2\pi / (k \Delta x)$. When considering a typical second-order scheme of computational fluid dynamics, the accuracy limit is found to be about $n_{PPW} \geq 50$ PPW. So to resolve the above cube, one needs 50 points in the minimum wavelength $\lambda = 0.034$ m or about 1500 points per dimension of the cube, which results in a mesh of about 3 billion (3×10^9) mesh points. The time-resolved simulation of the problem requires to compute a time series, that allows an acoustic wave to cross the whole cube, which is 0.042 s. Considering an equal ratio of space and time discretization ($CFL = 1 \Leftrightarrow \Delta t = \Delta x / c = 2 \times 10^{-5}$ s), at least about 2000 time steps have to be calculated to allow that. Currently, such large problems can only be handled on large parallel computing facilities and the simulation consumes a large amount of computational time. Therefore, the application in the industrial design process is not affordable. On the other hand, optimized high-order CAA methods can practically reach an accuracy limit of about $n_{PPW} \geq 7$ PPW. This limit results in a mesh spacing of 5 mm, or 200 points per dimension of the 1 m^3 cube. The resulting three-dimensional mesh has a point number of only 8 million. The time step size is also increased if the CFL number remains close to one. Less than 300 time steps are necessary for the waves to cross the whole computational domain at least once. Altogether the problem size can be reduced by a factor of 2500, due to the introduction of an optimized high-order scheme. As a consequence of this reduction, the problem becomes computable on a single modern desktop system within several hours. Even though the high-order method requires more arithmetic operations per point and time step than a similar low-order discretization, an advantage remains for the high-order method. This advantage is the mainspring for the continued development of optimized CAA methods.

Hydrodynamic modes of perturbation: The above consideration is valid only for acoustic waves in a homogeneous cube of air at rest. The presence of an inhomogeneous base flow adds more complications. When considering a perturbation about the mean state of the fluid, four different types of modes of perturbation are found according to Chu and Kovásznyai [25]. Two of these modes are of acoustic nature, running with the local speed of sound up- and downstream relative to the moving medium. The other two are described as vortical and entropy-mode wave; these hydrodynamic modes of perturbation are found to move with the flow speed, which complicates the situation. Due to the disparity of the length scales is impossible to resolve the hydrodynamic and all acoustic modes in the same frequency range. Moreover, and different from the acoustic perturbations, the hydrodynamic modes are significantly affected by viscosity and heat conduction. Therefore, the region of

interest for a numerical solution differs for the hydrodynamic and acoustic perturbations. This fact leads directly to the idea of a zonal approach, not only with respect to different numerical methods, but also to the different physics.

1.2.1. Zonal approaches

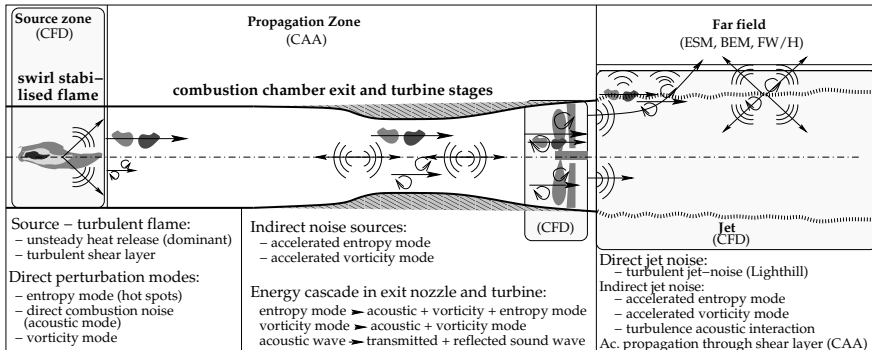


Figure 1.3.: Sources of sound in a generic combustion system with turbine and exhaust jet attached.

A relatively complex example for the application of a zonal approach is the combustion chamber of an aeroengine with the connected turbine and exhaust duct. As can be seen from the simplified sketch of Fig. 1.3, the system features several sources. One major source of perturbations is the combustion process itself. Some of the additional sources are described as linear or nonlinear interaction of perturbation modes with each other and the base flow according to Chu and Kovásznyai [25]. The sound sources further downstream are the turbine and the jet. Both have to be described by a compressible CFD approach. The turbine stages feature several nonlinear source mechanisms. There is the tonal noise generation at the blade passing frequency due to the interaction of the aerodynamic fields of rotor and stator blades and the turbulent broadband noise of the accelerated wakes of each turbine stage. In addition, accelerated flow inhomogeneities from upstream engine components generate noise according to first experimental reports by Sharland [119]. Finally, besides the first-order linear refraction of sound waves due to the shear layer of the jet, there is a nonlinear scattering of sound in the strong vorticity of the shear layer which leads to the spectral broadening of tonal components. The linear interaction of perturbations with the inhomogeneous base flow is covered by a linearized Euler model. The nonlinear effects of perturbations, which are interacting with each other, reduce the possibility of a simplified mathematical modeling. Furthermore, the direct perturbation sources as the direct noise generation by the turbulent flame,

the rotating potential flow field around the turbine rotor, the rotor–stator interaction in the turbine stages and the turbulent jet-noise cannot be described by an inviscid model. These regions require a solution of the full viscous Navier-Stokes equations, which has been indicated in Fig. 1.3 by the term (CFD). This CFD-like model does not necessarily imply the application of a low-order CFD scheme. However, the nonlinear viscid mathematical models which describe this zone are usually implemented with such numerical methods for historical reasons. The advantage of the zonal approach is obvious; well established and validated low-order methods can be applied for the regions of sound creation, while the sound propagation is covered by the newly developed CAA schemes. In an earlier stage, simplified models for the source may be used (e. g. a single Tyler-Sofrin [133] mode for a rotor-stator-stage).

The idea of a zonal approach gets a further boost when considering the typical magnitude of interest. While the hydrodynamic perturbations are usually high-amplitude phenomena, the audible range from the hearing threshold to the threshold of pain has a dynamic range of several decades. The hearing threshold is characterized by a particle displacement, in the range of the mean free path of a particle. The minimum audible pressure amplitude is 10 orders of magnitude below the ambient pressure in air according to Ehrenfried [31], then. A perturbation approach is introduced to overcome numerical difficulties due to the limited mantissa of a real number.

In the above example of Fig. 1.3, the combustion zone is featuring nonlinear interaction and chemical reactions. It could be considered by an incompressible LES or unsteady RANS simulation, which provides the relevant perturbation sources. This incompressible CFD simulation, in which the density is only a function of temperature, can only cover the incompressible phenomena as the low Mach number flow inside the combustion chamber. The acoustic wave propagation in the whole combustion system is then described by complementary systems of acoustic perturbation equations as it was developed by Ewert and Schröder [34] and later Bui et al. [19] and Seo and Moon [118]. The required acoustic sources are obtained from an analysis of the CFD simulation results. This limitation can however be overcome by an extension of the perturbation approach to allow the propagation of hydrodynamic and acoustic perturbations. So, fully, partially or only at the boundary overlapping zonal approaches become possible using a linearized Euler model. A partially overlapping zonal approach based on an unsteady RANS simulation of the source zone was for example described by Schemel et al. [114] using a sponge layer to couple the perturbations from the CFD simulation into the propagation zone.

In the above example of Fig. 1.3, we can also put in evidence some drawbacks associated with the zonal modeling. The sound propagation at the interface between the sound source and the propagation zone is usually not bi-directional. Therefore, reflections from the propagation zone cannot reach a point in the source zone. A standing wave in the whole duct cannot be described in this way. Reflected waves from connected duct systems are of special importance for combustion problems, as various authors report [52, 82, 103]. An impedance boundary condition could be used to add these reflections to the simulation of the source zone. Furthermore, the

propagation of noise through a region with strong sound sources requires a switching between the propagation zone and the source zone approaches. This requires the source zone method to correctly predict the propagation of perturbations. The problem is best addressed by using a numerical method, which is capable of handling both, the source and the propagation zone, with a high-order CAA method. This idea was for instance followed by Bogey and Bailly [12] and Schwartzkopff et al. [116]. Note that these source handling CAA methods fully replace the zonal approach for the acoustic propagation to the moderate far field.

1.2.2. High-order CAA schemes

The development of high-order CAA schemes followed the starting shot of Hardin and Lamkin [42] with some years of delay. Several methods were presented of which the finite-difference ones took a large share; the compact scheme of Lele [67] or the Dispersion Relation Preserving (DRP) scheme of Tam and Webb [127] were developed in this time, to name only some examples. Others used Discontinuous Galerkin methods [98] or spectral elements [93] in the frequency domain. The time integration for the finite difference and Discontinuous Galerkin methods is formulated explicitly. Unsteady acoustic problems require a high time resolution with a CFL-number around unity, such that the time explicit formulation has no disadvantage. Optimized Adams-Bashford schemes as in Tam et al. [128] and optimized Runge-Kutta schemes as the Low-Dissipation Low-Dispersion Runge-Kutta (LDDRK) of [50] or the 2N-storage schemes of Stanescu and Habashi [121] were developed. Problems of the finite-difference schemes in handling short waves were overcome by the introduction of selective artificial dissipation, in the earlier applications [128]. Later repeated filtering of the solution [12, 102, 142] or the implementation of a filter into a high-order optimized backward stencil [144] were found to be much more reliable and efficient, especially in connection with curvilinear non-equally spaced meshes.

1.2.3. Non-reflective boundary conditions

With the development of the field of CAA new key problems were introduced. Different from the elliptic equations associated with incompressible fluid dynamics, the aeroacoustic model is of a hyperbolic type. The hyperbolic system allows reflections from the boundaries to propagate through the whole computational domain. Therefore, the computation of a numerical solution to an aeroacoustic problem requires boundary conditions, which model an anechoic termination. This new key issue of CAA was addressed by several authors with different approaches. An overview about the non-reflective boundary conditions for computational aeroacoustics can be found in Tam [123].

In general, two classes of non-reflective boundary conditions can be identified from this overview: Firstly there are generalized characteristic-based boundary conditions, which formulate a radiation problem at the boundary to obtain an approx-

imation for outgoing waves. Examples for such conditions are presented by Giles [40], Thompson [131, 132], Tam and Webb [127] and Bogey and Bailly [11]. While Giles [40] and Thompson [131, 132] use an analysis of the Fourier transformed governing equations and characteristics, Tam and Webb [127] and Bogey and Bailly [11] formulate their boundary condition directly as a radiation problem from a compact source. The second type can be characterized as absorbing layer boundary conditions, which add dissipation to the differential equation in order to remove any perturbation before reaching the boundary. An early example for such a boundary condition, which finds application in CAA is the sponge layer presented by Israeli and Orszag [54]. The idea was later refined, in order to remove reflections from the interface to the sponge layer, obtaining the perfectly matched layer (PML) boundary condition [9, 48, 49]. Several authors developed different PML formulations [1, 2, 45] for Discontinuous Galerkin or Finite Element methods.

The one boundary condition which gives similar good reflection properties for all possible applications, is still not yet available. The ongoing development on the area is represented by Ehrenfried [30] and Hu et al. [51] to name only some of the more encouraging approaches. The present thesis uses three different boundary conditions, which were found to be complementary in terms of accuracy, possible application and computational effort. These boundary conditions are described in Section 3.5.

1.2.4. Impedance modeling in the time domain

The modeling of a partially-reflecting surface by its impedance is the major objective of the current work. The reflective properties of an acoustic lining or connected systems are described by a complex number, the impedance, in the frequency domain. In general, the inverse Fourier transform of a impedance boundary condition from the frequency- to the time domain leads to a convolution. This can be solved by a direct numerical approach, as has been shown recently by Burak et al. [20]. However, the method is still expensive. For some specific representations of the impedance as a function of frequency, it is possible to obtain a convolution free time-domain representation, e. g. by using derivatives and integrals as Tam and Auriault [124] or the z -transformation of a periodic frequency response as Özyörük and Long [88] and Rienstra [108]. Tam and Auriault [124] use a mass-spring-damper model as template for the frequency response of the impedance. Their model has been extended by Fung et al. [39] and Tam et al. [122] with higher order time derivatives, yielding higher powers of $i\omega$ without physical interpretation. Even though, these first works can be considered as a milestone in impedance modeling, further development in the area took a long time coming. The first attempts of Tam and Auriault [124] and Özyörük and Long [88], Özyörük et al. [90] were not able to handle grazing flow conditions on the impedance surface or the method was found to be unstable under several flow conditions. The problems are found to be associated with the simplified description of the grazing base-flow conditions on the lined surface by the Ingard/Myers boundary condition [85]. An instability was first reported by

Tester [129] in a numerical study of overflown impedance surfaces. Several groups were involved to the continued development of time-domain impedance modeling, [38, 39, 61, 88, 89, 90, 124]. The presence of an instability was either theoretically or numerically reported in all the cited papers considering nonzero base flow velocities. The theoretical description has provided more and more detailed information about the instability over the last 13 years [16, 107, 111, 124]. A detailed discussion of all aspects of time-domain impedance modeling is given in Chapter 4.

1.3. Relevant experiments

The implementation of a new time-domain impedance boundary condition cannot be performed without validation experiments. These experiments are summarized in this section. Some further experimental results are included to the discussion in Chapter 7.

1.3.1. Measurement of the normal incidence impedance

The measurement of the normal incidence impedance with a so called Kundt's tube¹ as sketched in Fig. 1.4 is well established and described by DIN 52215 (ISO 10534) [29]. It is based on a two-microphone method, which allows to split incoming and reflected waves, based on the observed pressure amplitude and phase at the two microphone positions. A plane wave assumption is used to reconstruct the sound field at the surface of the sample object and the normal-incidence impedance is calculated as the ratio between acoustic pressure and velocity-perturbation amplitude. However, this technique does not allow an impedance measurement in the presence of grazing flow over the surface. Such grazing flow conditions are found in all aircraft liners (aeroengine inlet, bypass ducts and exhaust as well as air conditioning), in operating conditions. An *in-situ* measurement of the impedance, as it is described in the next section, becomes necessary to account for the grazing flow.

Direct measurement of the impedance: A new method for the exact local measurement of the impedance is currently becoming available. This method makes use of a so called PU-probe, which is an instrument to measure the local pressure and velocity. The impedance is obtained directly from the measurement at the surface. The method is described by Lanoye et al. [66]. It is able to provide a highly resolved map of the local impedance and has been demonstrated to be successfully applied without flow [66]. However, currently there is no impedance data which was obtained by such probes under grazing flow conditions. Therefore, the method could not be considered in the current work.

¹Named in memoriam to the German Mathematician and Physician August Kundt (*November, 18th, 1839 – †May, 21st, 1894) who used a similar tube made of glass to visualize sound waves and measure the speed of sound in 1866 and later worked with Hermann von Helmholtz in Berlin [136].

1.3.2. *In-situ* measurement of the impedance

As described above, an *in-situ* measurement of the impedance of an acoustic liner with the exact flow conditions found in the application is very desirable. A group of NASA was one of the first who developed a measurement technique which allows a grazing flow on the impedance surface [68]. The experimental setup is sketched in Fig. 1.5(a). The liner sample is flush mounted to one side of a flow duct with square cross section. The pressure field in the hard walled sections up- and downstream of the liner sample and opposite to the liner sample is measured by microphones. The first experiments with flow in the 1980's used a traversing mechanism for the microphone, whereas nowadays a large number of flush mounted microphones are used for a simultaneous measurement [55, 56, 57, 59, 60, 68, 69]. The input acoustic field is controlled by a control loop using several speakers and one microphone to obtain the desired sound field. An anechoic termination is used for the downstream end only. Up till now there is no report of an impedance eduction involving higher modes, such that the measurable range is limited to frequencies below the cut-on of the first higher mode in the test section or a large error must be accepted for higher frequencies.

Similar experiments are found in different test facilities of which one of the first was the NLR acoustic flow duct facility [65]. This facility employs two settling chamber of an Eiffel-type wind tunnel² as reverberant chambers to measure the overall acoustic intensity in the test sections up- and downstream the liner. This measurement allows to calculate an overall energy dissipation due to the liner sample under grazing flow conditions. Published measurements are not limited below the cut-off of the first higher mode [84]. However, the different attenuation characteristics for higher modes lead to an increase of the error for frequencies above the cut-on of the first higher mode in the test section.

A comparison of the further American *in-situ* test facilities of Boeing, General Electric and B. F. Goodrich may be found in Jones et al. [55]. All these experiments use either the NLR or the NASA method to acquire the acoustic data. In this work, *in-situ* measurements, which were carried out in a new test facility at the DLR in Berlin [22, 46], are used. This test setup combines the features of NASA and NLR experiment. Microphones in the hard walled inflow- and outflow ducts are used to

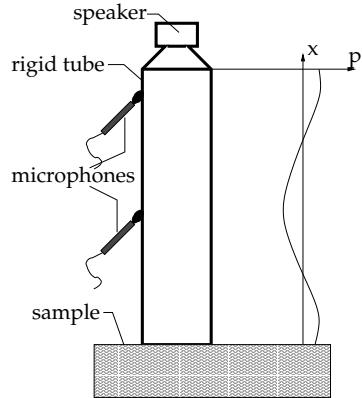


Figure 1.4.: Kundt's tube

²In memoriam to the French engineer Gustave Eiffel (*December, 15th, 1832 – †December, 27th, 1923 [136]), who first used a suction type wind tunnel design, which sucks air from the environment through the test section and blows it off to the free space afterwards.

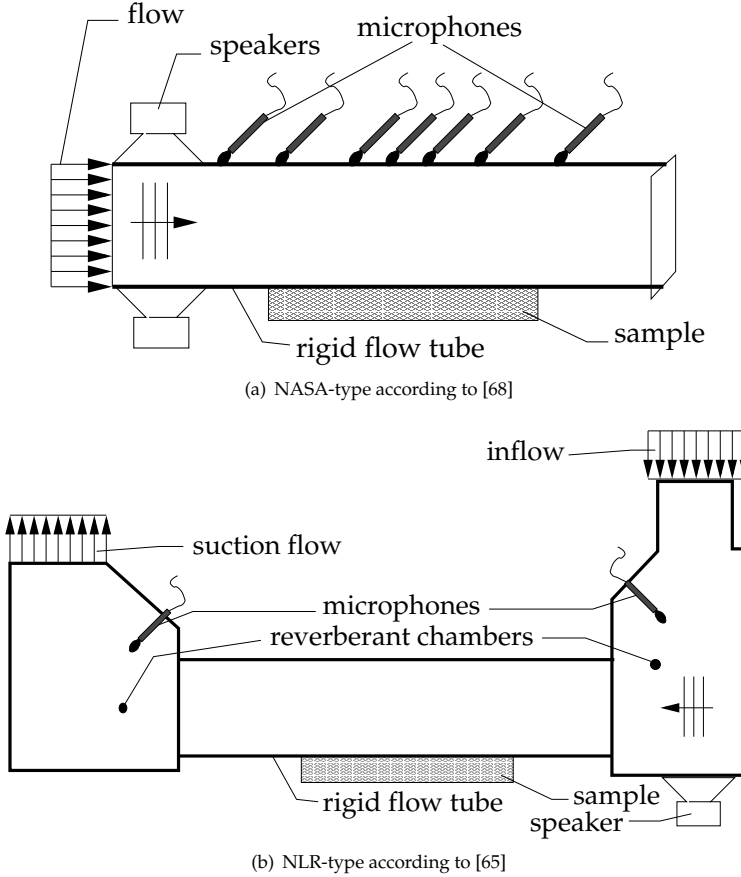


Figure 1.5.: Schematics of the different acoustic flow tube designs for in-situ impedance measurements

calculate the acoustic power up- and downstream the lined duct section. The measurement is made independent of reflections by a combined analysis of the up- and downstream excitation using a modal analysis [46]. This finally leads to a reflection independent measurement of the acoustic energy dissipation with a small number of microphones. Furthermore, the absence of microphones at the wall opposite to the sample allows to investigate two lined walls and cylindrical liner samples. Even though, there are no theoretical limitations which would disallow that, the method has not yet been applied to frequencies above the cut-on of the first higher mode.

As can be seen from the above summary of experimental methods, two general concepts find application: A detailed measurement of the sound pressure level opposite to the liner allows to calculate an exponential decay along the liner, whereas the measurement in the up- and downstream sections allows to calculate the insertion loss and energy dissipation due to the sample. These measurements are then used as input for a numerical impedance eduction. The different measurement methods are theoretically equivalent. However, practically they may show different error tolerance. The current work uses published experimental data of the NASA flow tube experiment [57] as well as data obtained in cooperation with the DLR from their flow tube to compare the usability of the different data for the impedance eduction.

1.4. Structure of this work

This work is organized as follows. First the mathematical models are presented in Chapter 2. Then the numerical CAA-method and the standard boundary conditions, which are used in the current work, are given in Chapter 3. The time-domain impedance modeling is reviewed and the implementation of the related boundary condition is described in Chapter 4. A method for validating the numerical solution and locating sources is presented in Chapter 5. The impedance eduction method used in the current work will be detailed in Chapter 6. Then, the results will be presented and compared to analytical solutions and experiments in Chapter 7. Finally conclusions are drawn in Chapter 8.

2. Mathematical modeling

In this section a class of mathematical models for time domain CAA methods will be presented. All of them are based on the idea of separating the nonstationary flow into a stationary base flow and an instationary perturbation. Such a perturbation approach has an advantage when considering a small acoustic perturbation, which would otherwise be hidden below the numerical noise of the mantissa of the digital representation of the base flow.

Here, the focus is put on the inviscid linear acoustic wave propagation in an arbitrary flow field. The inviscid modeling has the advantage that no resolved simulation of boundary layers is required, even though it is still possible for the base flow. Furthermore, the acoustic boundary layers are usually very thin and a resolved simulation of them in a current aeroengine on today's computing resources would result in a practically not yet solvable problem. A finite-difference method is used for the discretization as described in Chapter 3. Therefore, a differential formulation of the governing equations has been chosen here.

This section shortly sketches the development of several perturbation models, which are based on the inviscid Euler equations for the perturbation. However, it will be shown that the base flow can be any viscous or inviscid flow field. To increase the efficiency and accuracy, simplified mathematical models are developed, which are applicable in the propagation zone of the zonal approach described in Section 1.2.1. Several subsequent models with increasing limitations due to the modeling assumptions, which were implemented with the numerical method in Chapter 3, are presented. A vector notation without predefined limitation of the model to a specific coordinate system (2D, modal-axisymmetric or 3D) is used for the development. The mathematical form for the implementation into the numerical method is detailed in Appendix A.2. At the end of this chapter only the modal axisymmetric approach is presented and the particular features of the other coordinate systems are addressed in the Appendix A.2.1.

2.1. Governing equations

The governing equations describing a compressible perturbation in an instationary fluid flow are the Navier-Stokes equations, in general. These are the conservation law for the mass, the momentum balance and the energy balance given in the following according to the derivations of Pierce [95], Rienstra and Hirschberg [110], Spurk [120] and Zierep [148]. The primitive form of the balances is used in an Eulerian way of description in a fixed frame of reference. However, the formulation of the impedance boundary condition in Chapter 4 will be freely applicable with any

system of equations for the fluid motion. The derivation is carried out, starting from the physical quantities consisting of a value and the corresponding SI unit, which is denoted by a tilde above the symbol. Later the nondimensional quantities without tilde are introduced for the implementation with the numerical method.

2.1.1. Mass conservation of a fluid element

The mass conservation of a fluid element is written using the density $\tilde{\rho}$ and the velocity vector $\tilde{\mathbf{u}}$ as follows (comp. [120, 148]):

$$\frac{\partial \tilde{\rho}}{\partial t} + \tilde{\mathbf{u}} \cdot \tilde{\nabla} \tilde{\rho} + \tilde{\rho} \tilde{\nabla} \cdot \tilde{\mathbf{u}} = 0. \quad (2.1)$$

In the following, the material derivative $\tilde{D}(\cdot)/\tilde{D}\tilde{t}$ will be used for a more compact notation of the governing equations:

$$\frac{\tilde{D}(\cdot)}{\tilde{D}\tilde{t}} := \frac{\partial(\cdot)}{\partial \tilde{t}} + \tilde{\mathbf{u}} \cdot \tilde{\nabla}(\cdot). \quad (2.2)$$

The mass conservation of Eq. (2.1) is recast using the definition of the material derivative to:

$$\frac{\tilde{D}\tilde{\rho}}{\tilde{D}\tilde{t}} + \tilde{\rho} \tilde{\nabla} \cdot \tilde{\mathbf{u}} = 0. \quad (2.3)$$

2.1.2. Momentum balance over a fluid element

Here the Navier-Stokes equations describing the motion of a viscous fluid are considered as a starting point for the derivation. These equations combine the constitutive law for a Newtonian fluid with the balance of momentum. The equations are written using the pressure \tilde{p} , viscous stresses described by the shear-rate-tensor $\tilde{\tau}$ and the volumetric forces \mathbf{K} in addition to the variables introduced above, comp. [95, Eq. (10-1.14)]:

$$\tilde{\rho} \left(\frac{\partial \tilde{\mathbf{u}}}{\partial t} + \tilde{\mathbf{u}} \cdot \tilde{\nabla} \tilde{\mathbf{u}} \right) = \tilde{\rho} \mathbf{K} - \tilde{\nabla} \tilde{p} + \tilde{\rho} \tilde{\nabla} \cdot \tilde{\tau}. \quad (2.4)$$

In the following, the volumetric forces \mathbf{K} are neglected, as neither gravity nor magnetic forces are important in current aeroengines. The surface-forces have been split into the normal pressure forces \tilde{p} and the viscous stresses $\tilde{v} \tilde{\tau}$. Here, the shear-rate tensor is denoted by the symbol $\tilde{\tau}$. It describes the dissipation due to viscous effects in the fluid at motion. In Eq. (2.4) the kinematic viscosity \tilde{v} is denoted by the symmetric null-trace shear-rate tensor, according to Pierce [95, Eq. (10-1.10)], by:

$$\tilde{\tau}_{ij} = \frac{\partial \tilde{u}_i}{\partial \tilde{x}_j} + \frac{\partial \tilde{u}_j}{\partial \tilde{x}_i} - \frac{2}{3} \tilde{\nabla} \cdot \tilde{\mathbf{u}} \delta_{ij}.$$

Using the material derivative, the balance of momentum can be written as follows:

$$\frac{\tilde{D}\tilde{\mathbf{u}}}{\tilde{D}\tilde{t}} + \frac{1}{\tilde{\rho}} \tilde{\nabla} \tilde{p} = \tilde{v} \tilde{\nabla} \cdot \tilde{\tau}. \quad (2.5)$$

2.1.3. Energy balance over a fluid element

A starting point for the derivation is the entropy conservation of the inviscid theory from gas dynamics (e. g. Zierep [148]), which can be extended to a Kirchhoff-Fourier equation according to Pierce [95, Eq. (10-1.15)] to account for viscous effects and heat conduction:

$$\tilde{q} \tilde{T} \frac{\tilde{D} \tilde{s}}{\tilde{D} \tilde{t}} = -\tilde{\nabla} \cdot \tilde{\mathbf{q}} + \frac{\tilde{v}}{2} \sum_{i,j} \tilde{\tau}_{ij}^2, \quad (2.6)$$

where $\tilde{\mathbf{q}}$ denotes the heat conduction. From this equation, under the assumption of a reversible process in an ideal gas, one obtains the following form of the energy equation, which makes use of the pressure as dependent variable:

$$\frac{\tilde{D} \tilde{p}}{\tilde{D} \tilde{t}} + \gamma \tilde{p} \tilde{\nabla} \cdot \tilde{\mathbf{u}} = (\gamma - 1) \left(-\tilde{\nabla} \cdot \tilde{\mathbf{q}} + \frac{\tilde{v}}{2} \sum_{i,j} \tilde{\tau}_{ij}^2 \right). \quad (2.7)$$

A more detailed derivation is found in the Appendix A.1.1.

2.2. Nondimensional mathematical model

Equations (2.3), (2.5) and (2.7) are now used as a starting point for the following derivations. The implementation of the mathematical model benefits of a nondimensional form in which all terms are of a similar order of magnitude. Problem specific units are introduced instead of the SI system. The units are temporally and spatially constants such that all derivatives of the unit quantities are zero. The units itself must be nonzero. Furthermore, the most simple unit system is required to avoid conversion or conflicting definitions. This system is here obtained with the units given in Table 2.1.

The derivation of the above nondimensional form from Eq. (2.3), Eq. (2.5) and Eq. (2.7) is found in the Appendix A.1.2. In the following, the nondimensional quantities are written without tilde. The resulting nondimensional system of governing equations is

$$\frac{D \varrho}{D t} + \varrho \nabla \cdot \mathbf{u} = 0, \quad (2.8a)$$

$$\frac{D \mathbf{u}}{D t} + \frac{1}{\varrho} \nabla p = \frac{1}{\text{Re}_\infty} \nabla \cdot \boldsymbol{\tau}, \quad (2.8b)$$

$$\text{and} \quad \frac{D p}{D t} + \gamma p \nabla \cdot \mathbf{u} = (\gamma - 1) \left(-\nabla \cdot \mathbf{q} + \frac{1}{2 \text{Re}_\infty} \sum_{i,j} \tau_{ij}^2 \right). \quad (2.8c)$$

Table 2.1.: Units for the nondimensional formulation of the governing equations and the related SI units

Quantity	Unit	SI-unit	Description / unit measure
\tilde{x}	L_∞	m	typical length
\tilde{c}, \tilde{u}	c_∞	m s^{-1}	typical speed of sound
$\tilde{\rho}$	ρ_∞	kg m^{-3}	typical density
\tilde{t}	$\frac{L_\infty}{c_\infty}$	s	typical acoustic time scale
$\tilde{f}, [\tilde{\omega}]$	$\frac{c_\infty}{L_\infty}$	s^{-1}	typical acoustic [angular] frequency
\tilde{p}	$\rho_\infty c_\infty^2$	Pa	typical pressure
$\tilde{\nu}$	$c_\infty L_\infty$	$\text{m}^2 \text{s}^{-1}$	typical kinematic viscosity
\tilde{a}	$\frac{c_\infty^2}{L_\infty}$	m s^{-2}	acceleration scale
\tilde{I}	$\frac{\rho_\infty c_\infty^3}{L_\infty}$	W m^{-2}	intensity scale

The Reynolds number Re is defined here with the reference speed of sound c_∞ and the reference length L_∞ as

$$\text{Re} = \frac{c_\infty L_\infty}{\tilde{\nu}}. \quad (2.9)$$

The nondimensional Eqs. (2.8a), (2.8b) and (2.8c) exactly match the relations set up by Eqs. (2.3), (2.5) and (2.7). The physical quantity is obtained by multiplying the nondimensional value by its unit from Table 2.1.

2.3. Perturbation approach

The next step in the derivation of a simplified model for the propagation of perturbations from a known source is the introduction of a perturbation approach. Each nondimensional field-quantity is split into a base-flow component and a perturbation on top of it. The base flow is assumed to be time stationary. The decomposition

$$\varrho = \varrho_0 + \varrho', \quad \mathbf{u} = \mathbf{u}_0 + \mathbf{u}' \quad \text{and} \quad p = p_0 + p'$$

is used to replace the field quantities in Eq. (2.8) to obtain the following:

$$\frac{D\varrho'}{Dt} + (\mathbf{u}_0 + \mathbf{u}') \cdot \nabla \varrho_0 + (\varrho_0 + \varrho') \nabla \cdot (\mathbf{u}_0 + \mathbf{u}') = 0, \quad (2.10a)$$

$$\frac{D\mathbf{u}'}{Dt} + (\mathbf{u}_0 + \mathbf{u}') \cdot \nabla \mathbf{u}_0 + \frac{1}{\varrho_0 + \varrho'} \nabla (p_0 + p') = \frac{1}{\text{Re}_\infty} \nabla \cdot [\boldsymbol{\tau}_0 + \boldsymbol{\tau}'], \quad (2.10b)$$

$$\begin{aligned} \text{and} \quad \frac{Dp'}{Dt} + (\mathbf{u}_0 + \mathbf{u}') \cdot \nabla p_0 + \gamma (p_0 + p') \nabla \cdot (\mathbf{u}_0 + \mathbf{u}') \\ = (\gamma - 1) \left(-\nabla \cdot \mathbf{q} + \frac{1}{2\text{Re}_\infty} \sum_{ij} [\tau_{0,ij} + \tau'_{ij}]^2 \right). \end{aligned} \quad (2.10c)$$

Note that, $\frac{D}{Dt}$ is defined with the velocity vector in the transport term. It is expressed as follows after the velocity-field decomposition:

$$\frac{D(\cdot)}{Dt} := \frac{\partial(\cdot)}{\partial t} + (\mathbf{u}_0 + \mathbf{u}') \cdot \nabla (\cdot). \quad (2.11)$$

2.4. Nonlinear perturbed nonconservative nonlinear Euler model (PENNE [76])

To obtain the most general implemented model from Eq. (2.10), it is assumed that the effect of the viscosity is negligibly small for the perturbations. The resulting system of partial differential equations is called perturbed nonlinear, nonconservative Euler equations (PENNE) according to Long [76]. It is then given as:

$$\frac{\partial \varrho'}{\partial t} + (\mathbf{u}_0 + \mathbf{u}') \cdot \nabla \varrho' + (\varrho_0 + \varrho') \nabla \cdot \mathbf{u}' + \mathbf{u}' \cdot \nabla \varrho_0 + \varrho' \nabla \cdot \mathbf{u}_0 = 0, \quad (2.12a)$$

$$\frac{\partial \mathbf{u}'}{\partial t} + (\mathbf{u}_0 + \mathbf{u}') \cdot \nabla \mathbf{u}' + \frac{1}{\varrho_0 + \varrho'} \nabla p' + \mathbf{u}' \cdot \nabla \mathbf{u}_0 - \frac{\varrho'}{\varrho_0 (\varrho_0 + \varrho')} \nabla p_0 = 0, \quad (2.12b)$$

$$\text{and} \quad \frac{\partial p'}{\partial t} + (\mathbf{u}_0 + \mathbf{u}') \cdot \nabla p' + \gamma (p_0 + p') \nabla \cdot \mathbf{u}' + \mathbf{u}' \cdot \nabla p_0 + \gamma p' \nabla \cdot \mathbf{u}_0 = 0. \quad (2.12c)$$

The base flow solves the Navier-Stokes or Euler equations. A more detailed derivation may be found in Appendix A.1.3. The Equations (2.12) have been expressed in a matrix–vector notation, for easier implementation with the numerical method. The related matrix–vector expression is given in Appendix A.2.2, for 2D, 3D and axisymmetric assumptions for the solution, boundary conditions and base-flow field.

The nonlinear system may find application in connection with high-amplitude acoustic-wave propagation and the steepening of acoustic pulses and it includes the interaction of vortices and unsteady temperature variations with the acoustic field. Both are not covered by a linear model. The PENNE equations are used here to calculate a steady base flow field. When compared to a linear perturbation approach, the numerical effort is slightly increased due to the additional nonlinear terms.

2.5. Linearized Euler equations

In addition to the above inviscid assumption, the perturbations are assumed to be small when compared to the average field quantity. The pressure p' and density ϱ' perturbations are assumed to be small compared to the pressure p_0 and density ϱ_0 of the base flow respectively. The local average speed of sound:

$$c = \sqrt{\gamma p_0 / \varrho_0} \quad (2.13)$$

is the reference field quantity for the definition of a small perturbation of the velocity field ($|u'| \ll c$). Note that c is a nondimensional local speed of sound but the relations apply for the physical speed of sound too. In addition, it is assumed that the spatial and temporal derivatives of a perturbation are in the order of the perturbation itself. This assumption is usually well realized for acoustic perturbations in the audible range. The typical wave length is $\lambda = c/f$ for acoustic waves. Thus, the temporal derivatives of a small perturbation scale with the nondimensional angular frequency ω and the spatial derivatives with the Helmholtz-number $He = L_\infty \omega / c$. The definition He is independent of the dimensional or nondimensional notation, therefore the tilde omitted. Both scaling factors range from 10^{-2} to 10^2 for frequencies between 10 Hz and 40 kHz in hot air and air at standard conditions, respectively; assuming a typical length of $L_\infty = 1$ m.

For non-acoustic perturbations, e. g. vortices and non-isentropic perturbations the wave length is proportional to magnitude of the local flow speed $|u|$. Thus, the wave length can become very small in local stagnation regions. Such under-resolved hydrodynamic perturbations are cut-off by the finite grid resolution within the numerical method. Therefore, the case where a spatial derivative of the perturbation quantities becomes much larger than the perturbation itself is theoretical.

The derivatives of a perturbation are assumed to be in the same order as the perturbation itself in the following. In combination with the assumption of a small perturbation, one obtains a set of linearized perturbation equations. Equations (2.10) are considered as a starting point again, and any term of second and higher order in the perturbation quantities and their derivatives are neglected. The balances for

the average flow field are removed from the equations and the viscous terms are neglected for the perturbations as shown in Appendix A.1.3. The linearized Euler equations are then obtained; they are expressed as follows:

$$\frac{\partial \varrho'}{\partial t} + \mathbf{u}_0 \cdot \nabla \varrho' + \varrho_0 \nabla \cdot \mathbf{u}' + \mathbf{u}' \cdot \nabla \varrho_0 + \varrho' \nabla \cdot \mathbf{u}_0 = 0, \quad (2.14a)$$

$$\frac{\partial \mathbf{u}'}{\partial t} + \mathbf{u}_0 \cdot \nabla \mathbf{u}' + \frac{1}{\varrho_0} \nabla p' + \mathbf{u}' \cdot \nabla \mathbf{u}_0 + \frac{\varrho'}{\varrho_0} \mathbf{u}_0 \cdot \nabla \mathbf{u}_0 = 0 \quad (2.14b)$$

$$\text{and} \quad \frac{\partial p'}{\partial t} + \mathbf{u}_0 \cdot \nabla p' + \gamma p_0 \nabla \cdot \mathbf{u}' + \mathbf{u}' \cdot \nabla p_0 + \gamma p' \nabla \cdot \mathbf{u}_0 = 0. \quad (2.14c)$$

The corresponding matrix-vector form is specified in Appendix A.2.3 for the three coordinate systems considered in the present work. The linear system may be applied for a large range of problems involving the transport of hydrodynamic perturbations and the interaction of these perturbations with the base flow.

2.6. Isentropic pressure–density relation

Finally, the isentropic variant of the LEE is obtained by replacing Eq. (2.14c) with the isentropic pressure–density relation of acoustics:

$$\begin{aligned} p' &= \underbrace{\gamma \frac{p_0}{\varrho_0}}_{=c^2, \text{Eq. (2.13)}} \varrho' \\ p' &= c^2 \varrho' \end{aligned} \quad (2.15)$$

With this simplification one out of five partial differential equations is removed for the three dimensional problem. Two out of twelve are removed for the modal axisymmetric approach. As all of the differential equations are of similar structure, the numerical effort is similar. Thus, the reduction of one equation means a reduction of the problem size by 20 %. Furthermore, the above isentropic relation removes the entropy mode from the solution of the resulting system. This is a limitation on one hand. However, it possibly increases the stability, as the entropy-related instability mechanism is removed. The corresponding matrix–vector form is omitted in the appendix as it simply uses Eq. (2.15) to replace the pressure equation. The relation of the resulting model to the wave equation is described in the Appendix A.1.4

2.7. Modal axisymmetric approach

The modal axisymmetric approach goes back to an idea suggested by Michel [79]. The implementation of the approach described below was presented as [72]. At the same conference Zhang et al. [141] presented a similar development with the difference, that the computation of a complex-valued perturbation field was avoided

at the expense of an additional time integration. Both works were later published as articles [73, 142]. Here we assume, that acoustic waves propagate within a duct or radiate from a duct, in the presence of a nonuniform, axisymmetric base flow. A cylindrical coordinate system, as it is sketched in Fig. 2.1, is introduced. Furthermore, it is assumed that the flow duct is axisymmetric along the x -axis and as well all boundary conditions as the base flow are assumed to be constant in the azimuthal direction. Then it becomes possible to rewrite the three dimensional problem as an infinite series of two dimensional problems by using a Fourier-series approach for the azimuthal direction:

$$\boldsymbol{\phi}'(x, r, \varphi, t) = \text{Re} \left\{ \sum_{m=-\infty}^{\infty} \hat{\boldsymbol{\phi}}_m(x, r, t) e^{i m \varphi} \right\}, \quad (2.16)$$

where $\boldsymbol{\phi}'$ denotes perturbation field quantities

$$\boldsymbol{\phi}' := [\varrho', \mathbf{u}', p'], \quad (2.17)$$

and $\hat{\boldsymbol{\phi}}$ denotes the complex-valued perturbation amplitude, which is independent of the azimuthal angle. There is no simplification up to now. The φ -dimension has been developed into an infinite number of azimuthal modes m . However, in aeroengines the number of cut-on azimuthal modes is limited as we can assume a limited band of frequencies for the aeroacoustic excitation. Thus, Eq. (2.16) can be limited to the cut-on or close to cut-on $-M \dots M$ azimuthal modes as

$$\boldsymbol{\phi}'(x, r, \varphi, t) = \text{Re} \left\{ \sum_{m=-M}^M \hat{\boldsymbol{\phi}}_m(x, r, t) e^{i m \varphi} \right\}. \quad (2.18)$$

The derivative in φ -direction is given as:

$$\frac{\partial \boldsymbol{\phi}'(x, r, \varphi, t)}{\partial \varphi} = \text{Re} \left\{ \sum_{m=-M}^M i m \hat{\boldsymbol{\phi}}_m(x, r, t) e^{i m \varphi} \right\}. \quad (2.19)$$

Thus, the derivative of the complex-valued perturbation amplitude in the azimuthal direction is simply replaced by a multiplication with $(i m)$ and, due to the above assumptions, the derivatives of the base flow in the azimuthal direction cancel out.

The Fourier-ansatz implies a potential reduction of the problem size. Especially for the modal field of the aeroengine inlet, only a small number of modes is involved to the tonal sound field. In this case, the highly demanding three dimensional problem can be replaced by a small set of two dimensional problems. In addition, the concept of a two dimensional simulation is advanced over a three dimensional one in a Cartesian coordinate system in terms of the resolution of the azimuthal structure of the sound field close to the axis especially for higher azimuthal modes, as they are typically found in the aeroengine inlet of high-bypass-ratio ducted fan designs.

Real and imaginary part of the complex-valued perturbation amplitude $\hat{\phi}_m$ have to fulfill the differential equation, e. g. Eq. (2.14), in the cylindrical coordinate that is system sketched in Fig. 2.1. Moreover, each mode must fulfill the differential equation independently of the other modes. This results in a decoupled set of $2M + 1$ equations for the real and imaginary part of the complex-valued perturbation amplitude vector $\hat{\phi}_m$, which has to be solved numerically in 2D. In comparison to a fully two-dimensional or fully axisymmetric problem, the number of equations is doubled due to the complex variables. A complex expansion of the plane wave ($m = 0$) is included in the modal axisymmetric approach as well.

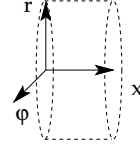


Figure 2.1.: Cylindrical coordinate system

3. CAA method

The numerical CAA method, which is adopted in the present work for the discretization of the different PDE systems described above, is detailed in this chapter. To implement a general purpose CAA method, which is capable of handling body-fitted meshes and curvilinear coordinate systems, a number of different techniques is combined. Besides own developments, concerning the filtering of the solution and the sound source, approaches and methods from the literature are recast, combined and extended by own ideas to obtain the implemented form of the CAA method. The techniques are summarized in this chapter. A special emphasis is put on the treatment of the domain boundaries. The impedance boundary condition is omitted here. As it represents the principal objective of the current work, it is introduced in the following Chapter 4.

3.1. Discretization schemes

3.1.1. Spatial discretization

The spatial discretization has been developed according to the dispersion-relation-preserving (DRP) scheme of Tam and Webb [127]. However, the wave-number range for the optimization is reduced to $|k \Delta x| < 0.95$. The scheme features an optimized fourth-order central-differencing scheme with a seven-point stencil. At the domain boundaries, optimized backward stencils of fourth order with also seven points find application. The wave-number range for the optimization of the backward schemes is further reduced with respect to the works of Tam and Webb [127] in the current work. For two- and three-dimensional problems the schemes are applied for each coordinate direction ξ_i in the computational domain. The coefficients of the discretization scheme may be found in Appendix B.1.

To give an overview of the accuracy associated with the spatial discretization, the results of a Fourier error analysis of the central DRP scheme and the boundary related seven-point-backward stencils are summarized in Figs. 3.1 and 3.2. Fig. 3.1 shows the numerical wave number according to Tam et al. [128, Eq. 2.5], which is found to be

$$k \Delta x \approx (k \Delta x)^* = -i \sum_{j=-N}^M a_j^{N,M} e^{ijk \Delta x}, \quad (3.1)$$

for an arbitrary finite difference discretization with constant grid spacing Δx . The ordinate of Fig. 3.1 is the relative wavenumber specified as $k \Delta x$. An idealized scheme calculating the first derivative, would give $(k \Delta x)^* = k \Delta x$ for all wave

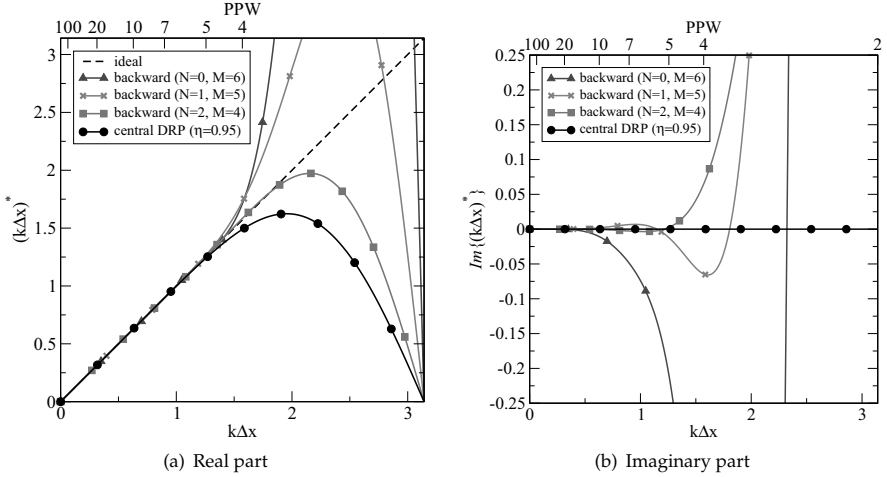


Figure 3.1.: Results of the Fourier error analysis for the spatial discretization. The real and imaginary part of the numerically evaluated relative wave number $(k\Delta x)^*$ as a function of the relative wave number $(k\Delta x)$

numbers k and grid spacings Δx . However, this is impossible to obtain with a finite number of points in the finite differencing stencil. With the discretization applied in the current work, a good representation is observed up to a resolution of about 5 PPW for the real part of $(k\Delta x)^*$ in Fig. 3.1(a). The imaginary part of $(k\Delta x)^*$ corresponds to the amplification or dissipation of waves [147]. Other than for the central schemes, it is impossible to find backward schemes with maximum order, which show no dissipation or amplification, comp. Eq. (3.1). The imaginary part of the numerical wave number $(k\Delta x)^*$ of the backward scheme depends on the wave-number range which is used for the optimization. For the schemes used in the current work, the range has been varied for each of the stencils to obtain an optimum for the usable range. The amplification or dissipation properties of the backward schemes are summarized in Fig. 3.1(b).

In order to have an estimate of the numerical dispersion error due to the scheme, the numerical group velocity is considered. It is expressed according to Tam et al. [128] as

$$v_{gr}^* = \frac{d(k\Delta x)^*}{d(k\Delta x)}.$$

Trends of v_{gr} are considered in Fig. 3.2. The numerical group velocity depends on the local derivatives; its deviation from one corresponds to the phase error due to

the spatial discretization scheme, when assuming ideal properties for the time discretization according to Tam et al. [128]

$$v_{gr} = \frac{d\omega}{dk} \stackrel{!}{=} \underbrace{\frac{d\omega}{d\omega^*}}_{\approx 1} \underbrace{\frac{d\omega^*}{dk^*}}_{=v_{gr}^*} \underbrace{\frac{dk^*}{dk}}_{=v_{gr}^*} \approx v_{gr}^* v_{gr}.$$

As can be seen from Fig. 3.2, the numerical group velocity remains within a range of 3 % error, marked by black lines in the figure, for a discretization with more than six points per wavelength (PPW). This is considered to be the usable range of the spatial discretization scheme.

3.1.2. Time stepping

The time stepping is performed by the fourth order low-dissipation-low-dispersion Runge–Kutta scheme (LDDRK) of Hu et al. [50] which appropriately alternates five- and six-stage algorithms. These algorithms are optimized in combination with respect to the error for harmonic wave propagation. The scheme is implemented in the memory efficient 2N storage form described by Stanescu and Habashi [121]. The coefficients of the 5/6-stage LDDRK scheme going back to Hu et al. [50], in the implemented form of Stanescu and Habashi [121], are given in Appendix B.1.2.

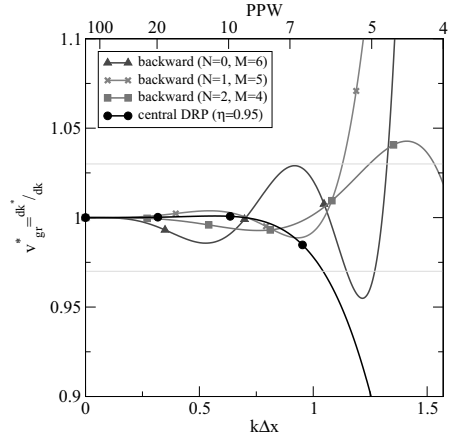


Figure 3.2.: Numerical group velocity for the discretization schemes

3.1.3. Low-pass filtering of the solution

According to Tam et al. [128] all high-order finite-differencing schemes are affected by spurious grid oscillations, which are related to not fully resolved short-wave components in the solution. These short waves are further classified as dispersive waves and parasite waves according to their group velocity [128]. The group velocity of the central scheme is plotted in Fig. 3.3 on the right scale to illustrate the three wavenumber ranges. The usable range of the scheme is denoted as long wave range. It is limited to resolutions of more than 6 PPW. Dispersive waves with an under-predicted group velocity are found between about 6 PPW and 3 PPW. Below 3 PPW parasite waves with negative group velocity arise. Due to the large modulus

of the group velocity in this range, the very short waves travel with a multiple speed of sound. They pollute the computational domain very fast according to Tam et al. [128]. Therefore, these authors introduced artificial-selective damping to remove the short-wave component.

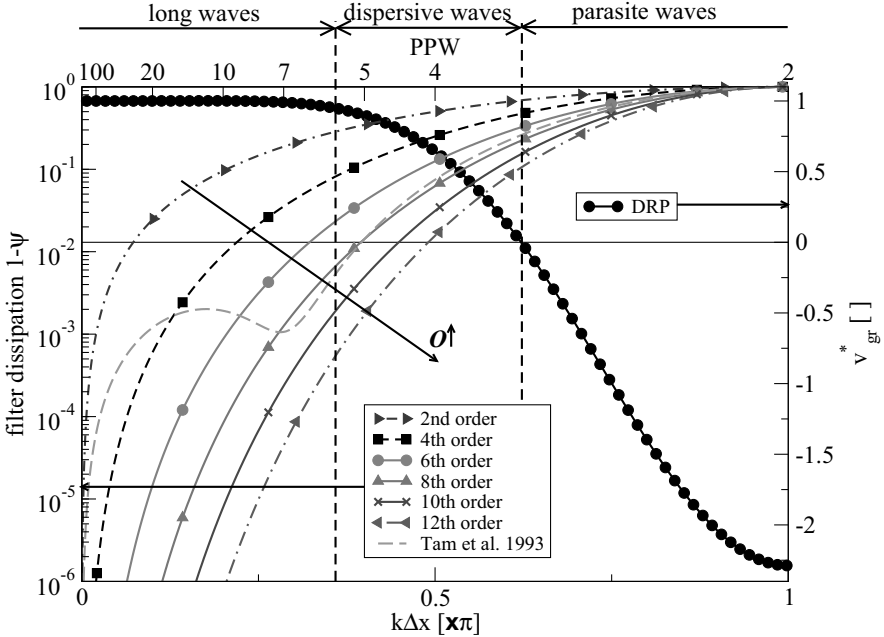


Figure 3.3.: Comparison of the filter dissipation for different filter choices

The approach is found to be insufficient for many practical problems, which is due to the highly-dissipative Gaussian template for the wavenumber response of the artificial-selective damping on one hand and due to the integration of it with the physical model on the other hand. Due to the template, the artificial damping is found to be not selective enough in the application. In consequence, actually resolved waves are affected by high dissipation. The filter characteristics of the artificial-selective damping stencil are shown in Fig. 3.3 on the left scale for comparison. A high attenuation of more than 0.1 % per application of the damping stencil is found up to 20 PPW. The integration of the artificial damping into the physical model causes difficulties for realistic problems. Unfiltered data is used to calculate the derivatives by the DRP scheme in every time step. The artificial-selective damping corrects only oscillations found in the older time step. For any realistic problem, which features singularities, as the leading or trailing edge of a liner are, this leads to an unlimited amplification of short wave components during the simulation.

To avoid the problem, a spatial low-pass filter is applied to the perturbation field in an additional step. It is implemented independently from the time stepping. Usually the filter is applied every other time step; larger intervals are also possible. After the filtering, the derivatives are calculated based on the filtered field. In this way, the propagation of short waves is effectively suppressed. The filtering increases the computational time as the whole perturbation field is updated. However, by applying large time intervals between the filtering operations, the negative impact of the filter on the computational time can be minimized.

A filter is in general defined as an approximation ϕ^* of a field variable ϕ at the point l which is based on $-N$ to M neighboring points. The symbol ϕ^* refers to the filtered field, whereas ϕ is the original unfiltered field. The filter is then defined with the filter coefficients w_j as

$$\phi_l^* = \phi_l - \sum_{j=-N}^M w_j \phi_{l+j}. \quad (3.2)$$

When considering the filter definition of Eq. (3.2), the transfer function of the filter in the wavenumber space is given by the response to a spatially harmonic excitation with the relative wavenumber $k \Delta x$ as

$$\Psi = 1 - \sum_{j=-N}^N w_j e^{i j k \Delta x}. \quad (3.3)$$

From Eq. (3.3) follows that a zero imaginary part, corresponding to a zero phase error, is achieved by a symmetric set of filtering coefficients ($M = N$) with $w_j = w_{-j}$. The filter coefficients are derived based on a Taylor-series expansion of the filter definition according to [147]. They are given in Appendix B.1.3. The dissipation of the filter, which is defined by $|1 - \Psi|$ is plotted for the filter functions applied in Fig. 3.3.

Eq. (3.2) can be seen as a correction of the original functional value due to the filter. Thus, a modification of the filter similar to the idea of the artificial-selective damping by Tam et al. [128] becomes possible. A filter coefficient σ_{filter} is introduced, $0 < \sigma_{\text{filter}} < 1$, which softens the effect of the filter

$$\phi_l^+ = \phi_l - \sigma_{\text{filter}} \sum_{j=-N}^N w_j \phi_{l+j}, \quad (3.4)$$

where ϕ^+ is the modified filtered field. This operation is found to be very useful for a control of the attenuation of waves in the transition zone of the filter and when using the simple one-dimensional filter in 2D and 3D.

A non-optimized seven-point-stencil filter of sixth order, which use the same stencil size as the DRP scheme, is not able to provide the desired properties in terms of

a sharp cut-off and low-dissipation in the pass-band [91, 102]. Thus, several optimized and non-optimized filter stencils up to 12th order were considered in a numerical study [91, 102]. Fig. 3.3 provides a qualitative information about the different filter orders for the non-optimized filters. In the numerical study, the 12th order as well as an eleven-point-stencil optimized low-dissipation filter of Bogey and Bailly [12], were not able to fully remove the short wave components and the related instability for some relevant cases. Furthermore, any optimized filters do not show a convergence to lower dissipation with increasing grid resolution. Thus, a grid refinement may result in an unexpected result when applying an optimized filter. The 10th order eleven-point-stencil filter was found to be best suited, cutting-off short waves and leaving the long waves nearly unaltered, down to a limit of about 7 PPW in this study. It is used in the following. It should be noted, that the choice of a non-optimized 10th order filter with eleven-point-stencil was also independently made by Zhang et al. [142] for a CAA method based on the compact scheme of Lele [67].

At domain boundaries, the eleven-point-stencil central filter cannot be applied. It is found, that a filtering with shorter filter stencils has a favorable effect on the stability, when applied at block boundaries ($N = 5 \dots 3$) and towards the wall ($N = 5 \dots 0$). However, to avoid too high dissipation due to these short filters, the filter coefficient σ_{filter} is reduced with decreasing filter order according to the empirical law

$$\sigma_{\text{filter}}^{(N)} = \left(\frac{2N+1}{11} \right)^2 \sigma_{\text{filter}}^{N=5}. \quad (3.5)$$

The combination of Eq. (3.5) and the low-order filter is not able to achieve the filtering performance of the 10th order filter. However, the short waves close to the wall are found to be sufficiently blocked and the long-wave dissipation is confined to an acceptable level.

3.2. Base-flow field

The base flow for a duct geometry with varying cross section or for an open duct aspirating air from the environment can be computed with the CAA method. Some of the simulations in the present work use a base-flow field, which was computed by using the nonlinear Euler model (PENNE, comp. section 2.4) in combination with the CAA method, on the mesh which was built for the simulation of the acoustic wave propagation. The boundary conditions are modified in order to specify a time-constant source in the sponge layers of both duct ends. It is based on the

gas-dynamic relations for a compressible stream filament (comp. [148]):

$$\frac{\varrho_{\text{rest}}}{\varrho} = \left[1 + \frac{\gamma - 1}{2} \text{Ma}^2 \right]^{\frac{1}{\gamma - 1}}, \quad (3.6a)$$

$$\frac{p_{\text{rest}}}{p} = \left[1 + \frac{\gamma - 1}{2} \text{Ma}^2 \right]^{\frac{\gamma}{\gamma - 1}}, \quad (3.6b)$$

$$\frac{T_{\text{rest}}}{T} = \left[1 + \frac{\gamma - 1}{2} \text{Ma}^2 \right], \quad (3.6c)$$

where $_{\text{rest}}$ denotes the quantities at rest. The connection of Mach number Ma and cross sectional area is given by

$$\frac{A}{A^*} = \frac{1}{\text{Ma}} \left[\frac{2}{\gamma + 1} \left(1 + \frac{\gamma + 1}{2} \text{Ma}^2 \right) \right]^{\frac{\gamma + 1}{2(\gamma - 1)}}. \quad (3.7)$$

The Mach number is given for one end of the duct e. g. from a measurement. Then the critical cross section is calculated using the Mach number and cross section of the duct in Eq. (3.7). This critical cross section is used to obtain the Mach number for the other end, for which no flow conditions are provided. The resulting Mach number is used together with the Eqs. (3.6) to compute the pressure and density at the other duct end. For the aspiration of air from the environment the Mach number at the other end is set to zero, resulting in the thermodynamic conditions at rest for this end. The boundary values are specified through a sponge layer, which is leading to a overdetermined system. However, the boundary conditions are fully correct for a non-dissipative stream trace, such that the non-conservative CAA method is able to obtain a valid inviscid compressible flow field.

3.3. Handling of curvilinear meshes

In this section, the necessary steps to apply the DRP scheme with curvilinear body-fitted meshes are described. First, a metric is defined, which implements the mapping between the general curvilinear physical mesh and the computational domain and vice versa. The equidistant orthogonal mesh in the computational domain features an unity spacing in each coordinate direction. Based on this metric, a normal vector at the domain boundary of the physical domain is derived.

3.3.1. Metric

To obtain the metric, a curvilinear coordinate system is introduced, which is used for the discretization of the physical domain. The discretization is defined, based on the position vector \mathbf{x} in Cartesian or cylindrical coordinates. By the discretization \mathbf{x}

is expressed as a function of the coordinate vector ξ in the computational domain. Then, using the chain rule, the derivative can be calculated as follows

$$\frac{\partial \phi}{\partial x_i} = \frac{\partial \phi}{\partial \xi_j} \frac{\partial \xi_j}{\partial x_i}, \quad (3.8)$$

where an implicit summation over duplicate indexes applies. The derivative in the computational domain $\frac{\partial}{\partial \xi_j}$ is calculated by the DRP scheme as it was described above. The step size in the computational domain is one for all directions. To obtain the derivative in the physical domain, the metric coefficients g_i^j of the mapping between computational domain and physical domain are required. These coefficients are calculated as inversion of $\frac{\partial x_i}{\partial \xi_j}$ as

$$g_i^j := \frac{\partial \xi_j}{\partial x_i} = \left[\frac{\partial x_i}{\partial \xi_j} \right]^{-1}. \quad (3.9a)$$

The derivative $\frac{\partial x_i}{\partial \xi_j}$ is calculated by the optimized discretization as earlier explained. Alternatively, non-optimized high order schemes according to [147] are applied.

In two dimensions, the inversion is given as

$$g_i^j = \frac{1}{\det \left[\frac{\partial x_i}{\partial \xi_j} \right]} \begin{pmatrix} \frac{\partial x_2}{\partial \xi_2} & -\frac{\partial x_1}{\partial \xi_2} \\ -\frac{\partial x_2}{\partial \xi_1} & \frac{\partial x_1}{\partial \xi_1} \end{pmatrix}. \quad (3.9b)$$

In three dimensions one obtains:

$$g_i^j = \frac{1}{\det \left[\frac{\partial x_i}{\partial \xi_j} \right]} \begin{pmatrix} \frac{\partial x_2}{\partial \xi_2} \frac{\partial x_3}{\partial \xi_3} - \frac{\partial x_2}{\partial \xi_3} \frac{\partial x_3}{\partial \xi_2} & \frac{\partial x_1}{\partial \xi_3} \frac{\partial x_3}{\partial \xi_2} - \frac{\partial x_1}{\partial \xi_2} \frac{\partial x_3}{\partial \xi_3} & \frac{\partial x_1}{\partial \xi_2} \frac{\partial x_2}{\partial \xi_3} - \frac{\partial x_1}{\partial \xi_3} \frac{\partial x_2}{\partial \xi_2} \\ \frac{\partial x_2}{\partial \xi_3} \frac{\partial x_3}{\partial \xi_1} - \frac{\partial x_2}{\partial \xi_1} \frac{\partial x_3}{\partial \xi_3} & \frac{\partial x_1}{\partial \xi_1} \frac{\partial x_3}{\partial \xi_3} - \frac{\partial x_1}{\partial \xi_3} \frac{\partial x_3}{\partial \xi_1} & \frac{\partial x_1}{\partial \xi_3} \frac{\partial x_2}{\partial \xi_1} - \frac{\partial x_1}{\partial \xi_1} \frac{\partial x_2}{\partial \xi_3} \\ \frac{\partial x_2}{\partial \xi_1} \frac{\partial x_3}{\partial \xi_2} - \frac{\partial x_2}{\partial \xi_2} \frac{\partial x_3}{\partial \xi_1} & \frac{\partial x_1}{\partial \xi_2} \frac{\partial x_3}{\partial \xi_1} - \frac{\partial x_1}{\partial \xi_1} \frac{\partial x_3}{\partial \xi_2} & \frac{\partial x_1}{\partial \xi_1} \frac{\partial x_2}{\partial \xi_2} - \frac{\partial x_1}{\partial \xi_2} \frac{\partial x_2}{\partial \xi_1} \end{pmatrix}. \quad (3.9c)$$

As can be seen, the two-dimensional case is a special case of the three-dimensional one. It is obtained by introducing a virtual third dimension, which is oriented perpendicular to the other two dimensions. This virtual third dimension is discretized by ξ_3 , such that $\frac{\partial x_1}{\partial \xi_3} = \frac{\partial x_2}{\partial \xi_3} = 0$ and $\frac{\partial x_3}{\partial \xi_3} = 1$ apply.

3.3.2. Normal vector of a domain boundary

A common variable in the formulation of both, non-reflective and partially or fully reflective boundary conditions, is the normal vector of a surface. This is defined by the outermost grid surface in 3D or grid line in 2D. A sketch of the normal vector for a 3D case is given in Fig. 3.4. The above definition of the metric can be used to construct this normal vector in a very easy way. The metric g_i^j defines a dual coordinate

system, in which each basis vector is oriented normal to the complementary set of two other basis vectors from the corresponding original system. The original basis is defined as $\left[\frac{\partial x_i}{\partial \xi_j} \right]$. Thus, the normal vector of a surface defined by ξ_2 and ξ_3 would be g_1^j . When comparing with Eq. (3.9c), this is correctly identified as the cross product of the coordinate derivatives in the dimensions 2 and 3 of the computational domain. Each line of the matrix g_i^j defines one basis vector, which is orthogonal to the two grid lines with a dimension not equal to the number of the line in the matrix. For the two dimensional case, no special formulation is required. When considering Eq. (3.9b) the construction of a normal vector in 2D by exchanging the components of a vector and altering the sign of one of the components is recovered from the definition using g_i^j .

The above consideration gives the direction of the normal vector. The orientation is obtained by the scalar product of the normal vector with $\Delta x_i(\Delta \xi_k)$, where k is the index of the coordinate line not included in the surface. $\Delta \xi_k$ is a variation of ξ_k along this line into the domain away from the boundary. If the scalar product is greater than zero, the normal vector points into the domain, whereas a negative scalar product indicates an outside orientation. The normal vector is then simply reoriented by a multiplication with -1 to obtain a standard orientation. In the current work the standard orientation for the normal vector is considered to be that the normal vector points outside from the domain.

Finally, the resulting vector is normalized to an unit length which altogether leads to the definition:

$$\mathbf{n}_k = n_{k,j} := -\text{sgn} \left(g_k^l \Delta x_l(\Delta \xi_k) \right) \frac{g_k^j}{\sqrt{g_k^n g_k^n}}, \quad (3.10)$$

The dimension of the mesh, which is not oriented inside the surface is denoted by k , while j is the running index to define the vector components. The vector \mathbf{n}_k defines the normal to the dimension(s) other than k . The normal vector points into direction k of the mesh if a Cartesian mesh is chosen. However, the definition does not require an orthogonal mesh at the wall. As the dual basis is used, the vector is always oriented perpendicular to the surface defined by the other dimensions with the order of accuracy that is used to calculate the derivatives $\frac{\partial x_i}{\partial \xi_j}$.

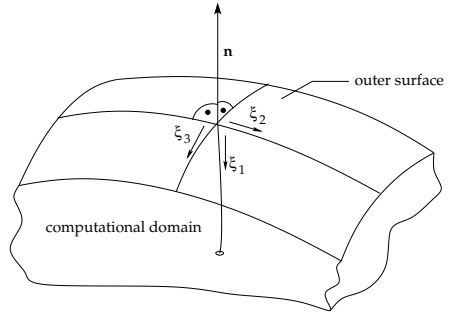


Figure 3.4.: Outer grid surface and normal vector \mathbf{n}_k ($k = 1$)

3.4. Wall modeling for CAA methods

The wall boundary condition is implemented in the current method according to the way pointed out by Tam and Dong [126]. They showed that the discretized system, which is obtained by the application of the DRP scheme, does not allow additional boundary conditions at a wall. The number of unknowns in the discretized system exactly matches the number of degrees of freedom. Their solution is to introduce an additional degree of freedom for each additional condition to the discretized system. This means one additional variable for each point at the wall and each boundary condition. Tam and Dong [126] implemented the wall boundary condition, which forces the normal velocity to be zero, by introducing ghost points adjacent to the wall outside the computational domain. These points store only the pressure perturbation. In the current work, the approach is implemented in a recursive way.

As well the impedance boundary condition as the condition at a hard wall can be stated as a condition to the time derivative of the normal velocity $u'_n(t)$. This condition is applied to the relation between the pressure gradient and the normal velocity, which has been obtained from the balance of momentum. As stated above, the mathematical model describing the sound propagation is usually based on a form of the linearized Euler equations; but it could as well be the nonlinear Euler equations. The model could even incorporate viscous effects by a form of the Navier Stokes equations. The momentum equation of all these mathematical models connects \mathbf{u}' to the pressure gradient. Therefore, the momentum equation can be expressed as follows

$$\frac{\partial \mathbf{u}'}{\partial t} = -f(q_0, \mathbf{u}_0, q', \mathbf{u}', \dots) - \frac{1}{q_0} \nabla p'. \quad (3.11)$$

The function f denotes all terms not containing the pressure. By appropriately assigning f , the above equation covers all of the mathematical models mentioned above. The balance of momentum normal to the wall is obtained by taking the scalar product of Eq. (3.11) and \mathbf{n}

$$\frac{\partial u'_n}{\partial t} = -f_n(q_0, \mathbf{u}_0, q', \mathbf{u}', \dots) - \frac{1}{q_0} \mathbf{n} \cdot \nabla p', \quad (3.12)$$

where the subscript n denotes the normal component of a vector.

The impedance boundary condition at the wall is formulated by a prescribed \dot{u}'_n . For a hard wall the condition $\dot{u}'_n = 0$ applies. The condition is used to calculate the resulting pressure in the ghost point through the momentum equation. A partly discretized momentum equation with dimension D for a point at the wall, with the

discretization applied only for the pressure is shown below

$$\begin{aligned} \frac{\partial u'_n}{\partial t} + f_n(\varrho_0, \mathbf{u}_0, \varrho', \mathbf{u}', \dots) + \\ \frac{1}{\varrho_0} \sum_{d=1}^D \left[\sum_{l=2}^D n_d g_d^{(l)} \frac{\partial p'}{\partial \xi_l} + n_d g_d^{(1)} \left(\sum_{j=-\hat{N}+1}^{\hat{M}} a_j^{\hat{N}, \hat{M}} p_j + a_1^{\hat{N}, \hat{M}} p_{\text{ghost}} \right) \right] = 0. \end{aligned} \quad (3.13)$$

The wall is located at the lower boundary of dimension $k = 1$ in the above example. The metric tensor is denoted as g_d^l . The finite difference stencil at the wall with the ghost point at $j = 1$ is obtained by setting $\hat{N} = 1$ and $\hat{M} = 6$ for a seven-point finite-difference discretization. The spatial discretization, using backward-differencing stencils where needed to fit the stencil into the computational domain, is applied to obtain f . The scalar product of f and the normal vector of the wall \mathbf{n} yields f_n . It is important to note that the pressure is not present in the functions f_n and f for the systems of governing equations mentioned above. A condition for the unknown ghost-point pressure p_{ghost} is obtained by using the prescribed u'_n from the impedance boundary condition

$$\begin{aligned} p_{\text{ghost}} = & - \frac{\varrho_0}{a_1^{\hat{N}, \hat{M}} \sum_{d=1}^D n_d g_d^{(1)}} \left(\frac{\partial u'_n}{\partial t} + f_n(\varrho_0, \mathbf{u}_0, \varrho', \mathbf{u}', \dots) \right) \\ & - \frac{1}{a_1^{\hat{N}, \hat{M}} \sum_{d=1}^D n_d g_d^{(1)}} \left\{ \sum_{d=1}^D \sum_{l=2}^D \left(n_d g_d^{(l)} \frac{\partial p'}{\partial \xi_l} \right) \right. \\ & \left. + \sum_{d=1}^D \left(n_d g_d^{(1)} \sum_{j=-\hat{N}+1}^{\hat{M}} a_j^{\hat{N}, \hat{M}} p_j \right) \right\}. \end{aligned} \quad (3.14)$$

Here, the only difference to the discretized system used throughout the computational domain is the additional ghost point. It leads to a shift of the finite-difference stencil towards the wall. This shift effects only the first three grid lines adjacent to the wall. Then Eq. (3.14) is used in a two-step predictor-corrector approach. The derivatives are first taken considering a zero pressure in the ghost point as

$$(\nabla p')^* = \sum_{d=1}^D \left[\sum_{l=2}^D g_d^{(l)} \frac{\partial p'}{\partial \xi_l} + g_d^{(1)} \sum_{j=-\hat{N}+1}^{\hat{M}} a_j^{\hat{N}, \hat{M}} p_j \right] \mathbf{e}_d.$$

These derivatives are then used with the standard implementation of the discretized system. Then p'_{ghost} is calculated based on Eq. (3.14), where u'_n is given by the impedance model. The remaining terms on the right hand side result from the spatial discretization of the momentum equation, which can be calculated independently of the ghost point pressure. The resulting corrected pressure in the ghost point is

then used to complete the pressure derivative for the three grid lines directly at the wall

$$(\nabla p')^+ = \sum_{d=1}^D \left[g_d^{(1)} a_1^{\hat{N}, \hat{M}} p_{\text{ghost}} \right] e_d.$$

The sum of $(\nabla p')^*$ and $(\nabla p')^+$ is the full gradient of the pressure in the wall region.

The mesh generation with commercial packages becomes much easier, if the ghost point does not have to be included in the grid. The recursive implementation, which is described above, applies for each single grid line lateral to the wall. The ghost point pressure can be independently calculated for each grid line. After the correction of the normal derivative has been performed for this line, the ghost pressure is not needed any more. Thus, the ghost point is not created and no storage is reserved in the mesh. The metric is based on the internal points without the ghost point as well.

3.5. Non-reflective boundary conditions

In the current work, three different non-reflective boundary conditions are implemented and applied. None of them provides the desired fully non-reflective characteristics under all circumstances. However, they are found to have complementary properties. The first is the radiation/outflow boundary condition of Tam and Webb [127] and Bogey and Bailly [11], which is presented in Section 3.5.1. The extension of these boundary conditions by a sound source according to Tam [123] is also presented there. The second non-reflective boundary condition uses a sponge layer according to Israeli and Orszag [54]. It includes a formulation for a non-reflective sound source and is described in Section 3.5.2. Finally, the perfectly matched layer boundary condition (PML) of Hu [49] is presented in Section 3.5.3. The PML features advanced reflection characteristics for higher modes close to cut-off in ducts [113]. It is found, that the implementation of the sound source with the PML means an extraordinary effort. As two reliable and accurate alternatives are available, the implementation of a sound source with the PML is omitted.

3.5.1. Radiation/outflow boundary condition

The physical background of the radiation and outflow boundary condition is a classification of the perturbations as entropy mode, vorticity mode or acoustic mode waves. According to an analysis of Chu and Kovásznyai [25], the interaction of these modes is a second-order effect, when considering small variations of the fluid state. For small perturbations, the acoustic waves travel with the speed of sound relative to a system moving locally with the fluid, whereas the entropy and vorticity modes move with the fluid at the flow speed as a pattern of “frozen turbulence” [95]. A detailed analysis may be found in Pierce [95]. The idea is now to formulate the non-reflective boundary condition by considering the asymptotic solution for a

compact source, which radiates any kind of perturbations. The governing equations are modified such that only outgoing characteristics are described and no boundary condition is necessary any more. The modeling of incoming perturbations is removed from the PDE system.

Radiation condition

Due to the different character of hydrodynamic and acoustic modes of perturbation an inflow or no flow boundary requires a different treatment than the outflow. The radiation boundary condition describes only the radiation of acoustic waves. It is applied as inflow or no-flow boundary condition, as hydrodynamic modes moving with the flow cannot approach an inflow. The outflow boundary condition requires an additional treatment of the entropy and vorticity modes. For both boundary conditions the approximate source position has to be specified in advance by a guess of the solution.

The radiation condition is presented first. Then the outflow boundary condition is developed as an extension to it. When considering a compact source and assuming that the origin of the acoustic waves is known, one can formulate the radiation condition based on a spherical wave equation for 3D or a cylindrical wave equation for axisymmetric and 2D problems. The radiation boundary condition for the spherical radiation in three dimensions is given according to Bogey and Bailly [11] as follows

$$\frac{\partial}{\partial t} \begin{pmatrix} \varrho' \\ u' \\ p' \end{pmatrix} + v_{gr} \left(\frac{\partial}{\partial r} + \frac{D}{r} \right) \begin{pmatrix} \varrho' \\ u' \\ p' \end{pmatrix} = 0 \quad (3.15a)$$

$$\frac{\partial}{\partial t} \phi' + v_{gr} \left(\frac{\partial}{\partial r} + \frac{D}{r} \right) \phi' = 0. \quad (3.15b)$$

where $D = 1$ applies for the originally considered spherical radiation. The group velocity is given by the same authors to

$$v_{gr} = \mathbf{u}_0 \cdot \mathbf{e}_r + c. \quad (3.16)$$

The geometric construction of the group velocity with respect to the radiation direction is sketched in Figure 3.5. The radiation condition is solved instead of the

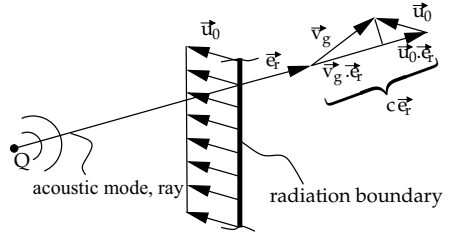


Figure 3.5.: Sketch of a computational domain with source Q inside, radiation vector and construction of the group velocity

interior PDE system at the outermost three grid lines at the non-reflective boundary. The assumed source position may influence the result significantly. The radiation condition has a wide range of applications. Good results may be obtained even when applied in the moderate far field. However, for the propagation of higher modes in flow ducts, this kind of boundary condition is inadequate due to the discrepancy of the group velocity.

Modifications: To obtain a two dimensional form of the radiation condition, $D = 0.5$ is used in Eq. (3.15) according to Tam and Webb [127]. An one-dimensional radiation condition would be obtained by replacing the radial direction in Eq. (3.15) with the normal vector of the radiation boundary and omitting the decay with r by setting $D = 0$ in Eq. (3.15). This formulation is applied as radiation condition in a ducted environment. In addition, this modification makes the radiation condition compatible to the wall boundary condition. The combination of wall and radiation boundary condition would otherwise lead to unstable solutions.

Outflow boundary condition

The outflow boundary condition is obtained by adding the transport of entropy and vorticity perturbations to the system. The situation at the outflow is sketched in Figure 3.6. The pressure perturbation p' is purely acoustic, whereas the entropy mode is added to the density perturbation ($\rho' = \rho'_a + \rho'_s$) and the vortical perturbation is superimposed to the acoustic velocity ($\mathbf{u}' = \mathbf{u}'_a + \mathbf{u}'_\omega$). The acoustic density perturbation is given by $\rho_a = c^{-2} p'$, whereas the acoustic velocity component is $\mathbf{u}'_a + u_0 \cdot \nabla \mathbf{u}'_a = -\rho_0^{-1} \nabla p'$. With these prerequisites, according to Bogey and Bailly [11], the outflow condition is obtained to

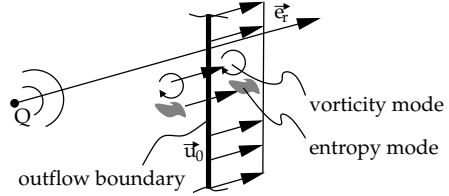


Figure 3.6.: Sketch of a computational domain with source Q inside, outflow of vorticity and entropy mode waves with the flow speed \mathbf{u}_0 and radiation unity vector \mathbf{e}_r

$$\frac{\partial \rho'}{\partial t} + \mathbf{u}_0 \cdot \nabla \rho' = \frac{1}{c^2} \left(\frac{\partial p'}{\partial t} + \mathbf{u}_0 \cdot \nabla p' \right), \quad (3.17a)$$

$$\frac{\partial \mathbf{u}'}{\partial t} + \mathbf{u}_0 \cdot \nabla \mathbf{u}' = -\frac{1}{\rho_0} \nabla p' \quad (3.17b)$$

$$\text{and} \quad \frac{\partial p'}{\partial t} + v_{\text{gr}} \left(\frac{\partial}{\partial r} + \frac{D}{r} \right) p' = 0. \quad (3.17c)$$

\dot{p}' occurs in Eq. (3.17a) and (3.17c). Thus, Eq. (3.17c) is used to obtain \dot{p}' . The result is used to eliminate \dot{p}' from Eq. (3.17a) yielding an expression for q'

$$\frac{\partial q'}{\partial t} + \mathbf{u}_0 \cdot \nabla q' = \frac{1}{c^2} \left(-v_{\text{gr}} \left(\frac{\partial}{\partial r} + \frac{D}{r} \right) p' + \mathbf{u}_0 \cdot \nabla p' \right). \quad (3.17d)$$

The above set of equations applies for the spherical radiation from a three-dimensional point source. The modifications, which have been detailed above, are applied to obtain the two- and one-dimensional outflow conditions.

Variations of the base flow have been neglected by the construction of the outflow boundary condition. This seems legitimate, as such variations would describe sources in the boundary region, which are not necessarily part of the numerical solution. However, it is found that strong variations of the mean flow may lead to problems with the outflow condition. These problems are observed when an instability wave, which is generated in a free shear layer, reaches the boundary. Furthermore, the outflow boundary condition of Eqs. (3.17b) to (3.17d) must not be applied at an inflow or no flow boundary. This would lead to an ill-posed problem, as the boundary condition for the incoming entropy and vorticity perturbations would be missing.

Automatic detection of radiation or outflow boundary condition

To automatically detect a local inflow, no-flow or outflow boundary, the normal vector \mathbf{n} of the outermost grid line according to Eq. (3.10) is used. The scalar product with the average velocity vector \mathbf{u}_0 leads to the following differentiation between radiation and outflow boundary condition

$$\mathbf{n} \cdot \mathbf{u}_0 \begin{cases} > 0, \text{ outflow boundary condition} \\ \leq 0, \text{ radiation boundary condition.} \end{cases} \quad (3.18)$$

The automatic detection is used in the following and the corresponding boundary condition is applied. The resulting formulation is denoted as radiation/outflow boundary condition.

Implementation of the sound source

The implementation of a sound source, which specifies an incoming wave at the boundary with the radiation/outflow boundary condition is described in this section according to the ideas of Tam [123]. Instead of formulating a radiation/outflow boundary condition for the whole perturbation field, as it was applied in the preceding sections, a decomposition of the field into a source contribution ($_{\text{in}}$) and a radiation/outflow contribution ($_{\text{out}}$) is considered. The state vector $\boldsymbol{\phi}'$ of the fluid is then written as superposition of the incoming source contribution and the outgoing

perturbation, for which the radiation/outflow condition applies

$$\boldsymbol{\phi}' = \boldsymbol{\phi}'_{\text{in}} + \boldsymbol{\phi}'_{\text{out}} \quad (3.19a)$$

$$\begin{pmatrix} \varrho' \\ \mathbf{u}' \\ p' \end{pmatrix} = \begin{pmatrix} \varrho'_{\text{in}} \\ \mathbf{u}'_{\text{in}} \\ p'_{\text{in}} \end{pmatrix} + \begin{pmatrix} \varrho'_{\text{out}} \\ \mathbf{u}'_{\text{out}} \\ p'_{\text{out}} \end{pmatrix}. \quad (3.19b)$$

The radiation/outflow boundary condition is applied for the outgoing field $\boldsymbol{\phi}'_{\text{out}} = \boldsymbol{\phi}' - \boldsymbol{\phi}'_{\text{in}}$. By using the definition of Eq. (3.19a), the radiation condition Eq. (3.15b) with an additional source yields

$$\frac{\partial}{\partial t} [\boldsymbol{\phi}' - \boldsymbol{\phi}'_{\text{in}}] + v_{\text{gr}} \left(\frac{\partial}{\partial r} + \frac{1}{r} \right) [\boldsymbol{\phi}' - \boldsymbol{\phi}'_{\text{in}}] = 0. \quad (3.20)$$

The outflow boundary condition from Eqs. (3.17a) to (3.17c) yields

$$\frac{\partial [\varrho' - \varrho'_{\text{in}}]}{\partial t} + \mathbf{u}_0 \cdot \nabla [\varrho' - \varrho'_{\text{in}}] = \frac{1}{c^2} \left(\frac{\partial [p' - p'_{\text{in}}]}{\partial t} + \mathbf{u}_0 \cdot \nabla [p' - p'_{\text{in}}] \right), \quad (3.21a)$$

$$\frac{\partial [\mathbf{u}' - \mathbf{u}'_{\text{in}}]}{\partial t} + \mathbf{u}_0 \cdot \nabla [\mathbf{u}' - \mathbf{u}'_{\text{in}}] = -\frac{1}{\varrho_0} \nabla [p' - p'_{\text{in}}] \quad (3.21b)$$

$$\text{and} \quad \frac{\partial [p' - p'_{\text{in}}]}{\partial t} + v_{\text{gr}} \left(\frac{\partial}{\partial r} + \frac{1}{r} \right) [p' - p'_{\text{in}}] = 0. \quad (3.21c)$$

The source $\boldsymbol{\phi}'_{\text{in}}$ is specified at the boundary in terms of spatial and temporal derivatives. This defines a von Neumann boundary condition. Arbitrary time and space functions can be specified through $\boldsymbol{\phi}'_{\text{in}}$. Limits are only given by the spatial and temporal resolution. Moreover, only acoustic waves make sense at an outflow.

3.5.2. Sponge layer

The current form of the simple sponge layer, which can also be used to add a sound source to the computation is based on an observation of Israeli and Orszag [54]. According to these authors, an additional damping term of Newtonian cooling or friction type in the PDE can act as an approximation of a non-reflective boundary condition. The additional term is defined as follows

$$\frac{\partial \boldsymbol{\phi}}{\partial t} = -f(\boldsymbol{\phi}) - \sigma_d(x) (\boldsymbol{\phi} - \boldsymbol{\phi}_{\text{in}}), \quad (3.22)$$

where $\boldsymbol{\phi}_{\text{in}}$ denotes the optional source term. The source value is also specified at the three outermost grid lines in terms of a Dirichlet boundary condition. If no source is specified at a boundary, the source term and the perturbation field of the outermost grid line are set to zero.

In practice the size of the sponge layer and the functional shape of the damping coefficient are essential for the non-reflective qualities of the sponge layer. The damping function towards the wall is given as

$$\sigma_d(\mathbf{x}) = \begin{cases} \exp \left\{ -\frac{1}{2} n_P \frac{d_{BC}^2}{\Delta x_{NC/F}^2} \right\} & , d_{BC} < \Delta x_{NC/F} \\ 0 & , \text{else} \end{cases} \quad (3.23)$$

where

$$d_{BC} = \sqrt{(x_i - x_{i,\rho})^2}$$

and $\Delta x_{NC/F} = \sqrt{(x_{i,e} - x_{i,\rho})^2}$

are the distance of the point from the boundary of the computational domain and the width of the sponge layer, respectively. This leads to a Gaussian distribution of the damping coefficient, which reaches a maximum at the outer surface of the computational domain. The damping is uni-directional, which leads to massive reflection of waves that propagate along the sponge layer at very low angles [113]. The simple sponge layer, which is defined by this boundary condition, however, provides good reflection characteristics with a well chosen damping distribution for waves impinging almost perpendicular to the boundary. In addition it is much easier and faster than the PML, which is described in the next section.

3.5.3. Perfectly matched layer (PML)

The perfectly matched layer (PML) boundary condition was initially developed for computational electrodynamics and goes back to Berenger [9]. The basic idea is to split the fluxes, in Berengers case of the Maxwell-equations, into the contribution of each coordinate direction. Then the coordinate direction, associated with the flux towards the outer surface is charged by an additional dissipation, which makes the damping of perturbations selective to the direction. In the frequency domain, this operation describes a stretching of the related coordinate by adding an imaginary part, according to [45]. The dispersion relation is preserved by this operation Hesthaven [45]. Hu first adopted the method as non-reflective boundary condition for CAA. Tam et al. [125] found this PML formulation to be unstable. The original PML was found to be an only weakly well posed mathematical problem for nonzero mean flow velocities by Hu [49]. He recovered the stability of the PML by introducing a Prandtl–Glauert transformation. The resulting boundary condition can be written using

$$\frac{\partial \phi'_1}{\partial t} := \phi' \quad (3.24a)$$

for two-dimensional and modal-axisymmetric cases as (comp. Hu [49]):

$$\begin{aligned}
\frac{\partial \phi'}{\partial t} = & \underbrace{-A \cdot \frac{\partial \phi'}{\partial x} - B \cdot \frac{\partial \phi'}{\partial r} - \frac{1}{r} C \cdot \phi' - D \cdot \phi' - (\sigma_x + \sigma_r) \phi'}_{\text{Euler equation}} \underbrace{- (\sigma_x + \sigma_r) \phi'}_{\text{Sponge layer}} \\
& - \sigma_r A \cdot \frac{\partial \phi'_1}{\partial x} - \sigma_x B \cdot \frac{\partial \phi'_1}{\partial r} - (\sigma_x + \sigma_r) \frac{1}{r} C \cdot \phi'_1 \\
& - \underbrace{\frac{\text{Ma}_x}{1 - |\text{Ma}|^2} A \cdot [\sigma_x \phi' + (\sigma_x \sigma_r) \phi'_1] - \frac{\text{Ma}_y}{1 - |\text{Ma}|^2} B \cdot [\sigma_r \phi' + (\sigma_x \sigma_r) \phi'_1]}_{\text{Prandtl-Glauert-transform}},
\end{aligned} \tag{3.24b}$$

where the two-dimensional case is obtained by setting $C = \mathbf{0}$ and $D = D_{2D}$ as shown in Appendix A.2.3. The three-dimensional PML is derived in the current work, extending the above conditions, under the assumption that the base flow is oriented in x -direction

$$\begin{aligned}
\frac{\partial \phi'}{\partial t} = & -A \cdot \frac{\partial \phi'}{\partial x} - B \cdot \frac{\partial \phi'}{\partial y} - C \cdot \frac{\partial \phi'}{\partial z} - D \cdot \phi' - (\sigma_x + \sigma_y + \sigma_z) \phi' \\
& - (\sigma_y + \sigma_z) A \cdot \frac{\partial \phi'_1}{\partial x} - (\sigma_x + \sigma_z) B \cdot \frac{\partial \phi'_1}{\partial y} - (\sigma_x + \sigma_y) C \cdot \frac{\partial \phi'_1}{\partial z} \\
& - \frac{\text{Ma}_x}{1 - |\text{Ma}|^2} A \cdot [\sigma_x \phi' + (\sigma_x \sigma_y) \phi'_1],
\end{aligned} \tag{3.24c}$$

It should be noted that the PML as well as the sponge layer do not modify the governing equations to disallow the wave propagation back into the computational domain. Therefore, it is still required to specify a boundary condition for each variable in order to state a mathematically well-posed problem. In the current work, the boundary value is specified to be zero for the outermost grid line. This corresponds to a Dirichlet type boundary condition. To avoid reflections at this boundary condition, the sponge layer or the PML should remove any perturbation before it reaches this boundary.

3.6. Sound source

In this section, the definition of a sound source at the boundary is described. In fact, this source is a boundary condition rather than a source in the sense of Lighthill's aeroacoustic analogy. However, the related boundary condition is referred to as sound source in the following.

3.6.1. Plane waves

First, plane waves are considered. A single plane wave in x_1 -direction is given as

$$\phi_{\text{in}} = \begin{pmatrix} \varrho' \\ u' \\ v' \\ w' \\ p' \end{pmatrix} = \text{Re} \left\{ \begin{pmatrix} \frac{1}{c^2} A \\ \frac{k}{\varrho_0 d} A \\ 0 \\ 0 \\ A \end{pmatrix} \exp[i(\omega t - k x)] \right\}, \quad (3.25)$$

under the assumption of a base flow in x_1 -direction and with d is defined as

$$d := (\omega - u_0 k) \quad (3.26)$$

A denotes the amplitude of the incoming wave and k is the wave number according to the dispersion relation

$$\left(\frac{\omega}{c} - \text{Ma}_x k \right)^2 - k^2 = 0.$$

The axial wave number is obtained to be

$$k = \frac{\omega}{c} \frac{-\text{Ma} \pm 1}{1 - \text{Ma}^2}. \quad (3.27)$$

The wave number is positive for waves propagating in positive x_1 -direction. A complex wave number corresponds to a cut-off mode.

This source formulation is used for the broadband time-domain impedance education with a multi-frequency excitation. This is obtained by superimposing the solutions for different frequencies. In this way, all frequencies from the experiment are investigated at once. The multi-frequency source involves a large number of trigonometric function calls, especially, if the radiation/outflow boundary condition is applied as sound source. To reduce the computational time, the source data is calculated in a preprocessing step. It is sampled on an adequately large time step and stored for each point inside the source region. The stored data for the sound source must be interpolated to the very fine resolved, subsequent time levels of the Runge–Kutta scheme. Therefor a filtering interpolation is introduced as it is described in the following section.

3.6.2. Generalization of the filtering approach for the interpolation of the source

The filtering interpolation is based on the following approach

$$\phi_{\text{in}}(t) = \sum_{j=1}^N w_j \phi_s(\tau_{I+j}). \quad (3.28)$$

The source data is assumed to be discretized by any non-constant time step τ and the offset is assumed to be correctly chosen, such that t is located as close as possible to the center of the source time interval $[\tau_{l+1} - \tau_{l+N}]$. The system defining the filter coefficients w_j is constructed based on a Taylor-series expansion of the above definition, according to the method used for the construction of a standard filter (comp. [147, Chapter 10])

$$\sum_{j=1}^N w_j = 1, \quad (3.29a)$$

$$\sum_{j=1}^N w_j (\tau_{l+j} - t) = 0, \quad (3.29b)$$

$$\vdots$$

$$\sum_{j=1}^N w_j (\tau_{l+j} - t)^{N-2} = 0 \quad (3.29c)$$

$$\text{and} \quad \sum_{j=1}^N w_j (-1)^j = 0. \quad (3.29d)$$

The last equation defines a low-pass filter. It imposes the condition that an oscillation of the source data should not be transferred to ϕ_{in} .

The above linear system of equations is set up once for each subsequent time level of the Runge–Kutta scheme. The coefficients w_j are obtained by solving it. The filter coefficients are calculated only one time. They are then used to interpolate the whole source vector ϕ_s for all grid points in the source region. The filter size is a free parameter. It is found that $N > 15$ points can lead to accuracy problems for the coefficient calculation and makes it slow. A too small point number, on the other hand, would require a fine time step in the stored source data to obtain an adequate accuracy. A filtering interpolation involving nine points inside the source data is found to be most efficient.

3.6.3. Modes in a cylindrical duct

In this section, the analytical solution in a cylindrical or annular duct with uniform base flow and arbitrary wall impedance is given. It is used to specify the modal

source in an axisymmetric duct. The eigenfunctions are given as

$$\phi_{\text{in}} = \begin{pmatrix} \varrho' \\ u' \\ v' \\ w' \\ p' \end{pmatrix}_{mn} = \text{Re} \left\{ \begin{pmatrix} \frac{1}{c^2} B(r) \\ \frac{k}{\varrho_0 d} B(r) \\ \frac{i}{\varrho_0 d} B'(r) \\ -\frac{m}{r \varrho_0 d} B(r) \\ B(r) \end{pmatrix} \exp[i(\omega t - m\varphi - kx)] \right\}, \quad (3.30a)$$

where $B(r)$ is given as a combination of amplitude A and Bessel and Neumann functions

$$B(r) = A \{ J_m(\mu_{m,n} r) + Q Y_m(\mu_{m,n} r) \}. \quad (3.30b)$$

The ordinal values m and n denote the azimuthal and radial mode order, respectively. The coordinate system is assumed to be oriented as shown in Fig. 2.1. The eigen-value $\mu_{m,n}$ is obtained from the boundary condition at the outer and inner radius r_a and r_i of an annular duct. In general, it can be complex to allow an arbitrary impedance on the surface. The axial wave number is obtained from the dispersion relation in the moving fluid

$$\begin{aligned} & \left(\frac{\omega}{c} - \text{Ma}_x k \right)^2 - k^2 - \mu_{m,n}^2 = 0 \\ \text{to} \quad k &= \frac{-\frac{\omega}{c} \text{Ma}_x \pm \sqrt{\left(\frac{\omega}{c} \right)^2 - \left(1 - \text{Ma}_x^2 \right) \mu_{m,n}^2}}{1 - \text{Ma}_x^2}. \end{aligned} \quad (3.31)$$

Making use of the impedance formulation for a moving surface by Ingard [53], the boundary condition at the outer radius is obtained to

$$u'_n Z = p' - \frac{k}{i\omega} u_0 p' \quad (3.32a)$$

$$\text{or} \quad i\omega u'_n Z = i(\omega - u_0 k) p'. \quad (3.32b)$$

The following velocity-pressure relation is obtained from the conservation of momentum under the assumption of an uniform mean flow

$$i(\omega - u_0 k) u'_n = -\frac{\partial p'}{\partial r}.$$

By combining this pressure-velocity relation with a given mode

$$p' = B(r) \exp[i(\omega t - m\varphi - kx)],$$

one obtains the radial component of the velocity perturbation to

$$u'_n = -\frac{B'(r)}{i(\omega - u_0 k)} \exp[i(\omega t - m\varphi - kx)]. \quad (3.33)$$

Here, the prime of B denotes the derivative with respect to the independent variable r . Combining Eqs. (3.32b) and (3.33) one obtains a boundary condition for the impedance wall, which can be used to obtain the eigenvalue of the radial distribution

$$-i\omega Z B'(r_{\text{wall}}) + (\omega - u_0 k)^2 B(r_{\text{wall}}) = 0. \quad (3.34)$$

For hard walls, the condition falls back to

$$B'(r_{\text{wall}}) = 0. \quad (3.35)$$

The in general complex ratio of the Bessel and Neumann functions, Q , is used to fit the boundary conditions at inner and outer wall. Without a center body, there is no contribution of the Neumann function ($Q = 0$). With a lined center body of the impedance Z_i , the boundary condition at the inner radius r_i is used to obtain the complex ratio of Bessel and Neumann functions according to

$$-i\omega Z_i (J'(\mu_{m,n} r_i) + Q Y'(\mu_{m,n} r_i)) + (\omega - u_0 k)^2 (J(\mu_{m,n} r_i) + Q Y(\mu_{m,n} r_i)) = 0.$$

This leads to the following explicit formulation of Q

$$Q = -\frac{-i\omega Z_i J'(\mu_{m,n} r_i) + (\omega - u_0 k)^2 J(\mu_{m,n} r_i)}{-i\omega Z_i Y'(\mu_{m,n} r_i) + (\omega - u_0 k)^2 Y(\mu_{m,n} r_i)}. \quad (3.36)$$

The impedance boundary condition at the outer wall, $r = r_o$, of impedance Z_o is used to obtain a transcendent equation. It is solved numerically in the current work to obtain $\mu_{m,n}$

$$\begin{aligned} & -i\omega Z_o (J'_m(\mu_{m,n} r_o) + Q Y'_m(\mu_{m,n} r_o)) \\ & + (\omega - u_0 k)^2 (J_m(\mu_{m,n} r_o) + Q Y_m(\mu_{m,n} r_o)) = 0. \end{aligned} \quad (3.37)$$

An iterative method is implemented with MATLAB, which uses the $\mu_{m,n}$ of the previous step or an initial guess to obtain k from Eq. (3.31) and Q from Eq. (3.36). Then, a zero search is employed for Eq. (3.37). Finally, the eigenvalues k_x and $\mu_{m,n}$ and the ratio Q are used to specify the sound source.

4. Time-domain impedance modeling

In this chapter, the time-domain impedance boundary condition which is the main objective of the present work, is developed and discussed. This boundary condition can for instance be used to model the acoustic lining of aeroengines. Today, such aircraft liners are typically designed as arrays of small Helmholtz resonators. Thus, the modeling of the Helmholtz resonator as a basic component is investigated in detail in the first part. The connection between geometry, model for the frequency response and time-domain impedance boundary condition is pointed out. The modeling of the flow effect and the related instability is reviewed from the literature. Finally, the implementation of the impedance boundary condition into the numerical method is described in detail.

4.1. The concept of acoustic impedance

The acoustic impedance of a surface is originally defined as the complex ratio of acoustic pressure and acoustic velocity at the surface for acoustic waves impinging perpendicular to the surface. This definition is extended to arbitrary angles of incidence by replacing the acoustic velocity with its component u'_n normal to the surface. In the current work locally-reacting surfaces¹ are considered. By using the complex amplitudes of pressure \hat{p} and velocity perturbation \hat{u}_n , the complex impedance of the surface is defined as

$$Z(i\omega) = \frac{\hat{p}(i\omega)}{\hat{u}_n(i\omega)}. \quad (4.1)$$

where $\hat{u}_n = \hat{\mathbf{u}} \cdot \mathbf{n}$ is the normal component of the complex amplitude of the velocity perturbation. Z is a complex function of the angular frequency. This dependence is emphasized by the independent variable $(i\omega)$ in the following. Due to the consideration of the Fourier transformed equations, Z is not explicitly depending on the time t . The consideration of Fourier transformed PDE's and their solution is referred to as frequency domain in the following. In contrast, the original equations are considered to be in the time domain. The non-dimensional impedance ζ is introduced by normalizing Z with the impedance of air $\varrho_0 c$

$$\zeta(i\omega) = \frac{Z}{\varrho_0 c}. \quad (4.2)$$

¹A locally-reacting surface is characterized by the direct dependency of the velocity perturbation normal to the wall to the pressure perturbation at the wall. In contrast, non-locally-reacting surfaces cannot be described by such a simple model and for instance add a dependency to the pressure gradient or higher derivatives of the pressure along the wall.

4.2. The Helmholtz resonator² in frequency domain

There are many methods to realize a locally-reacting surface. In the following sections, the realization by a perforate face over closed cavities is considered in more detail. This concept is frequently used as basic element of the acoustic lining in aeroengines. Provided the acoustic wave length is much longer than the size of each resonator element, it can be approximated as locally-reacting surface. A low-frequency limit of such a resonator is found in the single degree of freedom mass-spring-damper system shown in Figure 4.1. It is used to describe a locally-reacting surface in each wall point.

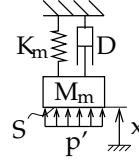


Figure 4.1.: Mechanical analog

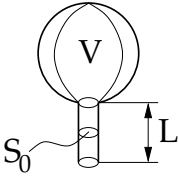


Figure 4.2.: Helmholtz resonator

The mass-spring-damper element shown in Fig. 4.1 is forced by the acoustic pressure on its surface. The equation of motion reads

$$M_m \ddot{x} = S p' - K_m x - D \dot{x}, \quad (4.3)$$

where S denotes the area of the surface element. To obtain the impedance, the velocity of the mass element is identified with the acoustic velocity component normal to the surface. Eq. (4.3) is multiplied by S^{-1} ; the mass M_m , spring rate K_m and damping rate D are replaced by the corresponding specific values m_m , k_m and d , which are related to the unit area. A complex ansatz is introduced for $u'_n = \hat{u}_n e^{i\omega t}$ and $p' = \hat{p} e^{i\omega t}$. Finally the impedance of the mass-spring-damper element shown in Figure 4.1 yields

$$Z = \frac{\hat{p}}{\hat{u}_n} = i\omega m_m + d + \frac{k_m}{i\omega}. \quad (4.4)$$

Now, the Helmholtz resonator shown in Figure 4.2 is used as a template, to identify the mechanical model parameters with the constructive details of the resonator, these are the cavity volume V , the neck length L and the open area of the neck S_0 , as shown in Figure 4.2. The damping rate per unit area d is only imprecisely described by theoretical predictions and needs exact measurements. Thus, the undamped Helmholtz resonator is considered first. An one-dimensional theory of the

²Named in memoriam to the German polymath Hermann von Helmholtz (*August 31st 1821 – †September 8th 1894 [136]) who dedicated his early working period to acoustics, including the development of an exact mathematical theory and a mechanical analogue of the resonator (Helmholtz, Theory of air Oscillations in Tubes With Open Ends, Jour. f. reine und angewandte Mathematik 57, p. 1-72, 1860, found in [95]). Hermann von Helmholtz for instance described such devices in a 1863 publication [44], where an ear plugged resonator was used as frequency-selective hearing aid to enhance the perception of pure tones.

Helmholtz resonator identifies the model parameters of the mechanical system as follows

$$m_m = \varrho_0 L \text{ and } k_m = \frac{S_0 \varrho_0 c^2}{V}, \quad (4.5a)$$

where m_m follows from an identification of the mass element as the air in the neck of the resonator and k_m is obtained by considering a quasi-static, adiabatic compression of the fluid in the cavity, due to the air pressed in from the neck. A detailed derivation can be found e. g. in Ehrenfried [31, page 368ff.]. By inserting the expressions Eq. (4.5a) into Eq. (4.4), one obtains the impedance of the Helmholtz resonator for low frequencies via the mechanical analogue

$$Z_{HR} = i\omega \varrho_0 L + d + \frac{1}{i\omega} \frac{S_0 \varrho_0 c^2}{V}. \quad (4.5b)$$

Please note, that m_m is the mass per unit area and k_m is the stiffness per unit area. The resonance angular frequency of the undamped Helmholtz resonator is obtained by the mechanical analogue. It reads

$$\omega_0 = \sqrt{\frac{k_m}{m_m}} = \sqrt{\frac{c^2 S_0}{V L}}. \quad (4.6)$$

At the resonance frequency the imaginary part of the impedance, the reactance, becomes zero. By fitting the damping parameter of the mechanical analogue, the resistance can be tuned. The imaginary part of the impedance outside the resonance does not contribute to the dissipation of acoustic waves. Rather it introduces a phase shift which leads to reflections at the transition between a hard wall and the liner, which is called hard-lined transition in the following.

4.2.1. Helmholtz resonator panels for acoustic lining

Typical acoustic linings for room acoustics or aeroengines use panels that include a large number of Helmholtz resonators. The area covered by the liner panel, S , is usually considered as a reference rather than the open area, S_0 . To take account for this fact, the ratio of open and treated area, σ , is introduced as (comp. e. g. Fuchs [36])

$$\sigma = \frac{S_0}{S}. \quad (4.7a)$$

Then, according to Fuchs [36], the mass per surface area and spring rate per surface area are obtained to

$$m_m = \frac{\varrho_0 L}{\sigma} \text{ and } k_m = \frac{S \varrho_0 c^2}{V}. \quad (4.7b)$$

This leads to a modified resonance frequency for such panels, which depends on the total area of the panel instead of the neck area

$$f_0 = \frac{\omega_0}{2\pi} = \frac{c}{2\pi} \sqrt{\frac{\sigma S}{VL}}. \quad (4.7c)$$

4.2.2. Neck correction

The aforementioned mechanical analogue assumes an ideal massless spring and an ideal mass with infinite stiffness. However, the medium inside the cavity volume, which is described as an ideal spring, has a finite mass. Furthermore, the moving air in- and outside the neck increases the moving mass according to Alster [4]. The additional mass is added by a length correction. The model assumes a solid-body motion of the mass. Therefore, it is limited to low frequencies for which the typical extension of the resonator is much smaller than the acoustic wavelength. Higher frequency models will be discussed in Section 4.3. Due to the additional mass, the predicted resonance frequency of the Helmholtz resonator may differ significantly from the result in the preceding section. E. g. Alster [4] found errors up to 143 % even with an end correction. The end correction leads to an increased mass:

$$m_m = \varrho_0 (L + \Delta L_i + \Delta L_o) \text{ or } m_m = \varrho_0 L (1 + \Delta_L).$$

As the ends of the neck can be acoustically different, the neck correction is split into a contribution of the medium in- and outside the neck according to Alster [4]. Both have to be added in order to obtain the effective mass. They are subsumed to the correction factor Δ_L . For a single resonator Alster [4] gives an analytical formula, which is found to be in a good agreement with the experimentally observed resonance frequency for a wide range of resonator types. However, the end correction for open ends remains empirical in Alster [4, Eq. (33)].

4.3. Extension to high frequencies

The theory of the Helmholtz resonator, which was presented in the preceding sections, is limited to low frequencies. This limitation is due to the assumptions of a solid body motion of the medium in the neck and a negligible mass for the fluid in the cavity volume. Furthermore, the changes in the volume are assumed to be quasi static. This limitations are dropped in the current section and three high frequency resonator models are presented.

4.3.1. The broadband $\lambda/4$ -resonator

A very simple principle of an acoustic lining is the $\lambda/4$ -resonator. It consists of a narrow channel, which is connected to the environment on one end and closed by a rigid wall on the other end. Due to the dimensions, the wave propagation in other

directions than along the channel axis is negligible. The impedance function of such an undamped $\lambda/4$ -resonator is described as

$$Z = -i \varrho_0 c \cot \left(\omega \frac{l}{c} \right) = -i \varrho_0 c \cot (\text{He}_l), \quad (4.8)$$

where l denotes the depth of the channel from the open end to the rigid closure and He_l the related Helmholtz number. The rigid wall boundary condition at the bottom of the duct leads to equal complex amplitudes for incoming and reflected plane waves at this side of the channel. In consequence, the ratio of incoming and outgoing pressure waves at the open end of the duct is described by a cosine function, whereas the acoustic velocity obeys to a sine function. This leads to the cotangent function describing the ratio of pressure and velocity at the open end in Eq. (4.8).

Even though, the resonator has a simple geometry, the model is not directly comparable to the mass-spring-damper analogue. However, for low frequencies, which lead to small Helmholtz numbers built with the depth of the cavity volume ($\text{He}_l \ll \pi$), the cotangent term can be approximated by a truncated Laurent series about $\text{He}_l = 0$ as (comp. [3, page 75, Eq. (4.3.70)]), which results in the following approximation

$$\begin{aligned} Z &\approx -i \varrho_0 c \left[\frac{1}{\text{He}_l} - \frac{\text{He}_l}{3} \right] \\ &\approx \frac{\varrho_0 c^2}{i \omega l} + \frac{i \omega \varrho_0 l}{3}. \end{aligned}$$

By considering terms of equal order in $i\omega$, the identification with terms in the mechanical analogue becomes possible. $1/3$ of the air in the $\lambda/4$ -resonator contributes to a mass-like term, whereas the whole air in the cavity acts as spring, for low frequencies. This illustrates that the continuous modeling of the high-frequency resonator does not clearly distinguish between a massless spring and an ideal incompressible mass. Rather both parts are described as a compressible medium with finite mass.

4.3.2. Ko's broadband impedance model

Another model, which describes the response of a resonator up to high frequencies is found in Ko [63]. The frequency response of a 1970s state-of-the-art liner is well described by this model, according to Ko [63]. The model is considered here, as it was used by Koch [64] to describe the frequency response of the liner, which is considered in Section 7.1.3 in a benchmark problem. As the $\lambda/4$ -resonator, Ko's model shows a cotangent. However, additional terms are found. Ko does not provide an explanation of these terms. Ko's model is stated as (comp. [63, Eq. (21)])

$$\zeta = R_f^* \left(1 + i \frac{f}{f_f} \right) - i \cot (kl), \quad (4.9a)$$

4. Time-domain impedance modeling

which reads in a dimensional notation

$$Z = \varrho_0 c R_f^* + \frac{i\omega}{\omega_f} \varrho_0 c R_f^* - i \varrho_0 c \cot(\text{He}_l). \quad (4.9b)$$

f_f is a characteristic frequency. It is related to the frequency for which the imaginary part of the first term becomes equal to the real part. Viscous damping effects are only described by $R_f = R_f^* \varrho_0 c$, such that the real part of the impedance, the resistance, remains constant for all frequencies. R_f corresponds to the damping term of the mechanical analogue. The $i f f_f^{-1}$ term corresponds to the mass reactance of the mechanical analogue, which is described by the $i\omega m_m$ term in Eq. (4.5b). The second purely imaginary term, the cotangent term in Eq. (4.9b), is only indirectly related to the mechanical analogue Eq. (4.5b), such that the Laurent series must be employed. The corresponding terms of the $\lambda/4$ -resonator, Eq. (4.8), on the other hand, can be directly identified due to the cotangent term found in both models. Ko's model corresponds to a damped $\lambda/4$ -resonator with an additional moving solid-body mass.

For the identification with the mass-spring-damper analogue, the active length l of the Ko's model is rewritten using the ratio of the prismatic volume V and its cross section S_V to obtain $l = V/S_V$. In Eq. (4.9a) l originally denotes the depth of the resonator cavity, which corresponds to an analogy with the $\lambda/4$ -resonator. Finally, one obtains the following low-frequency approximation of the model of Ko

$$Z = R_f + i\omega \left[\frac{R_f}{\omega_f} + \frac{\varrho_0}{3} \frac{V}{S_V} \right] + \frac{1}{i\omega} \varrho_0 c^2 \frac{S_V}{V}. \quad (4.10)$$

The cotangent term becomes separated into mass- and spring-like contributions, as it was found above for the $\lambda/4$ -resonator.

Comparing Eq. (4.10) to the mechanical analogue of Eq. (4.5b), the spring rate, which is the coefficient of the $(i\omega)^{-1}$ term, is slightly modified due to the use of the volume cross section S_V instead of the neck area S_0 . Furthermore, the geometrical representation of the mass m_m is replaced by the characteristic frequency ω_f and the damping parameter R_f . Therefore, the term can be interpreted as the mass-reactance term of the face sheet. An additional mass-reactance term $(\varrho_0 V)/(3 S_V)$ arises due to the first order approximation of the Laurent series which originates from the cotangent function. It describes a length correction for the moving medium in the cavity volume. The length correction for the masses moving outside the cavity must be applied in addition.

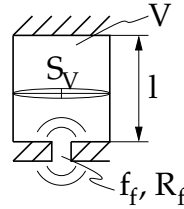


Figure 4.3.: High frequency resonator

4.3.3. The extended Helmholtz resonator model (EHR)

Finally, the model, which has been implemented to the CAA method is introduced in this section in the frequency domain, before its implementation is described in Section 4.5.2. According to Rienstra [108] it is called Extended Helmholtz Resonator (EHR) model. Similar to the two models shown above, the EHR features a cotangent term. It was introduced by Rienstra [108] as a high-frequency extension of the Helmholtz resonator model. It describes the impedance of a damped Helmholtz resonator in a very general form as

$$\zeta_{\text{EHR}}(i\omega^*) = R_f^* + i\omega^* m_f^* - i\beta^* \cot\left(\frac{1}{2}\omega^* T_l^* - i\frac{1}{2}\varepsilon\right) \quad (4.11a)$$

Or in a dimensional notation

$$Z_{\text{EHR}}(i\omega) = R_f + i\omega m_f - i\beta \cot\left(\frac{1}{2}\omega T_l - i\frac{1}{2}\varepsilon\right) \quad (4.11b)$$

$$= \frac{(R_f + i\omega m_f)(1 - e^{-\alpha}) + \beta(1 + e^{-\alpha})}{1 - e^{-\alpha}}, \quad (4.11c)$$

$$\text{with } \alpha = i\omega T_l + \varepsilon. \quad (4.11d)$$

The five parameters of this model R_f , m , ε , β and T_l have to be real and positive in order to achieve a passive and causal impedance $Z(i\omega)$, according to Rienstra [108]. $Z(i\omega)$ is a rational function that describes a periodic frequency response of the impedance given by the function $e^{-i\omega T_l}$.

The low frequency limit of the EHR is obtained in a similar way as the one of Ko's model approximating the cotangent function by a Laurent series

$$Z_{\text{EHR}}(i\omega) \approx R_f + \frac{1}{6}\varepsilon\beta + \frac{2\beta\varepsilon}{T_l^2 + (\frac{\varepsilon}{\omega})^2} + i\omega\left(m_f + \frac{\beta T_l}{6}\right) + \frac{1}{i\omega}\left(\frac{2\beta T_l}{T_l^2 + (\frac{\varepsilon}{\omega})^2}\right) \quad (4.12)$$

The identification of the parameters with the mechanical analogue is also similar to Ko's model. In accordance with Rienstra [108], R_f and m_f are found to correspond to the resistance and reactance of the face sheet, respectively. The model abstracts the panel geometry to a time delay parameter T_l in the cotangent, which can either be identified with the $\lambda/4$ -resonator depth l or the ratio $V/(cS)$ of the mechanical analogue. Moreover, a frequency dependent dissipative term which is scaling with ε , is added to the cotangent by Rienstra [108]. According to Rienstra [108], this corresponds to a damping inside the cavity fluid. The whole cotangent is scaled by the parameter β , which can be related to the open area ratio of the liner when comparing the formulations for resonator panels and the result for a single $\lambda/4$ -resonator.

Practical application of the EHR model: In the engineering practice the impedance is usually given in terms of a normalized impedance ζ as function of the physical frequency f . This means, that frequency- and time-scales remain dimensional, while the impedance is given nondimensional. To account for this, a hybrid dimensional / nondimensional form of the EHR is introduced. The parameters $R_f^* = R_f (\varrho_0 c_0)^{-1}$ and $\beta^* = \beta (\varrho_0 c_0)^{-1}$ are used from the nondimensional model. They are given with nondimensional unit in the following. ω and T_l are dimensional with the 1 s^{-1} and 1 s as unit respectively. m_f requires a special treatment as it directly combines time and impedance scales. Therefore, a dimensional $\hat{m}_f = m_f \varrho_0^{-1}$ is used, which has the unit 1 s . This convention will be used unless noted differently and the stars and hats are dropped in the following.

4.3.4. Comparison of the impedance models

The low-frequency limits for the impedance models presented in the preceding sections are summarized in Tab. 4.1. The table allows to identify the geometrical parameters of the mass-spring-damper model and the $\lambda/4$ -resonator with the model parameters of Ko [63] and Rienstra [108]. However, the parameter fit concerns only the low frequency range.

Table 4.1.: Low frequency limits of the impedance models assuming a dimensional notation.

	mass ($i\omega$)	friction (1)	spring ($\frac{1}{i\omega}$)
Single resonator	$\varrho_0 L$	d	$\varrho_0 c^2 \frac{S_0}{V}$
$\lambda/4$ resonator	$\frac{1}{3} \varrho_0 l$	-	$\varrho_0 c^2 \frac{1}{l}$
Realistic panel	$\frac{\varrho_0 L(1+\Delta_L)}{\sigma}$	d	$\varrho_0 c^2 \frac{S}{V}$
Ko [63]	$\frac{R_f}{\omega_f} + \frac{1}{3} \varrho_0 l$	R_f	$\varrho_0 c^2 \frac{1}{l}$
Rienstra [108]	$m_f + \frac{1}{6} \beta T_l$	$R_f + \frac{2\beta\varepsilon}{T_l^2 + (\frac{\varepsilon}{\omega})^2} + \frac{1}{6} \beta \varepsilon$	$\frac{2\beta T_l}{T_l^2 + (\frac{\varepsilon}{\omega})^2}$

Geometrical identification of the EHR-model parameters: The geometrical identification of the parameters in the EHR model can now be used in both directions. Firstly, it is possible to specify three out of the five model parameters of the EHR from the geometry, whereas two are found to be related to the damping for which

no geometrical parameters were given by the mechanical analogue. If the cavity damping parameter ε becomes sufficiently small ($\beta\varepsilon \ll R_f$), the friction becomes dominated by R_f and the specific mass and spring rate per unit area read

$$m_m = \varrho_0 m_f + \varrho_0 c_0 \frac{1}{6} \beta T_l; \text{ and } k_m = \varrho_0 c_0 \frac{2\beta}{T_l}.$$

For a given resonance frequency, under the assumptions that R_f , ε and m_f is very small, T_l is approximated as $T_l \approx 2/f_0$. Then β and m and R_f are obtained to

$$\beta = c \frac{\sigma S}{V} \frac{T_l}{2}, \quad (4.13a)$$

$$m = \frac{1}{\sigma} L (1 + \Delta_L) - c^2 \frac{\sigma S}{V} \frac{T_l^2}{12} \quad (4.13b)$$

$$\text{and } R_f = \frac{d}{\varrho_0 c_0}. \quad (4.13c)$$

The resistance is usually provided from airflow measurements through the perforate or from direct impedance measurements.

Secondly, the geometrical parameters of a liner panel can be calculated from the EHR model parameters. The ratio of panel area and volume is obtained from a comparison of the coefficients of the spring like term in Tab. 4.1, by using the partly nondimensional EHR

$$\frac{S}{V} = \frac{1}{c_0} \frac{2\beta T_l}{T_l^2 + \frac{\varepsilon^2}{\omega^2}}. \quad (4.14a)$$

For a panel with prismatic cells and negligibly thin separations between the cells, the ratio of the active panel area S and the cavity volume almost equals the inverse of the cell depth

$$\frac{1}{H} \approx \frac{S}{V} \approx \frac{S}{S H}. \quad (4.14b)$$

Furthermore, the mass-like term provides an expression for L/σ , where L is the corrected neck length and σ the open area ratio

$$\frac{L}{\sigma} = m_f + c_0 \frac{1}{6} \beta T_l. \quad (4.14c)$$

The above connections are used to calculate *educated geometrical parameters* from the impedance education (comp. Chapter 6) results in Section 7.2.

4.4. Models for a grazing flow on the impedance surface

In the presence of a nonzero base-flow velocity, the impedance surface is separated from the fluid in motion by a boundary layer attached to the impedance surface. The acoustic waves pass this boundary layer twice as incoming and reflected waves. Due to the boundary layer, the angle of incidence to the impedance surface is changed. For analytical models of hard walled ducts, the boundary layer is usually neglected and the base flow is abstracted as uniform flow. However, with a finite impedance of the surface, the boundary layer becomes important, due to the modification of the angle of incidence on the impedance surface.

The effective impedance of a surface under grazing flow conditions is defined as the modified impedance under flow conditions $Z' = \hat{p}/\hat{u}_n$. Where \hat{p} and \hat{u}_n are the complex amplitudes of pressure and velocity perturbation in the moving medium directly at the surface. In contrast, the impedance has been defined with the corresponding perturbation quantities in a fluid layer at rest with the surface. The parameters, which influence the effective impedance are identified in Appendix C using the boundary condition of Ingard [53] and Myers [85]. The effective impedance depends on the flow Mach number and the angle of incidence. This angle depends on the base flow conditions and the acoustic mode, such that the effective impedance of an uniform panel could change with the position. Exactly the desired Mach number and the acoustic mode have to be considered to measure the effective impedance. Moreover, it changes with the operation conditions. The practical application of the effective impedance is rejected due to this lack of generality. An independent definition of the impedance would be desirable.

Ingard [53] formulated an impedance boundary condition for grazing flow conditions, which makes use of the impedance, which can be measured without flow. The model for the infinitely thin shear layer on the impedance surface is obtained by considering a fluid particle, which moves from the moving fluid into the resting impedance surface. The displacement of such a physical particle should be continuous over the boundary layer, while the particle velocity may jump due to the infinitely thin shear layer. This consideration finally leads to a model, which makes use of the standard impedance definition without flow, and includes a convective term to model the flow effects. Myers [85] extended the consideration of Ingard by including the effect of the wall curvature under flow conditions in a generalized derivation of the impedance boundary condition with flow. The result of this consideration is used in the present work to model the flow effect. It is briefly resumed in Section 4.4.2.

Last but not least, with the availability of sufficient computer resources it becomes possible to consider a resolved boundary layer at the impedance surface using a no-slip condition for the base flow. Due to the zero flow speed at the impedance surface, the original impedance definition without flow is recovered. The Myers boundary condition becomes obsolete. It is replaced by the numerical simulation of the wave propagation through the boundary layer. Some relevant results for this method from the literature are summarized in the following Section 4.4.1.

4.4.1. A resolved boundary layer at the impedance wall

The obvious method to include the flow effect on the impedance, is a resolved boundary layer with no slip condition at the impedance surface. This method has been applied for instance by Zheng and Zhuang [145] and Reyman et al. [99]. Both use artificial profiles for the boundary layer. While Zheng and Zhuang [145] observe a convergence of the solution towards the solution using the Ingard/Myers boundary condition with a decreasing boundary layer thickness at the wall, Reyman et al. [99] use a finite-element approach with only two elements of quadratic order in the channel height to model the base flow. This leads to an artificially thickened boundary layer. In consequence, the modeling error due to the large boundary layer thickness probably leads to a wrong prediction of the NASA flow tube experiment. However, both groups [99, 145] use artificial boundary layer profiles.

Realistic boundary layers from a CFD simulation are considered by Burak et al. [20]. They show that a correct prediction of the NASA grazing-flow-tube experiment can be obtained by a high-order CFD code. Burak et al. [20] consider different CFD methods in combination with impedance boundary conditions. The results of Burak et al. [20], obtained by using a linearized Navier-Stokes solver together with a RANS model of the boundary-layer profile is most promising. The nondimensional wall distance y^+ of the first cell is chosen to be up to 160, with only small impact on the acoustic solution at most of the frequencies considered. Solely the frequency of 1 kHz shows significant differences between low Re and high Re modeling, which are attributed to a flow instability present at this frequency.

The publications of Zheng and Zhuang [145] and Reyman et al. [99] emphasize the importance of the correct boundary layer thickness for the acoustic solution with lined walls. The attenuation of acoustic waves by the liner as well as the presence of flow instabilities depends on it. However, the length scales of the boundary layer are much smaller than the acoustic scales. The resolved modeling requires an adequate grid resolution for both the acoustic scales and the boundary layer. When considering the thickness of the viscous sublayer as a minimum resolved length scale, the resolution would be dramatically increased from the acoustic limit. For many possible applications, for instance the radiation of fan-tone noise from an acoustically lined aeroengine inlet, a fully resolved boundary layer results in a substantial increase of the required spatial resolution and an extraordinary increase of the problem size, even if a RANS wall model can be applied for the flow, as observed by Burak et al. [20].

4.4.2. The Ingard/Myers boundary condition

The impedance definition of Eq. (4.1) can only find application if a layer of resting fluid adjacent to the impedance surface is present, which is not moving relatively to the surface, in average. The grazing flow along the surface is connected to this thin layer at rest by a boundary layer of finite thickness in reality. Theoretical considerations of the duct acoustics in hard-walled ducts commonly neglect this shear layer

and a plug-flow assumption finds application. However, this would directly lead to the problem of the effective impedance when applied for an impedance surface. For the following consideration it is necessary to assume an infinitely thin shear layer which connects the inner flow in the duct to the surface at rest. The perturbation quantities are altered over this shear layer. Therefore, the quantities \tilde{p} and \tilde{u}_n are introduced as the complex amplitudes of the pressure and normal velocity in the layer not moving with respect to the impedance surface. The impedance definition of Eq. (4.1) now applies for the unknowns \tilde{u}_n and \tilde{p} . The problem is shifted to the unknown relation between the perturbations in the resting and the moving layer of fluid. This relationship is obtained by Myers [85] assuming the continuity of the particle displacement over the infinite thin shear layer. The impedance boundary condition of Myers [85] is formulated as

$$\hat{u}_n(i\omega) = \frac{\hat{p}(i\omega)}{Z(i\omega)} + \underbrace{\mathbf{u}_0 \cdot \nabla \left(\frac{\hat{p}(i\omega)}{i\omega Z(i\omega)} \right)}_{\text{convective term}} - \underbrace{\frac{\hat{p}(i\omega)}{i\omega Z(i\omega)} \mathbf{n} \cdot (\mathbf{n} \cdot \nabla \mathbf{u}_0)}_{\text{curvature term}}. \quad (4.15)$$

The surface quantities at rest, \tilde{p} and \tilde{u}_n , are related to the perturbations inside the steadily moving fluid directly at the surface denoted by the complex amplitudes \hat{p} and \hat{u}_n . The wall normal \mathbf{n} is defined positive when pointing into the impedance surface. The additional terms of Eq. (4.15) in comparison to Eq. (4.1) describe the convection with the mean flow and the curvature of the impedance surface. Ingard [53] formulated a similar boundary condition, which applies for plane impedance surfaces. The boundary condition of Myers [85] adds the curvature effects with respect to this boundary condition. The two additional terms become zero without a mean flow ($\mathbf{u}_0 = \mathbf{0}$). In this case Eq. (4.15) returns to Eq. (4.1) as the assumed thin shear layer vanishes and the field variables on both sides are equal. The boundary condition applies only if the boundary layer thickness of the mean flow and the acoustic boundary layers are small compared to the acoustic wavelength [85].

A comparison of the Ingard/Myers boundary condition as a model for the boundary layer and resolved artificial boundary layers of different thickness is provided in Section 7.1.2.

4.4.3. Hydrodynamic surface waves and the instability

Numerical phenomenology

The implementation of an impedance boundary condition, which makes use of the Ingard/Myers boundary condition, seems to face a serious instability problem. Several authors, who employ an impedance boundary condition under nonzero mean-flow conditions, report an instability in their simulations. The instability is found in both time-domain [24, 61, 90] and frequency-domain [129] formulations. Only Ju and Fung [61] considered the instability observed by them with a refined mesh as a purely numerical problem. All other authors, including Tester [129] who first reported the problem, address it as a model-inherent instability of a Kelvin–Helmholtz

type. The free shear layer, which is necessary to support the Kelvin–Helmholtz instability, is found in the modeled shear layer of the Ingard/Myers boundary condition, which was described in the preceding section. The shear layer model describes a dissipative effect, which adds rotation and non-isentropy to the base flow. This is the energy source for the instability, which may grow spatially or temporally without bounds in the linear model.

To further isolate the problem, it is necessary to look at the conditions under which the instability was revealed:

- A nonzero mean flow is necessary for the instability to be present [107].
- Resolving the shear layer removes the instability in most cases [20, 99, 146].
- Some of the authors report the instability only for refined meshes [24, 61, 104].
- If the discretization of the convective term is dissipative or implicit or a filter is applied, the instability is likely to be removed [24, 71, 90, 105, 122].

Theoretical considerations

The instability is still subject to ongoing theoretical work [15, 17, 94, 107]. Rienstra [107] first classified the solutions in a cylindrical duct with impedance walls. Among the modes he found solutions with large imaginary part of the radial wave number. These modes are described as surface waves, as there is a large decay of the mode amplitude with increasing distance from the wall [15]. The decay is associated with the large imaginary part of the radial wave number found by Rienstra [107].

According to Rienstra [107] there may be up to four of such solutions for each azimuthal mode m with a nonzero mean flow. One of them is found to be potentially unstable, depending on the impedance and flow velocity at the surface, according to Brambley and Peake [17]. Without base flow, there are only two surface waves which are considered to be of acoustic nature, therefore.³ The other two surface waves are classified as hydrodynamic surface waves. These waves only appear in the presence of a nonzero base flow; they vanish with the base flow velocity in the near wall region approaching to zero. One of these waves can describe a spatially growing *convective instability* or even a temporally growing *absolute instability* of Kelvin–Helmholtz type.

The analysis of Rienstra [107] considers the limit for large angular frequencies in combination with an infinitely thin shear layer at the surface. For this limit, the instability is always present, independently of the actual impedance and flow conditions [107]. A refined analysis of the surface waves and the connected instability is provided in the work of Brambley and coauthors [15, 17]. They found that some of these surface waves may not be present for higher azimuthal modes m and a Helmholtz number built with the outer radius of the duct (He_r) in the range of m .

³These surface waves find for instance application in the touch pads of laptops (comp. e. g. the patent of Brenner and Fitzgibbon [18]).

Rienstra and Vilenski [111] recently also provide an extended analysis which uses a tanh-profile as template for the boundary layer. They show that the instability may be removed in the presence of a boundary layer of finite thickness. The presence of the instability is found to be depending on the momentum thickness of the boundary layer, the flow Mach number, the impedance and the excitation frequency according to the analysis of Rienstra and Vilenski [111]. The result provides an insight under which conditions the instability becomes present. However, it does not remove the instability of the Myers boundary condition.

Brambley [14] suggests a method to remove the instability, which is based on the idea of a finite membrane stiffness. This clearly contradicts the idea of a locally reacting surface. This leads to an additional term, scaling with a fourth power of the wave number k , in the impedance model. However, this term becomes important for large k for which a finite difference approximation of the fourth derivative becomes most inaccurate. Therefore, adding the k^4 -term suggested in [16] does not remove the instability in a preliminary study with the CAA method described in this thesis. Altogether, the latest analysis shows that the instability is present under realistic flow conditions for specific choices of impedance and flow parameters.

Experimental evidence

There are only few experiments in which an instability is found to dominate the observed sound field [41, 62, 77]. As reported by Jüschke and Ronneberger [62], regarding an experimental study of a lined cylindrical duct with a reactance dominated liner, an instability leads to a large amplification of pressure amplitudes. The flow resistance of the duct is found to be significantly increased at the same time. Großer [41] found in his analysis that the instability is a Kelvin–Helmholtz instability, which is present around the resonance frequency of a series of $\lambda/4$ resonators connected to a duct. However, his theoretical considerations are not able to provide a valid prediction of the conditions under which the instability is found.

De Metz and Farabee [77] describe several different mechanisms for the development of an instability in the flow over a single cavity. A feedback loop between the cavity oscillations and the Kelvin–Helmholtz instability of the adjacent shear layer is only one. Bauer and Chapkis [8] find the instability of an aircraft liner design to be related to a Strouhal-number of $Sr_l = l f / v = 0.2$ defined by the free stream velocity and the hole diameter l of the liner panel for a relatively thick shear layer. The instability is related to the convection time between the trailing and leading edge of the cavity. This is expressed by the scaling with the cavity diameter. De Metz and Farabee [77] suggest their observed instability is a shear-layer instability scaling with the momentum thickness δ_m . The Strouhal number with this thickness is found to be $Sr_\delta = 0.022$ for laminar and $Sr_\delta \approx 0.2$ for turbulent flows. They also describe the instability as half-jet instability. This kind of Kelvin–Helmholtz instability was theoretically described by Michalke [78] in the stability analysis of a free jet. The instability mechanism is obtained by a feedback loop through the cavity or the trailing edge of the cavity with the Kelvin–Helmholtz instability.

Even though no instability is reported by Jones et al. [57], the results of the NASA flow tube experiment indicate an unexpectedly strong near field around the trailing edge of the liner for 1 kHz. The pressure field at the opposite wall of the liner does not show a continued attenuation to the end of the liner for the resonance frequency of the thin ceramic tubes. The observed overall attenuation is high in this case, such that the possible instability is superimposed to a large decay along the liner. However, the instability is most likely to arise for the resonance frequency.

Altogether, the Kelvin–Helmholtz instability can be regarded as a rare observation as also found by Rienstra and Vilenski [111], which has to be avoided for any production aircraft liner according to Bauer and Chapkis [8]. One possible explanation for the missing wide experimental evidence is the connection of the instability to the shear layer thickness [111]. With a realistic shear layer thickness, the instability may be removed in the simulation [99, 145]. On the other hand, there are some reports of the so called liner self noise [8], which could be attributed to the Kelvin–Helmholtz instability. Self-noise amplitudes of up to 158 dB at the liner surface are reported by Bauer and Chapkis [8] and it is suggested to include the self-noise of a liner into the design as an important parameter. However, liner self-noise is related to various effects, such that the Kelvin–Helmholtz instability could not directly be linked to this statement. Bauer and Chapkis [8] and Jüschke and Ronneberger [62] report an increasing boundary layer thickness if an instability becomes present. This could be an effective limiting mechanism which reduces the observed amplitude of the instability to a non-dominant level. Furthermore, as the data of Jones et al. [57] suggests, a strongly limited instability could be considered as a reduced attenuation of the liner or experimental error, such that it would not be reported in many cases.

Conclusions about the surface waves and the instability

The observations in several numerical studies [24, 61, 104] show that the instability is a short-wave phenomenon. This is in accordance to the theoretical results of Brambley and Peake [17] and Rienstra [107]. From the list in the preceding sections one can extract two methods to suppress the instability. First, a filtering of the solution or coarsening of the grid seems to remove the instability. The other method of choice seems to be a resolved shear layer, as it was discussed in Section 4.4.1. As the applied time-domain CAA-methods use spatial filtering [102] or a selective artificial damping term [128] to suppress grid oscillations, filtering and coarsening both add dissipation. Therefore, the additional dissipation is considered as the basic mechanism, which disallows the development of an instability wave for some simulations. Additional dissipation seems to be alerting in the context of computational aeroacoustics at first glance. It could easily falsify the acoustic solution together with the suppression of the instability. On the other hand, hydrodynamic and acoustic solution could be understood as linear independent components of the solution to a linear problem. The large disparity of scales allows to filter the hydrodynamic solution out, such that there is a chance to remove the instability mode without impact to the acoustic solution.

4.5. Development of a time domain representation

In general, a time-domain representation for a wall-impedance model in the frequency domain is obtained by an inverse Fourier transform. The inverse Fourier transform of the impedance definition of Eq. (4.1) leads to a convolution as

$$p'(t) = z(t) * u'_n(t).$$

To obtain the current pressure perturbation at the wall, an integration over the time history of the normal velocity is required. There are reported attempts perform the convolution directly by applying a numerical integration [20]. However, the application of this method seems to be very limited due to the storage demands and the computational time. Therefore, in the following, a method is applied which reduces the effort for the calculation of the inverse Fourier transform. The method applies the integral, differential and the shifting theorems of the Fourier transform.

The implementation of the impedance model is considered as an extension of the wall model of Section 3.4. In Section 3.4 the time derivative of the normal velocity \dot{u}_n is set to zero, yielding the boundary condition for a rigid and impermeable surface at rest. In this section, the impedance model is used to alter this setting for a moving or permeable surface with a given impedance. The objective which is followed with the impedance model is the specification of \dot{u}'_n for the application as target value within the wall model of Eq. (3.14).

4.5.1. Impedance models based on the mass-spring-damper analogy

In the first step, for the sake of completeness, the mass-spring-damper model of Eq. (4.4) is considered as the frequency response of the complex impedance $Z(i\omega)$. As can be seen from the derivation of the model which is originally formulated in the time domain, the inverse Fourier transform of the resulting equation becomes straightforward by using the derivative and integral theorem

$$\hat{p} = d \hat{u}_n + i\omega m_m \hat{u}_n + k_m \frac{\hat{u}_n}{i\omega}, \quad (4.16a)$$

$$p' = d u'_n + m_m \dot{u}'_n + k_m U'_n \quad (4.16b)$$

$$\text{with} \quad \dot{U}'_n = u'_n. \quad (4.16c)$$

A time-domain impedance boundary condition based on a mass-spring-damper analogy was first considered by Tam and Auriault [124]. It can be written in the form

$$\frac{\partial u'_n}{\partial t} = \frac{1}{X_+} [p' - R_0 u'_n - X_- U'_n], \quad (4.17)$$

where the generic resistance parameter R_0 is identified as the dissipative term d of the mass-spring-damper model and the two reactance parameters are identified as mass-reactance $X_+ = m_m$ and spring-rate $X_- = k_m$. Tam and Auriault [124]

provide a stability analysis for the model Eq. (4.17). They show that the model is stable, provided that the three model parameters R_0 , X_- and X_+ are real and positive. Tam and Auriault [124] also point out, that the straightforward application of the mass-spring-damper model in connection with the Myers boundary condition is mathematically unstable. The model will not be considered in the following. However, it has been implemented extended by a treatment of the flow effects to the current CAA method [71].

4.5.2. Implementation of the extended Helmholtz resonator (EHR) with flow

A discrete-digital or time-discretized signal can be Fourier transformed by interpreting the sampled signal as a continuous analog signal multiplied by a series of delta functions in time. The resulting frequency response is a superposition of periodic functions. Due to the shifting theorem, the inverse Fourier transform of the resulting frequency response is a series of delta functions. In the context of electromagnetism these properties of the Fourier-transform are generalized to a theory referred to as z-transform. The first application of the z-transform in the CAA context was reported by Özyörük and Long [88]. They used it, to implement a time discretization of a generalized impedance model, based on a representation of the impedance as a complex fraction of polynomials of $i\omega$. A time-domain impedance model is obtained by a z-transform. Obviously this time-domain formulation does not need a convolution. However, due to the integration of the numerical time-marching method and the mathematical formulation of the impedance boundary condition in the works of Özyörük & Long, a transfer of the method to another impedance function seems challenging. This may be the main reason why for nearly ten years the group of Özyörük & Long [88, 89, 90] was the only one applying such z-transform-based time-domain impedance models.

The z-transform was also applied by Rienstra [108] to obtain the time-domain representation of the extended Helmholtz resonator model presented in Section 4.3.3. His work includes a review of the method of Özyörük & Long and distinguishing between the impedance model which undergoes the z-transform and the time integration method to obtain the time-domain impedance model. The steps of Rienstra [108] are followed here to obtain a time-domain impedance boundary condition based on the EHR model.

The derivation of a time-domain representation of the EHR-model of Eq. (4.11) requires the application of a generalized δ -function to obtain the inverse Fourier-transform of a periodic function $e^{-i\omega T_l}$

$$\delta(t - T_l) = \frac{1}{2\pi} \int_{-\infty}^{\infty} e^{-i\omega T_l} e^{i\omega t} d\omega. \quad (4.18)$$

Now consider the inverse Fourier transform of the product

$$\mathcal{F}^{-1} \{ \tilde{p}(i\omega) \} = \mathcal{F}^{-1} \{ Z(i\omega) \tilde{u}_n(i\omega) \} = z(t) * \tilde{u}'_n(t),$$

with

$$Z(i\omega) = e^{-i\omega T_l}.$$

Due to the periodic frequency response of $Z(i\omega)$ which is expanded to a single δ -function through the z -transform, one obtains

$$\frac{1}{2\pi} \int_{-\infty}^{\infty} z(\tau) \tilde{u}'_n(t - \tau) d\tau = z_n \tilde{u}'_n(t - T_l). \quad (4.19)$$

Considering an extended Helmholtz resonator including viscous effects and damping according to Eq. (4.11), $Z(i\omega)$ becomes a rational function of $e^{-i\omega T_l}$. Using the definition of α , Eq. (4.11d) in Eq. (4.11c) and multiplying the whole equation by the denominator $(1 - e^{-\alpha})$ yield

$$(1 - e^{-\alpha}) \tilde{p}(i\omega) = \left[(R_f + \beta + i\omega m_f) - (R_f - \beta + i\omega m_f) e^{-\alpha} \right] \tilde{u}(i\omega).$$

Now the inverse Fourier transform is applied to both sides, using the shifting theorem, Eq. (4.18), of the inverse Fourier-transform given by Eq. (4.19). This results in the following time-domain impedance boundary condition, for the extended Helmholtz resonator model without flow

$$\begin{aligned} \tilde{p}'(t) - e^{-\varepsilon} \tilde{p}'(t - T_l) &= (R_f + \beta) \tilde{u}'_n(t) \\ &- (R_f - \beta) e^{-\varepsilon} \tilde{u}'_n(t - T_l) + m_f \left(\frac{\partial \tilde{u}'_n}{\partial t}(t) - e^{-\varepsilon} \frac{\partial \tilde{u}'_n}{\partial t}(t - T_l) \right). \end{aligned} \quad (4.20)$$

The extended Helmholtz resonator with flow

In this section the Ingard/Myers boundary condition of Eq. (4.15) is used to model the grazing flow effect. Even though the resulting mathematical model is unstable under certain conditions, this seems to be the only way to obtain a time-domain impedance boundary condition which is able to handle a nonzero mean flow at the impedance surface. Equation (4.15) is divided by $i\omega$. The $i\omega m_f$ term is directly transformed to a time derivative. The flow effect is added to Eq. (4.20) by replacing the pressure with the result of the Ingard/Myers boundary condition. The implemented form of the boundary condition to \tilde{u}'_n is given as

$$\begin{aligned} \frac{\partial \tilde{u}'_n}{\partial t}(t) &= \frac{1}{m_f} \left[\mu(t) - (R_f + \beta) \tilde{u}'_n(t) \right] \\ &- \underbrace{\frac{1}{m_f} e^{-\varepsilon} \left[\mu(t - T_l) - (R_f - \beta) \tilde{u}'_n(t - T_l) \right] + e^{-\varepsilon} \frac{\partial \tilde{u}'_n}{\partial t}(t - T_l)}_{\text{storage term}}, \end{aligned} \quad (4.21)$$

where $\mu(t)$ is defined with the auxiliary variable P' , $\dot{P}' = p'$, to rewrite the time integration, which arises from the Ingard/Myers boundary condition.

$$\mu(t) = p' + \underbrace{u_0 \cdot \nabla P' - \mathbf{n} \cdot (\mathbf{n} \cdot \nabla u_0) P'}_{\text{convective and curvature terms}}, \quad (4.22a)$$

with the symbol s_p introduced as

$$\frac{\partial s_p}{\partial t} := u_0 \cdot \nabla p' - \mathbf{n} \cdot (\mathbf{n} \cdot \nabla u_0) p'. \quad (4.22b)$$

It can be written as:

$$\mu(t) = p' + s_p. \quad (4.22c)$$

Equations (4.22b), (4.22c) and (4.21) represent the implementation form of the EHR.

Implementation of the extended Helmholtz resonator model ⁴

The present-work implementation of a time-domain impedance boundary condition to a DRP-based CAA software, which started with Richter et al. [105], is based on an electronic prepublication of Rienstra [108]. Rienstra [108] points out several variants of the implementation of an extended Helmholtz resonator model. Besides this, he gives clear suggestions for the implementation of one of the extended Helmholtz resonator models. The present implementation does not strictly follow these suggestions. It is described in more detail in the following. Furthermore, some parallel development in the work of Chevaugneon et al. [24], who implemented the EHR with a CAA software based on a Discontinuous Galerkin method, is discussed and compared.

If m_f of an impedance surface defined by Eq. (4.11) is sufficiently large, the coupling of the time-domain impedance boundary condition through this parameter becomes possible. Therefore, the face-sheet reactance m_f is assumed to be nonzero in the following. Chevaugneon et al. [24] used a similar assumption for the implementation of the extended Helmholtz resonator for nonzero mean flow conditions.

The EHR requires the data at previous times $t - T_l$. As the coefficients are constant in Eq. (4.21); the whole expression for the old time levels can be stored in one variable per boundary point. With the simulation marching on in time, the full time series back to $t - T_l$ is required. In his publication, Rienstra [108] suggests to chose T_l such that it exactly matches to a multiple of the time step in the simulation. This limitation seems clear for multi-time-level high-order schemes. However, the subsequent time steps of the LDDRK method would have no high-order approximation

⁴The EHR has simultaneously been implemented as time-domain impedance boundary condition to a DRP-based [105] and a DG-based [24] CAA software. The implementations were carried out independently based on Rienstra [108] and both were presented at the AIAA-CEAS Aeroacoustics conference 2006.

of the older time level available. Moreover, a large number of subsequent time levels would have to be stored. To overcome the problem, an interpolation is used in the current work. The old time level $t - T_l$ is obtained from the storage term in Eq. (4.21), which has been stored at time levels close to $t - T_l$, by the filtering interpolation described in Section 3.6.2. The storage term is calculated and saved for each full step of the LDDRK only. The terms explicitly showing T_l in Eq. (4.21) are stored in one variable for each boundary point at every full time-step of the LDDRK. This is implemented using a circular buffer. Old time levels up to ten time steps before $t - T_l$ are stored to have an adequate number of time samples for the interpolation and avoid backward interpolation stencils. The limitation of T_l to a whole-numbered multiple of the time-step size is overcome with this operation.

Another difficulty in connection with the LDDRK applied with Eq. (4.21) is related to the time derivative $u'_n(t - T_l)$. It is not directly provided by the Runge-Kutta time marching scheme in 2N-storage form. To obtain a high-order finite difference approximation, seven time steps of u_n behind the current one are stored in an own circular buffer. The high-order time derivative, which is required for the storage term, is calculated by applying the seven point central differencing scheme (DRP) of Section 3.1.1 with this data.

Suppression of the instability with flow

In Section 4.4.3 additional dissipation was identified as a possible treatment of the instability of the Ingard/Myers boundary condition, as a result of a literature review. The additional dissipation is implemented in this work on the storage term and the whole convective part (s_p) of $\mu(t)$, which arises from the Ingard/Myers boundary condition (comp. Eq. (4.22)). The terms of the auxiliary storage variable, which are evaluated at the time level $t - T_l$ in Eq. (4.21) are summed up before filtering it spatially. The convective and curvature terms of $\mu(t)$ are filtered after the time integration has been performed with the LDDRK [48]. It is found in a preliminary study that a second-order filter (see Appendix B.1.3) is required to obtain a stable solution. This is the only filter stencil that does not respond with grid oscillations to a pulse like input. Furthermore, it is found that the average solution tends to drift from zero if a transition between lined surface and hard wall is present. This is attributed to numerical errors at the leading and trailing edge of the liner. To avoid an offset and give the acoustic field a more continuous shape in the vicinity of the leading and trailing edge of a liner, the filtering domain is extended by one point with a functional value of zero at these ends. The very dissipative treatment of the storage, convective and curvature terms has been extensively tested and the results will be reported in this work in Chapter 7.

4.5.3. Outlook: Generalization of time-domain impedance modeling

The mass-spring-damper model of Section 4.5.1 can be extended to a more general frequency response by adding higher-order derivatives and integrals, which

results in higher powers of $i\omega$ in the resulting frequency response. This method was used by Fung and Ju in various publications [37, 38, 61]. These authors consider a complex reflection coefficient of the surface instead of the impedance to define the boundary condition for a locally-reacting surface in the time domain. The generalization of the mass-spring-damper model is relatively straight forward in this way. The method corresponds to a development of the frequency response of the impedance into a Taylor series before applying the inverse Fourier transform. There is no direct identification of the coefficients with physical parameters of the liner. Thus, the modeling of a realistic liner panel by applying such extended mass-spring-damper analogies may require more additional parameters than the extended Helmholtz resonator model of Section 4.5.2. The approach may, however, be promising when considering a digital filter as model for the frequency response. This is for instance done by Polifke et al. [96] for an entirely real reflection coefficient of a combustion system inlet and outlet. Such a filter can include higher-order time derivatives and integrals as well as the information of older time steps. In this way, an impedance model based on a digital filtering may be seen as the generalization of time-domain impedance modeling on the expense of the physical interpretation of the model parameters.

5. Analysis and assessment of the numerical results

In this chapter, methods for the location of the sources of sound or numerical error in the solution are presented. The source power level (QPL) scale is introduced to present the relevant source strength in a compact way. Finally, the conservation of the acoustic energy as quality criterion for the solution is introduced.

5.1. Motivation

Due to the non-conservative character of the model equations and most of the numerical methods for computational aeroacoustics, a technique for validating the numerical solution for a specific problem is desirable in addition to the initial validation and verification of the method itself. Moreover, it seems almost impossible to validate the method including all possible settings for the time step size, numerical method, filter and all geometrical situations. Rather the numerical result for a specific problem has to be investigated with respect to its quality. This is done here by the conservation of energy in the solution. As the acoustic perturbation energy is a small fraction of the total energy in the flow in general, only the fluctuation quantities are considered for the validation. However, there is no universal conservation law of the acoustic energy compound alone in an arbitrary mean flow. The practical applicability of the validation method, therefore, depends on the possibility to find a definition of the acoustic energy for which a conservation law applies at least approximately with the current base-flow field. Due to the fluctuating character of the acoustic intensity, a time average energy conservation is investigated to make the result independent of the instationary energy distribution.

5.2. Source location

The idea of using the acoustic intensity for a source location goes back to Ehrenfried [32]. The average acoustic source strength of a process in general follows from a balance of the acoustic energy. This balance is averaged in time to obtain

$$\left\langle \frac{\partial e_a}{\partial t} \right\rangle_t + \langle \nabla \cdot \mathbf{I}_a \rangle_t = \langle q_s \rangle_t. \quad (5.1)$$

Under the assumption of a statistically stationary solution for the process, the average change rate of the specific acoustic energy e_a is zero. In consequence, the divergence of the time averaged acoustic intensity, is found to be equal to the average radiating acoustic source strength [104]

$$\nabla \cdot \langle \mathbf{I}_a \rangle_t = \langle q_s \rangle_t. \quad (5.2)$$

Based on Eq. (5.2) the average production of acoustic energy, which is considered as the source strength, can be calculated from the time averaged intensity.

5.2.1. Introduction of the QPL scale for the source power level

The source strength shows a large dynamic range. Its unit is Wm^{-3} , denoting a specific acoustic power. To obtain the acoustic power which is input in average, the source strength is related to a reference volume. The approximate volume of an expected major source region may be used for this purpose, such that the obtained acoustic source power is directly related to the observed acoustic power in the duct. For instance in the following experiment $V_{\text{ref}} \approx 10^{-5} \text{ m}^3$ is used. The average acoustic power input is then obtained to

$$P_{\text{in}} = \langle \nabla \cdot I_a \rangle_t V_{\text{ref}}. \quad (5.3)$$

This is the acoustic power which is input in average from a source with equally distributed additive superposing source strength all over the reference volume. For a better visualization of the large dynamic range of the acoustic source strength, a logarithmic scale is chosen which is based on the power spectral density (PSD). The average source strength can be negative, which means an annihilation of acoustic energy. Therefore, the absolute value of the source power is considered to obtain another logarithmic scale for the annihilation of acoustic energy. The resulting two logarithmic scales are put together adding the original sign of P_{in} to obtain negative values for sinks and positive ones for sources of acoustic energy. To obtain distinct scales with this properties, sources with an QPL below 0 dB are cut-off by a max operation in the logarithm. Accordingly, the acoustic source power level QPL, which gives the average acoustic power input on a PSD like scale can be defined as

$$\text{QPL} = \text{sgn}(P_{\text{in}}) 10 \log_{10} \left[\max \left(\frac{|P_{\text{in}}|}{10^{-12} \text{ W}}, 1 \right) \right]. \quad (5.4)$$

The QPL becomes zero, if the absolute value of the input source power is below the threshold of 10^{-12} W .

5.3. Intensity definitions

The definition of the acoustic intensity is, however, not unique. Different very universal definitions of an acoustic energy or generalized perturbation energy are presented in the following. The definition of Morfey [80] states the, up to now, most general expressions for an acoustic intensity and energy. They are defined by Morfey [80] as

$$e_a = \frac{p'^2}{2\varrho_0 c_0^2} + \frac{\varrho_0}{2} \mathbf{u}'_a \cdot \mathbf{u}'_a + \frac{p'}{\gamma p_0} \varrho_0 \mathbf{u}_0 \cdot \mathbf{u}'_a \quad (5.5a)$$

$$\text{and} \quad \mathbf{I}_a = (p' + \varrho_0 \mathbf{u}_0 \cdot \mathbf{u}'_a) \left(\mathbf{u}'_a + \frac{p'}{\gamma p_0} \mathbf{u}_0 \right). \quad (5.5b)$$

Applying these definitions with Eq. (5.2), a conservation of energy without any additional sources can be shown for the special case of a potential flow. This theoretically means a limitation to a purely potential base-flow field with a purely acoustic perturbation on top of it. In practice, due to the negligible interaction of the hydrodynamic and acoustic modes in a constant base-flow field as shown by Chu and Kovásznyai [25], the conservation of the acoustic energy can be extended to arbitrary perturbations in a constant flow field. For other flow conditions, e. g. entropy mode waves or vortices in any non-constant flow field, acoustic sources $\langle q_s \rangle_t \neq 0$ are present.

A generalized perturbation energy and the related energy flux was given by Myers [86]:

$$e_a = \frac{p'^2}{2q_0 c_0^2} + \frac{q_0}{2} \mathbf{u}'_a \cdot \mathbf{u}'_a + q' \mathbf{u}_0 \cdot \mathbf{u}'_a \quad (5.6a)$$

$$\text{and} \quad \mathbf{I}_a = (p' + q_0 \mathbf{u}_0 \cdot \mathbf{u}'_a) \left(\mathbf{u}'_a + \frac{q'}{q_0} \mathbf{u}_0 \right). \quad (5.6b)$$

This definition is also investigated here, as it could be advantageous for the identification of numerical errors in the presence of hydrodynamic perturbations. The original definition of the acoustic intensity by Morfey [80] is recovered from the generalized energy flux by replacing q' in Eq. (5.6b) by $p' c^{-2}$, with $c^2 = \gamma p_0 q_0^{-1}$.

A common problem of both definitions is the dependency on the acoustic velocity perturbation \mathbf{u}'_a . The acoustic velocity perturbation is not directly available, as the velocity perturbation \mathbf{u}' found in the CAA solution is a superposition of acoustic $\mathbf{u}'_a = \nabla \phi$ and vortical $\mathbf{u}'_w = \nabla \times \psi$ velocity perturbation, in general. A general method for splitting the acoustic and hydrodynamic velocity perturbation in an arbitrary base-flow field is not yet available. However, as long as \mathbf{u}'_w remains small \mathbf{u}'_a could be identified by the \mathbf{u}' of a numerical solution. This applies very well for the propagation of tones against the flow in the inlet of an aeroengine. In a more complex flow field, the identification leads to errors. In the wake of a flame for example an initial entropy perturbation causes acoustic perturbations and vortices to be generated in the combustion chamber exit nozzle with a strong gradient of the base flow. The arrival of the entropy perturbation in the nozzle triggers both other perturbation forms, such that the three modes of perturbation are correlated with a fixed phase.

5.4. Solution validation based on a global conservation of acoustic energy

The investigation of a global conservation of the acoustic energy to access the quality of a numerical solution, as it is presented in this section, is not a completely new idea. Eversman [33] introduced a prove of a numerical FEM solution based on the conservation of the acoustic energy according to the definition of Morfey [80]. The

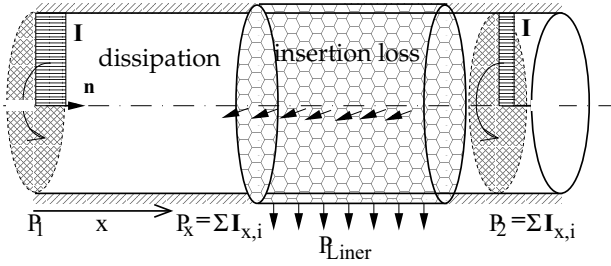


Figure 5.1.: Sketch explaining the application of the acoustic intensity to compare results and as quality criterion

approach is based on a balance of the acoustic energy flux entering the duct from the source boundary and the outgoing fluxes over the lined wall and the terminal plane of the duct. The situation is sketched in Fig. 5.1. The incoming acoustic power from the left boundary ($P = \int \mathbf{I} dS$) is denoted as P_1 , whereas P_{Liner} and P_2 denote the outgoing power over the liner and the right boundary, respectively. The time averaged acoustic energy flux in a hard-walled duct section, without sources, is constant. With liner, a global balance of the incoming and outgoing acoustic energy has to consider the flux over the liner P_{Liner} in addition. The acoustic energy flux through the duct decreases with the distance from the source along the liner, then. To prove a numerical result, the time averaged acoustic intensity component with an orientation parallel to the axis is integrated over a disc closing the duct section at a given axial position x (comp. Fig. 5.1). With liner, the cumulated flux over the lined wall from the source at x_0 to the axial position x is considered in addition. The resulting average acoustic energy flux P_a through a disc at the axial position x and the lined wall from the source position x_0 to x is then given as

$$\langle P_a(x) \rangle_t = \underbrace{\int_{S_{\text{disc}}(x)} \langle I_{a,x}(x) \rangle_t dS}_{\text{flux along the axis}} + \underbrace{\int_{x_0}^x \langle I_{a,n}(\xi) \rangle_t dS_{\text{shell}}}_{\text{flux over the wall}}, \quad (5.7)$$

where $I_{a,x} = \mathbf{I}_a \cdot \mathbf{e}_x$ denotes the axial component of the acoustic intensity, $\mathbf{n}(\xi)$ is the outer normal unit vector of the lined surface and x_0 is the position of the source boundary. $\langle P_a \rangle_t$ must be constant and equal to the input acoustic power in the absence of sources. However, the identification of a source, as such, obviously depends on the definition of the acoustic energy and intensity. In the absence of sources, the annihilation of acoustic power along x is attributed to numerical dissipation. The acoustic energy flux is a measure of the quality of the numerical solution, then.

5.5. Comparison of the intensity definitions

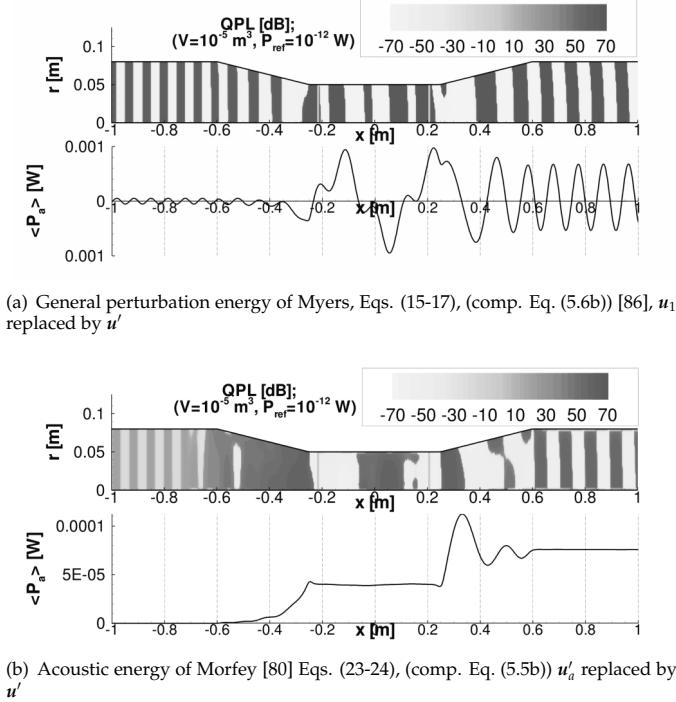


Figure 5.2.: Comparison of the intensity definitions: QPL (upper part of each figure) and overall acoustic power flux (lines below).

The different definitions of the energy flux are studied numerically by means of an axisymmetric flow duct which is excited by a harmonic entropy source, exciting q' constantly along an axial position with a given frequency, at the left end, shown in Fig. 5.2. To distinguish the effects of nozzle and diffuser, a straight duct section of about one wavelength of the acoustic perturbation is added between the acceleration and deceleration zone. The average flow field is based on a nonlinear Euler solution according to section 3.2. The Mach number ranges between $Ma = 0.17$ and $Ma = 0.51$ in the wide and narrow duct sections, respectively. Acoustic sources are expected only in the nozzle and diffuser, due to an indirect noise generation in the acceleration zones of the flow, for the definition following Morfey [80], whereas a generalized perturbation energy according to Myers [86] should not be generated or

annihilated at all for such a boundary value problem. Especially, all straight parts of the duct should be free of sources and feature a constant acoustic power flux in average independently of the intensity definition. The results of the preliminary investigation are shown in Fig. 5.2.

Location of sources: As can be seen from Fig. 5.2(a) the modified definition of Myers [86] locates sources all over the duct. The periodic pattern of negative and positive source strength corresponds to the wave length of the periodic entropy perturbation. Probably, the correlation between vorticity, acoustic and entropy mode leads to a misinterpretation by the modified energy definition of Myers [86]. Therefore, this definition is considered not successfully applicable for the location of sources.

The modified definition of the acoustic intensity by Morfey [80] results in a better identification. All sources in the inlet duct are completely removed, as can be seen in Fig. 5.2(b). The source strength in the straight duct section between nozzle and diffuser and in the straight outlet duct is reduced with respect to the modified definition according to Myers [86]. The remaining sources must be due to the vortical perturbations which are generated by the acceleration of entropy perturbations in the nozzle and diffuser. The entropy mode itself does not interfere with the acoustic intensity any more.

Integral acoustic power flux: Examples for the evaluation of the acoustic power flux from the preceding section are given in Fig. 5.2, in the lower part of each figure. The definition of Myers [86] leads to strong axial variations of the integral acoustic power flux all over the duct [Fig. 5.2(a)]. The definition of Morfey [80] produces a nearly constant energy flux in the straight duct sections [Fig. 5.2(b)], even though the overall velocity perturbation was used instead of the acoustic velocity. The remaining small variations in the ducts downstream the first contraction are probably due to the missing distinction of vortical and acoustic velocity component. The contraction and widening duct sections show variations, which are attributed to the indirect entropy noise generation. The wavelength of the initial harmonic entropy perturbation in the numeric experiment is much smaller than the length of the nozzle and diffuser sections. Thus, a pattern of positive and negative sources is found in these regions and the average acoustic intensity varies with the position.

6. Impedance eduction from measurements

This chapter shortly describes the impedance eduction process, which will be applied in Section 7.2. First, the definition of the objective function is described in Section 6.2. Two different types of experimental data as input are addressed. Then the flow effect on the impedance is addressed in Section 6.3. Different strategies are pointed out, which will be compared with the example of the NASA flow tube data in Section 7.2.1. Finally, the optimization algorithm is addressed at the end of this chapter.

6.1. Overview of the impedance eduction process

To calculate the impedance from *in-situ* measurements, an optimization procedure with the CAA-method is developed. The impedance of the liner is varied, in order to find an impedance which results in a similar pressure pattern as it is observed in the experiment. The optimization uses a control loop, which varies the parameters of the impedance model and controls the deviation from the experiment via an objective function. The five parameter EHR of Section 4.3 is used. The optimization problem can, therefore, be described as nonlinear problem with a control over the boundary. The EHR model requires all parameters to be real and positive to obtain a passive and causal impedance according to Rienstra [108]. Therefore, constraints have to be put in the optimization for all model parameters. A further constraint is necessary, as m_f , which is the coupling parameter, must not be zero and small m_f limit the CFL-number in the simulation, as it will be shown later. Furthermore, to avoid aliasing effects with discrete frequency data, the time lag T_l of the EHR model has to be limited to a band of frequencies of about ± 50 % of an initial guess.

6.2. Objective function

The objective function for the optimization process is defined by the deviation between the experimental data and the corresponding numerical result. The experimental data can be spatially resolved sound pressure level and phase information as well as modal amplitudes. The modal amplitudes are based on multiple microphone measurements to perform a wave splitting. This makes the data theoretically independent of the position of measurement. Currently, the wave splitting in the experiment is limited to a decomposition into up- and downstream running plane waves. The advantage of an impedance eduction with a time-domain impedance boundary condition is that only few model parameters describe a large range of frequencies. In case of the EHR, five model parameters describe the whole frequency

response. Assuming $\hat{p}_{\text{exp},i}^{(n)}$ to be the in general complex amplitude vector of the experimental data and $\hat{p}_{\text{num},i}^{(n)}$ to be the corresponding numerical result, where n runs over all frequencies and i over the different measurement positions, the objective function is defined as the square of the L_2 norm

$$\Xi = \sum_n \sum_i \left| \hat{p}_{\text{num},i}^{(n)} - \hat{p}_{\text{exp},i}^{(n)} \right|^2 \quad (6.1)$$

The numerical data is monitored at exactly the same spatial position as it was done in the experiment. To make the grid generation independent of the position of measurement, a spatial interpolation of the pressure data to the exact measurement position is implemented which is based on cubic splines. The optimization of three-dimensional problems with the present CAA-method is currently not fast enough for any realistic application. Therefore, the simulation is considered to be based on the two-dimensional or modal-axisymmetric approach. The interpolation is only one-dimensional then. The cubic-spline interpolation along the wall is used in the current work, to calculate the pressure data at the exact position of measurement. The interpolation is carried out for each full time step of the Runge-Kutta scheme and the time-dependent pressure data is stored. The Fourier transform is performed in a post-processing step. It is implemented in MATLAB as part of the objective function call.

Due to the different processing depth of the experimental data it is now necessary to distinguish between (a) sound pressure level and phase data at given positions and (b) post processed experimental data in form of transmission and reflection coefficients as input for the impedance eduction. In both cases the monitoring of the pressure and the Fourier transform are applied. The further steps differ for the two methods.

6.2.1. Impedance eduction based on raw sound pressure level data

In case (a), it is only necessary to calculate the complex pressure amplitude for each frequency from the sound pressure level and phase given from the experiment. Then the complex amplitudes are directly compared by the norm given in Eq. (6.1). In a first step only the magnitude of the sound pressure was considered to define the objective function [105, 106]. This also results in a good agreement with the experiment.

6.2.2. Impedance eduction based on energy transmission and reflection

For case (b), it is theoretically possible to use the acoustic intensity of Chapter 5 to obtain the energy reflection and transmission. However, it was not made use of this option in the current work, to keep the analysis as close as possible to the experiment. Especially in case of a resolved boundary layer, the resulting transmission and reflection could depend on the position of measurement. The experimental data is

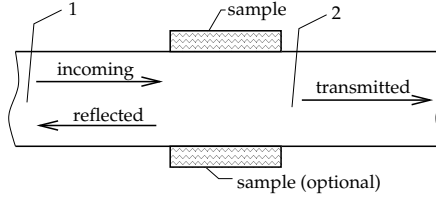


Figure 6.1.: Sketch of the set-up for the calculation of the transmission and reflection coefficient

based on a wave splitting which combines a downstream and upstream excitation of the liner sample in order to make the resulting energy transmission, reflection and dissipation independent of reflections from the anechoic terminations [46]. A simplified formulation is applied to calculate the transmission and reflection coefficient from the numerical simulation result, omitting two different excitations and reducing the problem by a factor of two therewith. In a first simulation the baseline pressure is obtained without liner. Then, the reflected pressure amplitude is calculated as $\hat{p}_{\text{refl}} = (\hat{p} - \hat{p}_{\text{base}})$. The transmitted pressure is simply identified with the pressure in the duct section following the liner sample, assuming perfect anechoic boundary conditions for the numerical simulation. The energy transmission and reflection is calculated based on the definition of these coefficients with flow according to Blokhintsev [10] (comp. Heuwinkel [46])

$$T = \frac{S_2 (\rho_0 c)_1}{S_1 (\rho_0 c)_2} \frac{(1 + \text{Ma}_2)^2}{(1 + \text{Ma}_1)^2} \left(\frac{\hat{p}_{\text{trans}}}{\hat{p}_{\text{base}}} \right)^2 \quad (6.2a)$$

$$R = \frac{(1 - \text{Ma}_1)^2}{(1 + \text{Ma}_1)^2} \left(\frac{\hat{p}_{\text{refl}}}{\hat{p}_{\text{base}}} \right)^2, \quad (6.2b)$$

where S is the cross sectional area of the duct and section 1 is considered to be the section with the incoming wave from the excitation and 2 is the section following the sample in the direction of sound propagation. The baseline amplitudes are denoted by the subscript base. The Mach number Ma is considered to be signed positive when the incoming acoustic waves propagate with the flow.

6.3. Flow effects

The resulting impedance depends on multiple parameters of which the base flow is one of the most important. The flow effects which have been described in section 4.4 have to be considered for the impedance eduction, as well. A resolved boundary layer of the base flow, according to section 4.4.1, would be most desired for an accurate impedance eduction. However, the required resolution for the boundary layer

may increase the problem size beyond the limits of a currently optimizable problem. Thus, the Ingard/Myers boundary condition must be used according to the consideration of section 4.4.2 including the stabilization by low-order filtering. In this case, a partially-resolved boundary layer or a plug-flow assumption are applied for the base flow. These two alternatives are compared in section 7.2.1 with respect to the reproduction of the impedances educed by Jones et al. [57] for the ceramic tubular liner in the NASA flow-tube experiment.

6.4. Optimization algorithm

Finally, the optimization algorithm has to be described. An own implementation of an optimization algorithm would go beyond the scope of the current work. Thus, a commercially available algorithm was chosen in accordance with Zhaung [143] for the optimization. The function *fmincon* from the MATLAB optimization toolbox evaluates the objective function. The objective function is implemented as MATLAB function, which performs the necessary post processing, calculates a Fourier transform of the microphone data and finally returns the objective function. The actual core of the objective function is a system call to the CAA-software, which can also run remotely on a different machine. The so called medium-scale algorithm of the constrained nonlinear MATLAB optimization procedure *fmincon* is used. It implements the BFGS Quasi-Newton method and a line search using a merit function [23]. Gradients are calculated by additional calls of the CAA-method through the MATLAB function.

The possibility of a development of an adjoint method from the discretized form of the equations was also considered to replace the calculation of gradients by MATLAB. In case of five model parameters, this could reduce the number of CAA runs to two, one forward in time with the original equations and one backward with the adjoint equations, instead of six for the calculation of a new optimization step. However, the development of the adjoint method is complicated due to the implementation of the impedance boundary condition, where the control takes place. Moreover, the current problem is controlled via a boundary condition. This is a nonstandard situation in the control theory, which usually considers a control over the whole volume. In consequence, when considering the possible reduction of the computational time for the optimization, which is currently between less than a day and up to one week for the cases presented below, the effort for implementing the adjoint method is much higher than the expected reduction of the computational time.

7. Results and Discussion

This chapter is separated into three parts. The first, Section 7.1, contains test cases for the validation and verification of the impedance model and the CAA method with theoretical data. Some further tests, which are presented in this section, consider the impact of realistic flow profiles and the suppression of the instability with the time-domain impedance boundary condition. In the second part, Section 7.2, the impedance eduction from *in-situ* measurements with four different liner samples is provided to further validate the method in comparison to published impedance data. The educed model parameters of the EHR are used to calculate an educed geometry, which allows an insight to the physics of the liner. The last part, Section 7.3, gives examples for applications of the EHR model. There is no strict separation of physical results and the validation of the numerical method. Both are presented and discussed together. The variety of benchmark cases is chosen to allow an assessment of the capability of the current CAA method for a broad range of applications.

7.1. Validation and verification of the impedance models

7.1.1. Verification of the impedance boundary condition with the analytical solution

First, annular ducts with constant inner and outer radius are considered in preparation for the code benchmark, which is carried out later in this section. No-flow and uniform base-flow conditions all over the duct (plug flow) are considered. The analytical solution of Section 3.6.3 is used for comparison. The geometry and test case definition is adapted from the more complex examples of the benchmark. The test cases for this first verification are summarized in table 7.1.

Azimuthal mode propagation with the flow in an annular duct with lined centerbody

The first test case, *A4*, considers an infinite cylindrical duct with lined centerbody. The wall impedance and the dimensions correspond to the semi-infinite duct of Section 7.1.3. There is no flow in the duct. The isentropic modal-axisymmetric model equations according to Section 2.6 are used. A simple sponge layer with sound source is applied at the source boundary, whereas the PML is used at the other end of the domain. The resulting pressure and velocity contours of the numerical and analytical solutions are compared in Fig. 7.1. The analytical solution uses the same contour levels as the numerical result. The solutions are in a perfect agreement with each other. As well the implementation of the impedance boundary condition as the

Table 7.1.: Annular duct cases considered for the verification.

case	r_i [m]	r_a [m]	PPW _x	N_r	He [-]	m [-]	Ma [-]	wall lined	ζ [-]
A4	0.8	1.2	23	31	20.85	4	0	inner	2 - 1 <i>i</i>
A4.5	0.8	1.2	39	31	20.85	4	+0.5	inner	2 - 1 <i>i</i>
B10	0.423557	1	23	101	50	10	0	outer	2 - 1 <i>i</i>
B10-2	0.423557	1	46	201	50	10	0	outer	2 - 1 <i>i</i>
B10.5	0.423557	1	11	101	50	10	-0.5	outer	2 - 1 <i>i</i>
B10.5-hard	0.423557	1	11	101	50	10	-0.5	none	-
B40.5	0.423557	1	15	101	50	40	-0.5	outer	2 - 1 <i>i</i>
B40.5-hard	0.423557	1	14	101	50	40	-0.5	none	-

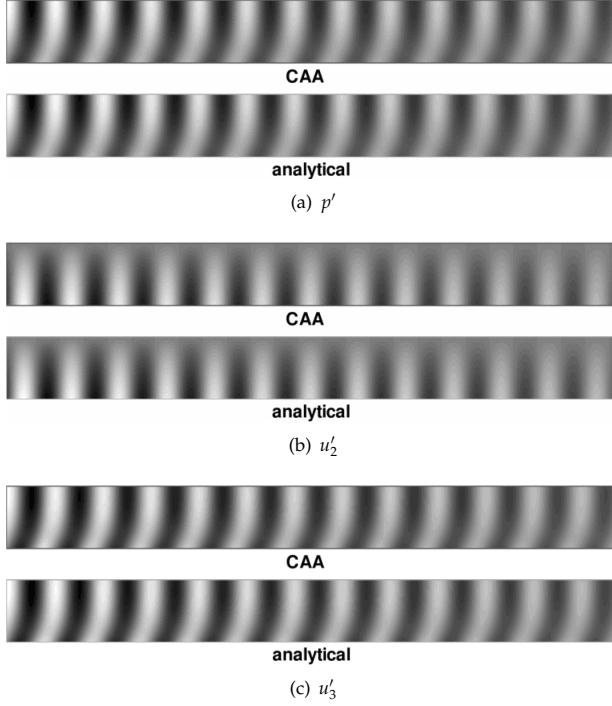


Figure 7.1.: Detailed comparison of numerical (top) and analytical solution (below) for case A4 (Tab. 7.1). Equal contour levels for analytical and numerical solution.

overall numerical method including the sound source and non-reflective boundary conditions is verified by the perfect agreement of analytical and numerical results. Moreover, the resulting pressure contours along a line of $y = 1.1$ m are compared in Fig. 7.2. They are also found in a perfect agreement for case A4. Due to the application of a PML boundary condition, the waves are damped for $x > 4.6$ m in the numerical solution. The PML removes the pressure perturbations before they can reach the domain boundary.

The second case A4.5 adds a base flow of $Ma = 0.5$. The waves are propagating with the flow in this case which is denoted by the positive Mach number in table 7.1. The boundary conditions are the same as above.

Three different situations are considered in Fig. 7.3. First the low-order filtering of the auxiliary liner variables which is described in Section 4.5.2 is studied with this case. In general, the filtering is necessary to avoid the instability of the In-

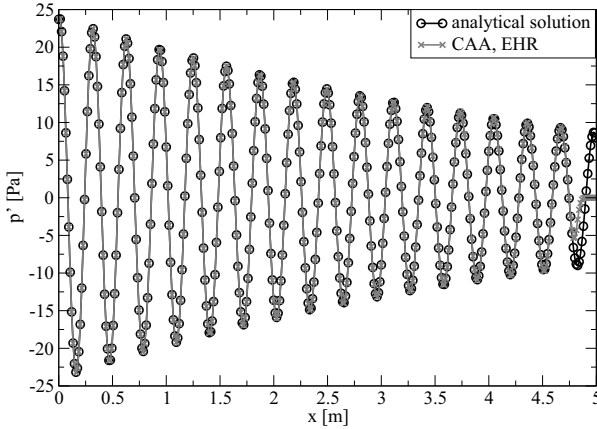
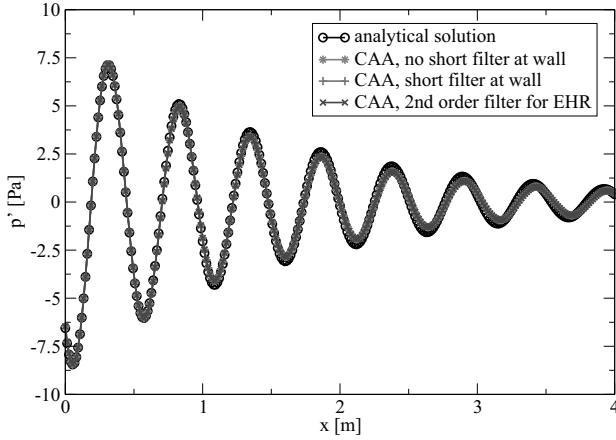


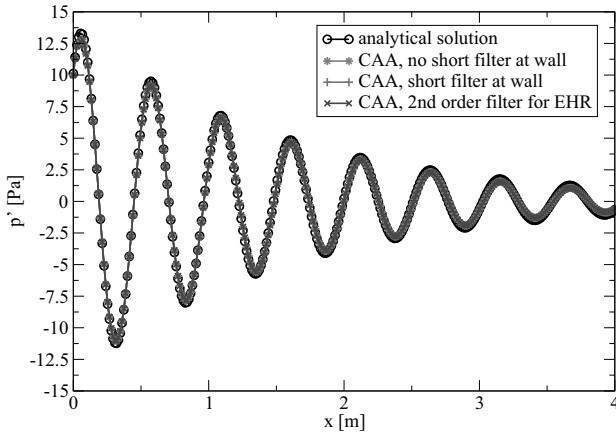
Figure 7.2.: Detailed comparison of numerical and analytical solution at a line $y = 1.1$ m for case A4 (Tab. 7.1).

gard/Myers boundary condition. However, in this example the five parameters of the EHR are chosen such that the real part of the impedance remains as large as possible for all frequencies. This avoids the instability. In addition, the impact of a smaller filter stencil with lower order close to the domain boundaries is studied by completely avoiding the reduced filter stencils. Note that this is not indicated for most of the applications of the method. It is, however, possible for A4.5 due to the equidistant and orthogonal grid with perfect unity aspect ratio. Furthermore, no singularities, as impedance jumps, are found in this infinite lined duct. The instantaneous pressure contour along the inner and outer walls are extracted in Fig. 7.3 for a comparison to the analytical solution. They are expected to be most affected by the low-order filtering. The numerical results are compared to the numerical solution without any low-order filtering. The comparison shows that the low-order filtering neither of the auxiliary variables nor the perturbation field close to the wall produces an observable deviation from the solution without any low-order filtering. There is, however, an observable small deviation from the analytical solution.

Summarizing the observations in case A4 and A4.5, the correct implementation of the EHR-based time-domain impedance boundary condition to the current CAA method is verified by the agreement of analytical solution and numerical result. Both of the problems are well resolved by about 23 PPW and 39 PPW in axial direction, respectively. The azimuthal mode number is low, such that 31 points in radial direction provide a sufficient resolution. Moreover, only few radial modes are cut-on in the corresponding hard-walled duct [28], such that a leakage into cut-on higher radial modes is impossible. Therefore, this test case is considered less challenging than the ones, which are considered in the following.



(a) along hard outer wall



(b) along lined inner wall

Figure 7.3.: Comparison of the pressure levels along the lined inner and outer walls of the annular duct with flow for case A4.5 (Tab. 7.1).

Higher modes in an annular duct with lined outer wall

In this section an annular duct with hard inner and lined outer wall is considered. The geometry and liner parameters correspond to the conditions found in the fan plane of the generic inlet configuration considered in Section 7.1.2. The boundary

conditions and mathematical model are the same as above, with the exception that the inner wall is acoustically hard and the outer wall is lined in the following. The mesh has 101 grid points in radial direction and an unity aspect ratio. The high resolution of the mesh allows to cover all higher radial modes which are cut-on in the current examples. Two cases are picked from the test matrix of the benchmark case considered below. The wave propagation without flow and against an uniform base-flow of $Ma = 0.5$ are considered for each case. The basic information of the cases is summarized in Tab. 7.1.

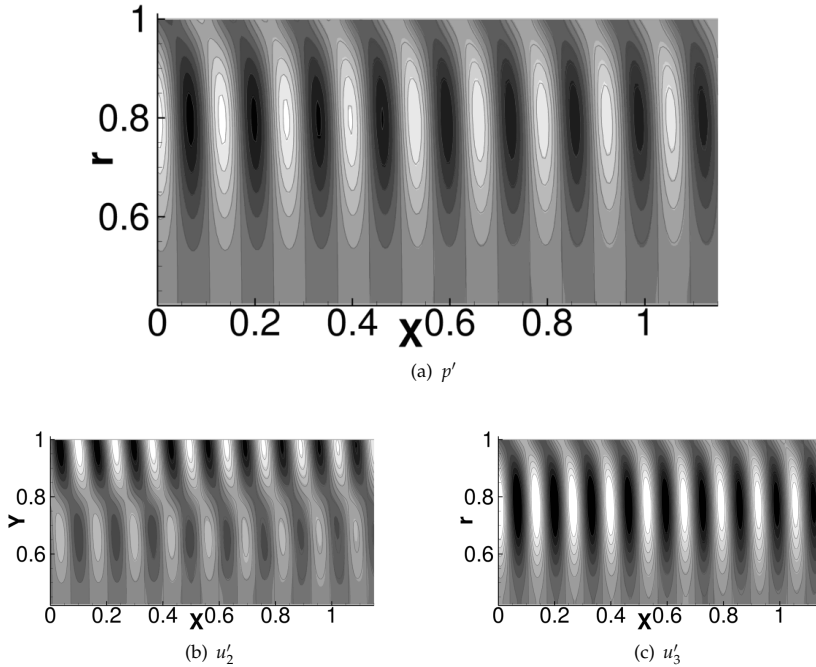


Figure 7.4.: Comparison of numerical (gray-scale-contours) and analytical solution (contour lines) for case B10 (Tab. 7.1). Equal contour levels.

First, a $m = 10$, $n = 1$ mode at a Helmholtz number of $He = 50$ is investigated. Perturbation pressure, and radial and azimuthal velocity are shown in Fig. 7.4 for case B10 without flow and in Fig. 7.5 for case B10.5 with sound waves propagating against the flow. The plots of q' and the axial velocity component u'_1 are omitted as both are found to correspond to a scaled pressure field. There is a very good agreement of analytical and numerical result for both cases. However, when comparing

the exact position of the contour lines, small differences are found (comp. Fig. 7.4 and 7.5). Especially the radial velocity distribution at the inner wall shows phase and amplitude errors, which indicates the presence of higher radial modes in the duct.

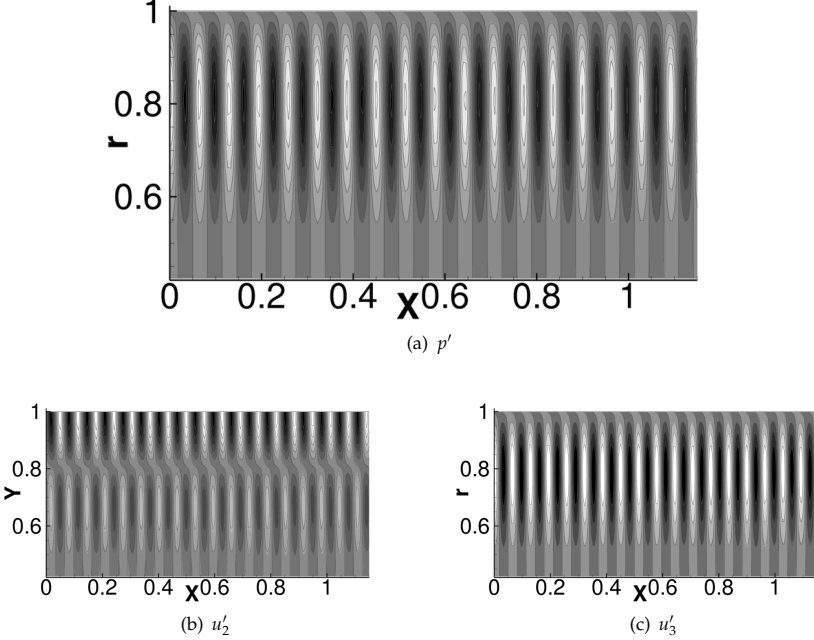
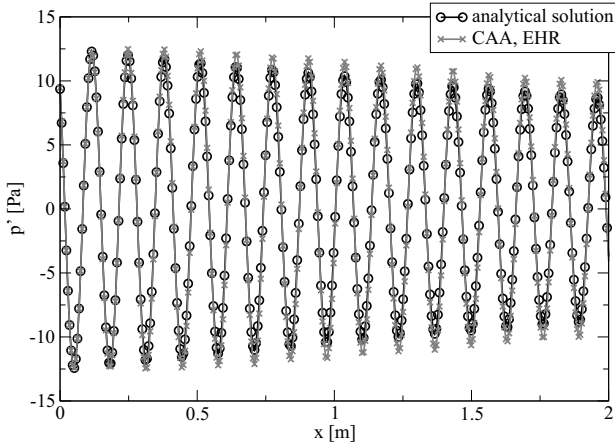


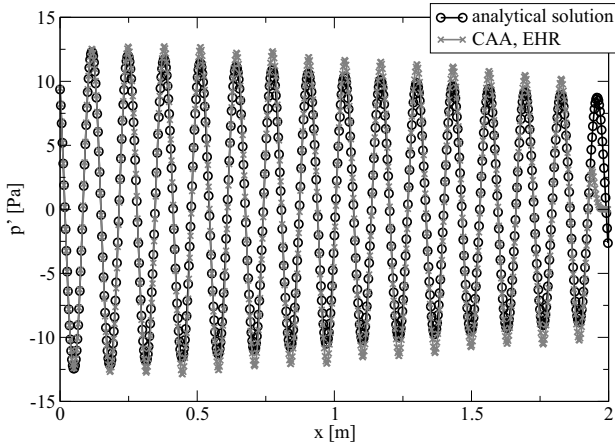
Figure 7.5.: Comparison of numerical (gray-scale contours) and analytical solution (red contour lines) for case B10.5 (Tab. 7.1). Equal contour levels.

The results are further analyzed by an axial line cut along $r = 0.94$ m, comparing the instantaneous pressure between analytical and numerical solution. It is shown in Fig. 7.6 for case B10. The good agreement of the instantaneous field data can only partly be supported by this line cut. The peak amplitude shows differences of up to 10 % for case B10. Furthermore, the instantaneous pressure at each sampling point, which should exactly match the analytical solution, is found to be different by about the same amount. The error increases with increasing distance from the source ($x = 0$ m).

The phenomenon is not related to the non-reflective boundary condition at the inlet. An early stage, where the waves not yet have reached the non-reflective boundary, shows similar differences. A possible reason for the observed deviation is, that



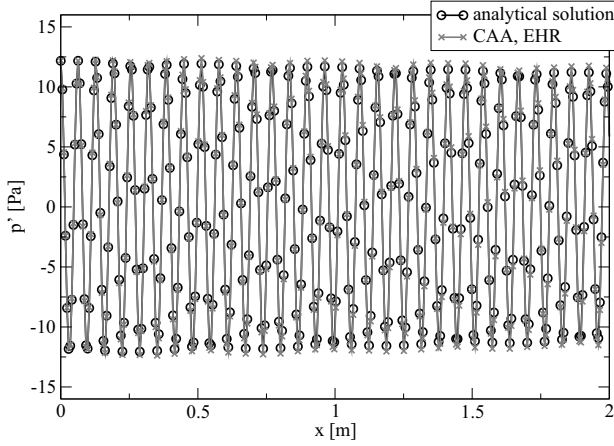
(a) B10



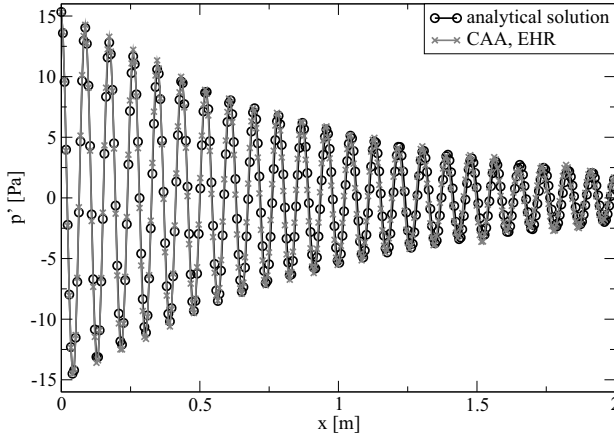
(b) B10-2 with refined mesh

Figure 7.6.: Comparison of numerical and analytical solution at $r = 0.94$ m without flow (cases from Tab. 7.1).

the solution is described as a superposition of Bessel and Neumann functions in radial direction. The spatial discretization as well as the filtering are not optimized for this type of functions. Errors of the radial discretization could lead to a leakage to higher radial modes. The presence of a large number of cut-on higher radial modes



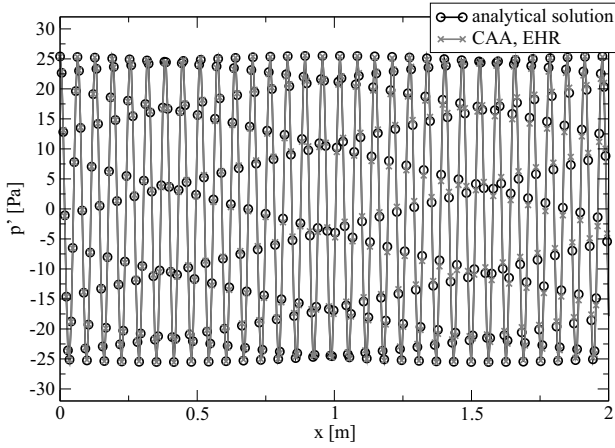
(a) B10.5



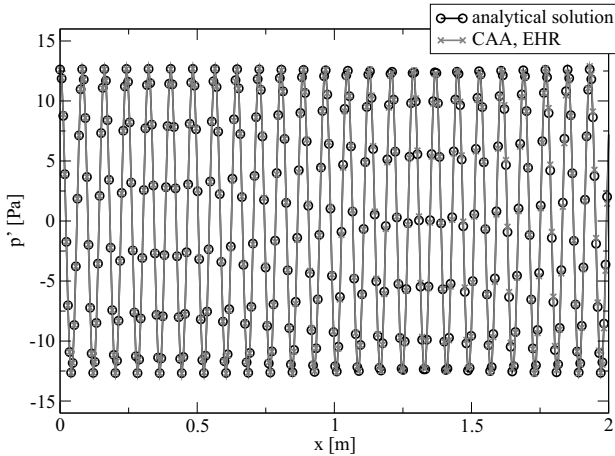
(b) B40.5

Figure 7.7.: Comparison of numerical and analytical solution at $r = 0.94$ m for waves propagating against the flow with liner (cases from Tab. 7.1).

complicates the situation, as it is a prerequisite for the leakage of energy to these modes. According to Rienstra and Eversman [109] nine and eleven radial modes are cut-on in the corresponding hard walled configurations without and with flow, respectively. A refinement of the mesh is carried out to prove the hypothesis (case B10-2 shown in Fig. 7.6). However, the almost doubled number of radial sampling



(a) B10.5-hard



(b) B10.5-hard

Figure 7.8.: Comparison of numerical and analytical solution at $r = 0.94$ m for modes propagating against the flow with hard walls (cases from Tab. 7.1).

points to 201 does not provide a significant improvement. The error level remains similar or even increases for the line at $r = 0.94$ m. Thus, other errors, as an excitation of higher modes by the source or small errors of the impedance boundary

condition, must be causing the small deviation. Even though the problem does only marginally influence the solution, it should be considered as a serious error source for the application of the method.

Now the wave propagation against the flow is considered. Fig. 7.7 shows the instantaneous pressure perturbation along a line at $r = 0.94$ m for case B10.5 and B40.5. Due to the larger axial wave number with flow, the axial resolution is only halve as large as for the corresponding cases without flow. Comparing the numerical result which is denoted by crosses and the analytical solution shown as circles, the symbols do not exactly meet. This indicates the presence of amplitude and phase errors. These errors are, however, smaller than the ones observed in the case without flow. The maximum amplitude error is less than 3 %. However, for smaller r there may be larger errors due to the relatively high amplitudes of higher radial modes there.

Finally, for the sake of completeness the corresponding fully hard-walled annular ducts with acoustic waves propagating against the flow are considered in Fig. 7.8. There are only small differences between numerical and analytical solution. For B10.5-hard the deviation between analytical and numerical solution increases with the propagation distance, whereas B40.5-hard case shows an alternating error pattern. However, the error remains much smaller than it has been observed with liner, even though the resolution is comparable between the hard-walled and the liner cases. A possible explanation is the smaller variation of the hard-walled modes in radial direction. The acoustic power in the duct is preserved for all cases with an error level below 1 % of the input energy.

7.1.2. Validation of the impedance models and the CAA method with a generic fully lined inlet duct

Geometry, benchmark source and numerical specifications

A generic aeroengine intake, for which numerical and semi-analytical solutions can be found in the literature [109], is considered in this section. It is used to further validate and study the properties of the time-domain impedance boundary condition. The inlet is equipped with a spinner. The acoustic waves are excited in the fan plane ($x = 0$ m) as single annular duct modes according to Section 3.6.3. The inlet geometry is given by the following functions according to Rienstra and Eversman [109].

$$R_i = \max \left\{ 0, 0.64212 - \sqrt{0.04777 + 0.98234 \left(\frac{x}{L} \right)^2} \right\},$$

$$R_o = 1 - 0.18453 \left(\frac{x}{L} \right)^2 + 0.10158 \frac{e^{-11 \left(1 - \frac{x}{L} \right)} - e^{-11}}{1 - e^{-11}},$$

where R_i denotes contour of the spinner and R_o the contour of the outer wall. $L = 1.86393$ m is the overall length of the inlet duct.

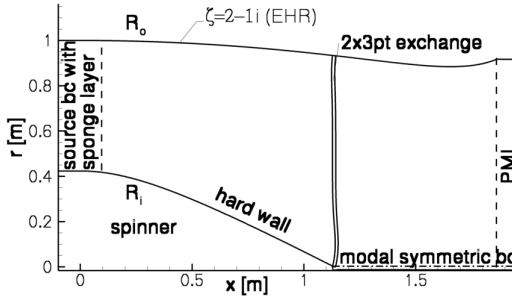


Figure 7.9.: Numerical set-up for of the generic aeroengine inlet according to [109].

A sketch of the numerical setup is provided in Fig. 7.9. The physical domain is extended by a source region (left) and a zone for the PML boundary condition at the inflow (right). The radius of the duct is kept constant in the extended zones. The overall grid size is 145 389 points. 1 206 points or $< 1\%$ of the overall domain are used to implement exchanges, 870 points to describe the modal-axisymmetric boundary condition and 12 165 points (8 %) to implement the non-reflective boundary conditions. There are 201 points in radial direction, which corresponds to the resolution of the refined mesh used in the preliminary study in Section 7.1.1. In the cylindrical duct section without spinner the aspect ratio is one and the radial extent of the duct is almost twice as large as over the spinner. Therefore, the minimum axial resolution in the current case is similar to the one of the original mesh used in the preliminary study of Section 7.1.1. The computational time for the case is 26 h for 50 000 iterations on one core of a dual core AMD Opteron 270 processor with 2.0 GHz and 8 GB main memory. This corresponds to a computational time of $13 \mu\text{s}$ per time step and grid point, which is typical for the current CAA method with the isentropic modal-axisymmetric model. The CFL number is 0.25.

The published results were obtained using a semi-analytic multiple-scales (MS) and a numerical finite element method (FEM), respectively [109]. The multiple scales method makes use of the WKB assumption to calculate the modes in a slowly varying duct [109]. In the MS, the duct modes for the lined cases are defined using the Myers boundary condition [109]. The FEM method solves a convective wave equation for the acoustic potential in the frequency domain [109]. An impedance boundary condition, which applies the Myers boundary condition in the frequency domain is implemented to the FEM [109]. Only cases considering a lined wall and nonzero base-flow conditions were picked from the publication of Rienstra and Eversman [109] for comparison. The outer contour of the duct is fully lined, whereas the spinner is hard walled. For a shorter notation the descriptors given in Tab. 7.2 are used in the following to identify the cases.

Table 7.2.: Benchmark cases for the sound propagation in a generic aeroengine inlet against the flow at $\text{Ma} = -0.5$ from [109]. The first radial mode is excited.

case	m [–]	He_{1m} [–]	hard wall cut-on radial modes [109]	PPW_x
R10-10	10	10	0	225
R10-16	10	16	2	93
R10-50	10	50	11	22
R20-50	20	50	9	23
R30-50	30	50	6	26
R40-50	40	50	3	30

Base flow

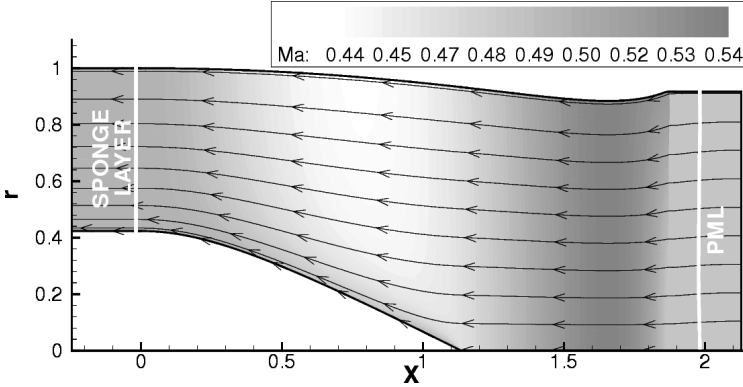


Figure 7.10.: Mach number contours for the generic aeroengine inlet case computed with the nonlinear Euler (PENNE) model.

The base-flow conditions are given as follows. The Mach number in the fan plane is $\text{Ma} = -0.5$. The other parameters have no influence, as the frequency and impedance are given nondimensional. In the following the coordinate system is chosen such, that the sound propagation is oriented positive with the x -axis. Thus, a negative Mach number denotes the flow direction and the direction of sound propagation are opposite. The base flow for the current investigation is based on an inviscid nonlinear Euler simulation as it is described in Section 3.2. The same mesh was used

for the calculation of the base flow. Thus, the current base flow is not exactly equal to the conditions used by the MS and FEM method.

Resulting relative pressure contours

The resulting normalized pressure amplitude contours are summarized in Fig. 7.11 to 7.16. A large variation of the Helmholtz and azimuthal mode number is covered by these examples. An estimate of the resulting axial resolution, which has been calculated with the real part of the axial wave number k_x at the source position and the overall maximum of the axial spacing Δx in the mesh, is summarized in Tab. 7.2. For comparison the figures from Rienstra and Eversman [109] as given below in Fig. 7.11 to 7.16, where MS denotes the multiple scales and FEM the finite element result. As can be seen from the figures, the location of the main lobe as well as the contours at the wall are in a good agreement the published FEM and MS results. In most cases the current CAA result combines elements from the FEM and MS results.

The largest observable difference is found at the inlet plane ($x = L$), where the contours show a strong decay for the current CAA results in all cases. The extension of the computational domain to implement the PML boundary condition is rather arbitrary. It is chosen in this case in accordance to the benchmark source of [109]. The current results indicate the presence of additional reflections from the sharp edge at the inlet plane. The pressure amplitude contours in Fig. 7.11 to 7.16 show distinct insular structures indicating reflections close to the inlet plane for the CAA result. These structures are observed in all plots apart from case R10-10 as isles or pinches. In the case R10-10 the strong attenuation of the cut-off mode reduces the amplitude below the minimum contour level before reaching the inlet plane. Therefore, possible reflections are not visible. The cut of the domain directly at the lip is not the typical situation in the application of a CAA method. A real aeroengine would have a lip extending to the outer wall of the nacelle and engine test facilities features bell shaped inlets, in order to have flow conditions similar to the in flight situation. The objective of the numerical simulation is to obtain the radiation of sound waves to the near field of the inlet. Therefore, the observed difference is considered an unessential error for the intended application.

Other observed differences are more important. One is found in the comparison of the absolute contour levels. While the contour lines for the low Helmholtz numbers in case R10-10 and R10-16 which are shown in Fig. 7.11 and Fig. 7.12, nearly reach the same maximum axial position as in the FEM and MS results, the higher Helmholtz numbers shown in Fig. 7.13 to 7.16 show an obvious reduction of the maximum axial extent of the related contours for the current CAA results. The difference could point to increased dissipation by the numerical method, which should not be observed with the relatively large axial resolutions (comp Tab. 7.2) used for these cases. The problem will further be addressed in the following by analyzing the acoustic power flux in the inlet.

Another difference is observed when directly comparing the FEM and CAA results. The FEM results show a radial variation in the fan plane with a node line and

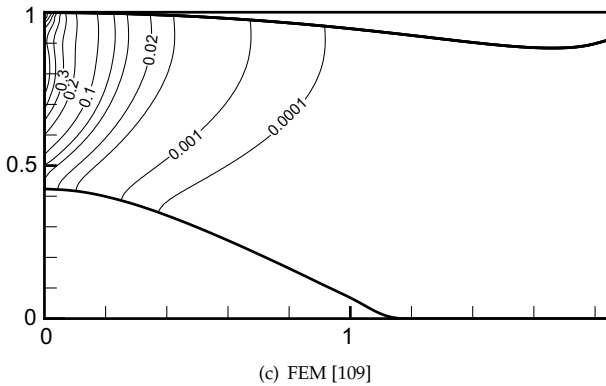
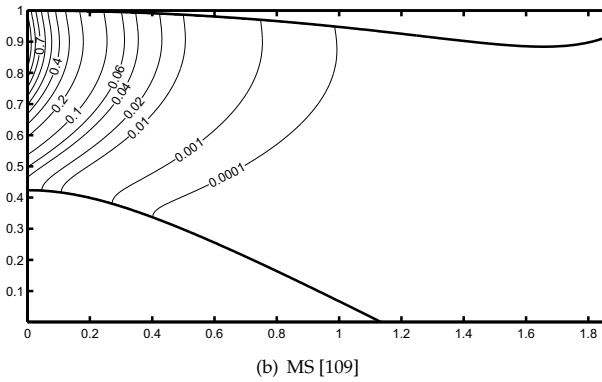
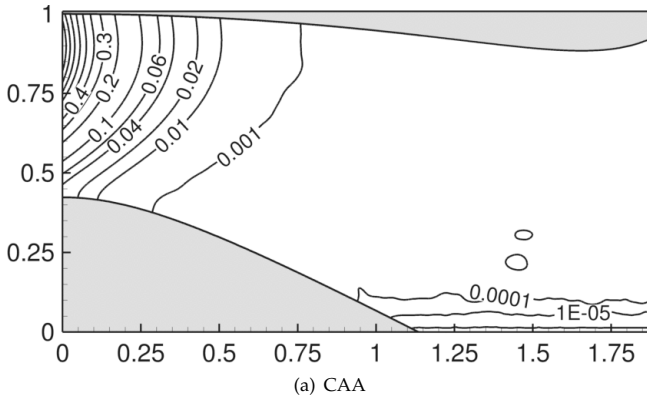


Figure 7.11.: Comparison of the current CAA results to the results of Rienstra and Eversman [109]; R10-10 described in Tab. 7.2.

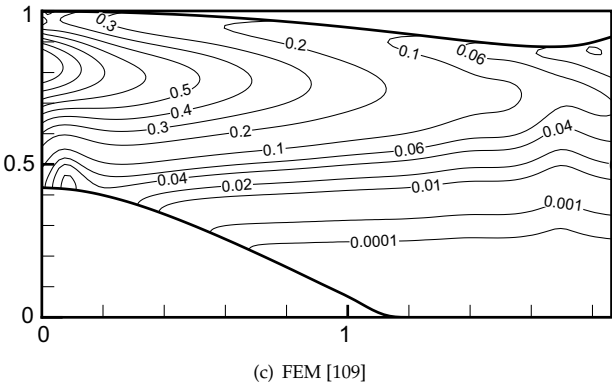
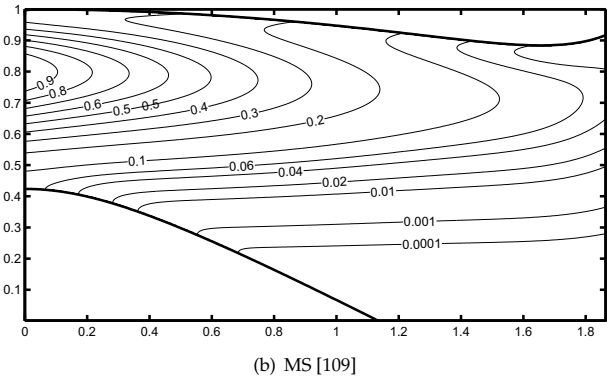
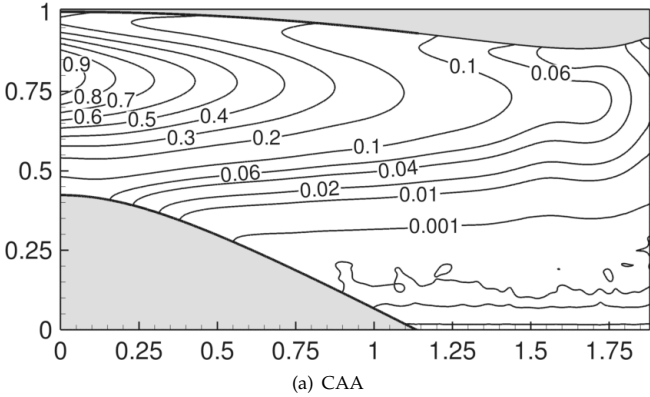


Figure 7.12.: Comparison of the current CAA results to the results of Rienstra and Eversman [109]; R10-16 described in Tab. 7.2.

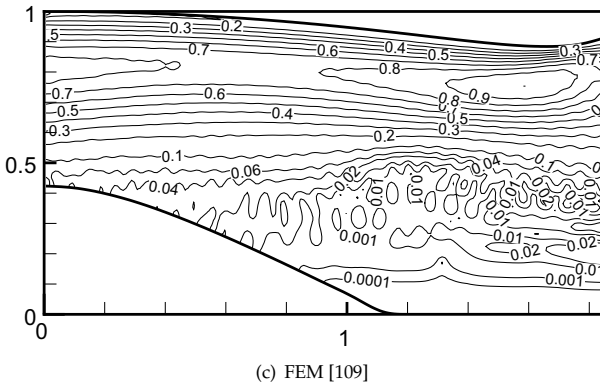
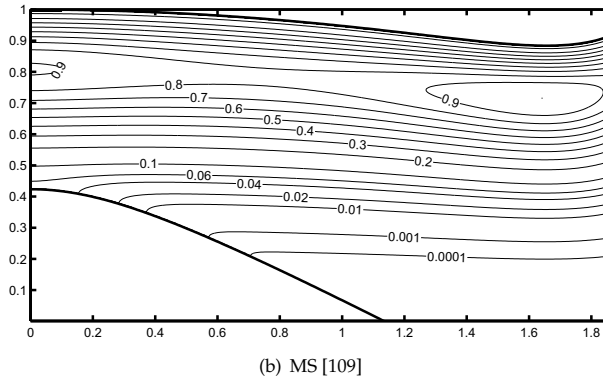
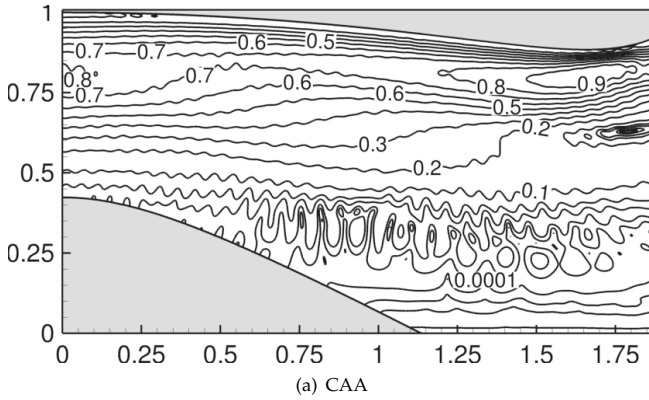


Figure 7.13.: Comparison of the current CAA results to the results of Rienstra and Eversman [109]; R10-50 described in Tab. 7.2.

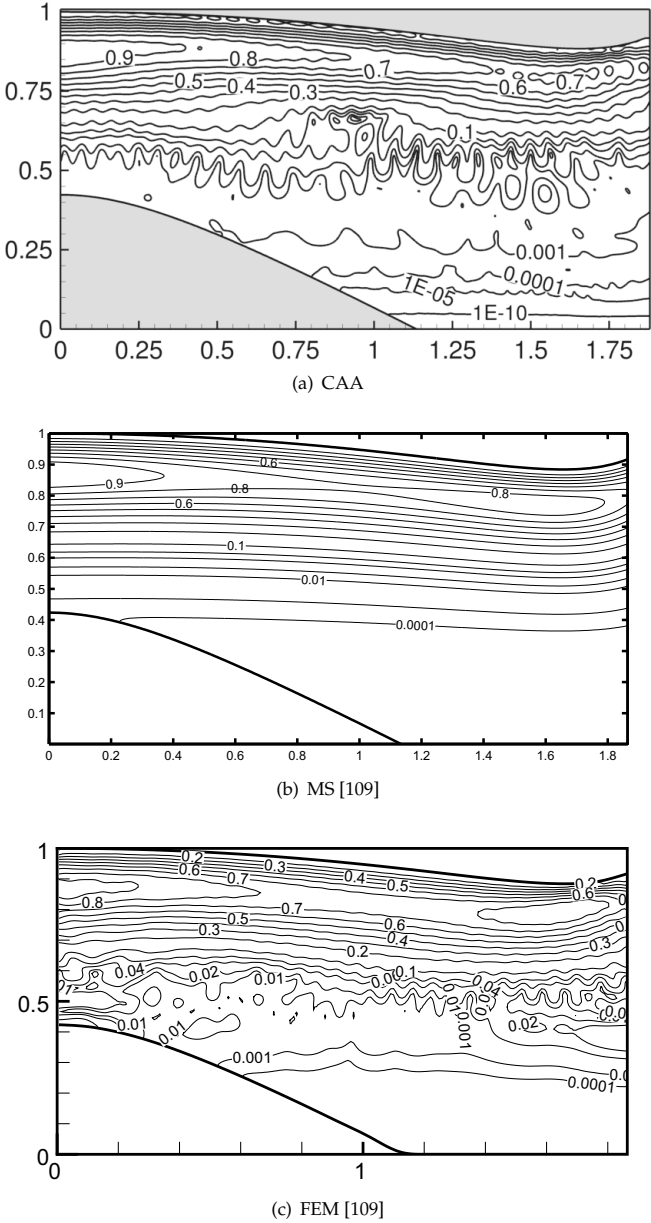


Figure 7.14.: Comparison of the current CAA results to the results of Rienstra and Eversman [109]; R20-50 described in Tab. 7.2.

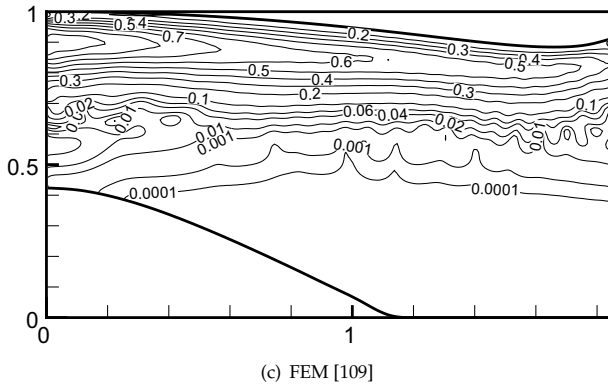
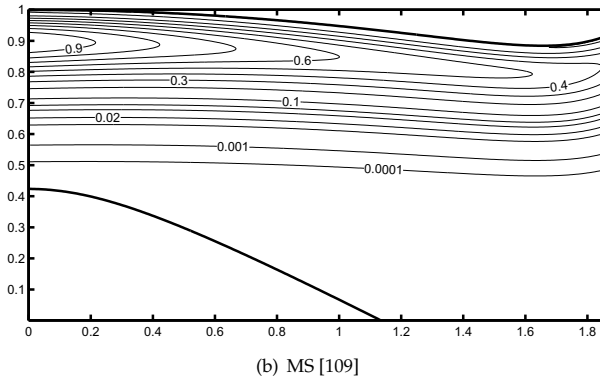
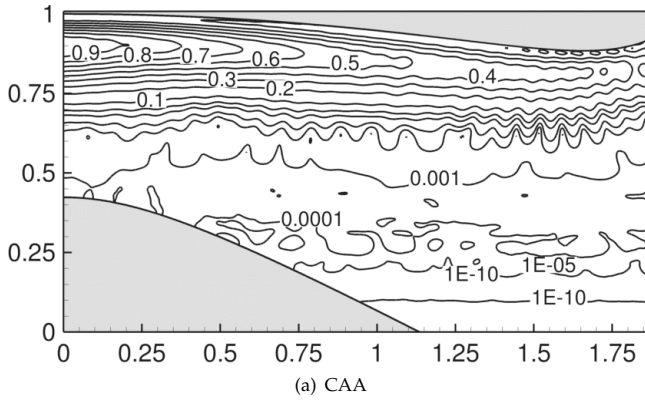


Figure 7.15.: Comparison of the current CAA results to the results of Rienstra and Eversman [109]; R30-50 described in Tab. 7.2.

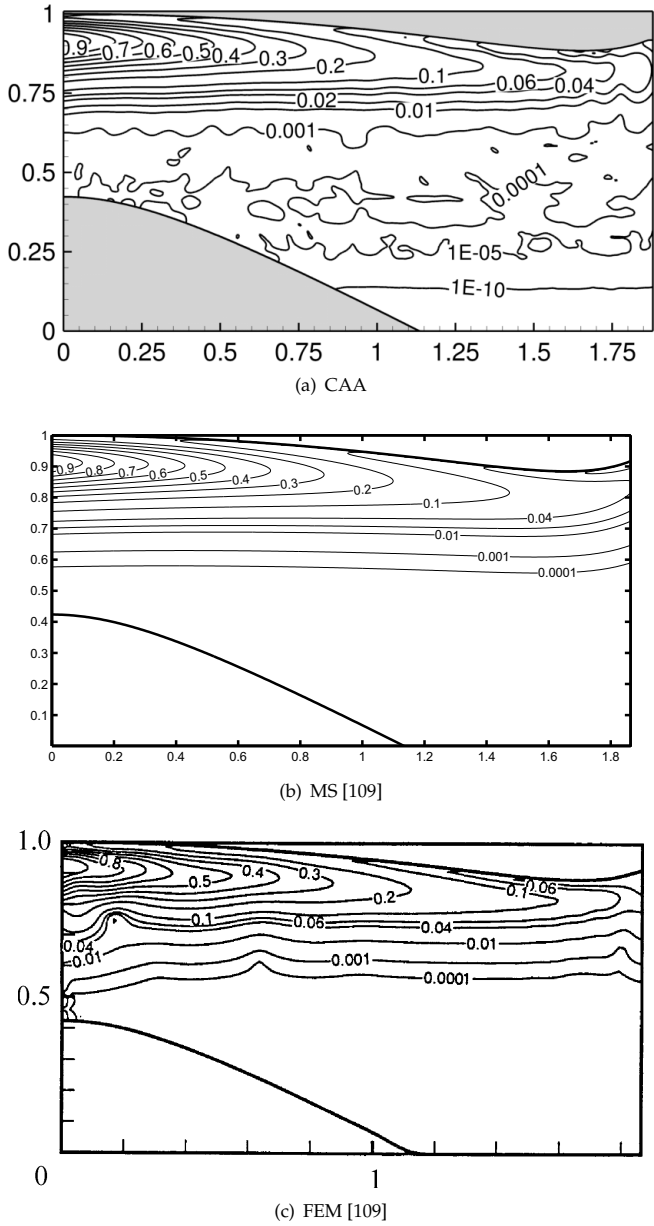


Figure 7.16.: Comparison of the current CAA results to the results of Rienstra and Eversman [109]; R40-50 described in Tab. 7.2.

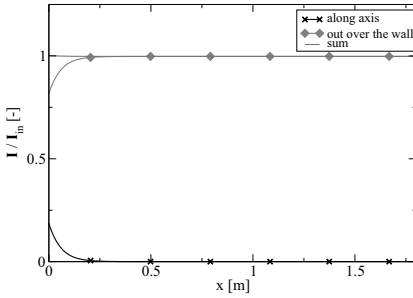
two local radial maxima around $r = 0.55$ m and $r = 0.85$ m for R20-50 in Fig. 7.14(b) and around $r = 0.55$ m and $r = 0.85$ m for R30-50 in Fig. 7.15(a). This indicates the presence of higher radial modes in the fan plane for the FEM result. Such variations are not found in the current result. However, the lower contour levels in the inlet show some wiggles which point to the presence of higher modes in the current result, too. The number of cut-on radial modes in the corresponding hard-walled configuration is cited from Rienstra and Eversman [109] in Tab. 7.2. The results show that, as well the FEM as the CAA results include higher radial modes for the higher Helmholtz number ($He = 50$) cases shown in Fig. 7.13 to Fig. 7.16. An artificially increased scattering into higher radial modes by the CAA method was found as a problem in the verification of the preceding section as well. The FEM results seem to be even more affected by the radial mode scattering at the source. However, the amplitude of these higher radial modes seem to be reduced with increasing propagation distance for the FEM results.

Higher radial modes also become visible at the inlet plane for the FEM result in case R10-50, R20-50 and R30-50. A similar strong scattering into a higher radial mode is only observed for one case, R10-50, with the current method. However, the radial mode number seems to be different from the FEM result. The different base flow conditions are considered to be the cause for the observed differences.

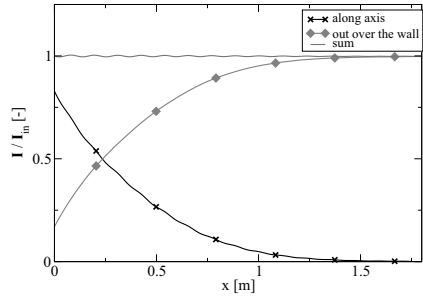
Altogether the results verify the implementation of the EHR-based time domain impedance boundary condition with the current CAA method. Small differences are attributed to the different mean-flow profiles. A comparison of the current result to earlier ones [106], using artificial base-flow conditions similar to the MS method, shows the strong influence of the mean flow. The question about numerical dissipation in the current result remains open up to now. It will be addressed in the following section by an analysis of the acoustic intensity.

Intensity based verification of the results

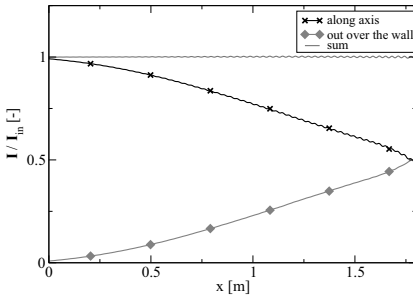
The acoustic energy conservation computed by Eq. (5.7) for the six test cases shown in Tab. 7.2 is given in Fig. 7.17 denoted as sum. The two summands of Eq. (5.7), which describe the flux along the axis, as well as the cumulated flux over the wall, are also given in the figures. The overall conservation of the acoustic power flux, which is observed as almost constant sum of the components, indicates a very low dissipation in the current numerical results. Small axial variations are found, which show the presence of small instationary components due to reflections or vortical perturbations in the solution. These perturbations are, however, orders of magnitude below the overall acoustic power flux. Altogether, the acoustic intensity verifies the current numerical result. The above observed smaller pressure amplitudes with respect to the FEM and MS results are not related to the dissipation of the numerical method, therefore.



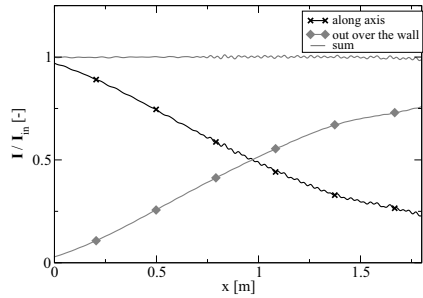
(a) R10-10



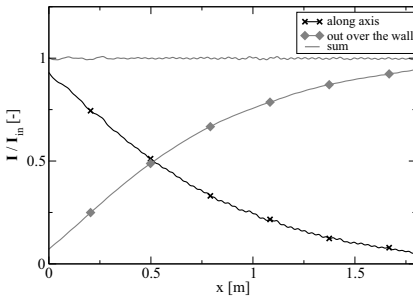
(b) R10-16



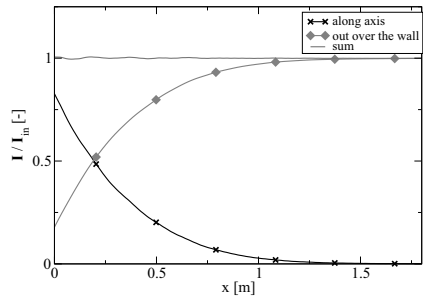
(c) R10-50



(d) R20-50



(e) R30-50



(f) R40-50

Figure 7.17.: Acoustic intensity flux related to the input at the source boundary for the current CAA result, case descriptors from Tab. 7.2.

Influence of low-order filtering and the resolved boundary layer at the wall

Finally, the generic inlet case is considered to study the impact of the low-order filtering in the EHR to suppress the instability of the Myers boundary condition (comp. Section 4.5.2). Furthermore, the idea to use a resolved boundary-layer profile at the wall instead of the Myers boundary condition is studied. It is found, that a specific impedance model and mesh allows to obtain a solution, which is later disturbed by the slowly growing instability. This early state solution is considered as benchmark source for the stabilization approaches. Case R10-50 from Tab. 7.2 is considered for the further investigation. As it features the lowest resolution and the largest number of cut-on radial modes, the results are considered to be representative for other cases.

Two different filtering stencils are considered for the liner variables, of which only the low-order filtering as it is described in Section 4.5.2 is successful in suppressing the instability for a large number of time steps. As can be seen from Fig. 7.19(b), the low-order filtering causes only small variations from the original result with the Myers boundary condition.

The resulting acoustic power flux along the axis is given in Fig. 7.19(a) for different artificial boundary layer profiles with different boundary layer thickness δ and zero velocity at the wall. The base-flow profiles are completely artificial. One of the boundary layer profiles is shown in Figure 7.18. Most of the profiles are constructed by sixth-order polynomials. One cosine profile is considered to study the influence of the functional shape. As can be seen from Fig. 7.19(a), the cosine profile almost exactly reproduces the result of the polynomial profile with the same boundary layer thickness. All resolved boundary layer cases predict a lower attenuation than the application of the Myers boundary condition would do. A convergence towards the result using the Myers boundary condition is observed with decreasing boundary layer thickness. This is similar to the reports of Zhuang [146] for a 2D channel. However, the current results indicate that the mesh is not fine enough to resolve a boundary layer, which fully reproduced the Myers boundary condition. No instability is observed with any of the resolved boundary layer profiles.

A boundary layer with 30 points thickness makes the acoustic power loss over the liner very small. The observed result for the axial power flux would only be expected for a hard walled duct not for a lined one. However, the interior acoustic field in this case looks more like in the lined duct cases with small perturbation am-

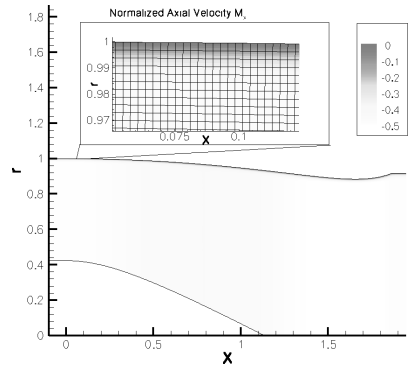


Figure 7.18.: Mean flow profile with three grid points of boundary layer for the generic aeroengine inlet

plitudes close to the wall. The lower attenuation is due to the refraction of acoustic waves away from the lined surface, which becomes completely inefficient due to this.

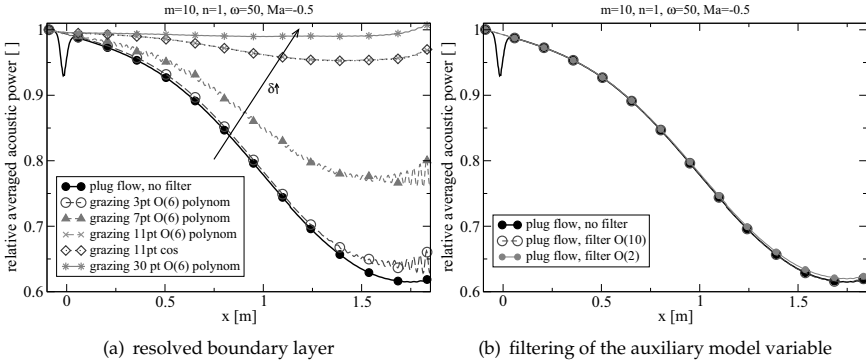


Figure 7.19.: Normalized acoustic power flux along the axis if the generic inlet configuration for case R10-50 from Tab. 7.2 to compare the stabilization approaches of (a) section 4.4.1 and (b) section 4.5.2.

With respect to the stabilization of the impedance boundary condition the conclusions of this investigation are:

- A second-order filtering of the storage term is required to stabilize the EHR for the current impedance model parameters and grid sizes, other choices may still be unstable or even be stable without filtering.
- The impact of a second-order filtering of the auxiliary variables of the Myers boundary condition on the observed acoustic field is found to be small. Thus, the method seems applicable in general. All verification results presented in this work use the low-order filtering of the storage variables of the EHR model unless other noted.
- A resolved boundary layer may, however, lead to significantly different results, depending on the boundary layer thickness.
- The result which has been obtained with the Myers boundary condition represents the limit for decreasing boundary-layer thickness.

7.1.3. Sound radiation from lined ducts

Two cases from the literature, considering the radiation of sound waves from lined ducts, are used as benchmark source in this subsection. The test cases cover two-di-

mensional channels with and without partial lining [64] as well as an axisymmetric annular duct with full, partial and without lining [28]. The emphasis is put on the cases with flow in the following. The whole validation including cases without flow can be found in Buske et al. [21]. The EHR model is used for both of the test cases.

Radiation of sound waves from two-dimensional lined ducts [64]

The first benchmark case uses the published analytical solution of Koch [64] for comparison. It considers the radiation of sound waves from a partially-lined two-dimensional duct. The lining of the upper and lower wall of the channel extends from $x = -2.17 H$ to $x = -1 H$, where $H = 0.1873$ m is the height of the channel and $x = 0$ denotes the exit plane of the semi-infinite channel. Koch [64] uses the broadband impedance model of Ko [63], to describe the frequency response of the liner panel. The impedance function is given according to Koch [64, Eq. (2)] by

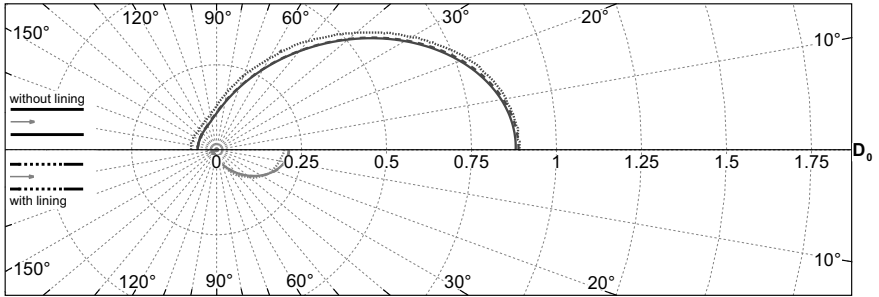
$$Z = R_* \left(1 + i \frac{f_*}{f_{0*}} \right) - i \cot(2\pi d_* f_*).$$

Expanding the reduced frequency $f_* = f H c^{-1}$ and the constants $c = 340$ m/s, $f_{0*} = 8.14$, $R_* = 1.4$ and $d_* = 0.136$ one yields the model parameters of the EHR model by comparison of the coefficients in Tab. 4.1

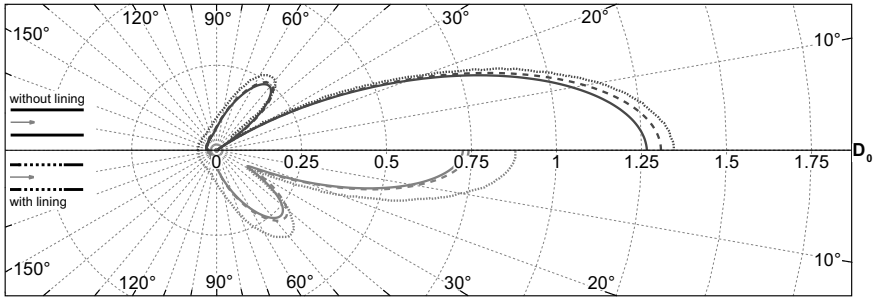
$$R_f = 1.4, \quad m_f = 1.507 \times 10^{-5} \text{ s}, \quad \beta = 1, \quad T_l = 1.497 \times 10^{-4} \text{ s} \quad \text{and} \quad \varepsilon = 0.$$

With these model parameters for the EHR, the maximum possible time-step size in the simulation is reduced to $\Delta t = 5.5 \times 10^{-8}$ s. This corresponds to a reduction by one order of magnitude with respect to the hard walled case ($\Delta t = 8.9 \times 10^{-7}$ s). The maximum time-step size with the EHR model is found to be proportional to the parameter m_f . The CAA simulation uses an equidistant orthogonal mesh of 267 521 points. The radiation boundary condition of Section 3.5.1 is applied at the outer boundaries of the computational domain. The sound source in the duct is implemented via a sponge layer according to Eq. (3.22). It uses 10 grid lines to prescribe a non-reflective source. The two-dimensional linearized Euler equations are used for the simulation. All cases of the benchmark source by Koch [64] consider a medium at rest for the sound propagation. The Ingard/Myers boundary condition is not required in this case. A summary of the test cases, which are going to be presented below, is given in Tab. 7.3.

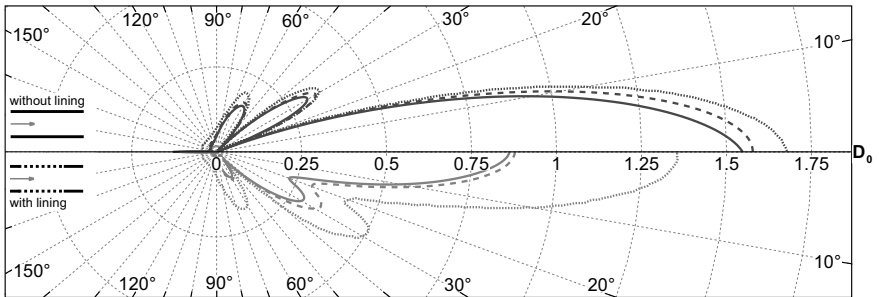
The test cases cover a wide variety of impedance values and frequencies. The lowest frequency from the benchmark source for $m = 0$ is omitted for a more clear presentation; it is found in a good agreement with Koch's result [21]. Figs. 7.20 to 7.22 show the resulting far-field characteristics, in terms of relative pressure amplitudes according to Koch [64], for the other cases. An acoustic intensity based AIBM far-field calculation is applied, which solves an inverse acoustic problem to obtain the far-field characteristics [137, 138]. As can be seen from the figures, the near-field



(a) K0.8-0 [21]

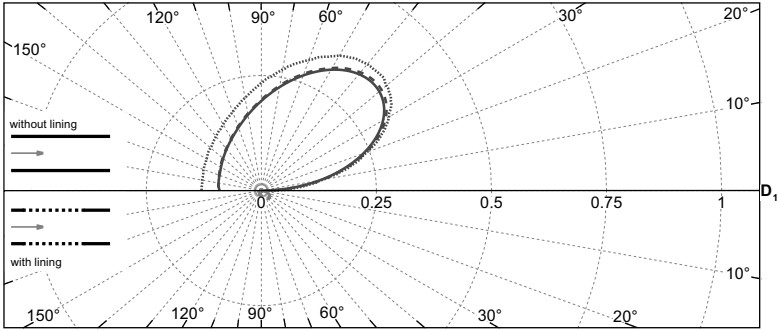


(b) K1.8-0 [21]

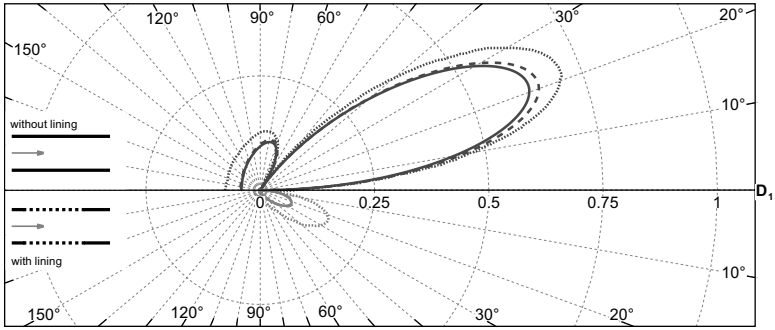


(c) K2.8-0 [21]

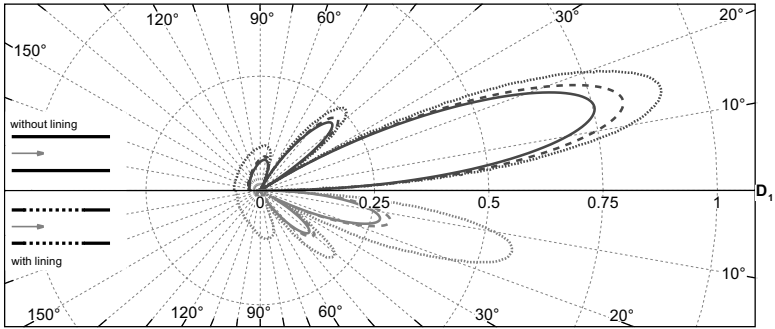
Figure 7.20.: Comparison of the CAA near field (dashed), CAA-AIBM far field prediction results (solid line) and the analytical solution (dotted) for the radiation from a partially lined duct without flow; mode $m = 0$; the case description is found in Tab. 7.3; the hard walled result is given in the upper part of each sub-figure for comparison.



(a) K0.8-1 [21]

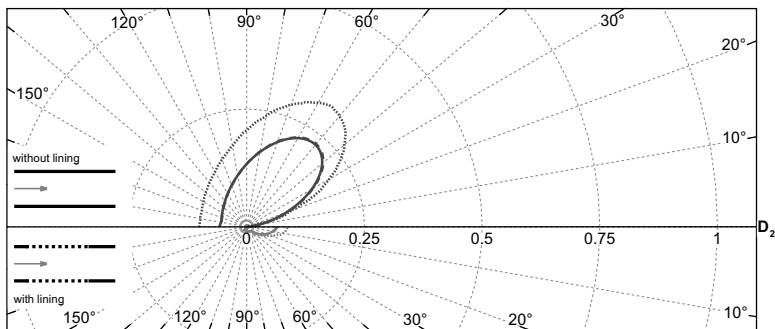


(b) K1.8-1 [21]

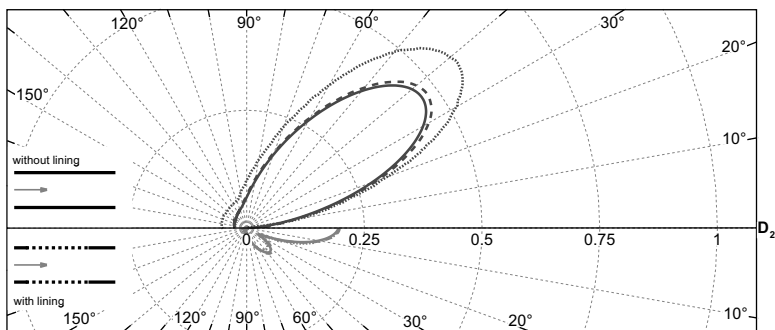


(c) K2.8-1 [21]

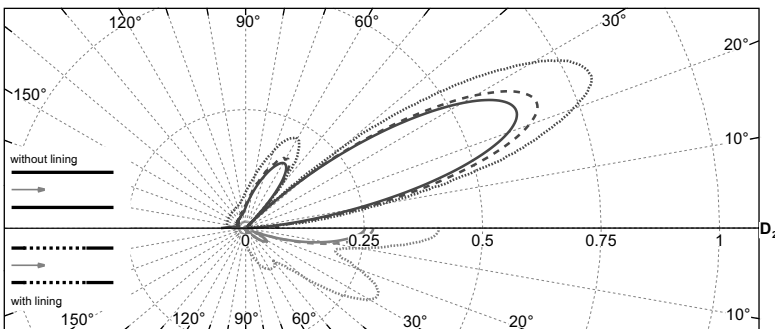
Figure 7.21.: Comparison of the CAA near field (dashed), CAA-AIBM far field prediction results (solid line) and the analytical solution (dotted) for the radiation from a partially lined duct without flow; mode $m = 0$; the case description is found in Tab. 7.3; the hard walled result is given in the upper part of each sub-figure for comparison.



(a) K1.2-2 [21]



(b) K1.8-2 [21]



(c) K2.8-2 [21]

Figure 7.22.: Comparison of the CAA near field (dashed), CAA–AIBM far field prediction results (solid line) and the analytical solution (dotted) for the radiation from a partially lined duct without flow; mode $m = 0$; the case description is found in Tab. 7.3; the hard walled result is given in the upper part of each sub-figure for comparison.

Table 7.3.: Benchmark cases for the radiation from a partially lined two dimensional channel from Koch [64]. The mode number corresponds to the two-dimensional hard-walled duct mode here.

case	$Z [-]$	$m [-]$	$f [\text{Hz}]$	$f_* = f H/c [-]$	PPW [-]
K0.8-0	$1.4 - i 1.09$	0	1453.5	0.8	37.5
K1.8-0	$1.4 + i 0.28$	0	3270.3	1.8	16.6
K2.8-0	$1.4 + i 1.56$	0	5087.1	2.8	10.7
K0.8-1	$1.4 - i 1.09$	1	1453.5	0.8	37.5
K1.8-1	$1.4 + i 0.28$	1	3270.3	1.8	16.6
K2.8-1	$1.4 + i 1.56$	1	5087.1	2.8	10.7
K1.2-2	$1.4 - i 0.40$	2	2180.2	0.8	25.0
K1.8-2	$1.4 + i 0.28$	2	3270.3	1.8	16.6
K2.8-2	$1.4 + i 1.56$	2	5087.1	2.8	10.7

characteristics of the CAA simulation on an arc with radius 1.5 m around the center line of the duct exit and the AIBM far-field characteristics are very similar with respect to the position and number of lobes. However, the amplitude differs.

With respect to the result of Koch [64], the amplitudes are too low for almost all cases. The deviation is smaller for the hard-walled cases. The shape of the radiation characteristics is still met for the lined duct cases. The reason for the lower amplitudes is probably artificial dissipation in the numerical simulation. The increased dissipation in the cases with liner is related to the smaller time-step size. The filtering of the solution is fixed to the iterations of the Runge-Kutta scheme. It is carried out for each other time step, independently of the time-step size. This leads to a increased number of filtering operations for a wave propagating with liner over a given distance. In the current example, there are ten times more filtering operations for the cases with liner than for the cases without. Due to the increased number of filter calls, the characteristics with liner show an increased dissipation. The increase of the deviation from the analytical solution with the frequency substantiates the assumption. The dissipation of the overall method increases with the wave number. A larger deviation is especially found for higher modes at higher frequencies, where the resolution reaches down to 10.7 PPW. There are, however, different error levels between the main and side lobes, which identify the reflections at the sound source as additional cause of error. The reflections are selective to the modal content. Waves impinging perpendicular to the source are less affected than higher modes with a small cut-off ratio [113]. In consequence, the source may excite re-

flected higher modes, which lead to altered radiation characteristics and feed the side lobes.

To further isolate the error, the simulation should be repeated with a larger number of time steps between two filtering calls. Further insight may also be provided by varying the source boundary condition. However, there is no perfect boundary condition for close to cut-off waves [113]. The PML, which was found to be best suited in such cases according to Schemel [113] is not implemented as source boundary condition yet. The repeated simulation is omitted here. Excluding the highest frequency from the benchmark, the presented results reach a sufficient level of consistency with the analytical solution of Koch [64] such that the verification can be considered successful.

Sound radiation from an annular duct with jet flow and a lined centerbody [28]

The benchmark case for this subsection considers the radiation of sound from an annular duct with fully or partially lined centerbody. It represents a simplified model for a so called short cowl aeroengine design with a lined outer wall of the core nozzle. In this design, the inner core of the engine is not fully encased by the bypass duct. The lining of the afterbody, which is the outer wall of the engine core extending downstream of the main nozzle, was found to have a large noise reduction potential by Richards et al. [100].

The analytical solution has been published by Demir and Rienstra [28] together with a variety of cases for code benchmarking. The analytical solution is based on a semi-infinite hard-walled duct with hard-walled or lined infinitely long centerbody. The outer diameter of the annular duct is 2.4 m, whereas the centerbody diameter is 1.6 m. There is a jet flow from the duct. The jet features a non-developing infinitely thin shear layer. The flow over the liner has a local Mach number of $Ma = 0.5$ and there is an ambient flow with $Ma = 0.3$. The sound waves propagate with the flow. Inside the jet and the annular duct the temperature is slightly increased, such that the speed of sound is $c = 350$ m/s. A single azimuthal duct mode is excited inside the duct. The wall impedance of the lined inner wall is $Z = 2 - i$ for all cases given by the benchmark source [28]. Only cases with jet flow and liner are picked of the large number of cases considered by Demir and Rienstra [28]. The test cases which are going to be presented in the following are summarized in Table 7.4.

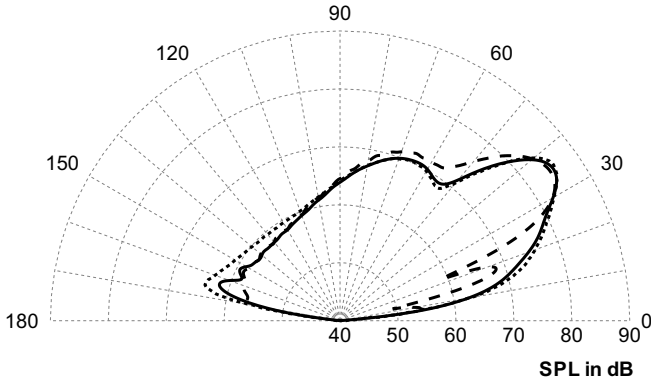
The results in this section were obtained using the current CAA method in combination with an acoustic intensity based far-field method (AIBM) of Yu et al. [137, 138]. The results were also published as [21]. The modal-axisymmetric linearized Euler equations are applied with a fully non-isentropic pressure equation. A grid stretching towards the boundary is used in combination with a radiation/outflow boundary conditions of Section 3.5.1 and a sponge layer [comp. Eq. (3.22)] at the outer boundaries. The sound source is prescribed by a sponge layer of 15 points according to Section 3.5.2. A lined duct mode according to Section 3.6.3 is specified at the source plane inside the lined duct via the sponge layer of Section 3.5.2 for the lined centerbody cases. The lined afterbody is excited by a single hard wall

Table 7.4.: Cases considered from Demir and Rienstra [28] for the sound radiation from an annular duct with lined centerbody. Only the first radial mode is excited.

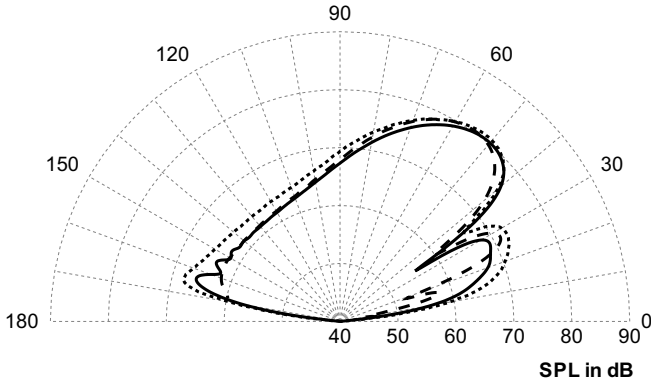
case	$Z = [-]$	$m [-]$	$n [-]$	$f[\text{Hz}]$	surface lined
D660-1	$2 - i$	4	1	660	whole centerbody
D660-2	$2 - i$	4	2	660	whole centerbody
D1095-1	$2 - i$	4	1	1095	whole centerbody
D1095-2	$2 - i$	4	2	1095	whole centerbody
D1095-3	$2 - i$	4	3	1095	whole centerbody
D660-AB	$2 - i$	4	1	660	afterbody only
D1095-AB	$2 - i$	4	1	1095	afterbody only

mode inside the annular duct. A more detailed case description may be found in Buske et al. [21]. The base-flow conditions used for the analytical solution cannot be directly adapted to the CAA simulation. This is due to the infinite-thin shear layer of the jet flow in the benchmark source, for which no modeling exists in the current CAA method. The shear layer has to be resolved, which is done in the current work by artificially increasing the shear layer thickness. This is obtained by repeated second order filtering (comp. Appendix B.1.3) of the infinitely thin shear layer. In addition to the filtering of the mean flow profile, the source terms arising from the spatial derivatives of the mean flow are also filtered with the same stencil. It is found that 15 filtering iterations are sufficient to obtain a stable and accurate solution. However, the presented results are based on a 50-times filtered base-flow profile.

Lined centerbody: The results obtained for a fully-lined centerbody are summarized in Fig. 7.23 and Fig. 7.24. The three line styles represent the CAA, AIBM and the analytical result for the relative far-field SPL. The near-field result, which has been obtained on an arc of $r = 6$ m and is scaled for a distance of $r = 46$ m is shown as dashed line. The CAA–AIBM far-field prediction for $R = 46$ m is shown as solid line. The corresponding analytical solution is shown as dotted line. Firstly, the comparison of the acoustic near-field (CAA) and far-field results (AIBM) shows a relatively good agreement of both results. There are, however, some essential differences. One is the position of the minimum radiation direction, which differs between the current CAA and AIBM results for D660-2, D1095-2 and D1095-3. Furthermore, there are additional small side lobes in the far field which are not found in the near field. Both observations are attributed to acoustic near-field effects, as the CAA result is monitored at a surface relatively close to the duct end.



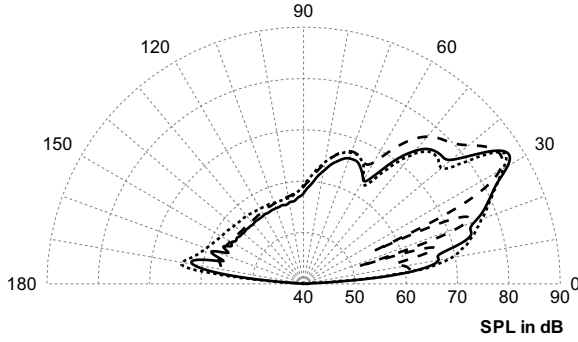
(a) D660-1 [21]



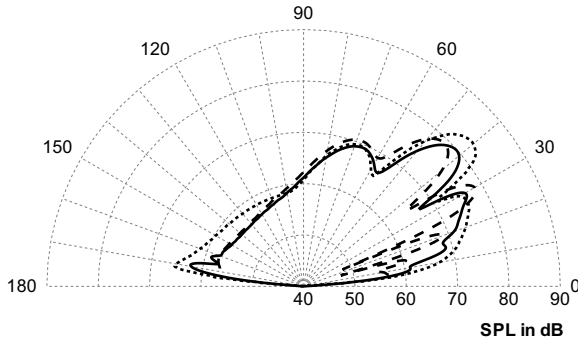
(b) D660-2 [21]

Figure 7.23.: Comparison of CAA (dashed), CAA–AIBM far-field (solid line) and the analytical solution (dotted) for the radiation from an annular duct with a lined centerbody $f = 660$ Hz (basic case informations in Tab. 7.4).

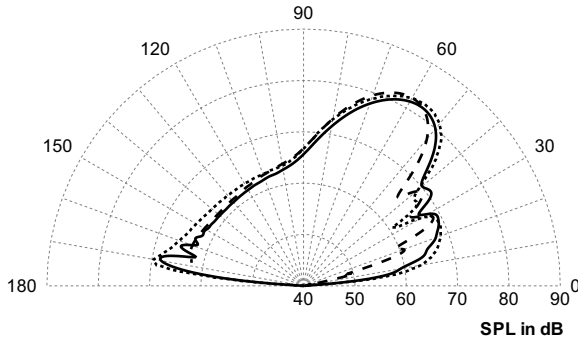
When comparing the current far-field results to the published result of Demir and Rienstra [28], the agreement is very good. The general shape of the directivity plots is very similar and the main lobe and first side lobe are well met. The angle is measured relatively to the duct axis with a zero angle in flow direction. It should be noted, that angles lower than 12 degrees are directly affected by the shear layer, such that the far-field characteristics are assumed to be incorrect for lower angles.



(a) D1095-1 [21]



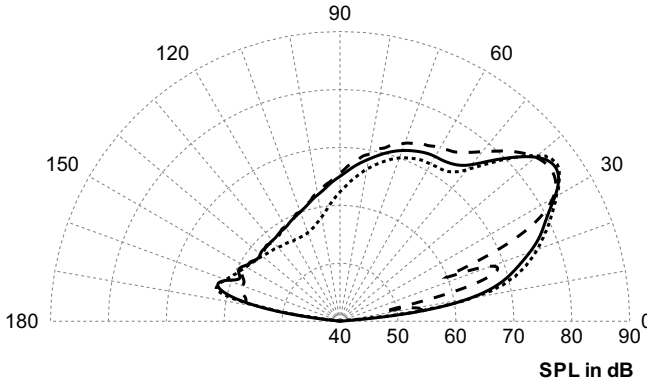
(b) D1095-2 [21]



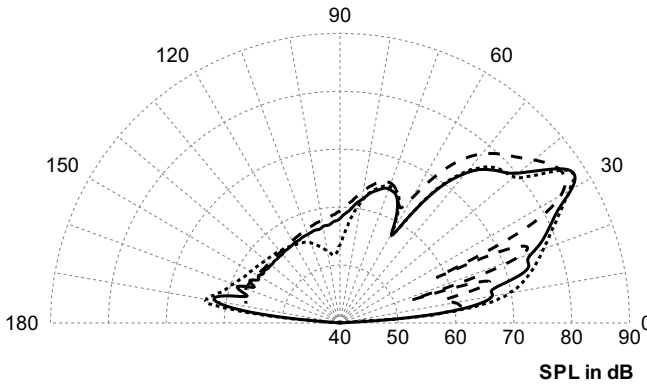
(c) D1095-3 [21]

Figure 7.24.: Comparison of CAA (dashed), CAA-AIBM far-field (solid line) and the analytical solution (dotted) for the radiation from an annular duct with a lined centerbody $f = 1095$ Hz (basic case informations in Tab. 7.4).

In fact the CAA results show a larger deviation from the analytical solution up to almost 30 degrees. The amplitude is over-predicted and side lobes are missing in this range of angles. However, on the background of the different shear layer, which is infinitely thin in the benchmark source and of finite thickness for the current result, this deviation is not surprising.



(a) D660-AB [21]



(b) D1095-AB [21]

Figure 7.25.: Comparison of the CAA near-field (dashed), CAA-AIBM far-field (solid line) and the analytical solution (dotted) for the radiation from an annular duct with a lined afterbody (cases according to Tab. 7.4). The analytical solution of Demir and Rienstra [28] with Kutta condition is used as reference.

Another observable difference concerns high angles between 120 and 180 degrees. The acoustic pressure amplitude of the backscattered waves is approximately one order of magnitude below the one of the main lobe. The CAA results show smaller amplitudes under these angles, too. This effect has been observed for several different radiation problems [135] and is related to the non-infinite upstream extent of the computational domain. Altogether, the results with fully-lined centerbody validate the implementation of the time-domain impedance boundary condition based on the EHR into the present CAA method including the instability treatment of the Myers boundary condition.

Lined afterbody: A lined afterbody is also considered by the benchmark source [28], which means the centerbody is lined outside the duct ($x > 0$) and hard walled inside ($x < 0$). The lined afterbody adds the problem of a hard to lined wall transition. Fig. 7.25 presents the results of the related two test cases. When compared to the fully-lined centerbody the sound pressure level in the far-field is increased. The CAA near-field and CAA-AIBM far-field results are found in a reasonable agreement with some observable near-field effects as blurred side lobes and slightly changing amplitudes. For both cases the back scattered waves show a distinct minimum in the near field, which is not found in the far field.

The analytical results, which have been obtained by a Wiener-Hopf technique compare two models for the hard-lined transition. One is the modeling as a discontinuity at which the perturbation field may show a jump. The other is the application of a so called full Kutta-condition, which keeps the stream traces parallel to the wall in a small vicinity of the transition point. There is an observable difference of both conditions [28]. The current simulations cannot, however, directly apply either one of the conditions. Rather the filtering of the solution leads to a condition, which keeps the stream traces smooth but not parallel in the vicinity of the hard-lined transition. There are no experimental investigations of the impedance jump up to now, but it is assumed that the physical reality will be a partial Kutta condition with smooth stream traces. Therefore, the results obtained by using a full Kutta-condition are considered for the benchmark. The results are in a good agreement with the analytical solution. The application of a far-field method even improves the agreement. Angles up to 30 degrees are affected by the shear layer and show higher amplitudes in combination with blurred lobes for the current result. From 30 to 60 degrees the current result underpredicts the benchmark source by less than 5 dB. The resolved shear layer, which is replacing the modeled infinite thin one from the benchmark source in the current simulation, probably affect the solution under these angles, as well. The backward angles are found in a perfect agreement.

Altogether the results in this section further validate the implementation of the EHR model as well as the whole CAA method including the boundary conditions. The strategy of artificially thickening an infinite thin shear layer by low order filtering in order to handle a jet flow as base flow for the current perturbation approach is also verified by these results. The filtering of the mean flow still leaves the number

of filtering iterations and the order of the filter free to choice. A preliminary study of these parameters is provided in Buske et al. [21].

7.1.4. Investigations using the benchmark data from the NASA grazing flow impedance tube (GIT) experiment

In this section the configuration of the NASA GIT experiment will be presented and used for a further investigation of the EHR model. However, a comprehensive validation with the GIT benchmark data is provided in the following Section 7.2.1.

Specification of experiment and numerical method used

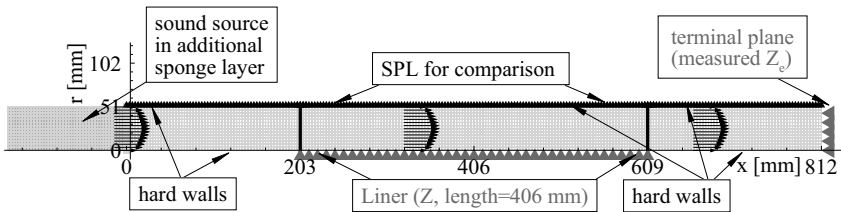


Figure 7.26.: Numerical model for the NASA-GIT [57] (height coordinate flipped with respect to the reference)

In a first step, the NASA GIT experiment is approximated by a two-dimensional model in the computation. Later a three-dimensional example will be provided. The numerical grid and the boundary conditions are summarized in Figure 7.26. The setup shown in Figure 7.26 is extended by a PML [Eq. (3.24)] downstream the terminal plane to obtain a reflection free outflow. Unlike the numerical model applied by Watson et al. [134] the sound source is also assumed non-reflective to upstream propagating waves, by using a sponge-layer in combination with the sound source [comp. Eq. (3.22)].

The computation domain is decomposed into three blocks. These blocks exchange all field data and each grid point is calculated in only one block. The model parameters of the EHR model are assumed to be constant along the one wall of the block in the middle. The other blocks have hard walls. There are very short waves present in the acoustic field in reaction to the impedance jumps at the block interfaces. As a side effect of the numerically motivated filtering, which has been described in Section 3.1.3 for the CAA scheme and in Section 4.5.2 for the liners auxiliary variables, the streamlines pass smoothly across the edges between the hard wall and the liner.

Assessment of the accuracy of the impedance representation

First the accuracy of the resulting frequency response of the impedance is assessed without flow. Furthermore, the flow effect on the effective impedance is studied with one example. The theoretical impedance function according to Eq. (4.11) is compared to the one, which is obtained from the CAA result. The model parameters for the EHR model are given as

$$R_f = 1. \times 10^{-6}; \quad \beta = 1.69; \quad \varepsilon = 0.69; \quad \frac{1}{m_f} = 479.3 \text{ s}^{-1}; \quad \frac{1}{T_l} = 2075 \text{ s}^{-1}.$$

The above impedance parameters are used in the following to prove the impedance model. The simple test calculates the effective impedance $Z' = \hat{p}/\hat{u}_2$ from pressure and velocity magnitude in several points on the liner. The time-resolved data is stored with the computation and the necessary Fourier transforms are implemented with MATLAB.

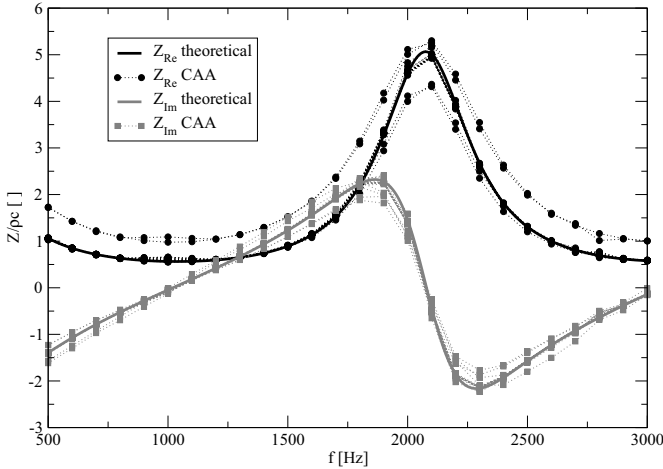


Figure 7.27.: Impedance calculated from the CAA result for the NASA-GIT setup

The 26 investigated frequencies reach from 500 Hz to 3 kHz in 100 Hz steps. 26 monitor points were placed along the lined wall in order to prove the impedance. The observed impedance should exactly match the theoretical impedance function according to Eq. (4.11) without flow. However, techniques like the filtering of the field and the filtering of the auxiliary variables of the EHR are required to stabilize the solution. The filtering adds an error in general. All results are plotted on top of each other in Fig. 7.27. As can be seen from the figure, the frequency response deviates for several points. The points closest to the hard-lined and lined-hard

transition show a larger resistance for frequencies around 1 kHz and 3 kHz. The observed resistance is more than twice as large as the specified value for some frequencies with small resistance. The second grid point from the impedance jump shows a smaller impedance around the anti-resonance. The value is 15 % smaller than the specified value for the largest resistance. Similar to this observation, the reactance does not meet the presetting and the largest deviations are observed for the four points, which are closest to the transitions. Besides these hard-lined and lined-hard transition effects, the calculated impedance function is in good agreement to the theoretical one for all other 22 points shown in Fig. 7.27. In general the implementation of the EHR is validated by this test. However, if the main attenuation effect of the liner is achieved by reflections at the hard-lined and lined-hard transitions, the current implementation may produce errors. These errors are grid dependent due to the grid dependent filtering.

Three-dimensional simulation of the NASA-GIT experiment

In this section the effect of a three-dimensional flow profile on the impedance is investigated. This provides an outlook on the capability of the EHR-based time-domain impedance boundary condition for three-dimensional simulations. Further examples for the application are found in Panek et al. [92].

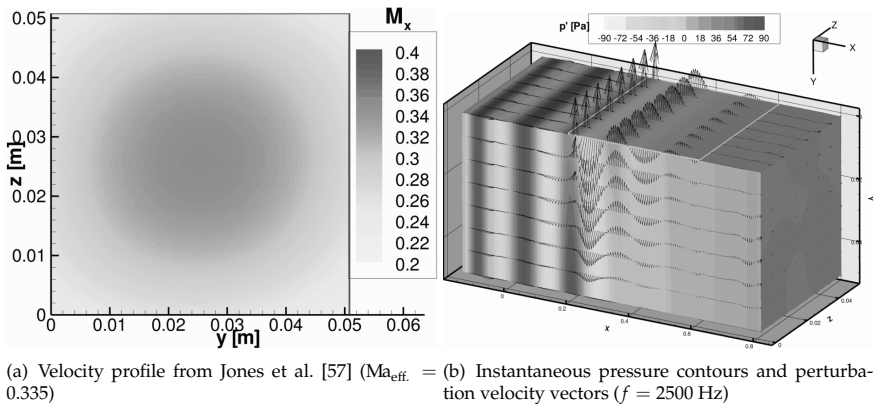


Figure 7.28.: Base flow and 3D CAA result for the NASA-GIT experiment.

An axial cut through the cross section of the channel with the three-dimensional flow profile, which is used for the 3D simulation is presented in 7.1.4. The three-dimensional base-flow profile has been measured by Jones et al. [57] with a Pitot probe, such that no data at the surface is available and a cubic extrapolation to the wall point had to be applied. The grid resolution of the equidistant orthogonal

mesh equals the resolution in the corresponding two-dimensional case. The CAA simulation uses only 15 grid points in height and depth of the duct each. Therefore, a fully resolved viscous sublayer cannot be applied for both, the two- and the three-dimensional simulation. The Ingard/Myers boundary condition is combined with the partial resolved boundary layer profile. The velocity at the surface is nonzero. An EHR fit to the measured termination impedance of Jones et al. [57] is used as boundary condition for the outflow of the computational domain.

The resulting instantaneous pressure contours in Fig. 7.28(b) qualitatively show the function of the stabilization approach by low-order filtering with a partly resolved shear layer in 3D. For a further investigation the three-dimensional geometry is excited by the same multi-frequency source as the two-dimensional case. Comparing the simulation times, the three-dimensional case takes 9.2 hours for 30 000 iterations or $16 \mu\text{s}$ per node and iteration, whereas a two-dimensional simulation takes 53 minutes for the same number of iterations, which means $24 \mu\text{s}$ per node and iteration. The resulting sound pressure level at the hard wall opposite to the

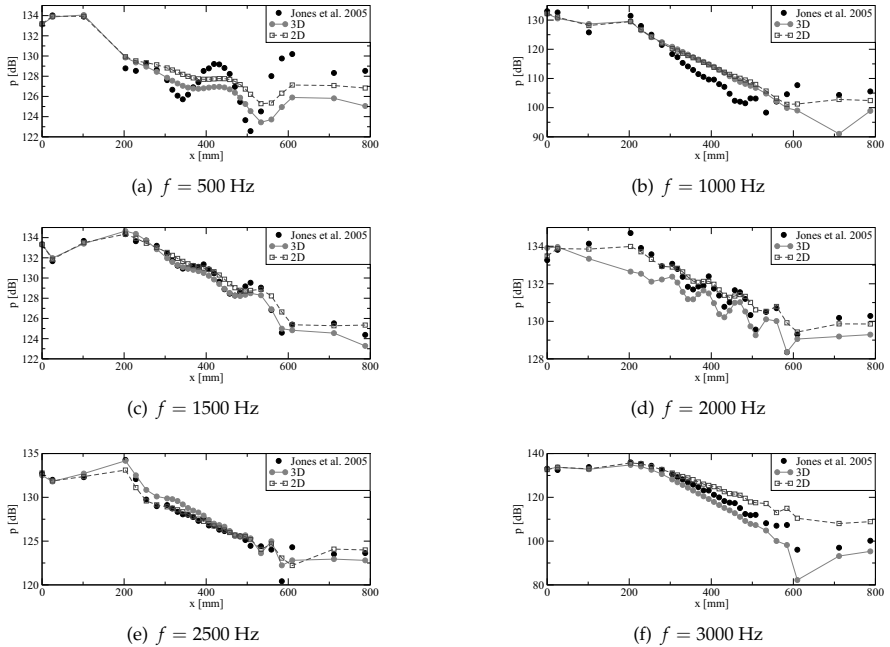


Figure 7.29.: Comparison of the three- and two-dimensional simulations for the NASA-GIT experiment

liner is detailed for selected frequencies in Fig. 7.29 in comparison to the analytical solution. The three-dimensional result is obtained at the centerline of the hard wall. As can be seen from the figures, there is a small difference between two- and three-dimensional simulation for most of the cases. Only $f = 500$ Hz and $f = 3000$ Hz show larger deviations. In general the three-dimensional simulation seems to show more pronounced oscillations along x . They are similar to oscillations found in the experiment.

From the relatively good agreement of three- and two-dimensional simulation can be concluded that the EHR model works well for both cases. The stabilization by low-order filtering is verified with this comparison as well. Furthermore, the differences show that the three-dimensional channel flow has an essential influence on the resulting sound field. The computational times for three-dimensional simulations do not allow an impedance eduction, yet. This could, however, be achieved in the near future by porting of the CAA software to a more efficient processor e. g. a graphics processing unit to reduce the turn around time.

7.1.5. Conclusions to the validation and code benchmark

The correct reproduction of the analytical solutions for annular ducts, as well as the good agreement of the current result for the large number of test cases from the literature, prove the correct implementation of the EHR-based time-domain impedance boundary condition. The majority of the examples considers two-dimensional or modal-axisymmetric mathematical models. However, one three-dimensional simulation verifies the applicability of EHR model in 3D.

The examples at the same time prove the suppression of the flow instability, which appears with the application of the Ingard/Myers boundary condition for a nonzero base flow. A low-order filter is applied. The effect of this engineering approach is investigated in detail with realistic test cases. The impact found to be very small in the case of a fully lined generic inlet duct. However, when considering hard-lined and lined-hard transitions, larger differences are observed for points in the vicinity of the transitions. As has been shown above from a literature review, the instability of the Myers boundary condition depends on many parameters. The current investigation can never cover all of them. Thus, even though the actual examples demonstrate the stability of the filtered Myers boundary condition, the approach may fail for other impedance functions, flow conditions or mesh sizes. Furthermore, the prediction of the conditions, under which the flow instability of the Kelvin-Helmholtz type occurs in reality, is probably not possible. An alternative is found in the application of a resolved boundary layer of the base flow. This has been shown, to essentially influence the resulting acoustic field in several cases. A resolved thick shear layer at the impedance surface is found to provide significantly other results than the Myers boundary condition. The three-dimensionality of the boundary layer profiles in a channel with square cross section is found to influence the acoustic field as well.

Among the limitations of the current CAA method, which have been exposed by

the thorough validation and verification, are a small leakage to higher modes for the modal-axisymmetric approach and remaining reflections from the source boundary for some of the cases. The impact of the observed errors on the acoustic solution is small, but their presence should alert from applying a CAA method without a prove of the solution. Another important question concerns the correct modeling of the transitions between hard wall and liner panel and vice versa. Analytical solutions apply a so called full Kutta condition [28]. Such a condition is not directly prescribed for the CAA simulation. However, the high-order filtering of the solution leads to a similar condition, provided that the grid resolution is well adjusted.

The maximum CFL-number is found to be proportional to the parameter m_f of the EHR model. Therefore, the time-step size had to be reduced far below the theoretical limit, which is obtained with the current numerical schemes for the LEE, in some of the cases. With a reduced time-step size, a more frequent filtering leads to increased dissipation observed in the solution. However, this could be avoided by reducing the filtering frequency.

7.2. Impedance eduction

In this section, the impedance eduction of Chapter 6 is applied with data from *in-situ* measurements as input. The resulting impedance is compared to published impedance data. A further validation of the result is provided by comparing the known geometrical parameters of the liner sample, to the ones calculated from the impedance-eduction result. Therefor the relations of Section 4.3.4 are applied. Four different samples are considered, of which one is axisymmetric and the other three are plane samples which are mounted to one side of the test section with quadratic cross section. Complex pressure amplitudes from the NASA-GIT experiment [57] are considered as input in Section 7.2.1. The influence of the base-flow profile and the imperfect anechoic termination in the experiment on the eduction result is studied. Then, energy dissipation, transmission and reflection coefficients from the DLR flow impedance test rig [22] are considered as input for the impedance eduction for two different plane liner sample in Section 7.2.2. Finally, the effect of a bias flow on the impedance of a large axisymmetric resonator is studied in Section 7.2.3 before general conclusions to the impedance eduction are drawn in Section 7.2.4

7.2.1. NASA impedance flow tube experiment

The impedance eduction in this section uses the published NASA-GIT data for a ceramic tubular liner sample as input (see Jones et al. [57]). The liner consists of densely-packed narrow ceramic tubes with a diameter of 0.6 mm and a length of 85.6 mm according to Jones et al. [57]. The surface porosity is given by Jones et al. [57] as $\sigma = 57\%$. Additional data with an increased frequency resolution of 100 Hz has been provided by Jones in a private communication [58]. The deviation of the numerical result from the measured SPL and phase

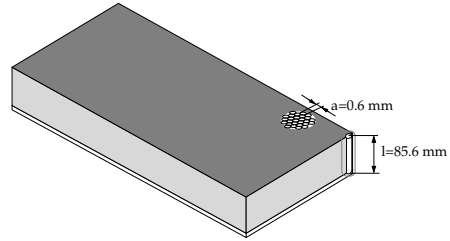


Figure 7.30.: Sketch of the ceramic tubular liner.

is used to define the objective function for the impedance eduction as described in Chapter 6. The resulting impedance function is compared to the eduction results of Jones et al. [57]. The discrepancy of the impedance is considered as a benchmark for the time-domain impedance eduction using the EHR model. In a preliminary investigation [105] the EHR was found to be not able to sufficiently reproduce the frequency response of the given impedance by a direct fit of the function in the frequency domain. Thus, the capability of the EHR as broadband impedance model will be tested by the impedance eduction as well.

In the following, three different set-ups will be considered for the broadband impedance eduction with input data sets for five different flow Mach numbers provided by Jones et al. [57, 58]. First the impedance eduction is carried out neglecting the boundary layers in the duct and assuming perfectly anechoic terminations. Then, the EHR is used to fit the measured termination impedance and the result is applied using an uniform flow and a partial resolved measured flow profile, respectively.

Numerical setup for the impedance eduction

As in the experiment, only the downstream propagation of acoustic waves parallel to the flow direction is considered. The mesh resolution in height direction is 30 points. Overall the mesh consists of 15 345 points. The radiation boundary condition of Section 3.5.1 is used as anechoic termination of the computational domain and at the same time implements the sound source. The parameters are limited for the eduction process, such that the CFL-number can be chosen to 0.3. The turn-around time of one function call, which means one CAA simulation with the impedance varied, is about 25 minutes for 15 000 time steps. This is required to obtain a non-transient solution of 0.01 s length. This corresponds to an exact multiple of the smallest common period time of the multi-frequency excitation signal and allows

a direct extraction of the excitation frequencies from the Fourier-transformed data. The whole optimization takes up to 41 steps with over 250 function calls in the most cases. This results in a computational time of approximately four days for each flow Mach number.

Uniform flow and anechoic terminations

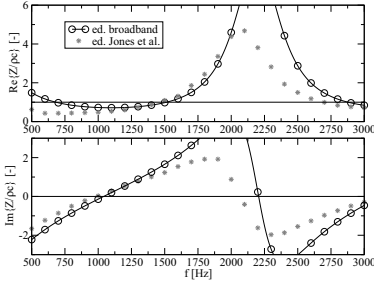
First the impedance eduction is carried out using an uniform flow in the duct. The termination is assumed to be fully anechoic using the radiation/outflow boundary condition of Section 3.5.1. Fig. 7.31 summarizes the resulting impedance functions for all published flow velocities. The Mach number given below corresponds to the effective Mach number from the experiment, which is used to specify the uniform flow profile. The impedance eduction results of Jones et al. [57] are plotted for comparison. All Mach numbers show relatively large differences in the frequency range around 2100 Hz. This corresponds to the anti-resonance of the ceramic tubular liner. When comparing the resulting sound pressure level and phase to the experiment by the figures given in the Appendix D.1.1, relatively large differences are observed for several frequencies for the phase as well as for the sound pressure level.

Table 7.5.: Model parameters of the EHR for a plug flow profile and fully anechoic terminations.

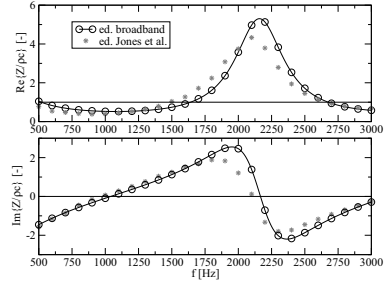
Ma [-]	$1/T_l$ [s^{-1}]	R_f [-]	$1/m_f$ [-]	β [-]	ε [-]	l [mm]	L [mm]
0	2195.9	$1. \times 10^{-6}$	106.1	2.442	0.6008	77.4	41.3
0.079	2158.6	$1. \times 10^{-6}$	226.8	1.661	0.6481	78.8	27.4
0.172	2092.2	$1. \times 10^{-6}$	883.9	1.898	0.5806	81.1	29.9
0.255	2100.9	$1. \times 10^{-6}$	482.2	1.681	0.6164	81.0	27.0
0.335	2084.4	$1. \times 10^{-6}$	1999.	1.672	0.5919	81.6	26.2

The five parameters of the EHR are shown in Tab. 7.5 for each flow Mach number. The parameter R_f is found to be very small in all cases. R_f correctly describes the negligible face sheet resistance of the faceless tubular liner. In fact $1. \times 10^{-6}$ is the lower limit set for the constraint optimization of this parameter. The cavity damping parameter ε is found to be relatively large, ranging from 0.58 to 0.65 with a variation of ± 5 % between the different flow Mach numbers. The resonance frequency is approximately identified as $f_0 \approx 0.5 T_l^{-1}$. It is found to be between 1042 Hz and 1098 Hz for the different flow velocities. The case without flow is out of range with respect to β . This leads to the large impedance peak shown in Fig. 7.31 (a) in the anti-resonance. Furthermore, m_f shows a relatively large variation with the flow velocity.

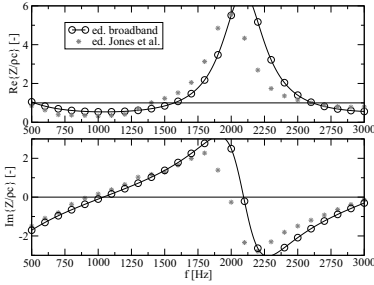
The physical interpretation of the model parameters allows more insight. The liner panel consists of multiple $\lambda/4$ -resonators. As can be seen from Tab. 4.1, the



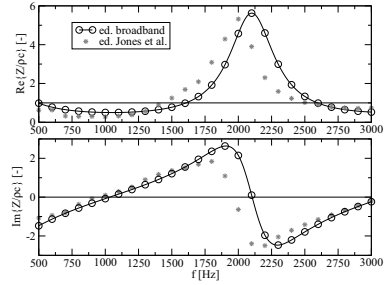
(a) $Ma = 0$



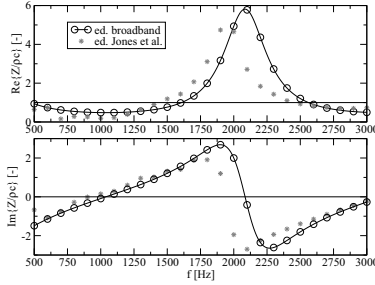
(b) $Ma = 0.079$



(c) $Ma = 0.172$



(d) $Ma = 0.255$



(e) $Ma = 0.335$

Figure 7.31.: Educued impedance with plug flow assumption and fully anechoic terminations in comparison to the result of Jones et al. [57].

frequency response of the impedance of a $\lambda/4$ -resonator with rigid thin pipes is described by a cotangent function. Comparing Eqs. (4.8) and (4.11), the time delay $2T_l$ of the EHR is identified with the $l = \lambda/4$ resonance $2T_l = l/(2c)$. In this way,

the cavity depth can be calculated from T_l as

$$l = \frac{1}{2} T_l c.$$

The educed cavity depth is shown in Tab. 7.5. The educed cavity depth ($l = 0.077 \dots 0.082$ m), seems to be consequently smaller than the real depth of the ceramic tubular liner, which is 0.0856 m according to Jones et al. [57]. The cavity damping is not modeled and therefore not present in the impedance model of the $\lambda/4$ -resonator, Eq. (4.8). However the results indicate, that there is a significant cavity damping which is described by the parameter ε . This is due to viscous effects inside the narrow cavities according to Jones et al. [57]. Different from the oversimplified model of Eq. (4.8), the current impedance eduction results in a nonzero face sheet reactance m_f . The parameter is used for the coupling of the model and could not be zero. A constraint is used in the optimization to ensure this. However, the limit for this parameter is not touched by the eduction result.

Comparing the mass-like terms of the mechanical analog, the $\lambda/4$ -resonator and the EHR shown in Tab. 4.1 for low frequencies one obtains

$$\frac{L}{\sigma} = \frac{1}{3} l = m_f + \frac{1}{6} c \beta T_l.$$

This means, that the relation of the effective neck length and the open area for the current liner, L/σ , should be a third of the cavity depth l on one hand and is connected to the m_f , β and T_l on the other hand. This is used to calculate the effective neck length from the impedance eduction result and the open area ratio. The educed corrected neck length L is given in Tab. 7.5. The result of $\text{Ma} = 0$ is not in line with the others; for all other cases it is in the expected range of $l/3 = 28.5$ mm.

Altogether, the impedance eduction in this section can be considered successful. However, the resulting impedance functions show relatively large deviations from the result of Jones et al. [57]. The same applies for comparison of the SPL and phase data between the eduction result and the published data by Jones et al. [57] which is shown in the Appendix D.1.1. Moreover, the educed geometry of the $\lambda/4$ tubes is in range of the real geometry, but systematically underpredicts the real cavity depth.

Modeling of the measured termination impedance

In the following the measured termination impedance of the NASA flow tube experiment is considered for the impedance eduction. The EHR model is directly fitted to the measured frequency response of the termination impedance. The results visualized in Fig. 7.32 and the model parameters are given in Tab. 7.6.

The given impedance from the experiment indicates a relatively good anechoic termination, with a real part of the impedance around unity and small imaginary parts. The magnitude of the pressure reflection factor, according to Ehrenfried [31], is calculated from the measured impedance. It remains below 10 % without flow and reaches up to 15 % for the higher flow speeds. The EHR model slightly overshoots

the reflection factor for the lower flow velocities. For the high flow speeds the fit of the termination impedance is improved. The Ingard/Myers boundary condition is not applied for the termination.

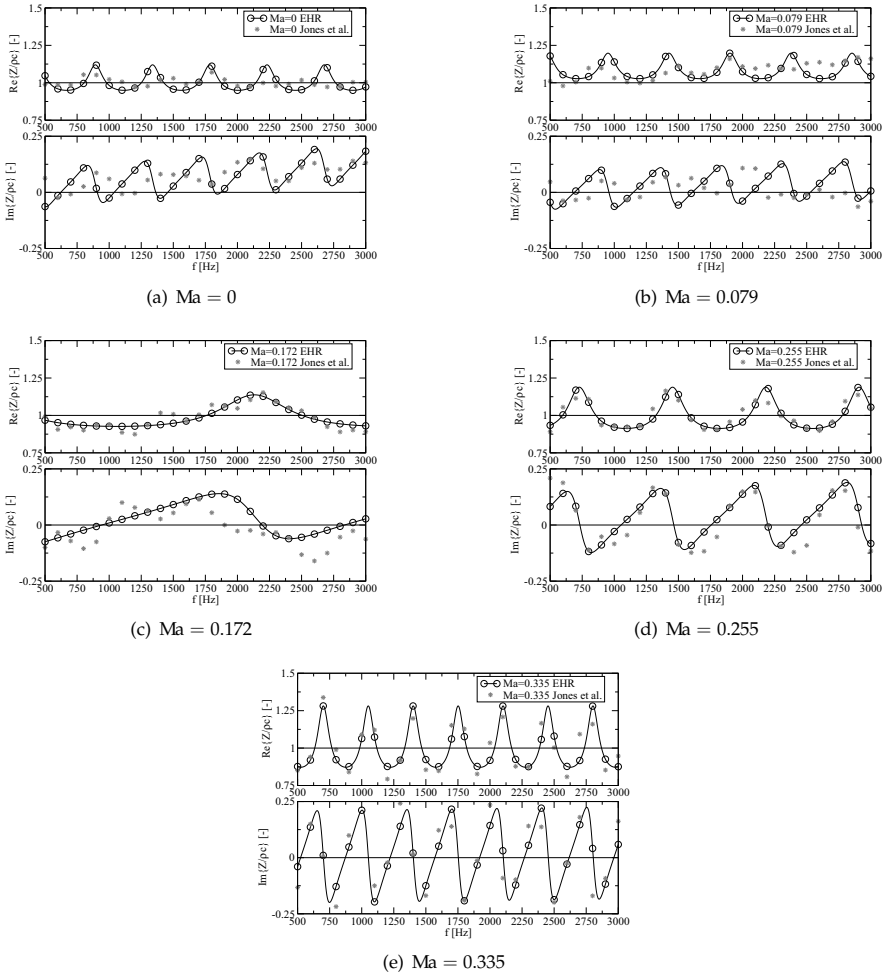


Figure 7.32.: Frequency response of the termination impedance. Fit by the EHR-model in comparison to the original data provided by Jones et al. [57].

Table 7.6.: Impedance model parameters for the termination impedance.

Ma [-]	$1/T_l$ [s ⁻¹]	R_f [-]	$1/m_f$ [-]	β [-]	ε [-]
0	446.1	0.903	235.1	0.100	0.636
0.079	475.6	0.981	1000.	0.100	1.000
0.172	2131.	0.874	1000.	0.118	0.965
0.255	727.2	0.850	1000.	0.145	0.918
0.335	346.8	0.732	2000.	0.268	1.000

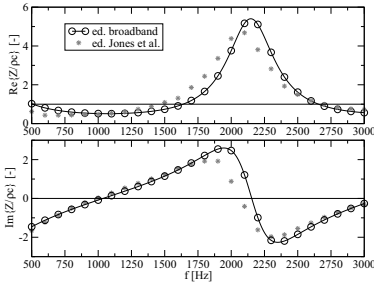
Uniform flow and measured termination impedance

In a first step, the termination impedance is applied together with a plug-flow assumption for the base flow. The results provide an insight to the effect of the termination impedance on the educed liner impedance. For more clarity of the presentation the resulting SPL and phase plots are given in the Appendix D.1.2. With the termination impedance, reflections become an essential part of the solution in particular around the anti-resonance showing only small attenuation of acoustic energy by the liner. Therefore, the agreement to the experimental data is improved particularly in this range of frequencies. Moreover, the peak level of the impedance function is decreased and becomes similar to the published eduction result of Jones et al. [57] in the frequency domain with the application of a termination impedance. However, the frequency of the phase shift between positive and negative imaginary part of the impedance is slightly increased with respect to the published data of Jones et al. [57]. The resonance frequency is also found to be increased in the current simulation.

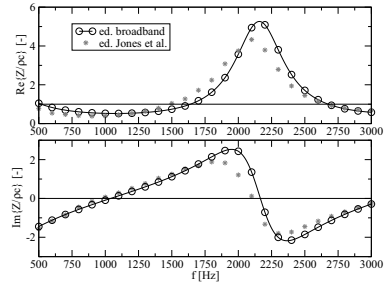
Table 7.7.: Model parameters of the EHR for a plug-flow profile with the measured termination impedance.

Ma [-]	$1/T_l$ [s ⁻¹]	R_f [-]	$1/m_f$ [-]	β [-]	ε [-]	l [mm]	L [mm]
0	2147.1	1×10^{-6}	235.1	1.661	0.6355	79.2	27.4
0.079	2157.9	1×10^{-6}	229.8	1.656	0.6516	78.8	27.3
0.172	2147.1	1×10^{-6}	194.4	1.691	0.6613	79.2	28.4
0.255	2210.2	1×10^{-6}	113.8	1.569	0.6495	76.9	27.9
0.335	2096.1	1×10^{-6}	970.6	1.676	0.6871	81.1	26.4

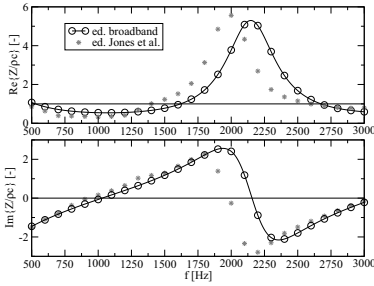
The educed EHR model parameters show only small variations with the flow velocity as can be seen in Tab. 7.7. The only exception is found in $Ma = 0.335$, where T_l and m_f are reduced. The educed effective depth of the cavity underpredicts than the real cavity depth, when considering the speed of sound in cold air as reference. This reduced length corresponds to an increased resonance frequency. However, it



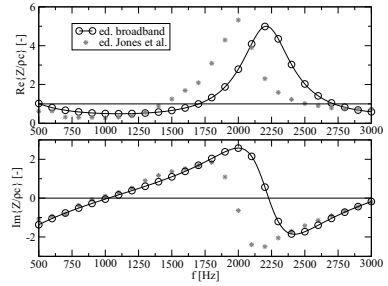
(a) $Ma = 0$



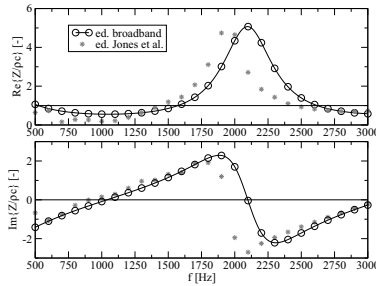
(b) $Ma = 0.079$



(c) $Ma = 0.172$



(d) $Ma = 0.255$



(e) $Ma = 0.335$

Figure 7.33.: Educued impedance with plug-flow assumption and EHR fit to the measured termination impedance in comparison to the result of Jones et al. [57].

could also be due to a higher speed of sound inside the cavity. The active length is calculated based on a speed of sound of $c = 340$ m/s in the cavity. However, due

to the large cavity damping, the temperature inside the ceramic tubes may increase. Assuming a temperature of $T = 323$ K, the speed of sound increases to $c = 360$ m/s, which would lead to the increase of the resonance frequency of the ceramic tubes to $f_0 = 1.05$ kHz, as it is observed in the current impedance eduction. The educed corrected neck length is found to be in the range of $l/3$. The variation of the educed cavity depth and corrected neck length with the grazing flow velocity is relatively small.

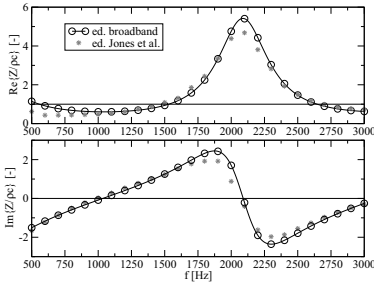
Measured flow profile and termination impedance

Finally, in this section the EHR fit of the measured termination impedance is considered together with the measured flow profile. The flow profile given by Jones et al. [57] is approximated by a cubic polynomial to provide the base-flow profile on the mesh of the acoustic simulation. Interpolation as well as extrapolation to the wall points are necessary. The velocity at the wall is nonzero. The filtered Ingard/Myers boundary condition is applied to model the flow effects. Only velocity data is available from the experiment. As the pressure and density have not been measured, an uniform density and pressure distribution is assumed for the base-flow field. The frequency response of the educed impedance is compared to the result of Jones et al. [57] in Fig. 7.34. Due to the partial boundary layer profiles, the agreement with Jones' impedance data is further improved in comparison to the preceding sections. The same applies for the resulting sound pressure level along the opposite wall, as can be seen from the series of figures given in the Appendix D.1.3.

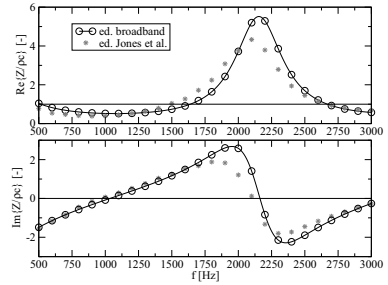
The $Ma = 0$ case has been considered again to prove the convergence of the method. The result in this section differs from the one of the preceding section. The resonance frequency is shifted. The figures given in the Appendix D.1.2 and D.1.3 show, that both impedances provide a good agreement for different frequencies, whereas others are not so well met. Thus, it is supposed that multiple local optima of the impedance function are present for this case. When comparing the impedance function, the small differences mainly concern the location of the anti-resonance, such that the impedance eduction can be considered successful, anyway.

Table 7.8.: Model parameters educed with the EHR for a realistic flow profile with termination impedance.

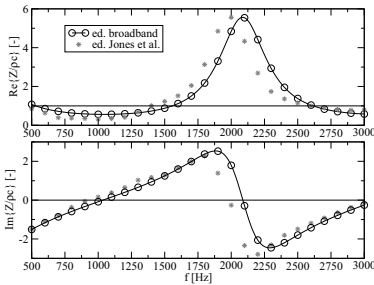
Ma [-]	$1/T_l$ [s ⁻¹]	R_f [-]	$1/m_f$ [-]	β [-]	ε [-]	l [mm]	L [mm]
0	2088.0	0.000279	836.6	1.805	0.6931	81.4	28.6
0.079	2154.5	$1. \times 10^{-6}$	203.9	1.688	0.6321	78.9	28.1
0.172	2086.1	$1. \times 10^{-6}$	999.0	1.767	0.6582	81.5	27.9
0.255	2093.5	$1. \times 10^{-6}$	999.0	1.699	0.6094	81.2	26.8
0.335	2130.7	$1. \times 10^{-6}$	281.5	1.747	0.6931	79.8	28.5



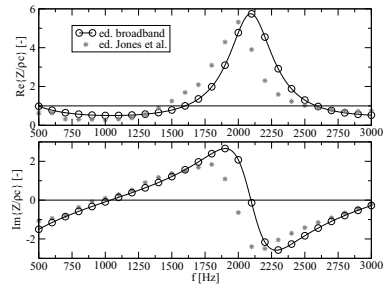
(a) $Ma = 0$



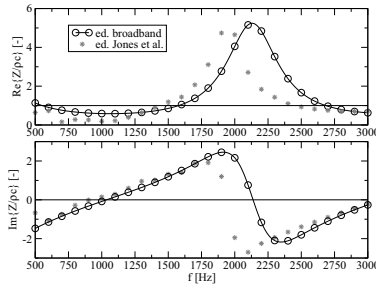
(b) $Ma = 0.079$



(c) $Ma = 0.172$



(d) $Ma = 0.255$



(e) $Ma = 0.335$

Figure 7.34.: Educued impedance with a partial boundary layer profile and an EHR fit to the measured termination impedance in comparison to the result of Jones et al. [57].

Finally, the educued model parameters for this case are summarized in Tab. 7.8. Two remarkable changes are observed. One is the face sheet mass reactance, which

is decreased for most of the cases with respect to the result of the preceding sections. The other is an increase of the parameter β , which controls the cotangent component of the impedance. The corresponding effective neck length and active cavity depth are found in the correct range again. The observed variations with the flow velocity are small. However, the educed cavity depth is systematically smaller than the real cavity depth, when assuming the ambient speed of sound.

Summary of the study with the NASA-GIT data

The general methodology for the impedance eduction, which has been developed in the current work, is similar to the one, described by Watson et al. [134] for the data of Jones et al. [57]. However, one major difference is obvious. The current CAA method operates in the time-domain, whereas the published impedance data is based on an eduction for each single frequency. The impedance eduction in the time-domain allows to simultaneously find the impedance for multiple frequencies. Therefore the five parameter EHR model is applied as template for the frequency response of the impedance. This has the advantage that the number of parameters in the optimization does not increase with the number of frequencies in the experiment, as it would be the case for the frequency domain method of Watson et al. [134].

The number of parameters is essential for the number of function calls, respective runs of the CAA method for a converged optimization. A side effect of the impedance model is the connection of the data over the whole frequency range. As this connection is based on the physical representation of the liner as Helmholtz resonator array, the resulting impedance function corresponds to this physical model. The effect of the connection is twofold. It may help to provide a valid impedance for frequencies, where the objective function shows a plateau and the frequency domain method could find multiple local optima, on one hand; on the other hand, the connection of all frequencies may produce additional local optima for the current method. The frequency response of the impedance function is forced by the EHR model, even if the liner cannot be described as an array of equal Helmholtz resonators.

However, the small deviation of the resulting SPL and phase data of the pressure from the experiment, validates the current impedance eduction results. The resulting impedance is in a reasonable agreement to the result of Jones et al. [57]. The observed differences mainly concern the range around the anti-resonance. The results also show that the EHR model is applicable to describe the ceramic tubular liner over the whole range of frequencies by one set of parameters. Moreover, the educed effective geometry of the liner is in a reasonable agreement to the real measures. The application of the measured termination impedance improves the agreement with the published data. All at all, the results validate the implementation of the EHR model.

7.2.2. Plane liner samples at the DLR flow impedance test facility

In this section two plane liner panels are investigated. They are sketched in Fig. 7.35. The measurements have been carried out in the DLR flow impedance tube test rig [22]. Additional measurements of the manufacturer of the samples, AleniaAermacchi S.p.A., are provided as impedance data from measurements with Kundts tube and *in-situ* measurements in the NLR flow impedance tube [22]. The different test facilities are described in Section 1.3. The available benchmark data is not directly comparable to the current results. The measurement with Kundts tube and the NLR flow tube uses an excitation level of 130 dB, whereas for the DLR flow tube measurements the excitation level is between 110 and 120 dB [22]. Furthermore, the impedance data from the NLR flow tube uses a higher flow speed.

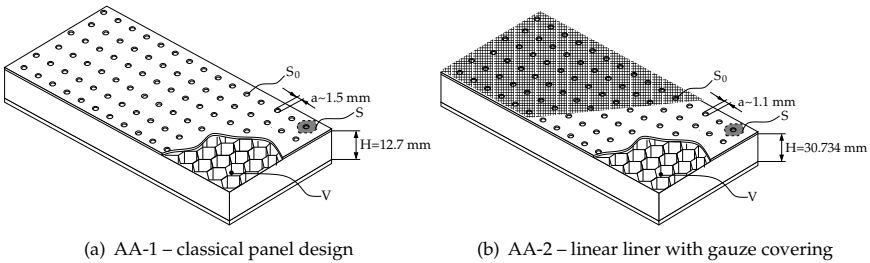


Figure 7.35.: A sketch of samples AA-1 and AA-2

The DLR test setup features a $80 \text{ mm} \times 80 \text{ mm}$ test section of 220 mm length, in which a liner can be mounted to replace the lower wall. The general topology is similar to the NASA-GIT experiment shown in Fig. 7.26. However, anechoic terminations are used for both duct ends in the DLR flow tube. Both liner samples fully fit into the test section and are sealed. Flush mounted microphones are positioned at the centerline of the upper wall in the up- and downstream duct sections. The microphone data is processed in order to calculate energy reflection and transmission coefficients according to Busse et al. [22].

The numerical set-up for the impedance eduction with both samples uses a mesh of 1375 points with a mesh spacing of 8 mm. The data collection in the simulation is reduced to four out of five positions up- and downstream of the sample each. The CFL number is 0.15 to allow relatively small m_f in the optimization process. The non-reflective boundary conditions are implemented via the radiation/outflow boundary condition of Section 3.5.1 and the simplified method of Section 6.2.2 is applied to calculate energy transmission and reflection. 35 000 time steps are calculated in total to obtain a non-transient time series of 0.1 s which takes 3 minutes in real time on one core of a dual core AMD Opteron 244 processor.

Results for a perforate single degree of freedom (SDOF) liner (AA-1)

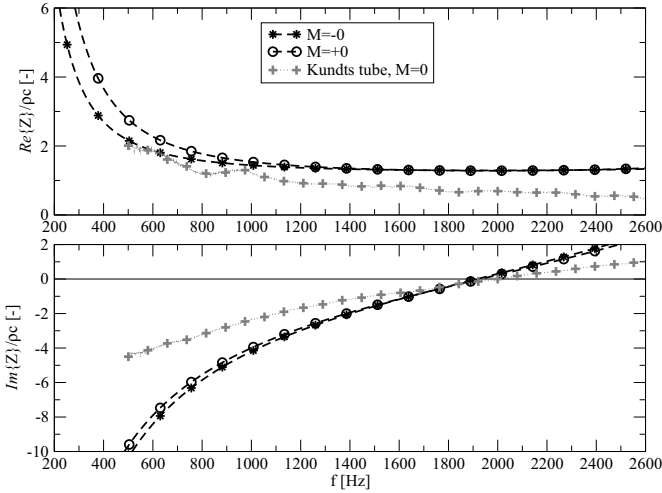


Figure 7.36.: Frequency response of the educed impedance in comparison to Kundts tube measurements of AleniaAermacchi S.p.A. [22] for AA-1.

The data processing from the experiment provides two different sets for the propagation of sound waves over the liner without flow. As only the the end of the duct used for the excitation is switched, the results should be equal for these cases. However, the test setup is not fully symmetric due to slightly different anechoic termination devices on both ends and the connected air supply from the compressor on one side. In fact, comparing the input data of the two cases found in Appendix D.2.1 only small differences are observed. The two different data sets of energy transmission and reflection are considered as input for the impedance eduction. The resulting impedance functions are plotted in Fig. 7.36. It should be noted that the experimental data from the DLR flow tube covers only frequencies between 210 Hz and 2110 Hz, since the current data processing is limited to plane waves in the experiment. The extended frequency range in the plot is obtained by evaluating Eq. (4.11) with the resulting model parameters from the impedance eduction. As can be seen from the figure, the impedance functions differ only for the low-frequency range. In this range the largest deviation between the two sets of input data is found, comparing the figures in Appendix D.2.1. Therefore, the current eduction result can be seen as resulting impedance error due to the different input.

For comparison the Kundts tube measurements of AleniaAermacchi S.p.A. are shown in Fig. 7.36. The current impedance eduction shows significant deviations from the Kundts tube measurements for AA-1. The real part of the impedance al-

most steadily decreases with the frequency for the Kundts tube measurements. This decrease continues beyond the resonance frequency which is marked by the zero crossing of the imaginary part. On the other hand, real and imaginary part of the impedance are coupled through the cotangent function in the EHR. Therefore, such a regime is not possible with the EHR model. The gradient of the imaginary part of the impedance is lower in the Kundts tube measurements than it is found with the current impedance education. Furthermore, the resonance frequency is found to be approximately 100 Hz lower for the current result.

Comparing the energy dissipation, transmission and reflection coefficients shown in the Appendix D.2.1 a good agreement is found. A significant deviation from the experimental data can only be observed for frequencies above 1700 Hz. The current impedance education is not able to reproduce the attenuation peak and the following drop for $Ma = 0$ in this case. The resonance frequency falls into this range, such that the prediction could be affected by the deviation.

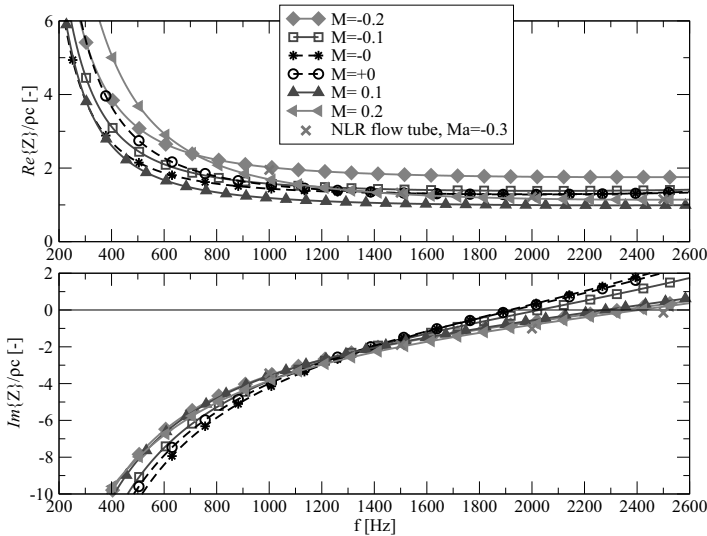


Figure 7.37.: Educued impedance comparison between the current result and NLR flow tube measurements of AleniaAermacchi S.p.A. [22, 117] for sample AA-1.

The results of the impedance education with sample AA-1 are summarized for all investigated flow Mach numbers in Fig. 7.37. The resonance frequency ranges from 1800 Hz to 2300 Hz for the results. For higher frequencies, the real part of the impedance increases for upstream sound propagation and decreases for downstream propagation. The low frequency range below 1 kHz shows indifferent effects. How-

Table 7.9.: EHR model parameters with plug flow profile for sample AA-1.

Ma [-]	$1/T_l$ [s ⁻¹]	R_f [-]	$1/m_f$ [-]	β [-]	ε [-]	L [mm]	H [mm]
-0.2	4769.4	1.590	499.0	2.804	0.116	1.52	12.73
-0.1	4139.4	1.205	306.4	3.73	0.0942	2.34	11.02
-0.0	3964.6	1.137	152.9	4.394	0.0701	2.98	9.76
+0.0	3964.8	1.016	209.0	4.177	0.128	2.77	10.28
+0.1	4647.3	0.860	460.4	2.925	0.0878	1.63	12.52
+0.2	4913.3	0.823	478.6	2.982	0.213	1.57	11.66

ever, the variations are in the same range as the difference between the two $Ma = 0$ cases and do not raise from the estimated error level of the processing chain. The flow effect on the imaginary part of the impedance is a decrease of the slope for all flow directions.

Impedance eduction results from NLR flow tube measurements of AleniaAermacchi S.p.A. are given in Fig. 7.37 for comparison. There are only few points of measurement, as the original frequency range of the NLR flow tube measurement is much larger than for the currently reported DLR experiment and the frequency resolution is relatively low. $Ma = \pm 0.3$ could not yet be achieved in the DLR experiment such that $Ma = -0.2$ is the case next to the NLR data; the green crosses (NLR, $Ma = -0.3$) are compared to the diamonds $Ma = -0.2$ now. With this comparison the differences observed with the NLR impedance data is similar to the observation with the Kundts tube measurements above. The real part shows a decay to higher frequencies for the NLR experiment. Furthermore, the real part is higher for the current eduction result than for the NLR experiment for all frequencies. The imaginary part shows a smaller slope for the few data points from the NLR measurement. This smaller slope could, however, be due to the difference in the flow velocity.

The educed five parameters of the EHR model are now used to calculate the corresponding geometrical parameters of the Helmholtz resonator panel. The Eqs. (4.14) are used to obtain the ratio of corrected neck length and open area ratio L/σ as well as the ratio of cavity volume and surface area S/V of one cell. From the first L , which corresponds to the thickness of the face sheet plus an additional length correction is obtained using $\sigma = 4.3\%$, as given by Busse et al. [22]. The thickness of the facing material is 1 mm. The ratio of surface area and prismatic volume corresponds to the inverse of the cell depth, which is $H = 12.7$ mm for AA-1. The educed EHR model parameters and the corresponding neck length and cavity height are given in Tab. 7.9. This quantity is also given in Tab. 7.9. The base flow has a strong influence on the educed effective neck length. It is reduced with the flow speed. The educed cavity depth also shows relatively large variations. The resulting cavity depth from the impedance eduction is up to 23 % smaller than the real depth. However, in general the geometrical parameters are in the correct range. The connection of the geometry and the EHR validates the current result. Furthermore, in this case the physical interpretation of the model parameters of the EHR model is validated by the corresponding geometry parameters.

Results for the SDOF liner with gauze covering (AA-2)

The comparison between Kundts tube measurements of AleniaAermacchi S.p.A. and the impedance eduction result without flow for the SDOF liner sample with gauze covering (AA-2) is given in Fig. 7.38. The comparison of energy coefficients has been put into Appendix D.2.2. As can be seen from Fig. 7.38, the agreement between the current impedance eduction and the Kundts tube measurements is much better than for AA-1. The real part of the impedance is in perfect agreement. The imaginary part has a lower gradient for the Kundts tube measurements. Moreover,

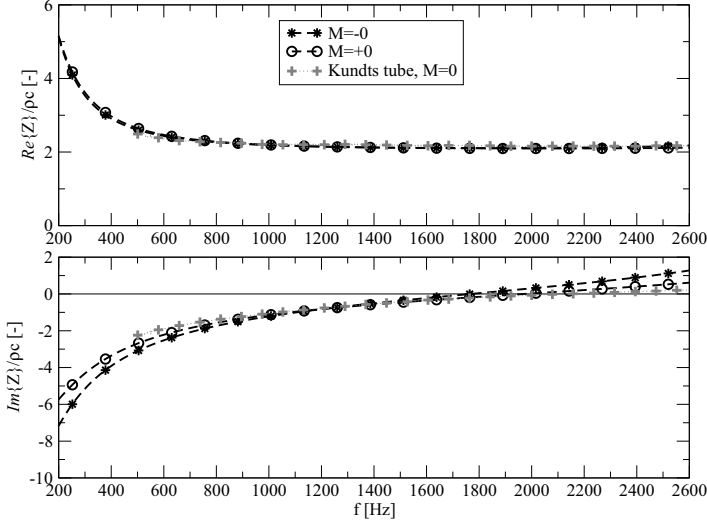


Figure 7.38.: Frequency response of the educed impedance in comparison to the Kundts tube measurements of AleniaAermacchi S.p.A. [22] for sample AA-2.

the different propagation directions show a small deviation without flow. This deviation is mainly observed in the imaginary part.

The influence of the base flow on the impedance of sample AA-2 is studied in Fig. 7.39. The impedance functions are almost on top of each other for the real part. The imaginary part shows a split into two different results for up- and downstream propagation, with a very small deviation of the corresponding two results varying the flow speed for each direction. As the test setup is not fully symmetric with respect to the up- and downstream propagation, the deviation is assumed to be a consequence of a small error in the input data (comp. Appendix D.2.2). Altogether AA-2 shows almost no influence of the base flow on the impedance.

The result of the impedance eduction is further investigated by the corresponding educed liner geometry. Sample AA-2 has a cavity depth of $H = 30.734$ mm and a, due to the gauze covering, not measurable open area ratio according to Busse et al. [22]. Therefore, the open area ratio is assumed to be equal to the one of AA-1 ($\sigma = 4.3$ %). The educed model parameters of the EHR model, as well as the related educed geometrical parameters are given in Tab. 7.10. Similar to the EHR model parameters, the geometrical parameters show only small variations. The only exception is found in $Ma = +0$, where the resonance frequency differs from the other results and the geometry parameters are also found to be different. The other

Table 7.10.: EHR model parameters educed with plug flow profile for sample A-A-2.

Ma [-]	$1/T_l$ [s ⁻¹]	R_f [-]	$1/m_f$ [-]	β [-]	ε [-]	L [mm]	H [mm]
-0.1	3616.5	2.0	583.7	1.460	0.165	1.07	31.78
-0.0	3629.9	2.0	541.5	1.483	0.147	1.07	31.65
+0.0	4059.2	2.0	686.6	1.157	0.167	0.76	36.30
+0.1	3639.9	2.0	541.5	1.483	0.147	1.07	31.56

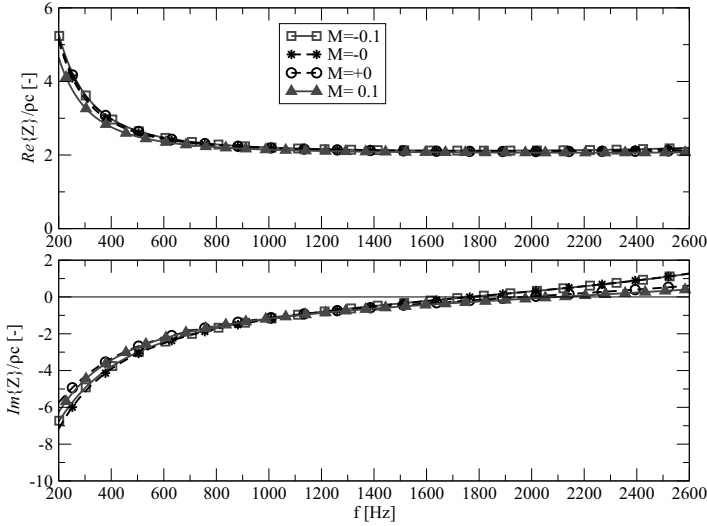


Figure 7.39.: Frequency response of the educed impedance for different Mach numbers for AA-2.

cases show a good agreement of the geometry parameters with each other and are very close to the real geometry with $H = 30.73$ mm according to Busse et al. [22].

Comparison of the results

When comparing the impedance eduction results without flow and the Kundts tube measurements, relatively large differences are found for the sample AA-1, whereas the sample AA-2 shows a nearly perfect agreement. The only relevant difference in the panel structure is the gauze which was added for sample AA-2. The gauze should reduce the development of large scale flow structures close to the liner and make it less sensitive for flow and high amplitude effects. The Kundts tube measurements were carried out with a much higher excitation level than measurements for the current impedance eduction. Therefore, the observed differences for sample AA-1 could be related to a nonlinear variation of the impedance with the amplitude. AA-2 behaves linear and the impedance is not affected by the excitation amplitude. Similar differences are observed with the NLR flow tube data, which points to the nonlinear behavior again. Further experiments, which vary the excitation amplitude, are required to bring the different experiments into accordance and verify the postulated nonlinear behavior of sample AA-1.

The current results prove the flow effect on the impedance of AA-1, whereas the impedance of the gauze covered linear liner panel AA-2 remains almost constant in

the investigated range of frequencies. The educed geometrical parameters, which were calculated from the impedance eduction result, are in a good agreement with the real panel geometry. Altogether, the good agreement of geometry and educed impedance verifies the correct impedance eduction based on the energy transmission and reflection.

7.2.3. Single axisymmetric resonator

The last example for the impedance eduction from measurements considers a large annular resonator with bias flow through the apertures. The sample consists of a large annular cavity of $V = 8.233 \times 10^{-3} \text{ m}^3$ around a circular flow duct of $D = 140 \text{ mm}$ in diameter [46, 47]. The cavity is connected to the flow duct by two rings of 104 apertures in total. The apertures have a diameter of 2.5 mm. The active length of the sample is only $l = 11 \text{ mm}$ [46]. The open area ratio is 6.79 % and the face sheet thickness 1 mm. In the experiment by Heuwinkel [46], Heuwinkel et al. [47], base flow conditions up to $\text{Ma} = \pm 0.1$ have been considered.

Specifications for the impedance eduction

The impedance eduction uses energy transmission and reflection coefficients to define the objective function. A plug flow assumption is used for the base flow. The effect of the bias flow on the base flow is neglected. The effect of the bias flow on the resulting impedance of the large resonator is, however, included in the measured energy transmission, reflection and dissipation data.

The corresponding numerical set-up for the impedance eduction uses a grid spacing of 4 mm, resulting in a total mesh of 5100 points. The axisymmetric isentropic variant of the model equations is applied. Only the real part is used in the computation setting the azimuthal mode number to zero. The radiation/outflow boundary condition of Section 3.5.1 is used as non-reflective boundary condition. It also implements a sound source at one end of the computational domain which is transparent to reflections from the hard-lined and lined-hard transitions. 21 000 time steps are calculated with a CFL number of 0.5, which results in a turn-around time of 34.4 minutes on one core of a dual core AMD Opteron processor 244.

Results

The impedance functions resulting from the eduction are presented in Fig. 7.40. Without base flow, the real part of the impedance increases with the bias flow velocity. The resistance is zero without bias flow. With base flow the resistance first decreases for bias flow velocities up to $v_{\text{jet}} = 6$, while it increases for higher bias flow velocities. The imaginary part of the impedance shows a smaller slope when a bias flow is added for zero base flow. This decrease steadily depends on the bias flow velocity for zero base flow speed. The observation is also found for higher bias flow velocities than $v_{\text{jet}} = 6$ for the sound propagation against the flow at $\text{Ma} = -0.1$.

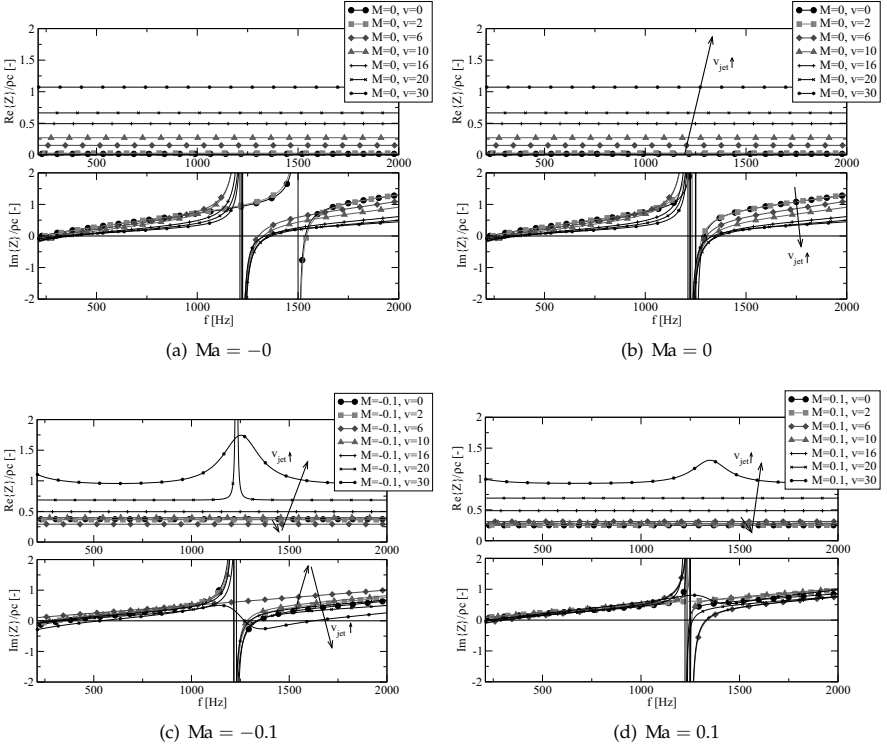


Figure 7.40.: Educed impedance for different bias flow velocities v_{jet} and base flow Mach numbers Ma .

The sound propagation in flow direction shows no clear trends for the effect of the bias flow on the imaginary part of the impedance. Without base flow, the first zero crossing of the imaginary part, which corresponds to the first resonance frequency is found between $f_{0,1} = 220 \dots 375$ Hz for the different bias flow velocities. A second resonance, is found with the third zero crossing of the imaginary part around $f_{0,2} = 1280 \dots 1370$ Hz. However, some of the cases show a significantly higher $f_{0,2}$. The energy dissipation reaches a local maximum for both of these frequencies. For the sound propagation against the flow the resonances are moved to higher frequencies in most of the cases. For the sound propagation against the flow, the resonance frequency is reduced.

The energy transmission, reflection and dissipation coefficients found by the impedance eduction are given in Appendix D.2.3. In general, they are in a very good

agreement with the experimental results of Heuwinkel [46]. An exception must be made for the sound propagation with a base flow at $Ma = 0.1$, where the characteristic peaks of the dissipation curve are not found in the numerical result for some of the cases.

It should be noted that the energy dissipation of the sample DLR-1C is lower than for the samples investigated in the preceding section. Different from the other samples, the liner produces relative large reflections for some frequencies. The active length of the sample is very small such that it is meshed by only four grid points in axial direction. This is unfavorable for the resulting impedance representation, but an increase of the mesh size would increase the time for the optimization. Therefore, the sample is considered to be at the limit of the current method.

To further study the eduction results, the five parameters of the EHR model for the optimal impedance function are summarized in Tab. 7.11 and Tab. 7.12. Further information is provided by the last three columns of the table. Eqs. (4.14) are used to calculate the resulting neck length based on the open area ratio of 6.79 % and the cavity volume based on the active surface $S = \pi D l$ from the EHR model parameters. Furthermore, a resonance frequency f_0 which is based on the corrected neck length and the resulting volume–open area ratio is provided. Due to the large face sheet mass reactance m_f , it is not possible to use the approximation $f_0 \approx 0.5 T_l^{-1}$ here.

First of all, the resulting cavity volumes are out of the expected range for the sound propagating with the flow at $Ma = 0.1$. The experimental data shows a relatively large scattering such that a better eduction result could not be obtained. Therefore, the $Ma = 0.1$ cases will be excluded from the following discussion. The result of $Ma = -0.1$, $v_{jet} = 30$ m/s is dropped from the discussion for the same reason. Omitting these cases the following conclusions can be drawn from the tables:

- The cavity damping parameter of the EHR model is found to be zero or very small in most of the cases.
- Without flow the face sheet resistance increases with the bias flow velocity increasing. With flow the effect is only observed for higher bias flow velocities beyond $v_{jet} = 6$ m/s.
- Without any flow the volume of the resonator is educed with about 10 % error and the educed neck correction is between 1.5 ... 1.6 mm. This corresponds to a reasonable value between 60 % to 64 % of the aperture diameter for the correction.
- Without base flow the moving mass of the Helmholtz resonator denoted by the corrected neck length L decreases with increasing bias flow velocity.
- Without base flow the effective cavity volume decreases with the bias flow velocity up to $v_{jet} = 6 \dots 10$ m/s. It increases for higher bias flow velocities.

Table 7.11.: Educed EHR model parameters for sample DLR-1C without flow.

Ma [-]	$v_{jet} [\frac{m}{s}]$	$1/T_l [s^{-1}]$	$R_f [-]$	$1/m_f [-]$	$\beta [-]$	$\epsilon [-]$	$L [mm]$	$V [l]$	$f_0 [Hz]$
-0.0	0	1256	.013	30.1	.08	0.	2.5	8.2	217
-0.0	2	1256	.025	30.0	.10	0.02	2.6	6.5	239
-0.0	6	1276	.157	34.7	.16	0.	2.4	4.0	312
-0.0	10	1240	.271	46.0	.16	0.01	2.0	4.1	343
-0.0	16	1235	.496	76.1	.15	0.01	1.4	4.4	399
-0.0	20	1226	.664	82.3	.12	0.	1.2	5.6	378
-0.0	30	1223	1.07	89.3	.08	0.	1.0	8.4	336
0.0	0	1250	.016	29.1	.09	0.	2.6	7.3	224
0.0	2	1233	.028	30.1	.11	0.	2.6	6.1	247
0.0	6	1212	.150	36.1	.16	0.	2.4	4.2	308
0.0	10	1209	.270	45.5	.17	0.	2.0	4.0	343
0.0	16	1220	.493	67.0	.14	0.	1.5	4.8	370
0.0	20	1226	.664	82.3	.12	0.	1.2	5.6	378
0.0	30	1223	1.07	89.3	.08	0.	1.0	8.4	336

Table 7.12.: Educued EHR model parameters with plug flow profile for sample DLR-1C.

Ma [-]	$v_{jet} [\frac{m}{s}]$	$1/T_f [s^{-1}]$	$R_f [-]$	$1/m_f [-]$	$\beta [-]$	$\epsilon [-]$	$L [mm]$	$V [l]$	$f_0 [Hz]$
-0.1	0	1216	.37	63.1	.131	0.	1.5	5.2	354
-0.1	2	1216	.36	51.7	.108	0.	1.7	6.3	305
-0.1	6	1218	.36	44.8	.090	0.	1.8	7.5	266
-0.1	10	1217	.40	47.3	.088	0.	1.7	7.7	270
-0.1	16	1217	.50	58.0	.089	0.	1.5	7.6	295
-0.1	20	1230	.69	79.4	.084	0.014	1.1	8.0	329
-0.1*	30	1253	.89	190.7	.239	0.58	1.1	2.8	557
0.1*	0	1233	.25	43.6	.017	0.	1.6	39	123
0.1*	2	1250	.25	38.0	.010	0.66	1.8	69	88
0.1	6	1250	.31	51.0	.106	0.	1.7	6.2	306
0.1*	10	1250	.28	36.4	.011	0.	1.9	60	92
0.1	16	1250	.49	51.0	.099	0.	1.6	6.6	297
0.1*	20	1223	.69	49.7	.048	0.50	1.5	14	210
0.1*	30	1350	.91	37.5	.099	0.70	2.1	6.5	267

- The resonance frequency is in the range of 200 ... 400 Hz. The resonance frequency increases with the bias flow velocity to reach a maximum between $v_{\text{jet}} = 16 \dots 20$ m/s. With flow the tendency is not clear from the results.

The educed geometry parameters without any flow are in range of the original geometry. Furthermore, the cases without base flow show a sensitivity to the propagation direction. The deviation of the results indicates the overall error development from the experimental result through the impedance eduction. Even though the variation of each model parameter is small, the geometry parameters are recovered with a variation of up to 11 % for the cavity volume and 14 % for the effective neck length. The results clearly identify an effect of the bias flow on the impedance. The variation of the geometrical parameters and of the resonance frequency is significantly larger than the error level, which is identified by the deviation of the educed impedance for waves propagating parallel and in opposite direction to the axis of the test set-up without flow. The corrected neck length is reduced with increasing bias flow velocity, whereas the educed cavity volume is reduced for relatively small bias flow velocities and increases again with higher bias flow speeds. This reduction of the neck length has also been described by Ronneberger [112].

For the wave propagation with flow, the resonance frequency is outside the range of measurement. The experiment could not be extended to lower frequencies due to the resonance of the speaker which is used for the excitation. In this case the impedance eduction results in a set of parameters, which fails to recover the geometry and resonance frequency. Therefore, the presence of the resonance frequency is considered important for a correct broadband impedance eduction. Altogether, this last example for an impedance eduction from measurements demonstrates the applicability of the method for *in-situ* measurements of axisymmetric liner samples. Even though the sample DLR-1C reaches the limits of the current impedance eduction process a large number of valid results could be obtained. Due to the physical background of the EHR model, faulty eduction results (denoted by a star in Tab. 7.12) could be identified.

7.2.4. Conclusions to the eduction results

The large number of impedance eduction results, which has been presented in Section 7.2, demonstrates the capability of the EHR model. A representation of the impedance by one set of parameters, which approximates the experimentally observed data very well, is obtained for almost all samples with and without flow. The four liner samples cover a variety of relevant liner designs. The structure of the liner panels ranges from thin $\lambda/4$ -tubes over typical inlet liner designs, including a so called linear liner with gauze covering, to a single resonator with multiple apertures connected to a large annular volume. Energy transmission and reflection as well as pressure amplitudes are considered as input for the impedance eduction from the experiment. Plane samples as well as a cylindrical resonator have been considered.

The eduction is validated by the agreement of the current broadband time-domain impedance eduction result with the published impedance eduction data of Jones et al. [57] for the NASA-GIT experiment with a ceramic tubular liner. The observed differences mainly concern the anti-resonance and the peak magnitude of the impedance. Due to the low attenuation around the anti-resonance the variation of the impedance produces only small variations in the objective function here. Small deviations at this frequency range compensate for a much larger error around the first and second resonance. In addition, it is found that the termination impedance has a significant influence on the resulting liner impedance and the remaining overall error with respect to the pressure amplitude data. The influence of a partially resolved boundary layer profile at both walls is found to be less significant.

Besides the comparison to data from Kundts tube as well as NLR flow tube measurements published by Busse et al. [22] for some of the other samples, a validation of the educed liner impedance is provided by the calculation of measurable geometry parameters from the educed EHR parameter set for all samples. These educed geometry parameters are in a good agreement with the real measures of the liner samples for most of the cases. Large differences are only observed in one case, where the resonance frequency of the sample is out of the measured frequency range. However, the resulting impedance functions show only small difference to valid results in the frequency range considered by the experiment. Moreover, all eduction results show a certain scattering of the EHR model parameters, when varying the propagation direction of the sound wave in the experiment without flow. The geometry which is calculated back based on these parameters shows the same scattering. As the results should be independent of the propagation direction, the scattering is considered as a measure of the overall error from the measurement and the eduction process.

The impedance eduction results in a set of model parameters, which best approximate the experimentally observed sound field with the current CAA method. These model parameters can directly be applied to a realistic aeroengine in a two- or three-dimensional simulation as it is shown for instance in [92] using the educed parameters of sample AA-2 in a three dimensional configuration. Systematic errors e. g. due to the approximation of the hard-lined transition by the CAA method are expected to cancel by this application.

7.3. Applications as broadband impedance model

This section is intended to give examples of the potential of the EHR model in the application. All three applications which are given in the following, make use of the connection of the EHR model parameters to the geometry of the resonator. The first two examples demonstrate the applicability of the EHR model to describe the impedance of a volume, which is connected to a duct system. These examples deal with problems, which have been investigated experimentally in the framework of the CombustionNoise initiative. The first example, which is presented in

Section 7.3.1, is a benchmark of the CAA method with a generic model experiment for the entropy noise generation. The second example in Section 7.3.2 uses a pulse excitation of the averaged flow field in a combustion chamber to calculate a qualitative spectrum of the system response. The last application, which uses the CAA method to predict the attenuation of low frequency noise from an airfield by large resonators, is presented in Section 7.3.3.

7.3.1. Modeling of the plenum impedance in an experiment for entropy noise

In this section a model experiment for the indirect noise generation in combustion systems is investigated. This indirect noise is generated by initially silent accelerated hydrodynamic perturbations according to [25]. The model experiment uses an axisymmetric flow duct. To reduce the mesh size and at the same time obtain a better approximation for installations inside the plenum, the EHR is used to model the plenum impedance. The geometrical setup and the experimental data of heat supply, flow parameters and acoustic measurements in the outlet duct are provided by Bake et al. [6].

Case description

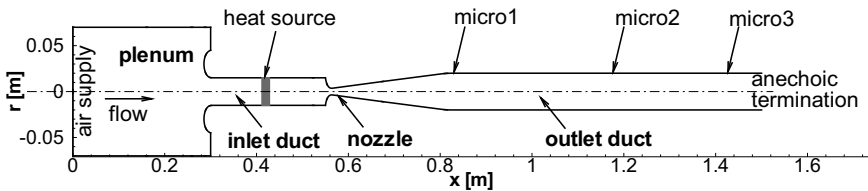


Figure 7.41.: Schematic of the model experiment with the electrical heated inlet duct (left, heating red) and the outlet duct with three microphones right. The plenum (left) has been modeled by the EHR.

The validation experiment [6, 7] uses an electrical heat source in an axisymmetric duct with nozzle. The flow comes from the left in Figure 7.41 into the plenum, which is followed downstream by the heated inlet duct that acts as model for the combustion chamber. Then the flow is accelerated into the nozzle with a diameter of 7.5 mm and decelerated in a long diffuser, which ends in the outlet duct with an anechoic termination to the open space. The outlet duct features four microphone positions in the experiment, of which only three have been covered by the computational domain.

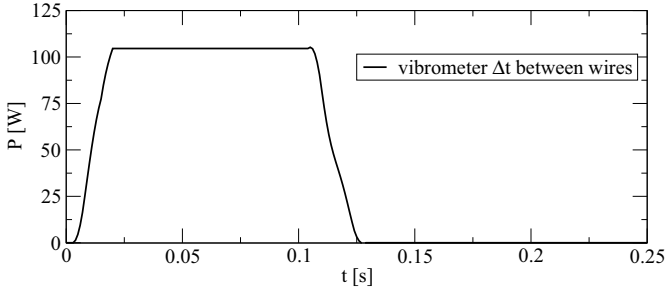


Figure 7.42.: Overall input power calculated from temperature measurements.

The electrical heating is performed through six modules, which are stringed with thin platinum wires [6]. The resulting flow temperature was measured through the resulting density variation by a LASER-vibrometer [6].

Heat source

The overall heat supply is given in Figure 7.42. The heating is triggered by a rectangular pulse of 0.1 s length. The heat supply is idealized as volumetric heat input in the computation. The overall measured power P is equally distributed in the source volume. The single wire layers are powered successively in order to obtain a more sharp switch on pulse, as it was performed in the related experiment. To specify the heat source in the simulation, the vibrometer measurement is filtered and flattened. The measured pulse shape is assumed to be proportional to the heat supply of one wire layer. In this way, the overall power of the wire modules can be calculated as shown in Figure 7.42. The overall power is then equally distributed to the source region of the numerical model with a time delay of $\Delta t = u_{x,0} \Delta x^{-1}$ for the downstream grid lines.

Meshing

The setup is meshed by a structured axisymmetric mesh, which consists of 31 878 points in 6 subdomains. The mesh is optimized to be orthogonal, equidistant and have an aspect ratio close to unity. Especially the local grid spacings in axial and radial direction are nearly equal. The typical grid spacing ranges from 5×10^{-4} m to 1×10^{-3} m in the inlet and outlet duct respectively. The smallest mesh size of 3×10^{-4} m is reached in the throat of the nozzle. The different grid spacings between the inlet and outlet duct arise, as nearly one half of the radial grid lines are terminated in the round wall of the nozzle. This meshing strategy allows to have large variations in diameter on a short length without extensive grid stretching and skewing. The resolvable frequency range for acoustic waves reaches up to 34 kHz,

when considering a conservative accuracy limit of approximately 10 PPW. The only exception is found in the upstream acoustic wave, which cannot be resolved by a linear approach in case of a transonic flow regime. The propagation of hydrodynamic perturbations can be resolved up to approximately 1 kHz in the inlet duct, even at the lowest mass flow rates. The resolution in the nozzle is much better. The outlet duct can only resolve half of the frequency range given above. However, the hydrodynamic perturbations in the straight outlet duct with constantly low mean flow Mach number do not contribute to the acoustic field in our simulation. The high-frequency component is simply removed by the filter. The CFL number is chosen to be 0.75 and 10^6 time steps are calculated to reach a real time of 0.4 s at least. The structured meshing of the plenum without three-dimensional installations would require additional 7 subdomains and more than doubles the grid size if an equidistant mesh spacing is used [103].

Mean flow field

The average flow state is a required prerequisite to simulate the propagation of small perturbations in the test setup. It is calculated with the CAA method solving a nonlinear Euler equation as described in section 3.2 on the mesh described above. To improve the convergence speed, a tree point stencil filter of second order is used for the mean flow calculation all over the domain. With this filter the CFL number could be increased up to 1. A steady state solution is obtained after 50 000 iterations.

Pressure response in comparison to the experiment

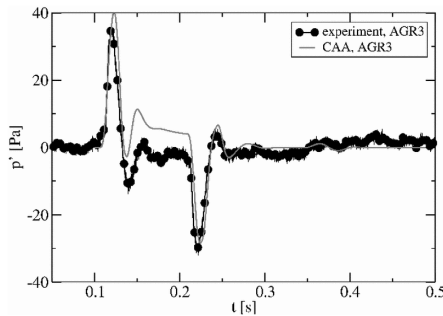


Figure 7.43.: Pressure response at the microphones in the exhaust duct for $Ma = 0.73$

In this section the pressure response at a microphone in the outlet duct is compared between the numerical solution and the experiment. Previous CAA simulations of the experimental setup indicate a strong dependency of the observed pressure response to the unknown impedance of the settling chamber Z_{Plenum} [101].

This plenum impedance has not yet been measured. It is estimated by the analogy of the low-frequency limit of the EHR to the mechanical analogue [comp. Eq. (4.13)]. The real part of the impedance, the resistance is not covered. The plenum geometry is given as cavity with a volume of $V = 4.6$ l and the active area of the neck is $S = 7.1$ cm². The plenum has only a negligibly short neck to the duct. Thus the neck length fully depends on a length correction. The usual empirical length correction for the waves moving inside the cavity is in the order of the neck radius, which would lead to $L = 1.5$ cm, whereas the consideration of a length correction for cylindrical volumes by Alster [4] would result in $L = 0.2$ cm. Depending on the length, the resonant frequency is obtained to be $f_0 \approx 44 \dots 170$ Hz. f_0 is approximate the inverse of the half response time T_l . Consequently, the nondimensional model parameters are obtained to $\beta \approx 0.3 \dots 0.17$ and $m_f \approx 2 \times 10^{-5}$. The damping of the cavity volume due to the installations and the inflow is not clear, but definitely nonzero. The same applies to the face sheet reactance, which probably increases with the flow velocity. The theoretical consideration gives an estimate for the parametric range of the EHR. The parameters are chosen as follows: $T_l = 1/270$ s, $\beta = 0.4$ and $m_f = 1/20000$. A moderate face sheet resistance of $R_f = 0.5$ and cavity damping of $e^{-\varepsilon} = 0.8$ are assumed.

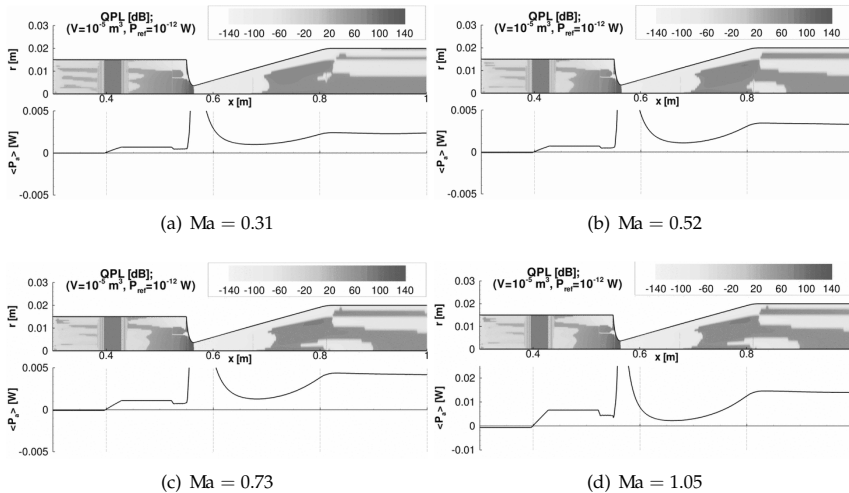


Figure 7.44.: Average acoustic source strength QPL (top as contour plot) and axial acoustic power flux P_a (below as lines).

The result obtained with this representation of the plenum closely approximates the experimentally observed pressure response, as can be seen from Fig. 7.43. How-

ever, there are still some differences in the detail. The relatively free choice of possible EHR parameters strongly influences the observed result such that it cannot be considered as a validation of the method.

Quality analysis and source location

In this section the intensity based source location of section 5.2 is applied in order to verify the numerical solution and at the same time locate acoustic sources. The results of the intensity analysis are presented in Fig. 7.44. All flow speeds are based on the impedance model considered above for the plenum. The direct source strength of the heat input is visible with the QPL-scale in the region between $x = 0.4$ m to $x = 0.436$ m. However, the acoustic energy input by the direct source (QPL ≈ 70 dB) is several orders of magnitude below the maximum observed energy input in the duct. The indirect source strength which is found in the nozzle and diffuser is much larger (QPL ≈ 120 dB). The most powerful acoustic sources are found in the nozzle throat. Due to the sinks found in the diffuser, only a small fraction of the source strength in the nozzle radiates to the downstream duct section.

Some additional acoustic sources are located further downstream in the diffuser. However, these sources may originate from the simplification of the acoustic velocity perturbation u'_a to the overall velocity perturbation. A strong, large vortex is generated by the entropy perturbation passing the inhomogeneous flow field in the nozzle. This vortex is correlated with the acoustic waves in the exhaust duct. Both originate from the passage of the initial entropy perturbation through the nozzle. Therefore, the vortical perturbation contributes to the modified intensity according to Morfey [80] in time average and is faulty identified as acoustic energy.

Below the contour plots the overall acoustic power flux in time average $\langle P_a \rangle_t$ is given for each flow speed in Fig. 7.44. While the color map is the same for all figures, the overall acoustic power has been adjusted to represent the observed levels better. The heat module is identified as source again by the almost linear increase of the acoustic power. The acoustic power flux is negative upstream (left in Fig. 7.44) of the heating module and positive downstream of the module, which indicates the dominance of the direct sound sources on the effective flux of acoustic energy in the inlet duct. The acoustic power flux in the straight duct sections between heat module and nozzle is approximately constant, which validates the CAA solution (The small decrease and variation in front of the nozzle is due to an interpolation error for the two grid blocks involved in the integration there). The intense increase of the acoustic power flux in the nozzle leads to large amplitudes of $\langle P_a \rangle_t$. For a better presentation the peak has been cut-off in Fig. 7.44. The intense right running acoustic waves originating from the nozzle are then annihilated in the diffuser directly following the nozzle throat, which is indicated by the decrease of $\langle P_a \rangle_t$. Finally the acoustic power flux in the diffuser becomes very low and increases again to the outlet. The acoustic power flux becomes constant again, even though there are remaining acoustic sources identified by the QPL in the outlet duct.

Altogether it has been shown that the CAA method including the EHR model

and the analysis of the acoustic intensity are well applicable for the model experiment and have high potential to be applied in realistic combustion problems as well. A further improvement of the acoustic intensity analysis by splitting acoustic and hydrodynamic velocity perturbations is appreciated to remove a possible misidentification of vortical perturbations with the acoustic intensity. The strong local flux of acoustic energy between the strong sources in nozzle and diffuser may be reduced by another intensity definition.

7.3.2. Modeling of the plenum impedance in a combustion chamber

In this section a premixed swirling flame enclosed by an approximately cylindrical shell with one open surface opposite to the burner is considered. This configuration has been investigated experimentally and numerically within the CombustionNoise initiative Zhang et al. [140] as a simplified model of a premixed swirl burner in a gas turbine combustor. The set-up features the typical aspiration of hot gases by an enclosed flame without the production of indirect noise due to the acceleration in the combustion chamber exit nozzle.

Case description

Even though the combustion chamber is not fully axisymmetric, due to the installation of windows and cooling devices which are necessary for the optical access to the chamber, it can be approximated by the axisymmetric approach very well. However, the swirl nozzle of the burner can not be covered by the modal-axisymmetric approach due to the complex geometry. Therefore, the inflow is modeled as an acoustic impedance using the boundary condition of Section 4.3. The five model parameters of the EHR are calculated based on Eq. (4.14) and the assumption that a sufficiently large cavity damping is caused by the installations inside the plenum of the burner. The geometric parameters are estimated to be $V = 7.6 \text{ l}$, $S_0 = 56.6 \text{ cm}^2$ and $L = 14.5 \text{ cm}$. The length correction is usually found to be in the order of one to two times the diameter of the resonator neck. The neck of the burner is much longer than the diameter. Therefore the effect of the length correction remains small. The resonance frequency is obtained as $f_0 \approx 100 \dots 122 \text{ Hz}$ depending on the length correction. For small m_f , f_0 is approximately the inverse of the halved response time T_l . Consequently the model parameters of the EHR are obtained as $\beta \approx 0.6$ and $m_f \approx 10^{-4}$. The parameters for the EHR are chosen as follows in the simulation: $T_l = 1/250 \text{ s}$, $\beta = 0.6$ and $m_f = 1/2000$. The latter is necessary to obtain a larger maximum time step size for the simulation and does not significantly change the low frequency impedance. The face sheet resistance is assumed to be very small ($R_f = 0$) and a considerable cavity damping is obtained by setting $e^{-\varepsilon} = 0.75$. The impedance is applied at the inflow of the chamber ($x = 0 \text{ m}$, $y = 0 \dots 0.06 \text{ m}$). The rest of the chamber is assumed to be hard walled.

Base flow field

Two different base flow conditions are considered. A steady RANS simulation and the averaged flow field obtained from an LES simulation, which were both carried out by Zhang et al. [140] using CFX, have been made available to the author by Zhang and Bender [139]. These results are applied as the base-flow regime and the linearized non-isentropic Euler equations for a cylindrical geometry are used. The resulting mean flow conditions are very similar at first glance as can be seen from Fig. 7.45. However, the flame cone and the recirculation zones differ between the RANS (Fig. 7.45(a)) and averaged LES results (Fig. 7.45(b)).

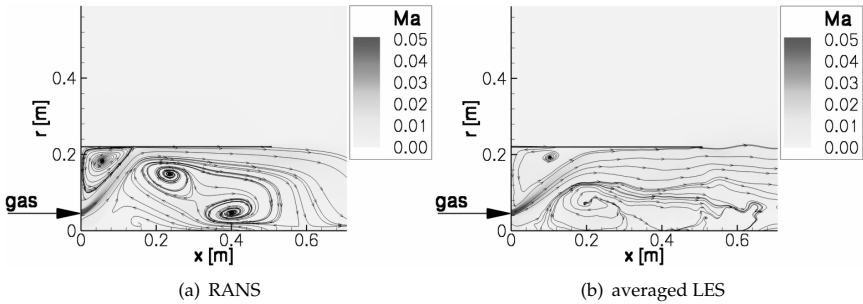


Figure 7.45.: Mach number and stream traces for the average flow fields provided by Zhang et al. [140].

Simulation of the response to a short fluctuation in heat release

The CAA method is now used to compute the spectral peak frequencies of the system consisting of the averaged combustor flow field and the geometrical boundary conditions. A short heating pulse simulating an instationary fluctuation in the heat release is used as an excitation. The pulse length is chosen short enough that the frequency band given from the experiment is excited almost uniformly. The pulse is added in a square region covering a large fraction of the averaged flame front position. The resulting process is statistically stationary after all perturbations have left the computational domain through the non-reflective boundaries or the impedance wall.

Results

For the CAA simulation, only the cylindrical combustion chamber and a cut-out of the exterior are meshed using 0.87×10^5 grid points. The computation of 10^5 time steps takes 33 h on a dual core Athlon 64 X2 CPU with 2.2 GHz using a parallel

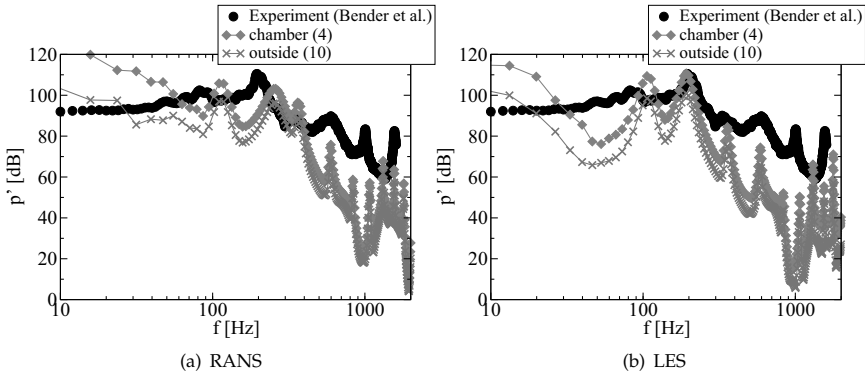


Figure 7.46.: Fourier transform of the swing-off response in the combustion chamber, experimental data from Zhang and Bender [139].

processing with MPI (comp. [130]). The resulting swing-off response to the heating pulse is given for the two different mean flow conditions in Fig. 7.46. The EHR model is used as boundary condition for the inflow section, whereas the remaining part of the bottom of the model combustion chamber is assumed to be hard walled. The RANS-based mean flow conditions lead to an over prediction of all peak frequencies as shown in Fig. 7.46(a). In contrast the experimental spectrum is qualitatively and quantitatively well met for the LES-based average flow field, as can be seen from Fig. 7.46(b). All spectral peak frequencies in the low range (≤ 1 kHz) are correctly identified. Only the lowest peak is clearly missed. The decay with the frequency cannot be correctly predicted because the pulse excitation is not entirely equivalent to the excitation by the flame. Furthermore, the RANS-based mean flow leads to the growth of instabilities with the linearized Euler equations. For the result shown in Fig. 7.46, the simulation was stopped before the instability became observable. No such instability is found with the averaged LES flow field as mean flow.

Finally, a source location is considered in Fig. 7.47. The QPL clearly identifies the heated region (square around $x = 0.06$ m and $y = 0.08$ m) as the major source of sound. The location for the artificial heating pulse is chosen such that the majority of the reaction zone is covered. Therefore, no further information could be obtained from this region. However, an excitation further downstream close to the chamber exit also featured the major source in the heated region. As expected the direct noise clearly dominates the configuration. In addition to this direct source, some indirect sources are found as thin lines of positive and negative source strength along the free shear layers of the swirling flow inside the combustion chamber. The source strength may also be connected to the vorticity generated in the non-isentropic, non-

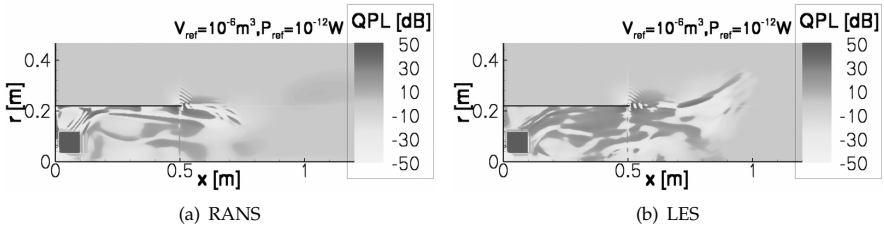


Figure 7.47.: Source location for the swing-off response of the enclosed swirl combustor flow.

potential flow field. Furthermore, a vortex shedding from the wall of the chamber is faulty identified as strong acoustic source by the QPL. A decomposition into acoustic and hydrodynamic velocity field is highly desired to overcome the problem.

Altogether, the current numerical result provides a good prediction of the experimentally observed peak frequencies, when using the averaged LES data as base flow field and a correct EHR parameter set for the plenum. It demonstrates that the combination of average flow field and geometrical boundary conditions including the impedance of the burner plenum can fully determine the resulting frequency response of the investigated burner. The application of the EHR model for the plenum impedance significantly reduces the problem size. At the same time it allows a much better representation of the impedance, than a simplified axisymmetric meshing of the complex plenum would. However, it must be noted that the result highly depends on the choice of parameters for the impedance model of the plenum.

7.3.3. Effect of large Helmholtz resonators on the propagation of low frequency noise

This last example deals with the propagation of low-frequency noise of a jet aircraft at take-off. The major source is the jet. Obviously the acoustic lining of the internal pathway of noise is not promising to reduce this kind of noise. A reduction is, however, highly demanded by the operators and residents of an airport. Large areas for constructional measures of noise reduction are available. However, the required height of acoustic screens for the low-frequency noise in the current example exceeds the limit for a safe operation of the airport. To overcome the problem and achieve a significant noise reduction for the urban areas around the runway of the airport, the concept of an acoustic lining of the internal path of sound has been adopted for the outdoor sound propagation. Large scale resonators with very broadband low frequency attenuation characteristics are applied to virtually enlarge a building or earthwork, which is raised for noise reduction. The application of such large resonators to improve the acoustics of a building goes back far to the ancient Greek

theaters using vases as it is described by Vitruv. The ancient techniques have been rediscovered by the master-builders of the Middle Ages for their Cathedrals using large resonators fixed into the wall for the acoustic enhancement of the building. Nowadays, the lining of the top edge of acoustic screens was proposed by Möser [81].

The characteristic of the noise source, which is an aircraft at ground operation and take-off has been systematically investigated by Pott-Pollenske et al. [97]. According to their results, the major contribution is found in the low-frequency range around 200 Hz. Their results are A-weighted, such that the maximum sound pressure is observed at a lower frequency. Furthermore, in the current example the large scale atmospheric boundary layer plays a major role for the sound propagation. These effects are studied in this section using the EHR model and the CAA method. To reduce the problem size a two-dimensional numerical model problem is considered.

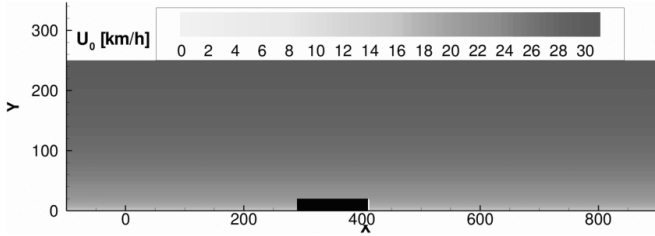
Model setup for the propagation of low-frequency sound waves including atmospheric boundary layer effects

The simulation is carried out in 2D with a monopole line source elevated by 1.5 m above the runway. As a rough model for the low-frequency aircraft noise radiation at take-off multiple low frequencies are excited. The excited frequencies are ranging from $f = 10, 20 \dots 90$ Hz. All frequencies have the same source amplitude and phase, such that the resulting signal could be described as a periodic pulse signal. The ground surface is approximated as a flat hard wall. The domain for the simulation ranges from 250 m left of the runway to 912 m right of the runway. Overall about 1 million points are used with a mesh spacing of $\Delta x = \Delta y = 0.5$ m. The mesh allows to resolve frequencies up to 100 Hz. The time-step size is chosen depending on m_f . For the current examples a CFL number of 0.1 is used. To compute a full period of the propagated pulse signal, which is 0.1 s in real time, 30 000 time steps are necessary. The parallel simulation using MPI takes 14 hours on two cores of an AMD Opteron 244 processor.

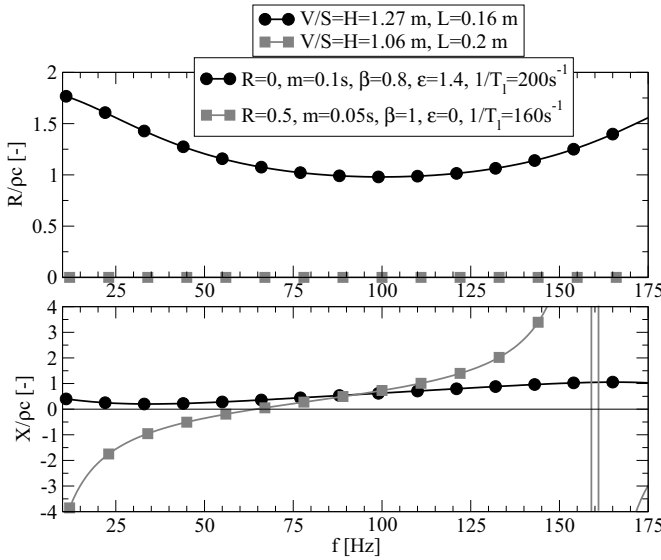
The intended solution to the low-frequency noise problem involves the installation of a building or earthwork to shield the noise from the urban areas. The exact shape is a complex geometrical form with elliptic recesses towards the runway. A simplified geometry is used to study the effect of the installation. The maximum height of the fence is 20 m in a distance of 290 m from the runway. The fence is modeled as a box with an extend of 122 m in the direction of sound propagation. The acoustic treatment on top of the fence is modeled by the EHR model.

The situation with wind is studied considering a typical wind speed of 20 km/h at 13 m over the ground, blowing off the runway towards the urban areas. This is considered as the critical situation, because the related atmospheric boundary layer leads to a refraction of the sound waves towards the ground. Herein $u_0 \sim h^{1/7}$ is considered as template for the atmospheric boundary layer.

The impedance function is designed such that a broadband attenuation in the low frequency range is provided. This is achieved by tuning the resonators to a



(a) Wind speed distribution used for the simulations.


 (b) Impedance functions for a large Helmholtz resonators ($\sigma = 50\%$; L denotes the effective neck length including corrections).

low resonant frequency and using large Helmholtz resonator volumes. However, the treatment could be build as $\lambda/4$ or $\lambda/2$ tubes as well. The impedance functions plotted in Fig. 7.3.3 could be achieved by resonators with a volume of 1 m^3 and large faces sheet or cavity damping respectively. A nonzero face sheet resistance is assumed for the second resonator by setting $R_f = 0.5$.

Baseline solution without lining of the top roof

The sound field shown in Fig. 7.48(a) results from the multi-tone harmonic-pulse excitation described above. The diffraction of waves can clearly be observed at the edges of the not lined fence. The fence alone creates a zone of silence behind it-

self. However, due to diffraction, the low-frequency noise which passes the building above, begins to enter this zone. In addition, the atmospheric boundary layer with the steep gradient towards the ground pushes the sound waves further down. To obtain a quantitative measure for the attenuation, the averaged sound intensity levels over all excited frequencies are normalized by the source intensity and related to the radius as measure for the cylindrical radiation surface around the line source. This finally leads to a local averaged sound power attenuation for all frequencies included in the source signal. The attenuation is plotted on a dB scale in Fig. 7.48(b), Fig. 7.49(b) and Fig. 7.50(b) with and without treatment of the top roof, respectively.

As can be seen from Fig. 7.48(b) the fence without liner on top is only able to reduce the noise behind the building by 2 to 6 dB. The result for observers in a larger distance may even be worse due to diffraction effects of the atmospheric boundary layer.

Finally the path of sound over the building is studied using stream traces of the acoustic intensity. These stream traces indicate that the noise, which is found in the shadow behind the fence passes it immediately at the top roof and then enters the zone of silence from above. Therefore, a treatment of the top roof is considered promising.

Shading with treatment on the top

The instantaneous pressure plots for the same excitation, but with a liner at the top roof are plotted in Fig. 7.49(a) and Fig. 7.50(a). It can be observed, that the acoustic waves do not pass along the top face of the fence any more. Due to the treatment, the waves show a decay of the pressure towards the top of the fence. Furthermore, the secondary point source exciting waves from the edge of the top which is located most far away from the runway ($x = 372$ m), is not visible with the treatment. Thus, it can be expected, that the treatment improves the acoustic shielding of the fence.

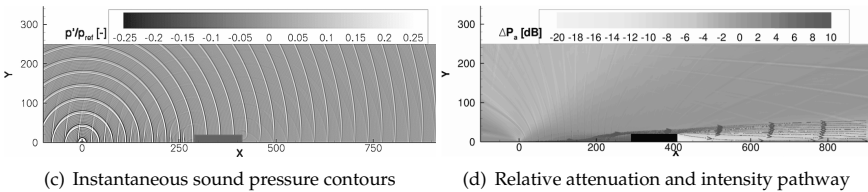


Figure 7.48.: Instantaneous pressure plot and average sound power attenuation with wind and without liner for $f = 10, 20, \dots 90$ Hz.

This is studied in the following, by the means of the relative acoustic intensity (comp. Fig. 7.49(b) and Fig. 7.50(b)). Due to the treatment, a zone of silence behind the building is created, which produces up to 10 dB attenuation at an observer

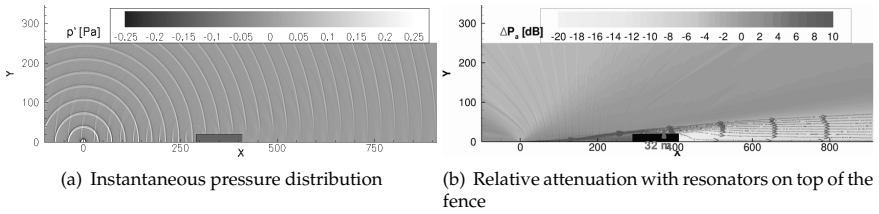


Figure 7.49.: Instantaneous pressure and average sound power attenuation with wind and with the liner impedance shown as black lines in Fig. 7.3.3(b) for $f = 10, 20, \dots 90$ Hz.

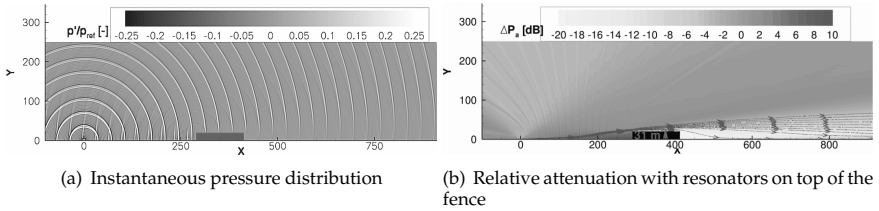


Figure 7.50.: Instantaneous pressure plot and average sound power attenuation with wind and with the liner impedance shown as red line in Fig. 7.3.3(b) for $f = 10, 20, \dots 90$ Hz.

position 800 m from the runway for the low-frequency range considered.

The stream traces of the acoustic intensity gain further insight. Like for a ray-tracing method they show the pathway of sound. The building with acoustic treatment all over the top is found to be virtually higher than the original building. While the acoustic waves pass the original building directly over the hard walled top at 20 m altitude from ground, the path traces with acoustic treatment are found at a height of above 30 m over ground for both impedance functions investigated. Acoustic waves passing the building at a lower altitude are absorbed by the treatment. Furthermore, a reflection of waves towards the sky is found, which leads to an increase of the relative power level under an angle of approximately 10 degrees from the edge of the building which is closer to the runway with the horizon. Due to the increased virtual height of the fence, the sound intensity close to the ground is significantly decreased.

Altogether, the EHR model with the Myers boundary condition has been successfully applied to simulate the effect of large scale Helmholtz resonators on the low-frequency sound wave propagation in the vicinity of an airfield. The results

demonstrate, that the additional treatment of a building, which acts as a fence to shield the low-frequency noise from urban areas may effectively improve the observed noise reduction. The improvement for the current examples is around 6 dB for the currently investigated resonators with respect to the same building without the passive acoustic treatment on the top roof.

7.3.4. Conclusions to the application examples

The three examples demonstrate a variety of applications for the EHR model. While the examples in the preceding sections are closely related to the acoustic lining of the inlet and bypass duct of aeroengines, the current examples extend the application to combustion chambers of aeroengines and gas turbines. The outdoor sound propagation is also considered with the method. However, the computational time and resource consumption is not competitive in comparison to the usually applied ray methods in this case. All three examples use an initial guess for the EHR model parameters. This guess which is based on the approximate geometry of the plenum or resonator and an estimate of the damping parameters based on the installed devices. It is, however, able to essentially improve the reproduction of the experimental result. The results in this section underline the wide variety of applications and the importance of impedance modeling. Connected duct systems and resonators are approximated by the EHR model rather than meshing their complex geometry. In many cases, as in the first two examples, this means that an axisymmetric simulation becomes possible. Therefore, the problem size is significantly reduced with respect to a fully three-dimensional simulation of the complex geometry which is modeled by the EHR in the examples. The base flow is identified as another important parameter of influence by the above examples.

8. Conclusions and Outlook

The correct implementation of the EHR model is firstly verified by the very good agreement of the results to the analytical solution for annular ducts with lining. A set of further benchmark tests against previously published data demonstrates the capability of the model. Theoretical predicted propagation and radiation characteristics are well predicted. However, the limitations of the current CAA method in terms of numerical dissipation and reflections are pointed out in some cases. The method is intended for the simulation of the sound propagation in the inlet, bypass duct or hot-stream channel of an aeroengine and the radiation to the immediate near field of it. The studied benchmark cases feature geometrical complexity and complex base-flow conditions as they are expected to be found here. The excellent agreement between the numerical results and the theoretical predictions demonstrates the reliability of the method.

A possible flow instability at an impedance wall under grazing flow conditions is removed for the Ingard/Myers boundary condition by low-order filtering of selected terms of the impedance model. Besides a comparison between non-filtered and filtered solutions for one case which demonstrates an only small impact on the numerical solution, the approach is verified by all presented results. The low-order filtering allows correct predictions by the Ingard/Myers boundary condition with a low number of grid points. An artificially thickened boundary layer is also investigated, as it is theoretically able to completely avoid the instability. It is found that, with decreasing boundary layer thickness, the solution converges to the one which is obtained with the Ingard/Myers boundary condition. However, an artificial thickening of the boundary layer, to resolve it, should be considered with care. It affects the result much more than a filtering of the auxiliary variable with the Ingard/Myers boundary condition does. All at all, when considering the efficiency as the main objective, the application of the Ingard/Myers boundary condition is the optimal approach, whereas a fully resolved boundary layer profile can provide correct predictions with high computational costs.

The EHR model is applied to deduce the impedance from measurement data for a wide variety of SDOF liners. The good agreement to the published impedance data is a further validation of the method. The EHR model is shown to properly describe the impedance for several different liners in a broad range of frequencies under various flow conditions. The effect of a grazing base flow on the resulting impedance is also pointed out by the results. For the ceramic tubular liner design and the so called linear liner with gauze covering it is not detectable from the variation of the impedance deduction results. The other liners show an influence. The resulting model parameters can directly be used in a simulation of the liner in its realistic installation situation in an aeroengine.

The relation of the effective panel geometry to the educed model parameters of the impedance boundary condition allows further insight to the effect of grazing base-flow conditions and a bias flow through the apertures. The grazing flow effect on the educed geometry shows no clear trends for the current results, whereas a bias flow through the apertures reduces the effective neck length. Without flow, the educed geometrical parameters of the liner are in a good agreement with the panel geometries, which further validates the results. However, the geometrical identification of the model parameters fails when the first resonance of the liner is outside the range of frequencies considered by the measurement.

Finally, the time-domain impedance boundary condition serves as replacement for the geometrically very complex and large inflow plenum in two problems from combustion noise and is used to model an acoustic impedance for the outdoor sound propagation. The impedance boundary condition greatly improves the result and at the same time reduces the numerical problem size in all cases.

A method to validate the numerical results is provided. The conservation of the acoustic energy for each numerical solution is monitored with this method and a detailed analysis is provided for some of the numerical results. The acoustic intensity is also applied to identify radiating sources. The results are in agreement with the theory. The presented analysis of the acoustic intensity is not limited to finite difference CAA methods; it is well suited for aeroacoustic simulations in general.

Outlook: The hard-lined and lined-hard transitions are found to be essential for the experimentally observed acoustic field. The current results are grid dependent, due to the filtering of the field and it seems that the minimum resolution limit is increased due to the presence of such transitions. To overcome this limitation and develop a model for the transition, an experimental investigation, for instance by LASER-optical methods or hot wire anemometry, would be required. Furthermore, the currently available measurements are limited to frequencies up to 3 kHz. This is mainly due to a limitation of the available experiments to frequencies below the cut-off of the first higher mode in the flow tube. An extension of the experiments and the impedance-eduction method to higher modes is required to prove the applicability of the EHR model to describe the frequency response in this whole range. Moreover, with the general methodology of the current work it is also possible to develop higher-order impedance models which allow to describe more complex liner designs. A class of such models can be obtained by using digital filters as a template for the time-domain representation and by applying then the inverse z -transform to obtain a frequency response of the impedance. However, in the digital filter case, the physical interpretation of the related model parameters would not be as simple as for the extended Helmholtz resonator. Another important task which has been raised with the current work, is the separation of the acoustic and hydrodynamic velocity perturbation. This is highly demanded for a general application of the acoustic-intensity-based quality analysis and source location. Furthermore, such a decomposition would allow to study the source strength of the radiating aerodynamic sources far in excess to applications of CAA methods.

Appendix

A. Supplemental material for the mathematical models

A.1. Derivations

A.1.1. Manipulation of the energy equation

Starting point is the Kirchhoff–Fourier equation according to Pierce [95, Eq. (10-1.15)]:

$$\tilde{\varrho} \tilde{T} \frac{\tilde{D} \tilde{s}}{\tilde{D} \tilde{t}} = -\tilde{\nabla} \cdot \tilde{\mathbf{q}} + \frac{\tilde{\nu}}{2} \sum_{i,j} \tilde{\tau}_{ij}^2, \quad (\text{A.1})$$

where the Fourier law for the thermal conduction is given as

$$\tilde{\mathbf{q}} = -\tilde{\kappa} \nabla \tilde{T}.$$

The change rate of the specific entropy in a volume element equals to the ratio of heat input and temperature [83, Eq. (4.2)]

$$d\tilde{s} = \frac{\dot{\tilde{q}} d\tilde{t}}{\tilde{T}}. \quad (\text{A.2})$$

Considering a reversible process for the heat input into an ideal gas, one can use the specific enthalpy to rewrite the above relation. After multiplying with the absolute temperature \tilde{T} one obtains:

$$\tilde{T} d\tilde{s} = d\tilde{h} - \frac{d\tilde{p}}{\tilde{\varrho}}.$$

The heat input for a reversible process is set into relation with the specific enthalpy \tilde{h} . The specific enthalpy is equal to the change of temperature with constant pressure [83, Eq. (2.69)]:

$$d\tilde{h} = C_p d\tilde{T}.$$

By using this relation in connection with the constitutive equation for an ideal gas

$$\frac{\tilde{p}}{\tilde{\varrho}} = \mathcal{R} \tilde{T}, \quad (\text{A.3})$$

one obtains

$$d\tilde{h} = \frac{C_p}{\mathcal{R}} \left(\frac{d\tilde{p}}{\tilde{\varrho}} - \frac{\tilde{p} d\tilde{\varrho}}{\tilde{\varrho}^2} \right).$$

The above expression for $d\tilde{h}$ is used in Eq. (A.2) to obtain

$$\begin{aligned} d\tilde{s} &= \frac{C_p}{\mathcal{R}\tilde{T}} \left(\frac{d\tilde{p}}{\tilde{q}} - \frac{\tilde{p} d\tilde{q}}{\tilde{q}^2} \right) - \frac{d\tilde{p}}{\tilde{T}\tilde{q}} \\ &= (C_p - \mathcal{R}) \frac{d\tilde{p}}{\tilde{p}} - C_p \frac{d\tilde{q}}{\tilde{q}}. \end{aligned}$$

The second relation is realized using the ideal gas law Eq. (A.3) to eliminate \tilde{T} . Finally, the relation $\mathcal{R} = C_p - C_v$ is introduced to arrive at the expression:

$$d\tilde{s} = C_v \frac{d\tilde{p}}{\tilde{p}} - C_p \frac{d\tilde{q}}{\tilde{q}}. \quad (\text{A.4})$$

For further modifications it is useful to introduce the ratio of the specific heats γ , which is defined as

$$\gamma = \frac{C_p}{C_v}. \quad (\text{A.5})$$

Then making use of the ideal gas equation (A.3) and the above definitions Eqs. (A.5) and (A.4) in Eq. (A.1) results in:

$$\begin{aligned} \frac{C_v}{\mathcal{R}} \left(\frac{\tilde{D}\tilde{p}}{\tilde{D}\tilde{t}} - \gamma \frac{\tilde{p}}{\tilde{q}} \underbrace{\left(\frac{\tilde{D}\tilde{q}}{\tilde{D}\tilde{t}} \right)}_{=-\tilde{q}\tilde{\nabla}\cdot\tilde{\mathbf{u}}, \text{ mass conservation}} \right) &= -\tilde{\nabla}\cdot\tilde{\mathbf{q}} + \frac{\tilde{v}}{2} \sum_{i,j} \tilde{\tau}_{ij}^2. \\ &= -\tilde{q}\tilde{\nabla}\cdot\tilde{\mathbf{u}}, \text{ mass conservation} \end{aligned}$$

Finally, the preceding relation is simplified by using $\mathcal{R} = C_p - C_v$ and by making use of the conservation of mass, Eq. (2.3), to eliminate the terms depending on \tilde{q}

$$\frac{1}{\gamma - 1} \left(\frac{\tilde{D}\tilde{p}}{\tilde{D}\tilde{t}} + \gamma \tilde{p} \tilde{\nabla}\cdot\tilde{\mathbf{u}} \right) = -\tilde{\nabla}\cdot\tilde{\mathbf{q}} + \frac{\tilde{v}}{2} \sum_{i,j} \tilde{\tau}_{ij}^2. \quad (\text{A.6})$$

A.1.2. Nondimensional form of the equations

The unit quantities of Table 2.1 are used to rewrite the governing equations. For the mass conservation introducing the non-dimensional quantities results in:

$$\begin{aligned} \frac{\tilde{D}\tilde{q}}{\tilde{D}\tilde{t}} + \tilde{q}\tilde{\nabla}\cdot\tilde{\mathbf{u}} &= \frac{c_\infty}{L_\infty} \frac{D\varrho_\infty\varrho}{Dt} + \frac{\varrho_\infty}{L_\infty} \varrho \tilde{\nabla}\cdot(c_\infty \mathbf{u}) \\ &= \frac{c_\infty\varrho_\infty}{L_\infty} \left(\frac{D\varrho}{Dt} + \varrho \tilde{\nabla}\cdot\mathbf{u} \right) = 0. \end{aligned} \quad (\text{A.7a})$$

The balance of momentum Eq. (2.5) is rewritten in the same manner obtaining the factor $\frac{a_\infty^2}{L_\infty}$ which is the unit of an acceleration:

$$\frac{a_\infty^2}{L_\infty} \left(\frac{D\mathbf{u}}{Dt} + \frac{1}{\varrho} \nabla p \right) = \frac{a_\infty^2}{L_\infty} \left(\nu \tilde{\nabla}\cdot\boldsymbol{\tau} \right). \quad (\text{A.7b})$$

The energy balance in terms of the pressure Eq. (2.7) is rewritten to a nondimensional form by the factor $\frac{\varrho_\infty c_\infty^3}{L_\infty}$ which is an unit of power:

$$\frac{\varrho_\infty c_\infty^3}{L_\infty} \left(\frac{Dp}{Dt} + \gamma p \nabla \cdot \mathbf{u} \right) = (\gamma - 1) \frac{\varrho_\infty c_\infty^3}{L_\infty} \left(-\nabla \cdot \mathbf{q} + \frac{\nu}{2} \sum_{ij} \tilde{\tau}_{ij}^2 \right). \quad (\text{A.7c})$$

A.1.3. Transformation to the nonlinear PENNE equations

To obtain the nonlinear mathematical model some further manipulations are applied to the sets of Eq. (2.10)

$$\begin{aligned} \frac{\partial \varrho'}{\partial t} + (\mathbf{u}_0 + \mathbf{u}') \cdot \nabla \varrho' + (\varrho_0 + \varrho') \nabla \cdot \mathbf{u}' + \mathbf{u}' \cdot \nabla \varrho_0 + \varrho' \nabla \cdot \mathbf{u}_0 \\ + \underbrace{\mathbf{u}_0 \cdot \nabla \varrho_0 + \varrho_0 \nabla \cdot \mathbf{u}_0}_{=0, \text{ mass conservation of the base flow}} = 0, \end{aligned} \quad (\text{A.8a})$$

$$\begin{aligned} \frac{\partial \mathbf{u}'}{\partial t} + (\mathbf{u}_0 + \mathbf{u}') \cdot \nabla \mathbf{u}' + \frac{1}{\varrho_0 + \varrho'} \nabla p' + \mathbf{u}' \cdot \nabla \mathbf{u}_0 - \frac{\varrho'}{\varrho_0 (\varrho_0 + \varrho')} \nabla p_0 \\ - \underbrace{\frac{1}{\text{Re}_\infty} \nabla \cdot \boldsymbol{\tau}'}_{\approx 0} \\ + \underbrace{\mathbf{u}_0 \cdot \nabla \mathbf{u}_0 + \frac{1}{\varrho_0} \nabla p_0 - \frac{1}{\text{Re}_\infty} \nabla \cdot \boldsymbol{\tau}_0}_{=0, \text{ momentum balance of the base flow}} = 0 \end{aligned} \quad (\text{A.8b})$$

and

$$\begin{aligned} \frac{\partial p'}{\partial t} + (\mathbf{u}_0 + \mathbf{u}') \cdot \nabla p' + \gamma (p_0 + p') \nabla \cdot \mathbf{u}' + \mathbf{u}' \cdot \nabla p_0 + \gamma p' \nabla \cdot \mathbf{u}_0 \\ - \underbrace{(\gamma - 1) \frac{1}{2 \text{Re}_\infty} \sum_{ij} [2 \tau_{0,ij} + \tau'_{ij}] \tau'_{ij}}_{\approx 0} \\ + \underbrace{\mathbf{u}_0 \cdot \nabla p_0 + \gamma p_0 \nabla \cdot \mathbf{u}_0 - (\gamma - 1) \left(-\nabla \cdot \mathbf{q} + \frac{1}{2 \text{Re}_\infty} \sum_{ij} \tau_{0,ij}^2 \right)}_{=0, \text{ energy balance of the base flow}} = 0. \end{aligned} \quad (\text{A.8c})$$

The balance of momentum Eq. (A.8b) has been derived by using a relation found by Long [76]:

$$\frac{1}{\varrho_0 + \varrho'} = \frac{1}{\varrho_0} \frac{\varrho_0}{\varrho_0 + \varrho'} = \frac{1}{\varrho_0} \frac{\varrho_0 + \varrho' - \varrho'}{\varrho_0 + \varrho'} = \frac{1}{\varrho_0} \left(1 - \frac{\varrho'}{\varrho_0 + \varrho'} \right) = \frac{1}{\varrho_0} - \frac{\varrho'}{\varrho_0 (\varrho_0 + \varrho')}.$$

The acoustic Reynolds number Re_∞ , comp. Eq. (2.9), is usually very large. Therefore, the viscous effects due to the perturbation are very small and in most cases can be neglected. The energy Eq. (A.8c) shows some terms featuring products of the base-flow shear-rate tensor of the with the perturbation shear-rate tensor. These terms can be neglected by assuming that the gradient of the perturbation is small compared to the corresponding quantity of the averaged flow field.

A.1.4. Relation of the linearized Euler equations to the wave equation and concluding remarks

The relation of the linearized Euler equations to the convective wave equation of aeroacoustics is pointed out here, for completeness. The pressure–density relation of Eq. (2.15) is equal to the one found e. g. in Ehrenfried [31, Eq. (2.1.15)], under the assumption that the speed of sound in the base-flow field is uniform. Eqs. (2.14a) and (2.14b) return to the form of [31, Eqs. (2.1.8) and (2.1.11)], under the assumption of an uniform base flow:

$$\begin{aligned} \frac{D_0 \varrho'}{D_0 t} + \varrho_0 \nabla \cdot \mathbf{u}' &= 0 \\ \text{and} \quad \frac{D_0 \mathbf{u}'}{D_0 t} + \frac{1}{\varrho_0} \nabla p' &= 0, \end{aligned}$$

where the substantial derivative is defined with the base flow as,

$$\frac{D_0(\cdot)}{D_0 t} = \frac{\partial(\cdot)}{\partial t} + \mathbf{u}_0 \cdot \nabla(\cdot).$$

Taking the substantial derivative of the first and the divergence of the second equation multiply by ϱ_0 under the assumption of an irrotational perturbed flow-field and making use of the pressure–density relation Eq. (2.15), one recovers a convective wave equation of the form:

$$\frac{1}{c^2} \frac{D_0^2 p'}{D_0^2 t} - \nabla \cdot \nabla p' = 0.$$

In a medium at rest the above equation simplifies to the standard wave equation, as for example found in Ehrenfried [31, Eq. (2.1.23)].

A.2. Matrix–Vector form of the mathematical models for implementation

The implementation of the mathematical model follows the scheme

$$\frac{\partial \Phi'}{\partial t} = -\mathbf{A} \cdot \frac{\partial \Phi'}{\partial x} - \mathbf{B} \cdot \frac{\partial \Phi'}{\partial y} - \mathbf{C} \cdot \frac{\partial \Phi'}{\partial z} - \mathbf{D} \cdot \Phi'$$

for the three dimensional form. \mathbf{D} carries the source terms, which are introduced by derivatives of the base flow field. For the two dimensional form, the matrix \mathbf{C} becomes zero and \mathbf{D} is modified under the assumption of a base flow, which is constant in x_3 -direction. Thus only a modified \mathbf{D}_{2D} is given, which directly corresponds to the form how the two dimensional equations are implemented via compiler flags.

The 3D axisymmetric form uses a cylindrical coordinate system to state the governing equations. Thus, a modified definition is used in the form:

$$\frac{\partial \Phi'}{\partial t} = -\mathbf{A} \cdot \frac{\partial \Phi'}{\partial x} - \mathbf{B} \cdot \frac{\partial \Phi'}{\partial r} - \frac{1}{r} \mathbf{C}_{\text{Axi}} \cdot \Phi' - \mathbf{D}_{\text{Axi}} \cdot \Phi'.$$

Furthermore, a Fourier decomposition (with the ordinal number m , which corresponds to the azimuthal mode number) of the field in azimuthal direction is introduced to cover higher modes. A complex amplitude of Φ' is considered. This approach does not allow a non-linear model for $m \neq 0$. The axisymmetric form shares the matrices \mathbf{A} and \mathbf{B} with the three dimensional form. Thus, only \mathbf{C}_{Axi} and \mathbf{D}_{Axi} are given for this case.

A.2.1. Gradient and divergence for the specific coordinate systems

The gradient and divergence of a vector and a scalar are specified here. The modal axisymmetric approach is a special case, as in addition to the application of a cylindrical coordinate system, a Fourier series ansatz is applied for the azimuthal direction of the perturbation field as it was described in Section 2.7.

A.2.2. Nonlinear equations

Three-dimensional (3D) nonlinear equations

$$\mathbf{A} = \begin{pmatrix} u_0 + u' & q_0 + q' & 0 & 0 & 0 \\ 0 & u_0 + u' & 0 & 0 & \frac{1}{q_0 + q'} \\ 0 & 0 & u_0 + u' & 0 & 0 \\ 0 & 0 & 0 & u_0 + u' & 0 \\ 0 & \gamma(p_0 + p') & 0 & 0 & u_0 + u' \end{pmatrix} \quad (\text{A.9a})$$

$$\mathbf{B} = \begin{pmatrix} v_0 + v' & 0 & q_0 + q' & 0 & 0 \\ 0 & v_0 + v' & 0 & 0 & 0 \\ 0 & 0 & v_0 + v' & 0 & \frac{1}{q_0 + q'} \\ 0 & 0 & 0 & v_0 + v' & 0 \\ 0 & 0 & \gamma(p_0 + p') & 0 & v_0 + v' \end{pmatrix} \quad (\text{A.9b})$$

$$\mathbf{C} = \begin{pmatrix} w_0 + w' & 0 & 0 & \varrho_0 + \varrho' & 0 \\ 0 & w_0 + w' & 0 & 0 & 0 \\ 0 & 0 & w_0 + w' & 0 & 0 \\ 0 & 0 & 0 & w_0 + w' & \frac{1}{\varrho_0 + \varrho'} \\ 0 & 0 & 0 & \gamma(p_0 + p') & w_0 + w' \end{pmatrix} \quad (\text{A.9c})$$

$$\mathbf{D} = \begin{pmatrix} \frac{\partial u_0}{\partial x} + \frac{\partial v_0}{\partial y} + \frac{\partial w_0}{\partial z} & \frac{\partial \varrho_0}{\partial x} & \frac{\partial \varrho_0}{\partial y} & \frac{\partial \varrho_0}{\partial z} & 0 \\ -\frac{1}{(\varrho_0 + \varrho') \varrho_0} \frac{\partial p_0}{\partial x} & \frac{\partial u_0}{\partial x} & \frac{\partial u_0}{\partial y} & \frac{\partial v_0}{\partial z} & 0 \\ -\frac{1}{(\varrho_0 + \varrho') \varrho_0} \frac{\partial p_0}{\partial y} & \frac{\partial v_0}{\partial x} & \frac{\partial v_0}{\partial y} & \frac{\partial v_0}{\partial z} & 0 \\ -\frac{1}{(\varrho_0 + \varrho') \varrho_0} \frac{\partial p_0}{\partial z} & \frac{\partial w_0}{\partial x} & \frac{\partial w_0}{\partial y} & \frac{\partial w_0}{\partial z} & 0 \\ 0 & \frac{\partial p_0}{\partial x} & \frac{\partial p_0}{\partial y} & \frac{\partial p_0}{\partial z} & \gamma \left(\frac{\partial u_0}{\partial x} + \frac{\partial v_0}{\partial y} + \frac{\partial w_0}{\partial z} \right) \end{pmatrix} \quad (\text{A.9d})$$

Axisymmetric nonlinear equations

As the resulting PDE is nonlinear, the assumption of constant m for the azimuthal direction does not apply with non-linear wave propagation. Therefore, the modal approach cannot be applied with nonlinear waves. The axisymmetric variant of the governing equations is not modal but purely axisymmetric here:

$$\mathbf{C}_{\text{Axi}} = \begin{pmatrix} v_0 & 0 & \varrho_0 + \varrho' & 0 & 0 \\ 0 & 0 & 0 & 0 & 0 \\ 0 & 0 & 0 & -(2w_0 + w') & 0 \\ 0 & 0 & w_0 & v_0 + v' & 0 \\ 0 & 0 & \gamma(p_0 + p') & 0 & \gamma v_0 \end{pmatrix} \quad (\text{A.10a})$$

$$\mathbf{D}_{\text{Axi}} = \begin{pmatrix} \frac{\partial u_0}{\partial x} + \frac{\partial v_0}{\partial r} & \frac{\partial \varrho_0}{\partial x} & \frac{\partial \varrho_0}{\partial r} & 0 & 0 \\ 0 & \frac{\partial u_0}{\partial x} & \frac{\partial u_0}{\partial r} & 0 & -\frac{1}{\varrho_0(\varrho_0 + \varrho')} \frac{\partial p_0}{\partial x} \\ 0 & \frac{\partial v_0}{\partial x} & \frac{\partial v_0}{\partial r} & 0 & -\frac{1}{\varrho_0(\varrho_0 + \varrho')} \frac{\partial p_0}{\partial r} \\ 0 & \frac{\partial w_0}{\partial x} & \frac{\partial w_0}{\partial r} & 0 & 0 \\ 0 & \frac{\partial p_0}{\partial x} & \frac{\partial p_0}{\partial r} & 0 & \gamma \left[\frac{\partial u_0}{\partial x} + \frac{\partial v_0}{\partial r} \right] \end{pmatrix} \quad (\text{A.10b})$$

Two-dimensional nonlinear equations

$$\mathbf{D}_{2\text{D}} = \begin{pmatrix} \frac{\partial u_0}{\partial x} + \frac{\partial v_0}{\partial y} & \frac{\partial \varrho_0}{\partial x} & \frac{\partial \varrho_0}{\partial y} & 0 & 0 \\ -\frac{1}{(\varrho_0 + \varrho') \varrho_0} \frac{\partial p_0}{\partial x} & \frac{\partial u_0}{\partial x} & \frac{\partial u_0}{\partial y} & 0 & 0 \\ -\frac{1}{(\varrho_0 + \varrho') \varrho_0} \frac{\partial p_0}{\partial y} & \frac{\partial v_0}{\partial x} & \frac{\partial v_0}{\partial y} & 0 & 0 \\ 0 & 0 & 0 & 0 & 0 \\ 0 & \frac{\partial p_0}{\partial x} & \frac{\partial p_0}{\partial y} & 0 & \gamma \left(\frac{\partial u_0}{\partial x} + \frac{\partial v_0}{\partial y} \right) \end{pmatrix} \quad (\text{A.11})$$

A.2.3. Linearized model equations

The linearized model equations are obtained by dropping the nonlinear terms from the above set of equations. Furthermore, the momentum equations are recast in a slightly modified form.

Three-dimensional linearized governing equations

$$\mathbf{A} = \begin{pmatrix} u_0 & \varrho_0 & 0 & 0 & 0 \\ 0 & u_0 & 0 & 0 & \frac{1}{\varrho_0} \\ 0 & 0 & u_0 & 0 & 0 \\ 0 & 0 & 0 & u_0 & 0 \\ 0 & \gamma p_0 & 0 & 0 & u_0 \end{pmatrix} \quad (\text{A.12a})$$

$$\mathbf{B} = \begin{pmatrix} v_0 & 0 & \varrho_0 & 0 & 0 \\ 0 & v_0 & 0 & 0 & 0 \\ 0 & 0 & v_0 & 0 & \frac{1}{\varrho_0} \\ 0 & 0 & 0 & v_0 & 0 \\ 0 & 0 & \gamma p_0 & 0 & v_0 \end{pmatrix} \quad (\text{A.12b})$$

$$\mathbf{C} = \begin{pmatrix} w_0 & 0 & 0 & \varrho_0 & 0 \\ 0 & w_0 & 0 & 0 & 0 \\ 0 & 0 & w_0 & 0 & 0 \\ 0 & 0 & 0 & w_0 & \frac{1}{\varrho_0} \\ 0 & 0 & 0 & \gamma p_0 & w_0 \end{pmatrix} \quad (\text{A.12c})$$

$$\mathbf{D} = \begin{pmatrix} \frac{\partial u_0}{\partial x} + \frac{\partial v_0}{\partial y} + \frac{\partial w_0}{\partial z} & \frac{\partial \varrho_0}{\partial x} & \frac{\partial \varrho_0}{\partial y} & \frac{\partial \varrho_0}{\partial z} & 0 \\ \frac{1}{\varrho_0} \left(u_0 \frac{\partial u_0}{\partial x} + v_0 \frac{\partial u_0}{\partial y} + w_0 \frac{\partial u_0}{\partial z} \right) & \frac{\partial u_0}{\partial x} & \frac{\partial u_0}{\partial y} & \frac{\partial u_0}{\partial z} & 0 \\ \frac{1}{\varrho_0} \left(u_0 \frac{\partial v_0}{\partial x} + v_0 \frac{\partial v_0}{\partial y} + w_0 \frac{\partial v_0}{\partial z} \right) & \frac{\partial v_0}{\partial x} & \frac{\partial v_0}{\partial y} & \frac{\partial v_0}{\partial z} & 0 \\ \frac{1}{\varrho_0} \left(u_0 \frac{\partial w_0}{\partial x} + v_0 \frac{\partial w_0}{\partial y} + w_0 \frac{\partial w_0}{\partial z} \right) & \frac{\partial w_0}{\partial x} & \frac{\partial w_0}{\partial y} & \frac{\partial w_0}{\partial z} & 0 \\ 0 & \frac{\partial p_0}{\partial x} & \frac{\partial p_0}{\partial y} & \frac{\partial p_0}{\partial z} & \gamma \left(\frac{\partial u_0}{\partial x} + \frac{\partial v_0}{\partial y} + \frac{\partial w_0}{\partial z} \right) \end{pmatrix} \quad (\text{A.12d})$$

Linearized modal-axisymmetric governing equations

$$\mathbf{C}_{\text{Axi}} = \begin{pmatrix} v_0 - i m w_0 & 0 & \varrho_0 & -i m \varrho_0 & 0 \\ 0 & -i m w_0 & 0 & 0 & 0 \\ -\frac{w_0^2}{\varrho_0} & 0 & -i m w_0 & -2 w_0 & 0 \\ \frac{v_0 w_0}{\varrho_0} & 0 & w_0 & v_0 - i m w_0 & -\frac{i m}{\varrho_0} \\ 0 & 0 & \gamma p_0 & -i m \gamma p_0 & \gamma v_0 - i m w_0 \end{pmatrix} \quad (\text{A.13a})$$

$$\mathbf{D}_{\text{Axi}} = \begin{pmatrix} \frac{\partial u_0}{\partial x} + \frac{\partial v_0}{\partial r} & \frac{\partial \varrho_0}{\partial x} & \frac{\partial \varrho_0}{\partial r} & 0 & 0 \\ \frac{1}{\varrho_0} \left(u_0 \frac{\partial u_0}{\partial x} + v_0 \frac{\partial u_0}{\partial r} \right) & \frac{\partial u_0}{\partial x} & \frac{\partial u_0}{\partial r} & 0 & 0 \\ \frac{1}{\varrho_0} \left(u_0 \frac{\partial v_0}{\partial x} + v_0 \frac{\partial v_0}{\partial r} \right) & \frac{\partial v_0}{\partial x} & \frac{\partial v_0}{\partial r} & 0 & 0 \\ \frac{1}{\varrho_0} \left(u_0 \frac{\partial w_0}{\partial x} + v_0 \frac{\partial w_0}{\partial r} \right) & \frac{\partial w_0}{\partial x} & \frac{\partial w_0}{\partial r} & 0 & 0 \\ 0 & \frac{\partial p_0}{\partial x} & \frac{\partial p_0}{\partial r} & 0 & \gamma \left[\frac{\partial u_0}{\partial x} + \frac{\partial v_0}{\partial r} \right] \end{pmatrix} \quad (\text{A.13b})$$

Linearized two-dimensional governing equations

$$\mathbf{D}_{\text{2D}} = \begin{pmatrix} \frac{\partial u_0}{\partial x} + \frac{\partial v_0}{\partial y} & \frac{\partial \varrho_0}{\partial x} & \frac{\partial \varrho_0}{\partial y} & 0 & 0 \\ \frac{1}{\varrho_0} \left(u_0 \frac{\partial u_0}{\partial x} + v_0 \frac{\partial u_0}{\partial y} \right) & \frac{\partial u_0}{\partial x} & \frac{\partial u_0}{\partial y} & 0 & 0 \\ \frac{1}{\varrho_0} \left(u_0 \frac{\partial v_0}{\partial x} + v_0 \frac{\partial v_0}{\partial y} \right) & \frac{\partial v_0}{\partial x} & \frac{\partial v_0}{\partial y} & 0 & 0 \\ \frac{1}{\varrho_0} \left(u_0 \frac{\partial w_0}{\partial x} + v_0 \frac{\partial w_0}{\partial y} \right) & \frac{\partial w_0}{\partial x} & \frac{\partial w_0}{\partial y} & 0 & 0 \\ 0 & \frac{\partial p_0}{\partial x} & \frac{\partial p_0}{\partial y} & 0 & \gamma \left(\frac{\partial u_0}{\partial x} + \frac{\partial v_0}{\partial y} \right) \end{pmatrix} \quad (\text{A.14})$$

B. Supplemental material for the CAA method

B.1. Discretization schemes

This appendix summarizes the discretization schemes.

B.1.1. Spatial discretization

Consider a discretization of the form:

$$\frac{\partial \phi}{\partial \xi} \doteq \sum_{j=-N}^M a_j^{N,M} \phi_{l-j},$$

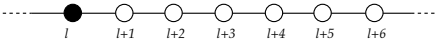
where l is the index the derivative is calculated for and the coefficients a_j are defined by the numerical scheme.

Central DRP

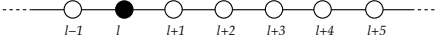
$$N = 3, M = 3 \quad \cdots \text{---} \underset{l-3}{\bigcirc} \text{---} \underset{l-2}{\bigcirc} \text{---} \underset{l-1}{\bigcirc} \text{---} \underset{l}{\bullet} \text{---} \underset{l+1}{\bigcirc} \text{---} \underset{l+2}{\bigcirc} \text{---} \underset{l+3}{\bigcirc} \text{---} \cdots$$

$$\begin{aligned} a_{-3}^{N=-3, M=3} &= -0.019408956520410941487537255049161731932458 \\ a_{-2}^{N=-3, M=3} &= 0.16096915941497709928348235352998026106316 \\ a_{-1}^{N=-3, M=3} &= -0.76371144926872137410435294191247532632895 \\ a_0^{N=-3, M=3} &= 0. \\ a_1^{N=-3, M=3} &= -a_{-1}^{N=-3, M=3} \\ a_2^{N=-3, M=3} &= -a_{-2}^{N=-3, M=3} \\ a_3^{N=-3, M=3} &= -a_{-3}^{N=-3, M=3} \end{aligned}$$

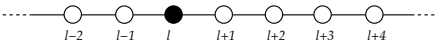
Optimized fourth order backward stencils

$N = 0, M = 6$ 

$$\begin{aligned} a_0^{N=0,M=6} &= -a_6^{N=6,M=0} = -2.2219902954809613859765704546589404 \\ a_1^{N=0,M=6} &= -a_5^{N=6,M=0} = 4.7937139708231946144678659038618207 \\ a_2^{N=0,M=6} &= -a_4^{N=6,M=0} = -4.8887154219014803402387769892811775 \\ a_3^{N=0,M=6} &= -a_3^{N=6,M=0} = 3.7241945556599418409859936218708754 \\ a_4^{N=0,M=6} &= -a_2^{N=6,M=0} = -1.9475764115885354499368986580520868 \\ a_5^{N=0,M=6} &= -a_1^{N=6,M=0} = 0.64080276257284296548277779947966337 \\ a_6^{N=0,M=6} &= -a_0^{N=6,M=0} = -0.10042916008504576552695652935653925 \end{aligned}$$

$N = 1, M = 5$ 

$$\begin{aligned} a_{-1}^{N=1,M=5} &= -a_5^{N=5,M=1} = -0.19275393397114015670013031922280788 \\ a_0^{N=1,M=5} &= -a_4^{N=5,M=1} = -1.1617462897578052505309642583597451 \\ a_1^{N=1,M=5} &= -a_3^{N=5,M=1} = 2.2833737916894651931443149806000292 \\ a_2^{N=1,M=5} &= -a_2^{N=5,M=1} = -1.4942869230903372823604513541795313 \\ a_3^{N=1,M=5} &= -a_1^{N=5,M=1} = 0.79138992627937021495654335012659431 \\ a_4^{N=1,M=5} &= -a_0^{N=5,M=1} = -0.2681591974297292679807469539809972 \\ a_5^{N=1,M=5} &= -a_{-1}^{N=5,M=1} = 0.042182626280174218003082842187723145 \end{aligned}$$

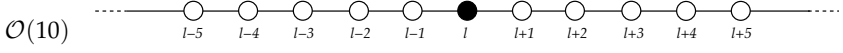
$N = 2, M = 4$ 

$$\begin{aligned} a_{-2}^{N=2,M=4} &= a_4^{N=4,M=2} = 0.043961792318923609279579522990388796 \\ a_{-1}^{N=2,M=4} &= a_3^{N=4,M=2} = -0.44665643971666746381288248812779784 \\ a_0^{N=2,M=4} &= a_2^{N=4,M=2} = -0.50947801953384086459664104040712118 \\ a_1^{N=2,M=4} &= a_1^{N=4,M=2} = 1.2919072955902599630917393369600177 \\ a_2^{N=2,M=4} &= a_0^{N=4,M=2} = -0.51171625718486879463853256311267614 \\ a_3^{N=2,M=4} &= a_{-1}^{N=4,M=2} = 0.1551341504041561236704183102119714 \\ a_4^{N=2,M=4} &= a_{-2}^{N=4,M=2} = -0.02315252187794980542889788921456784 \end{aligned}$$

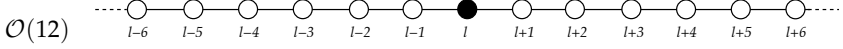
B.1.2. Temporal discretization

The two sets of coefficients for the alternating five/six stage Low-Dispersion Low-Dissipation Runge–Kutta scheme (LDDRK) are given below for the 2N-storage form, which has been implemented according to Stanescu and Habashi [121]:

$a_1^{(5)} =$	0;	$a_1^{(6)} =$	0
$a_2^{(5)} =$	-0.6051226;	$a_2^{(6)} =$	-0.4412737
$a_3^{(5)} =$	-2.0437564;	$a_3^{(6)} =$	-1.0739820
$a_4^{(5)} =$	-0.7406999;	$a_4^{(6)} =$	-1.7063570
$a_5^{(5)} =$	-4.4231765;	$a_5^{(6)} =$	-2.7979293
$a_6^{(5)} =$	—;	$a_6^{(6)} =$	-4.0913537
$b_1^{(5)} =$	0.2687454;	$b_1^{(6)} =$	0.1158488
$b_2^{(5)} =$	0.8014706;	$b_2^{(6)} =$	0.3728769
$b_3^{(5)} =$	0.5051570;	$b_3^{(6)} =$	0.7379536
$b_4^{(5)} =$	0.5623568;	$b_4^{(6)} =$	0.5798110
$b_5^{(5)} =$	0.0590065;	$b_5^{(6)} =$	1.0312849
$b_6^{(5)} =$	—;	$b_6^{(6)} =$	0.15
$c_1^{(5)} =$	0;	$c_1^{(5)} =$	0
$c_2^{(5)} =$	0.2687454;	$c_2^{(5)} =$	0.1158485
$c_3^{(5)} =$	0.5852280;	$c_3^{(5)} =$	0.3241850
$c_4^{(5)} =$	0.6827066;	$c_4^{(5)} =$	0.6193208
$c_5^{(5)} =$	1.1646854;	$c_5^{(5)} =$	0.8034472
$c_6^{(5)} =$	—;	$c_6^{(5)} =$	0.9184166.



$w_{-5}^{N=5} =$	$w_5^{N=5} =$	$-1/1024$
$w_{-4}^{N=5} =$	$w_4^{N=5} =$	$5/512$
$w_{-3}^{N=5} =$	$w_3^{N=5} =$	$-45/1024$
$w_{-2}^{N=5} =$	$w_2^{N=5} =$	$15/128$
$w_{-1}^{N=5} =$	$w_1^{N=5} =$	$-105/512$
$w_0^{N=5} =$	$=$	$63/256.$



$w_{-6}^{N=6} =$	$w_6^{N=6} =$	$1/4096$
$w_{-5}^{N=6} =$	$w_5^{N=6} =$	$-3/1024$
$w_{-4}^{N=6} =$	$w_4^{N=6} =$	$33/2048$
$w_{-3}^{N=6} =$	$w_3^{N=6} =$	$-55/1024$
$w_{-2}^{N=6} =$	$w_2^{N=6} =$	$495/4096$
$w_{-1}^{N=6} =$	$w_1^{N=6} =$	$-99/512$
$w_0^{N=6} =$	$=$	$231/1024.$

C. The effective impedance with flow

The boundary condition of Myers [85] allows an insight on which parameters influence the effective impedance of a surface. To obtain the effective impedance, all perturbations are assumed to be harmonic with angular frequency ω . Then Eq. (4.15) is rewritten into the following form:

$$Z = \frac{\hat{p}}{\hat{u}_n} + \frac{Z}{i\omega \hat{p}} \frac{\hat{p}}{\hat{u}_n} \mathbf{u}_0 \cdot \nabla \frac{\hat{p}}{Z} - \frac{\mathbf{n} \cdot (\mathbf{n} \cdot \nabla \mathbf{u}_0)}{i\omega} \frac{\hat{p}}{\hat{u}_n}. \quad (\text{C.1})$$

Defining the effective impedance as $Z' = \frac{\hat{p}}{\hat{u}_n}$ in the presence of a grazing mean flow, Eq. (C.1) can be written as:

$$Z' = \frac{\hat{p}}{\hat{u}_n} = Z / \left[1 + \frac{Z}{i\omega \hat{p}} \mathbf{u}_0 \cdot \nabla \frac{\hat{p}}{Z} - \frac{\mathbf{n} \cdot (\mathbf{n} \cdot \nabla \mathbf{u}_0)}{i\omega} \right], \quad (\text{C.2})$$

where Z' is the effective acoustic impedance. Z is the impedance in the original definition without flow and the mean flow does not alter this impedance as nonlinear effects are neglected for now. In practice there is a change of the impedance due to the grazing flow, which is considered to be a nonlinear effect. For a two-dimensional plane impedance wall oriented along the x -direction, as shown in Figure C.1, Eq. (C.2) can be simplified to:

$$Z' = Z / \left[1 + \frac{Z}{i\omega \hat{p}} \mathbf{u}_0 \cdot \nabla \left(\frac{\hat{p}}{Z} \right) \right]. \quad (\text{C.3})$$

This result can be directly derived from the Ingard [53] boundary condition. Eq. (C.2) and Eq. (C.3) constitute the basis for the calculation of the effective impedance.

If assuming plane harmonic waves in a plug-flow in the x -direction with unity amplitude ($e^{i(k_x x - \omega t)}$), Eq. (C.3) can be further simplified into the following form verified by Ju and Fung [61]:

$$\hat{u}_n = \frac{\hat{p}}{Z'}, \quad (\text{C.4a})$$

$$\text{where } Z' = Z / \left(1 - u_0 \frac{k_x}{\omega} \right) \quad (\text{C.4b})$$

$$= Z / \left(1 - \frac{u_0}{c} \frac{k_x}{k} \right) \quad (\text{C.4c})$$

$$= Z / (1 - M_x \cos \theta) \quad (\text{C.4d})$$

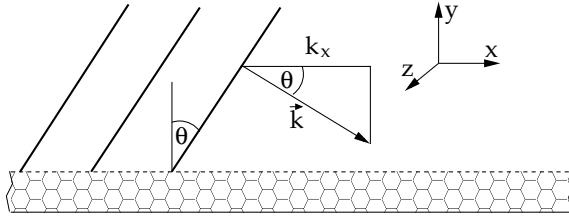


Figure C.1.: Sketch to visualize the incident angle in the effective impedance definition

denotes the effective plane-wave impedance with the incident wave angle, measured from the inner normal of the surface as shown in Fig. C.1, defined as $\theta = \cos^{-1}[k_x/k]$ depending on k and u_0 through k_x .

The result indicates, that the effective impedance of a surface depends on the angle θ , under which the acoustic waves impinge onto the surface. The normal incidence wave would feature a different effective impedance than any grazing incidence mode. The angle may even change along an uniform liner, leading to a variation of the effective impedance. Therefore, the measurement of the effective impedance has to be performed *in situ* such that the angle of incidence exactly matches the conditions under which the impedance surface is used. Furthermore, the flow velocity changes the effective impedance through M_x . This finally makes the effective impedance a very fragile definition, with nearly no practical relevance. However, the connection Eq. (C.2) puts up a possible method to obtain the effective impedance, which was applied by Li et al. [71].

D. Detailed resources for the impedance eduction

etailed plots comparing the experimental input for the objective function with the resulting numerical quantities from the impedance eduction are given in this appendix. In the first Section D.1, the sound pressure level along the opposite wall of the liner is considered for comparison. It is calculated as:

$$L_p = 20 \log_{10} \left(\frac{\hat{p}(f)}{\sqrt{2} \cdot 2 \cdot 10^{-5} \text{ Pa}} \right),$$

where $\hat{p}(f)$ denotes the complex perturbation pressure amplitude resulting from the Fourier transform of a data set with multiple time length of the full period time of f . The resulting sound pressure level is normalized by the first microphone of the experiment. The phase is considered to be the phase angle of the complex pressure amplitude \hat{p} . It is unfolded to fit the range of the experiment.

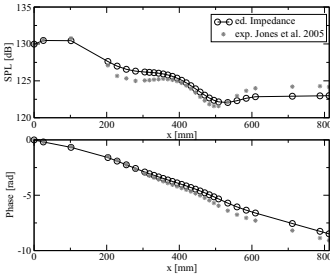
In the other two sections the energy transmission, reflection and dissipation are considered as input for the objective function. These quantities show a large dynamic range between 0 and 1. To obtain a better overview a decibel scale is applied:

$$L_{r,t,\Delta} = 10 \log_{10} ([t \mid r \mid \Delta]).$$

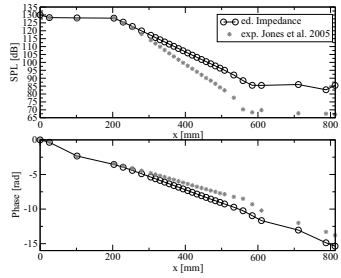
This decibel scale directly allows to calculate the transmission and reflection by adding the value to the source value. The dissipation describes the acoustic power, which is absorbed by the liner. $L_{\Delta} = 0$ dB would be a perfect absorbing liner with no transmission and reflection.

D.1. SPL and phase data comparison for the NASA-GIT experiment

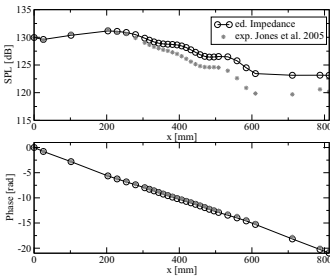
D.1.1. Uniform flow and anechoic terminations



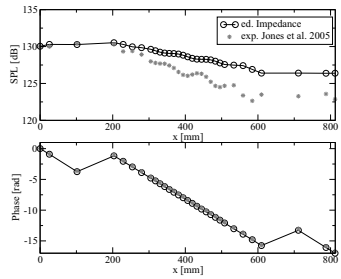
(a) $f = 500$ Hz



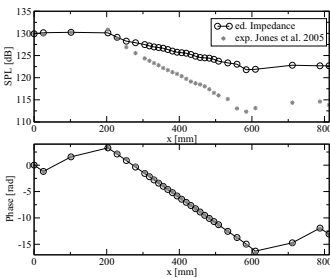
(b) $f = 1000$ Hz



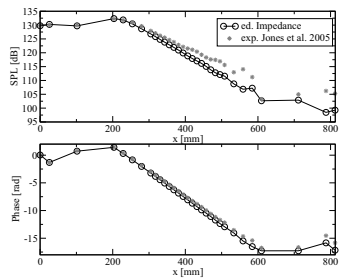
(c) $f = 1500$ Hz



(d) $f = 2000$ Hz

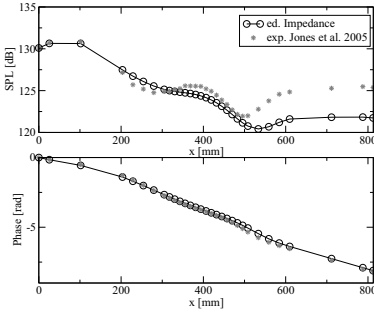


(e) $f = 2500$ Hz

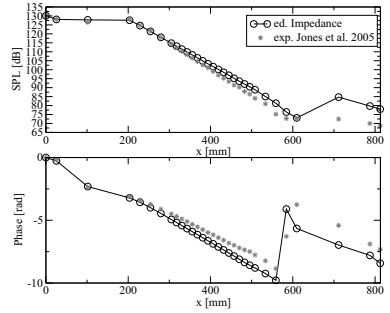


(f) $f = 3000$ Hz

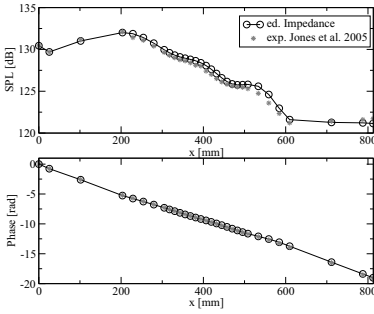
Figure D.1.: Comparison to the experiment of Jones et al. [57] without termination impedance, no flow



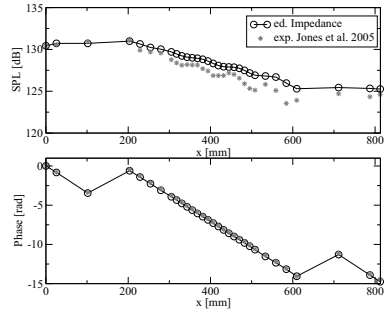
(a) $f = 500$ Hz



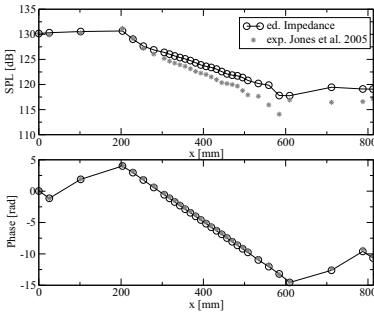
(b) $f = 1000$ Hz



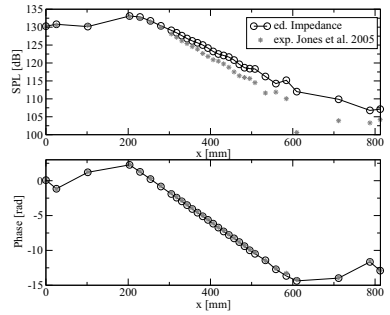
(c) $f = 1500$ Hz



(d) $f = 2000$ Hz



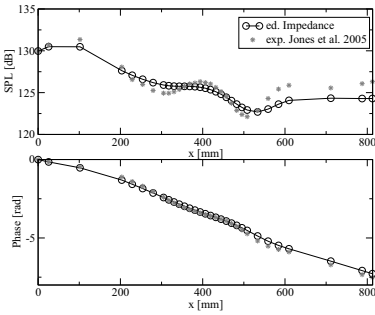
(e) $f = 2500$ Hz



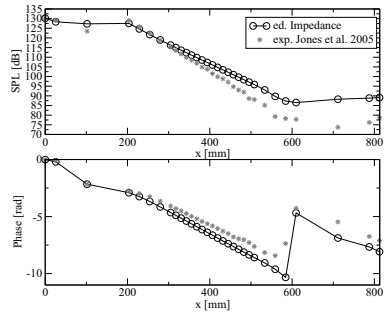
(f) $f = 3000$ Hz

Figure D.2.: Comparison to the experiment of Jones et al. [57] without termination impedance and plug flow, $Ma = 0.079$.

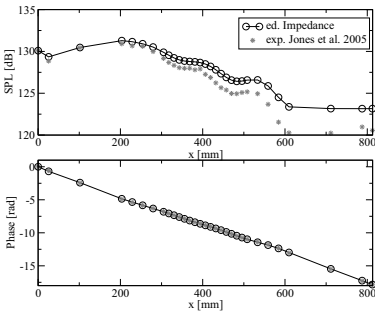
D. Detailed resources for the impedance eduction



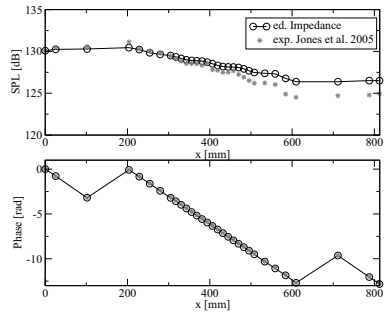
(a) $f = 500$ Hz



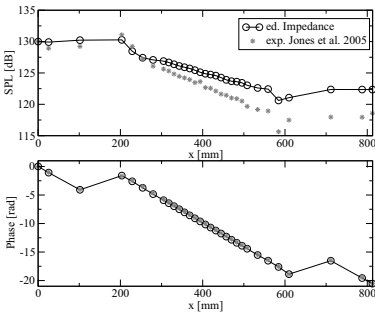
(b) $f = 1000$ Hz



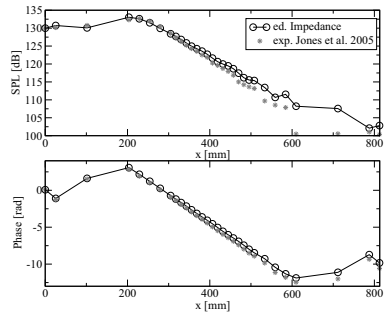
(c) $f = 1500$ Hz



(d) $f = 2000$ Hz

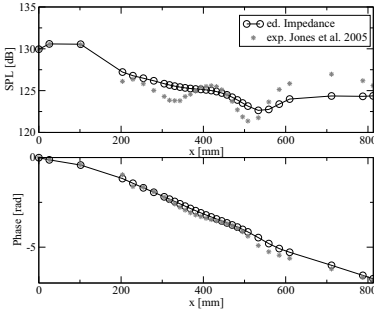


(e) $f = 2500$ Hz

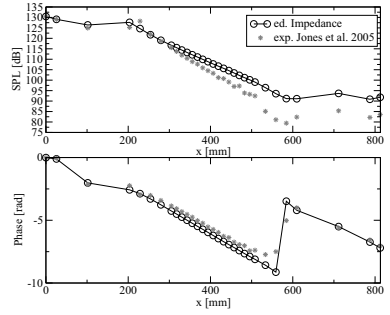


(f) $f = 3000$ Hz

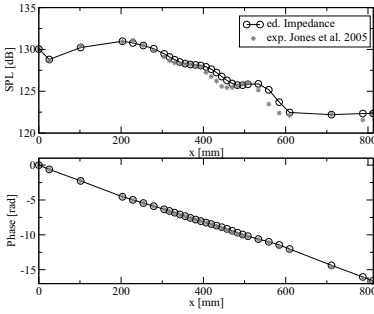
Figure D.3.: Comparison to the experiment of Jones et al. [57] without termination impedance and plug flow, $Ma = 0.172$.



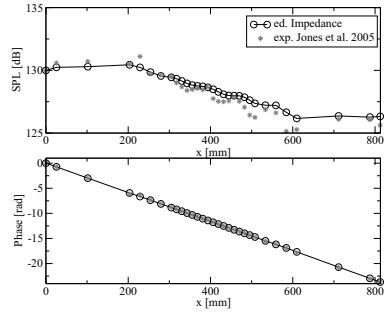
(a) $f = 500$ Hz



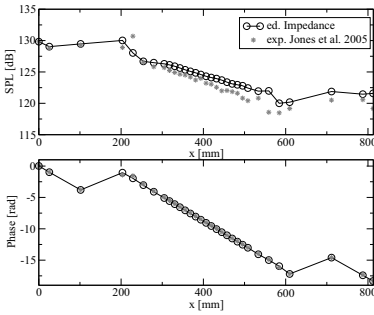
(b) $f = 1000$ Hz



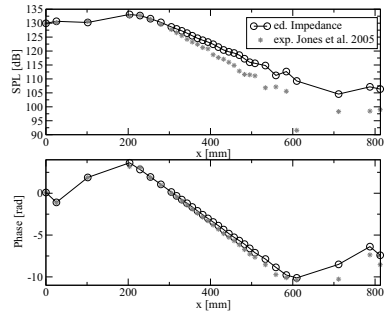
(c) $f = 1500$ Hz



(d) $f = 2000$ Hz

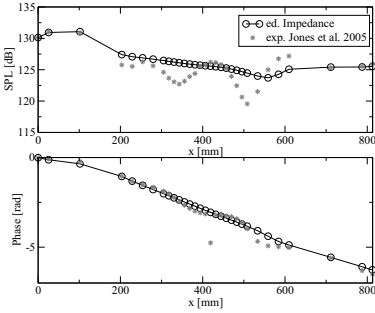


(e) $f = 2500$ Hz

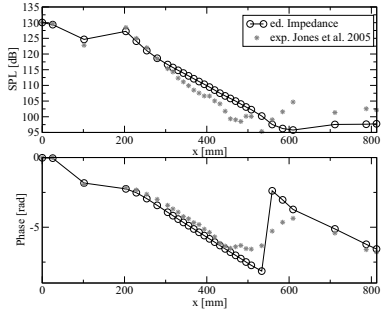


(f) $f = 3000$ Hz

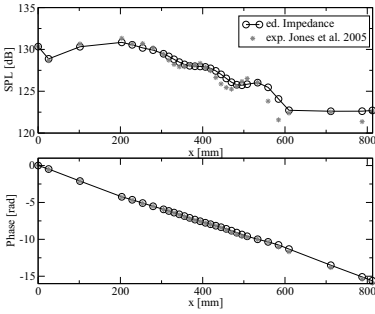
Figure D.4.: Comparison to the experiment of Jones et al. [57] without termination impedance and plug flow, $Ma = 0.255$.



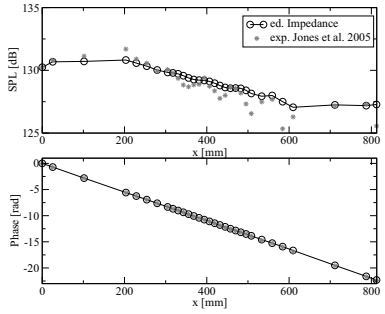
(a) $f = 500$ Hz



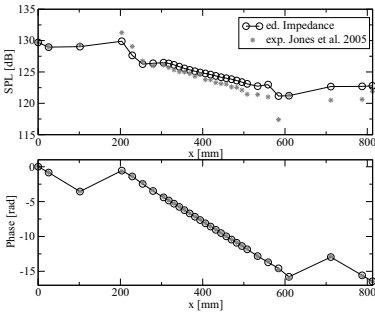
(b) $f = 1000$ Hz



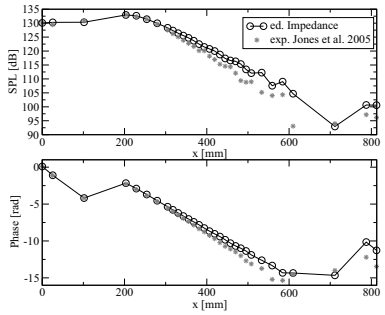
(c) $f = 1500$ Hz



(d) $f = 2000$ Hz



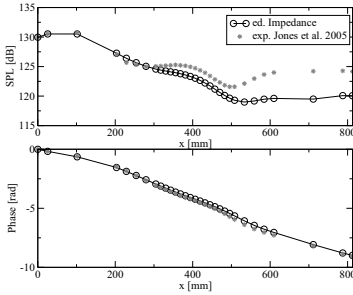
(e) $f = 2500$ Hz



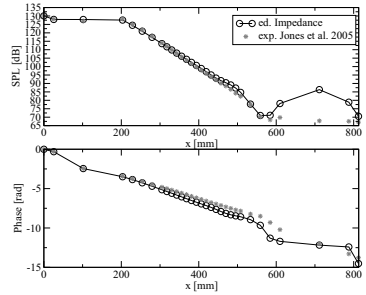
(f) $f = 3000$ Hz

Figure D.5.: Comparison to the experiment of Jones et al. [57] without termination impedance and plug flow, $Ma = 0.335$.

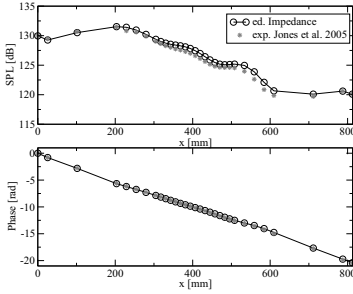
D.1.2. Uniform flow and measured termination impedance



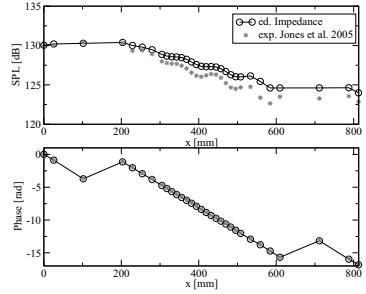
(a) $f = 500$ Hz



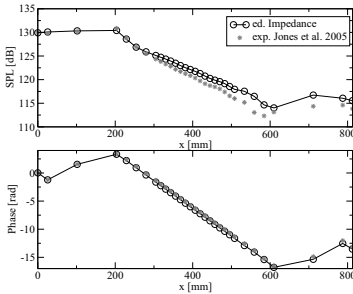
(b) $f = 1000$ Hz



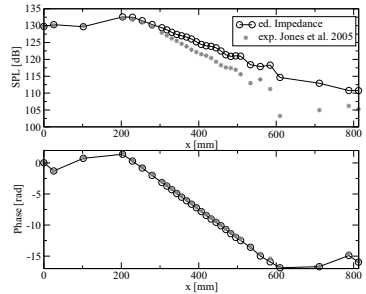
(c) $f = 1500$ Hz



(d) $f = 2000$ Hz



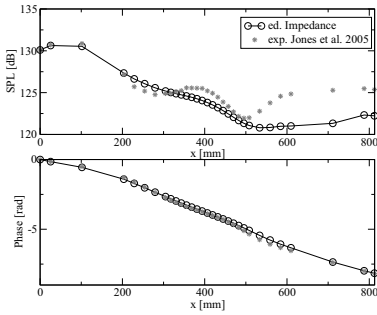
(e) $f = 2500$ Hz



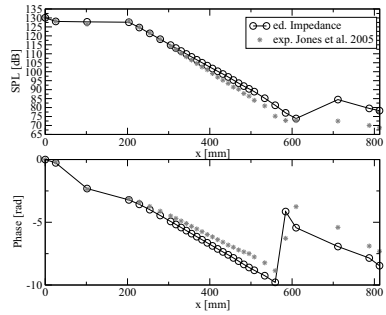
(f) $f = 3000$ Hz

Figure D.6.: Comparison to the experiment of Jones et al. [57] with termination impedance, no flow.

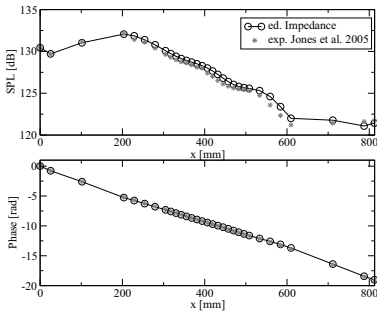
D. Detailed resources for the impedance eduction



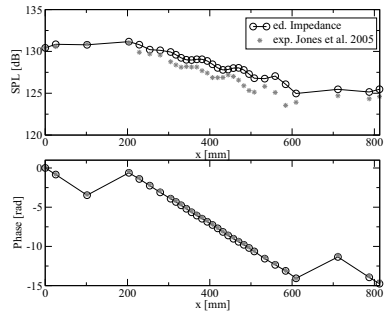
(a) $f = 500$ Hz



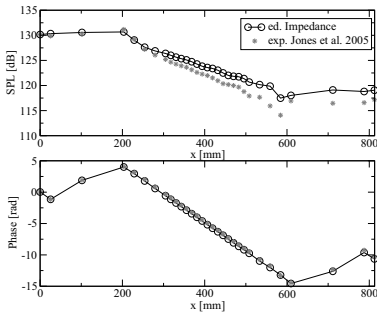
(b) $f = 1000$ Hz



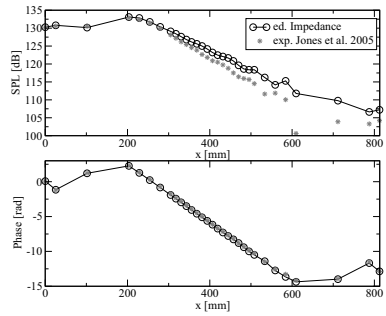
(c) $f = 1500$ Hz



(d) $f = 2000$ Hz

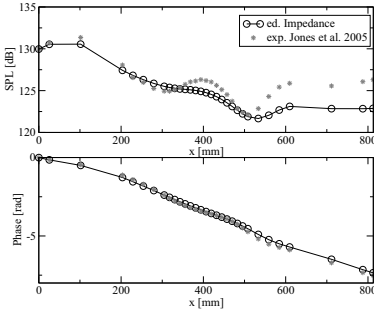


(e) $f = 2500$ Hz

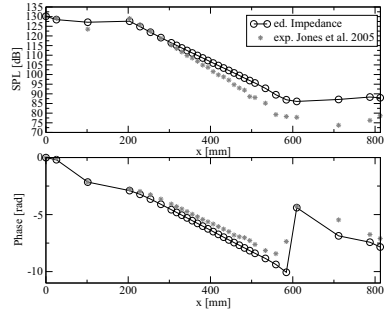


(f) $f = 3000$ Hz

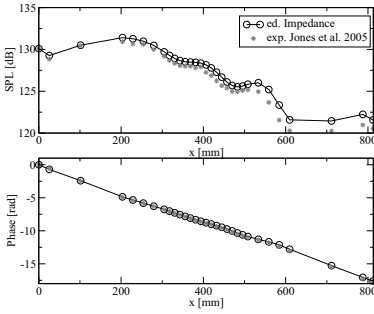
Figure D.7.: Comparison to the experiment of Jones et al. [57] with termination impedance and plug flow, $Ma = 0.079$.



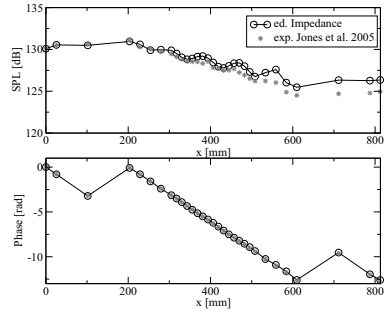
(a) $f = 500$ Hz



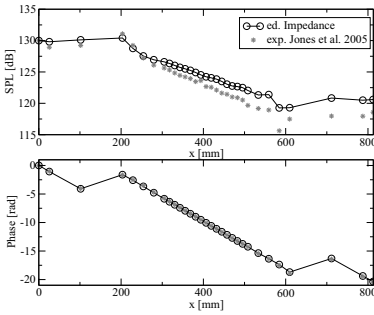
(b) $f = 1000$ Hz



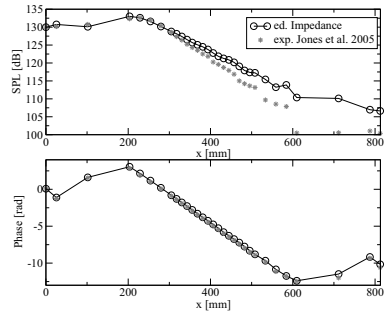
(c) $f = 1500$ Hz



(d) $f = 2000$ Hz



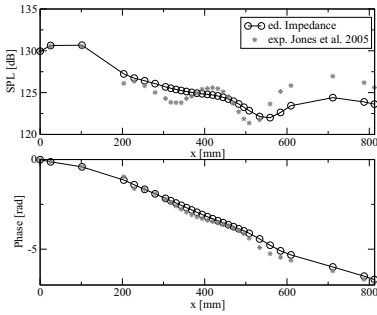
(e) $f = 2500$ Hz



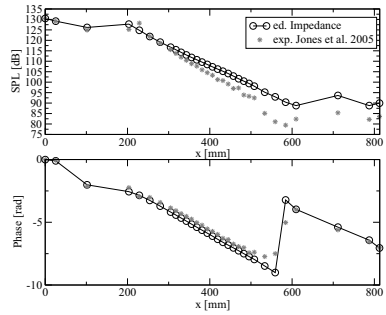
(f) $f = 3000$ Hz

Figure D.8.: Comparison to the experiment of Jones et al. [57] with termination impedance and plug flow, $Ma = 0.172$.

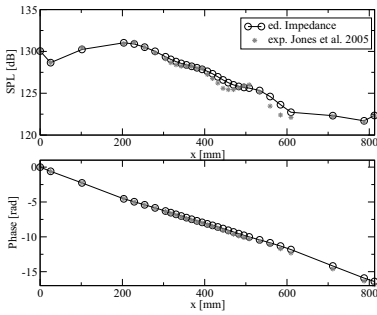
D. Detailed resources for the impedance eduction



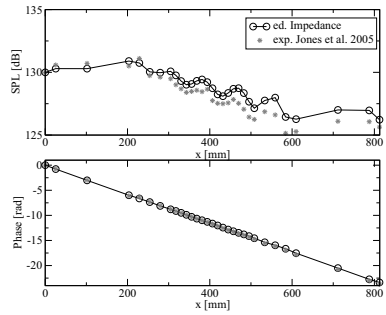
(a) $f = 500$ Hz



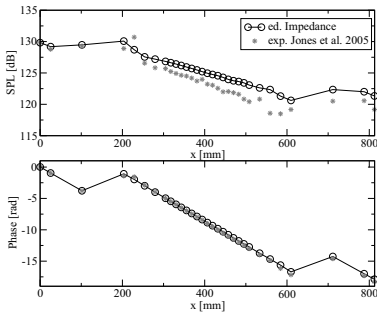
(b) $f = 1000$ Hz



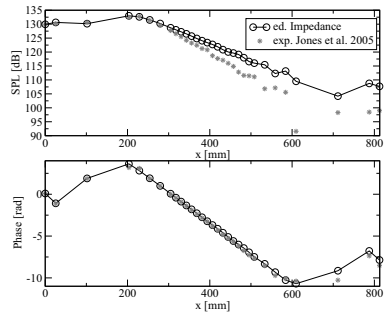
(c) $f = 1500$ Hz



(d) $f = 2000$ Hz

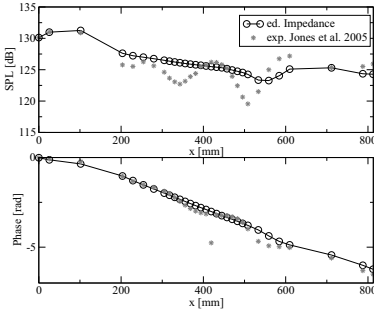


(e) $f = 2500$ Hz

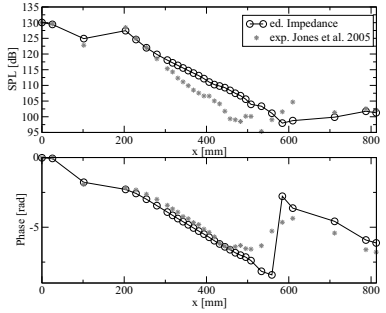


(f) $f = 3000$ Hz

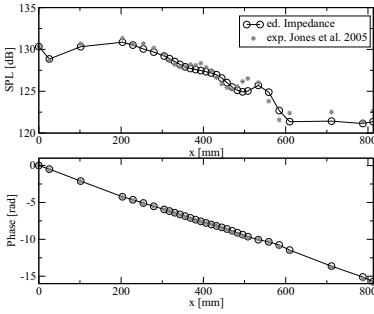
Figure D.9.: Comparison to the experiment of Jones et al. [57] with termination impedance and plug flow, $Ma = 0.255$.



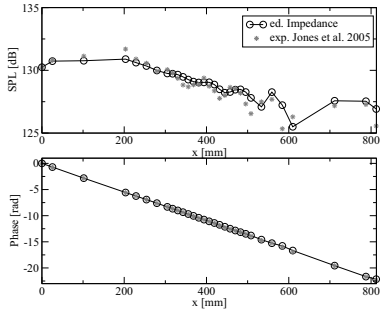
(a) $f = 500$ Hz



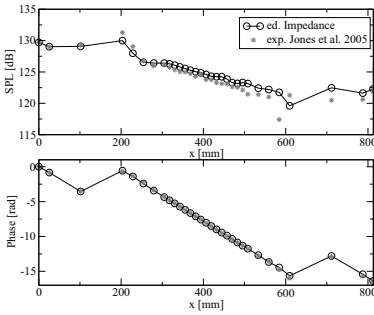
(b) $f = 1000$ Hz



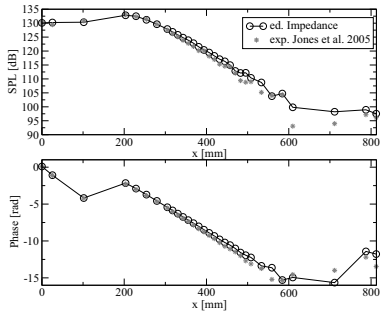
(c) $f = 1500$ Hz



(d) $f = 2000$ Hz



(e) $f = 2500$ Hz



(f) $f = 3000$ Hz

Figure D.10.: Comparison to the experiment of Jones et al. [57] with termination impedance and plug flow, $Ma = 0.335$.

D.1.3. Measured flow profile and termination impedance

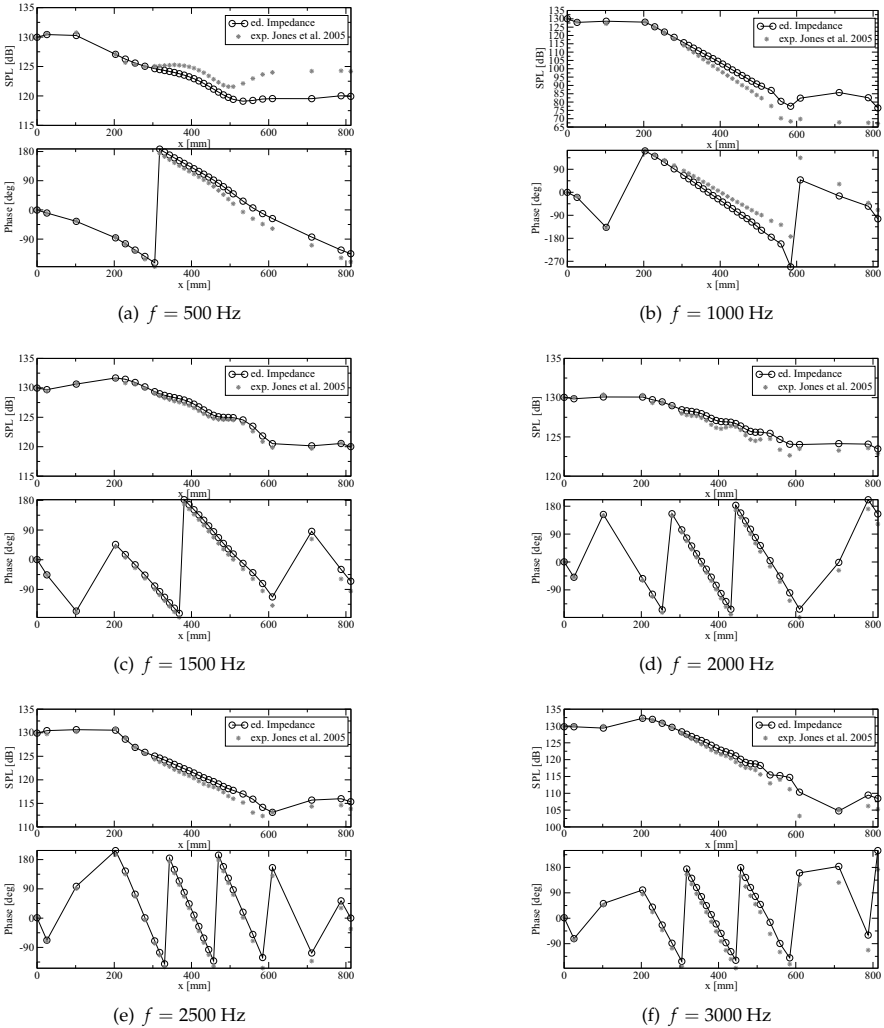
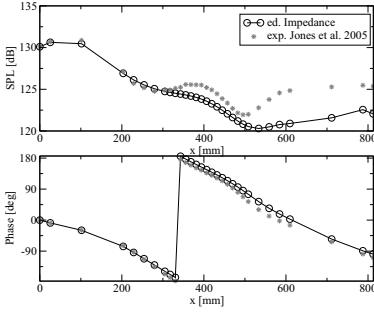
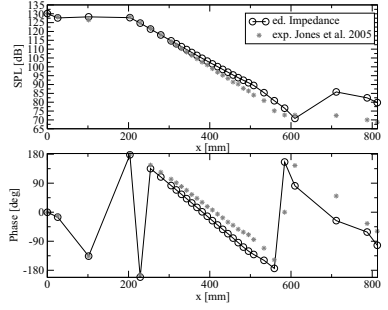


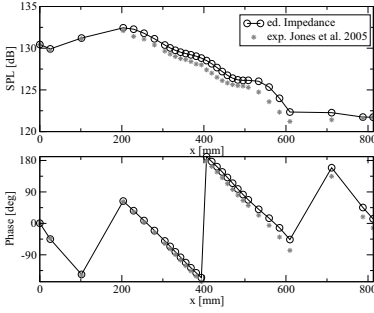
Figure D.11.: Comparison to the experiment of Jones et al. [57] with termination impedance and no flow.



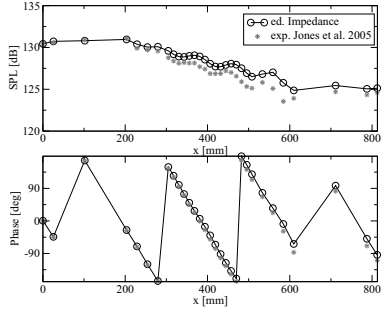
(a) $f = 500$ Hz



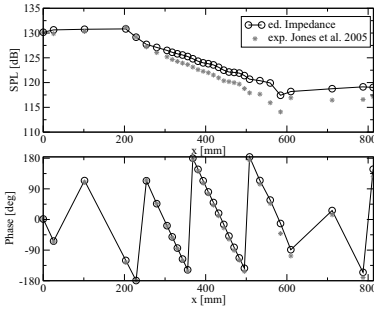
(b) $f = 1000$ Hz



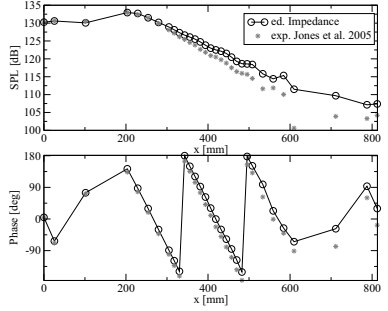
(c) $f = 1500$ Hz



(d) $f = 2000$ Hz



(e) $f = 2500$ Hz



(f) $f = 3000$ Hz

Figure D.12.: Comparison to the experiment of Jones et al. [57] with termination impedance and flow profile, $Ma = 0.079$.

D. Detailed resources for the impedance eduction

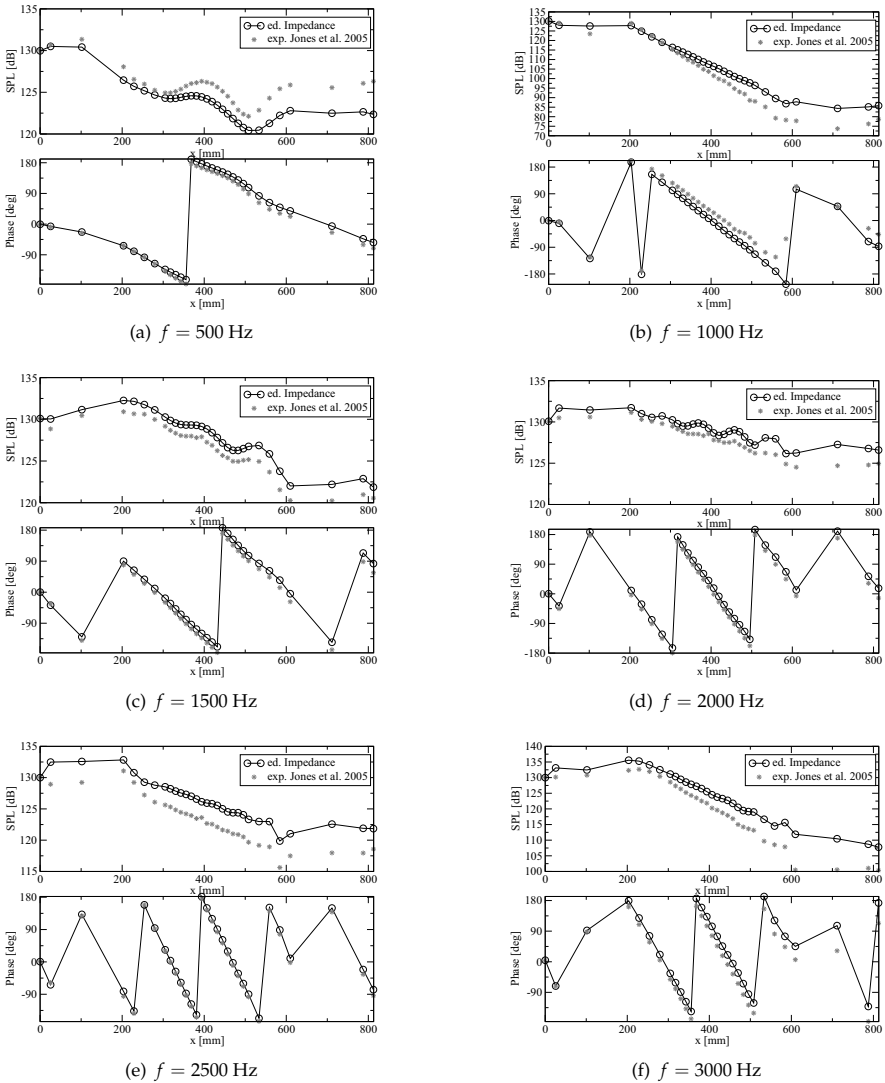
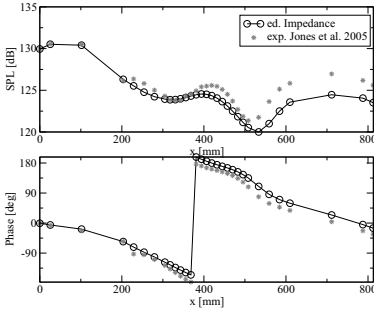
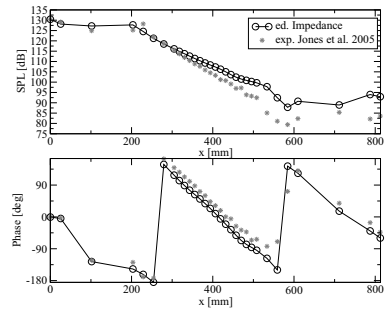


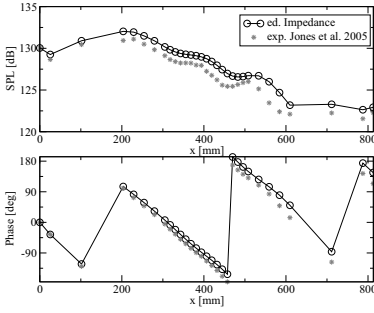
Figure D.13.: Comparison to the experiment of Jones et al. [57] with termination impedance and flow profile, $Ma = 0.172$.



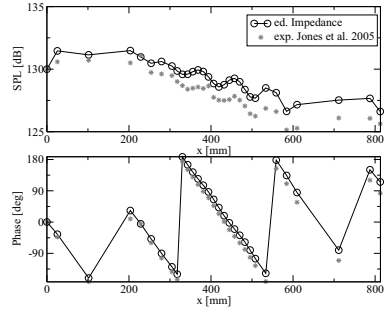
(a) $f = 500$ Hz



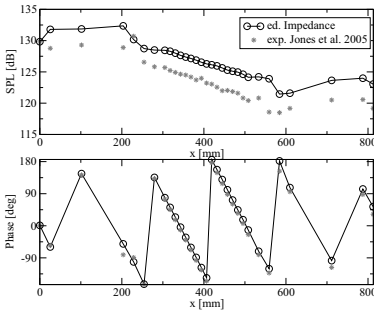
(b) $f = 1000$ Hz



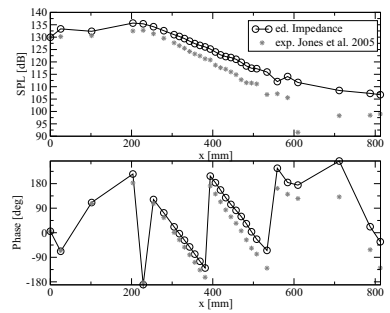
(c) $f = 1500$ Hz



(d) $f = 2000$ Hz



(e) $f = 2500$ Hz



(f) $f = 3000$ Hz

Figure D.14.: Comparison to the experiment of Jones et al. [57] with termination impedance and flow profile, $Ma = 0.255$.

D. Detailed resources for the impedance eduction

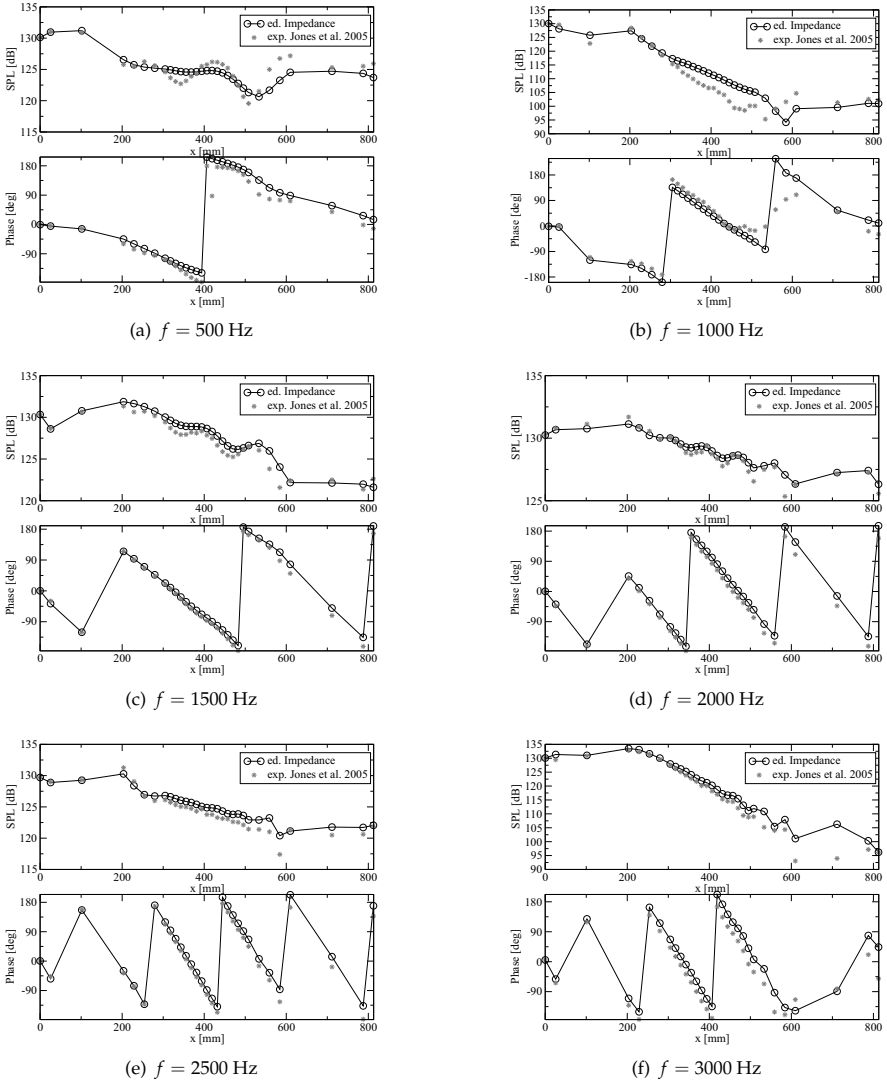


Figure D.15.: Comparison to the experiment of Jones et al. [57] with termination impedance and flow profile, $Ma = 0.335$.

D.2. Comparison of energy transmission, reflection and dissipation coefficients from the impedance eduction

D.2.1. Perforate SDOF liner (AA-1)

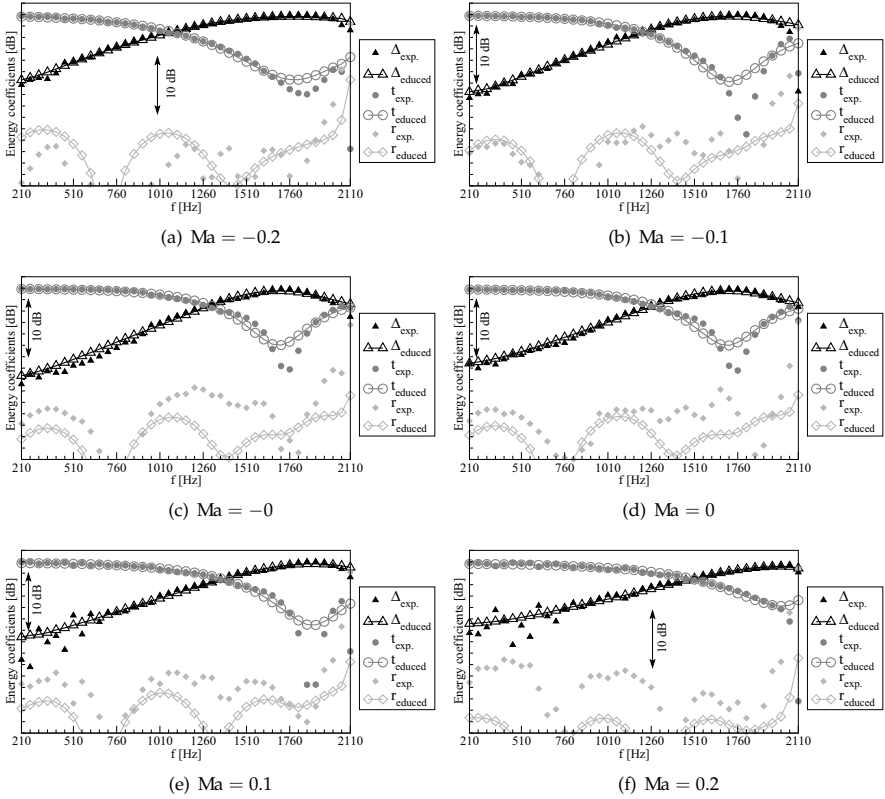


Figure D.16.: Comparison of the resulting energy transmission and dissipation coefficients to the experimental result of Busse et al. [22] for sample AA-1.

D.2.2. SDOF liner with wire mesh (AA-2)

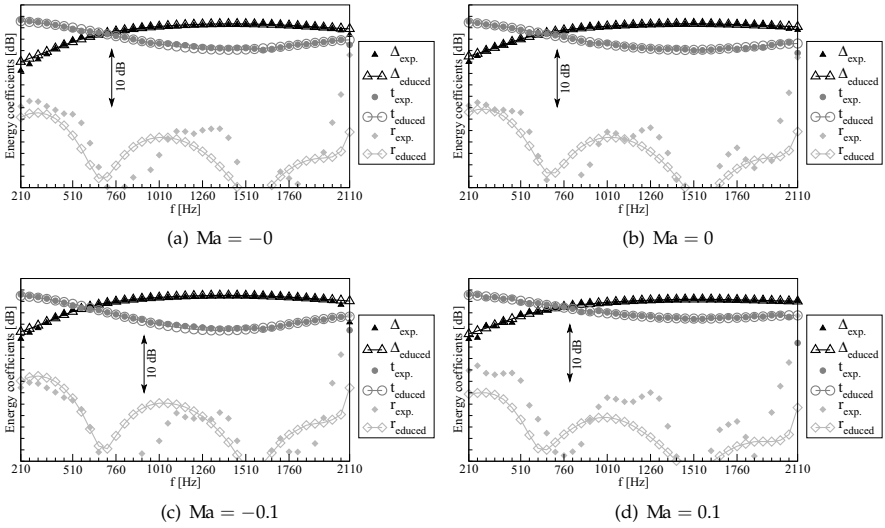


Figure D.17.: Comparison of the resulting energy transmission and dissipation coefficients to the experimental result of Busse et al. [22] for sample AA-2.

D.2.3. Axisymmetric samples with large cavity volume (DLR-1C)

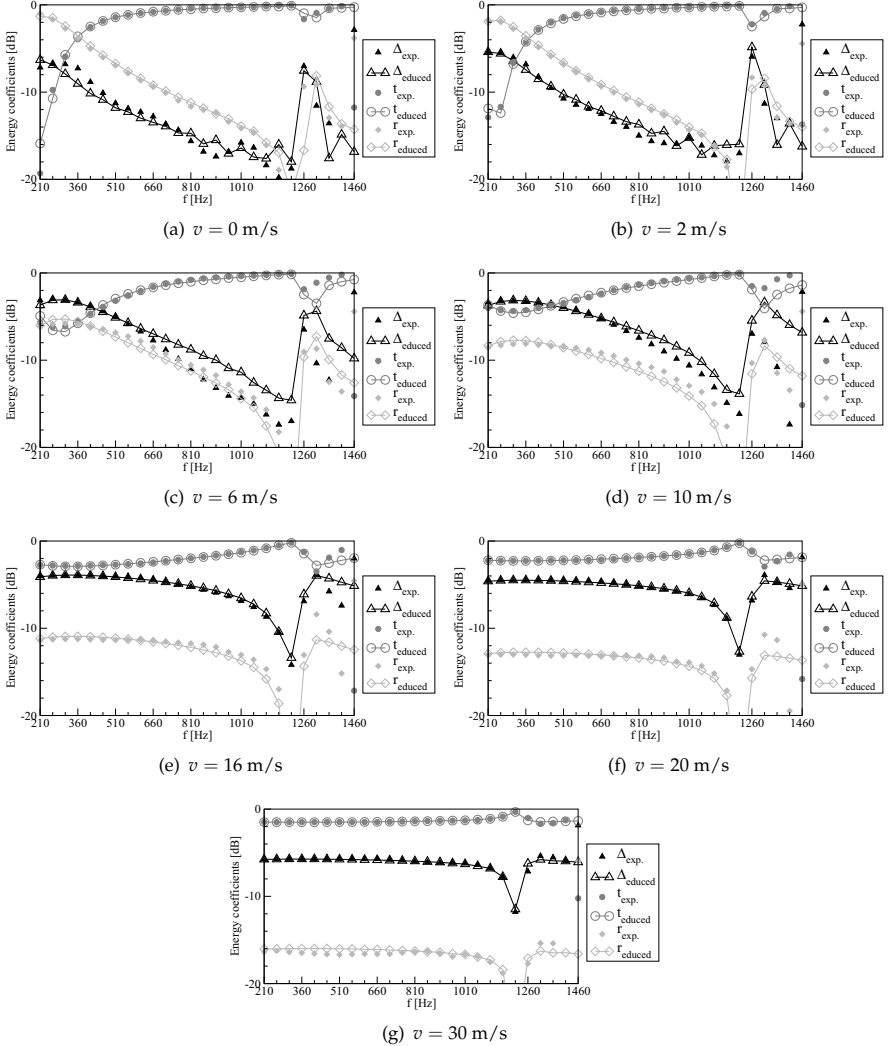


Figure D.18.: Comparison of the resulting energy transmission and dissipation coefficients to the experimental result of Heuwinckel [46] for $\text{Ma} = 0$.

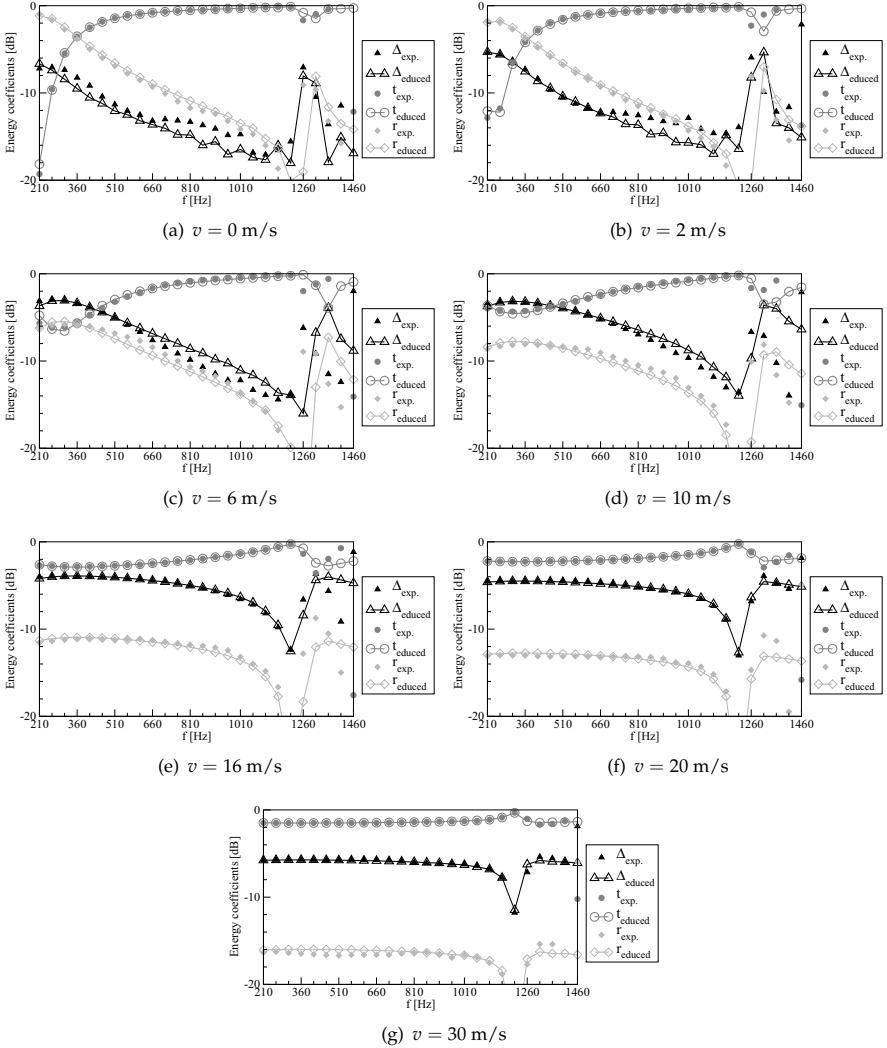


Figure D.19.: Comparison of the resulting energy transmission and dissipation coefficients to the experimental result of Heuwinkel [46] for $Ma = -0$.

D.2. Comparison of energy transmission, reflection and dissipation coefficients

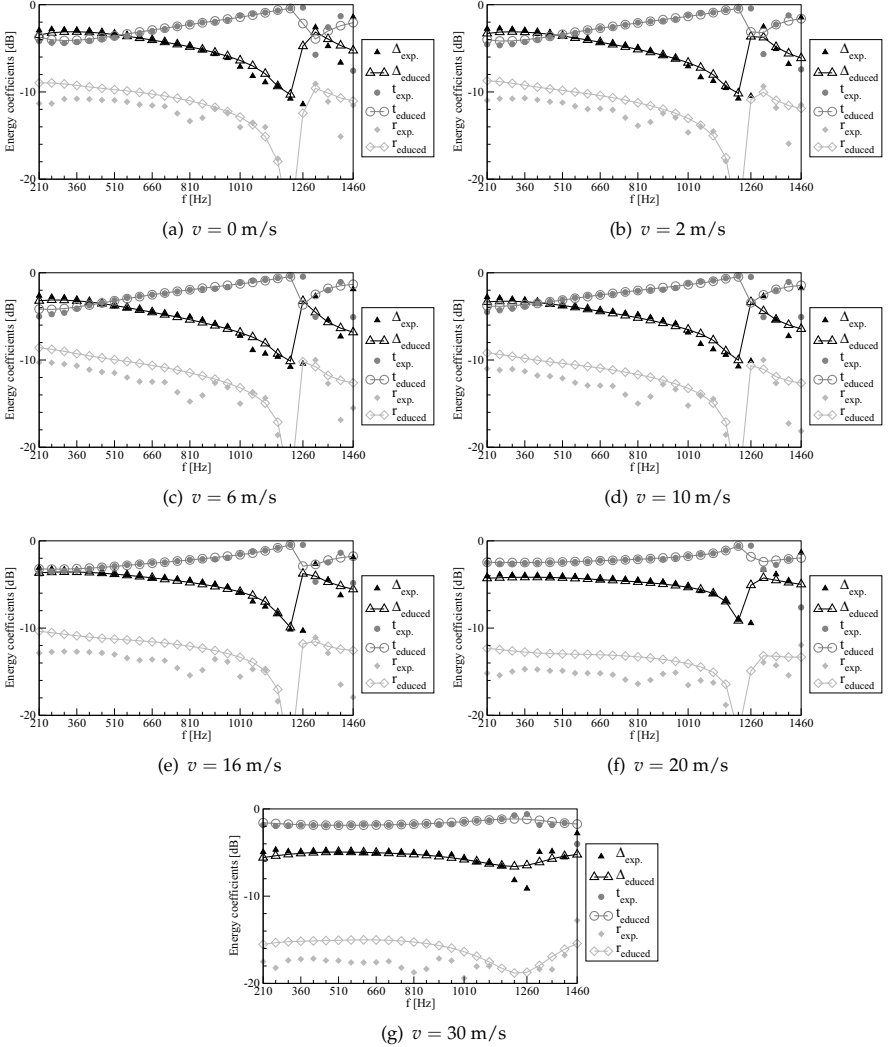


Figure D.20.: Comparison of the resulting energy transmission and dissipation coefficients to the experimental result of Heuwinckel [46] for $Ma = -0.1$.

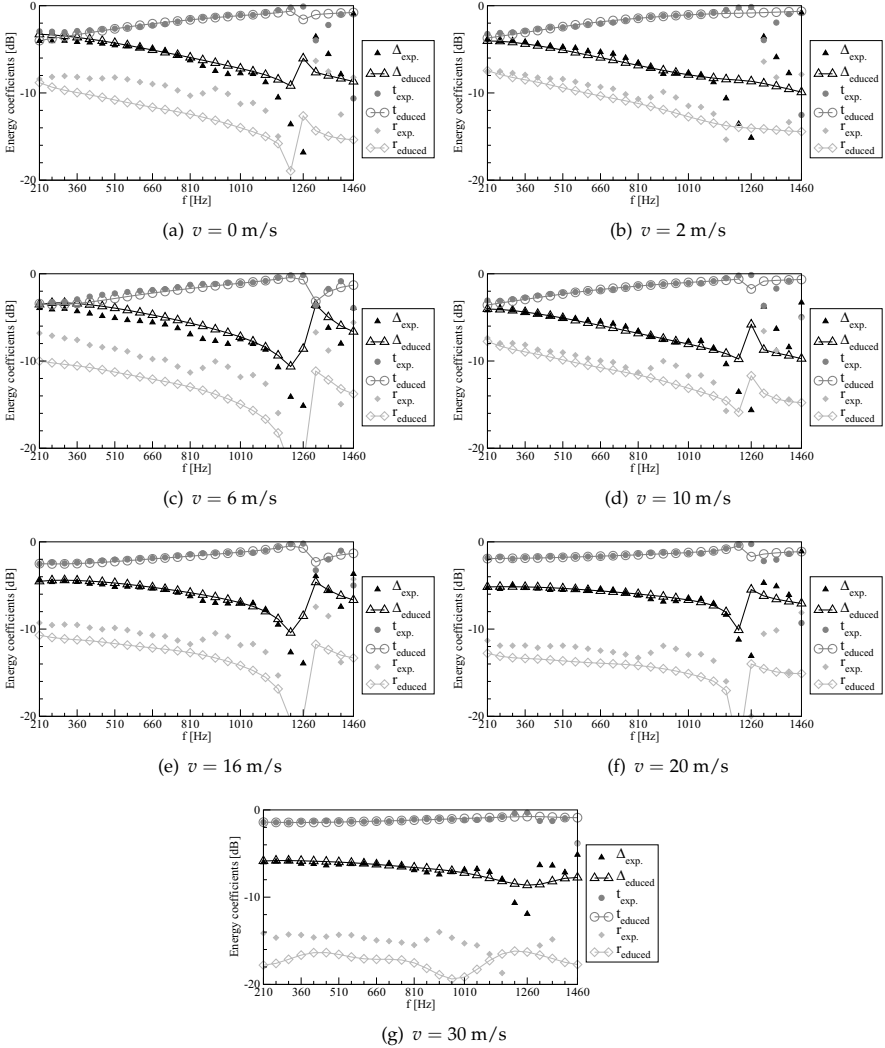


Figure D.21.: Comparison of the resulting energy transmission and dissipation coefficients to the experimental result of Heuwinkel [46] for $\text{Ma} = 0.1$.

Bibliography

- [1] S. Abarbanel and D. Gottlieb. "A Mathematical Analysis of the PML Method." *Journal of Computational Physics*, **134**, 357–363. 1997.
- [2] S. Abarbanel, D. Gottlieb, and J. S. Hesthaven. "Well-posed Perfectly Matched Layers for Advective Acoustics." *Journal of Computational Physics*, **154**, 266–283. 1997.
- [3] M. Abramowitz and I. A. Stegun, eds. *Handbook of Mathematical Functions*. Applied Mathematics Series 55. National Bureau of Standards, Washington. URL <http://www.math.sfu.ca/~cbm/aands/>, tenth printing, December 1972, with corrections. 1972.
- [4] M. Alster. "Improved Calculation of Resonant Frequencies of Helmholtz Resonators." *Journal of Sound and Vibration*, **24(1)**, 63–85. 1972.
- [5] N. Andersson, L.-E. Eriksson, and L. Davidson. "Large-Eddy Simulation of Subsonic Turbulent Jets and Their Radiated Sound." *AIAA Journal*, **43(9)**, 1899–1912. 2005.
- [6] F. Bake, N. Kings, and I. Röhle. "Experimental Investigation of the Fundamental Entropy Noise Mechanisms in Aero-Engines." In "11th CEAS-ASC Workshop, Experimental and Numerical Analysis and Prediction of Combustion Noise," CEAS-ASC, Lisbon, Portugal. Paper 12. 2007.
- [7] F. Bake, U. Michel, and I. Röhle. "Investigation of Entropy Noise in Aero-Engine Combustors." In "ASME Turbo Expo 2006," GT2006-90093. ASME, Barcelona, Spain. 2006.
- [8] A. B. Bauer and R. L. Chapkis. "Noise Generated by Boundary-Layer Interaction with Perforated Acoustic Liners." *Journal of Aircraft*, **14(2)**, 157–160. 1977.
- [9] J.-P. Berenger. "A perfectly matched layer for the absorption of electromagnetic waves." *Journal of Computational Physics*, **114**, 185–200. 1994.
- [10] D. I. Blokhintsev. *Acoustics of a nonhomogeneous moving medium*. National Advisory Committee for Aeronautics, Washington. 1956.
- [11] C. Bogey and C. Bailly. "Three-dimensional non-reflective boundary conditions for acoustic simulations: Far field formulation and validation test cases." *Acta Acustica united with Acoustica*, **88**, 462–471. 2002.

- [12] C. Bogey and C. Bailly. "A family of low dispersive and low dissipative explicit schemes for flow and noise computations." *Journal of Computational Physics*, **194**, 194–214. 2004.
- [13] G. Boudier, N. Lamarque, C. Sensieau, G. Staffelbach, L. Gicquel, T. Poisson, and V. Moureau. "Investigating the Thermo-Acoustic Stability of a Full Gas Turbine Combustion Chamber Using Large Eddy Simulation." In "11th CEAS-ASC Workshop, Experimental and Numerical Analysis and Prediction of Combustion Noise," CEAS-ASC, Lisbon, Portugal. Paper 6. 2007.
- [14] E. J. Brambley. "Models for Acoustically-Lined Turbofan Ducts." AIAA Paper 2008–2879. 2008.
- [15] E. J. Brambley and N. Peake. "Classification of aeroacoustically relevant surface modes in cylindrical lined ducts." *Wave Motion*, **43**, 301–310. 2006.
- [16] E. J. Brambley and N. Peake. "Surface-Waves, Stability, and Scattering for a Lined Duct with Flow." AIAA Paper 2006–2688. 2006.
- [17] E. J. Brambley and N. Peake. "Stability and acoustic scattering in a cylindrical thin shell containing compressible mean flow." *Journal of Fluid Mechanics*, **602**, 403–426. 2008.
- [18] M. C. Brenner and J. J. Fitzgibbon. "Surface Acoustic Wave Touch Panel System." US Patent US4644100 (A) 1987-02-17, Canadian Patent CA1277004 (C) 1990-11-27. 1987.
- [19] P. T. Bui, W. Schröder, and W. Meinke. "Source term evaluation of the APE-RF system." AIAA Paper 2008–2678. 2008.
- [20] M. O. Burak, M. Billson, L.-E. Eriksson, and S. Baralon. "Validation of a Time & Frequency Domain Grazing Flow Acoustic Liner Model." *AIAA Journal*, **47(8)**, 1841–1848. 2008.
- [21] C. Buske, C. Richter, F. Thiele, C. Yu, and M. Zhuang. "Validation of a Zonal Method Computing the Sound Radiation from Lined Ducts." AIAA Paper 2009–3169. 2009.
- [22] S. Busse, C. Richter, F. Thiele, C. Heuwinkel, L. Enghardt, I. Röhle, U. Michel, P. Ferrante, and A. Scofano. "Impedance Deduction Based on Insertion Loss Measurements of Liners under Grazing Flow Conditions." AIAA Paper 2008–3014. 2008.
- [23] R. H. Byrd, J. C. Gilbert, and J. Nocedal. "A Trust Region Method Based on Interior Point Techniques for Nonlinear Programming." *Mathematical Programming*, **89(1)**, 149–185. 2000.

-
- [24] N. Chevaugnon, J.-F. Remacle, and X. Gallez. "Discontinuous Galerkin Implementation Of The Extended Helmholtz Resonator Model In Time Domain." AIAA Paper 2006-2569. 2006.
- [25] B.-T. Chu and L. S. G. Kovásznyai. "Non-linear Interactions in a viscous heat-conducting compressible gas." *Journal of Fluid Mechanics*, **3(2)**, 494-514. 1958.
- [26] E. Commission. "White Paper - 'European Transport Policy for 2010: time to decide'." Technical report, Luxembourg. URL http://ec.europa.eu/transport/white_paper/documents/doc/lb_com_2001_0370_en.pdf. 2001.
- [27] T. E. Commission. "European Aeronautics: A Vision for 2020." Technical report. URL <http://www.acare4europe.org/html/documentation.asp>. 2001.
- [28] A. Demir and S. W. Rienstra. "Sound Radiation from an Annular Duct with Jet Flow and a Lined Centerbody." AIAA Paper 2006-2718. 2006.
- [29] DIN 52215 (ISO 10534). "Schallabsorptionsgrad im Rohr."
- [30] K. Ehrenfried. "Absorbing Boundary Conditions for a Linear Hyperbolic System with Uniformly Characteristic Boundary." AIAA Paper 2004-2968. 2004.
- [31] K. Ehrenfried. *Strömungsakustik*. Mensch und Buch Verlag AG, Berlin. ISBN 3-89820-699-8. 2004.
- [32] K. Ehrenfried. Private communication about the source location by using the acoustic intensity. 2008.
- [33] W. Eversman. "Acoustic Power in Lined Ducts." AIAA Paper 2004-2904. 2004.
- [34] R. Ewert and W. Schröder. "Acoustic perturbation equations based on flow decomposition via source filtering." *Journal of Computational Physics*, **188**, 365-398. 2003.
- [35] J. E. Ffowcs-Williams and D. L. Hawkings. "Theory relating the noise of rotating machinery." *Journal of Sound and Vibration*, **10(1)**, 10-20. 1969.
- [36] H. V. Fuchs. *Schallabsorber und Schalldämpfer*. Springer, Berlin, Heidelberg, New-York. ISBN 3-540-35493-X. 2004.
- [37] K.-Y. Fung and H. Ju. "Time domain impedance boundary conditions." *International Journal of Computational Fluid Dynamics*, **18**, 503-511. 2004.
- [38] K.-Y. Fung and H. B. Ju. "Broadband time-domain impedance models." *AIAA Journal*, **39(8)**, 1449-1454. 2001.

- [39] K.-Y. Fung, H. B. Ju, and B. Tallapragada. "Impedance and its time-domain extensions." *AIAA Journal*, **38(1)**, 30–38. 2000.
- [40] M. B. Giles. "Nonreflecting Boundary Conditions for Euler Equations Calculations." *AIAA Journal*, **28(12)**, 2050–2058. 1990.
- [41] J. Großer. *Modellbildung für die Schallverstärkung in nachgiebig ausgekleideten Stomungskanälen*. Ph.D. thesis, Georg-August-Universität zu Göttingen. 2003.
- [42] J. C. Hardin and S. L. Lamkin. "Aeroacoustic Computation of Cylinder Wake Flow." *AIAA Journal*, **22(1)**, 51–57. 1984.
- [43] J. C. Hardin and S. L. Lamkin. "Computational aeroacoustics - Present status and future promise." In "Aero- and hydro-acoustics; Proceedings of the Symposium, Ecully, France, July 3-6, 1985 (A87-13585 03-71). Berlin and New York, Springer-Verlag, 1986, p. 253-259.", (253–259). 1986.
- [44] H. von Helmholtz. *Die Lehre von den Tonempfindungen als physiologische Grundlage für die Theorie der Musik*. F. Vieweg, Braunschweig. URL <http://vlp.mpiwg-berlin.mpg.de/references?id=lit3483>, the Virtual Laboratory Max-Planck-Institute for the History of Science, Berlin. 1863.
- [45] J. S. Hesthaven. "On the analysis and construction of perfectly matched layers for the linearized Euler equations." *Journal of Computational Physics*, **142**, 129–147. 1998.
- [46] C. Heuwinkel. "Experimentelle Untersuchung der akustischen Eigenschaften perforierter Liner." Diplomarbeit, Technische Universität Berlin. 2006.
- [47] C. Heuwinkel, L. Enghardt, and I. Röhle. "Experimental investigation of the acoustic damping of perforated liners with bias flow." *AIAA Paper* 2007-3525. 2007.
- [48] F. Q. Hu. "On Absorbing Boundary Conditions for Linearized Euler Equations by a Perfectly Matched Layer." *Journal of Computational Physics*, **129**, 201–219. 1996.
- [49] F. Q. Hu. "A Stable Perfectly Matched Layer For Linearized Euler Equations In Unsplit Physical Variables." *Journal of Computational Physics*, **173(2)**, 455–480. 2001.
- [50] F. Q. Hu, M. Y. Hussaini, and J. L. Manthey. "Low-dissipation and Low-dispersion Runge-Kutta Schemes for Computational Acoustics." *Journal of Computational Physics*, **124(1)**, 177–191. 1996.
- [51] F. Q. Hu, X. D. Li, and D. K. Lin. "PML absorbing boundary condition for non-linear aeroacoustics problems." *AIAA Paper* 2006–2521. 2006.

-
- [52] A. Huber and W. Polifke. "Impact of Fuel Supply Impedance on Combustion Stability of Gas Turbines." In "ASME Turbo Expo, GT2008-51193," Berlin, Germany. 2008.
- [53] U. Ingard. "Influence of fluid motion past a plane boundary on sound reflection, absorption, and transmission." *Journal of the Acoustical Society of America*, **31(7)**, 1035–1036. 1959.
- [54] M. Israeli and S. A. Orszag. "Approximation of radiation boundary condition." *Journal of Computational Physics*, **41(1)**, 115–135. 1981.
- [55] M. G. Jones, T. L. Parrott, and W. R. Watson. "Comparison of Acoustic Impedance Education Techniques for Locally-Reacting Liners." AIAA Paper 2003–3306. 2003.
- [56] M. G. Jones, M. B. Tracy, W. R. Watson, and T. L. Parrott. "Effects of Liner Geometry on Acoustic Impedance." AIAA Paper 2002–2446. 2002.
- [57] M. G. Jones, W. R. Watson, and T. L. Parrott. "Benchmark Data for Evaluation of Aeroacoustic Propagation Codes with Grazing Flow." AIAA Paper 2005–2853. 2005.
- [58] M. G. Jones, W. R. Watson, and T. L. Parrott. "Comprehensive Benchmark Data for Evaluation of Aeroacoustic Propagation Codes with Grazing Flow." Private communication of additional data for the liner considered in AIAA Paper 2005–2853. 2005.
- [59] M. G. Jones, W. R. Watson, T. L. Parrott, and C. Smith. "Design and Evaluation of Modifications to the NASA Langley Flow Impedance Tube." AIAA Paper 2004–2837. 2004.
- [60] M. G. Jones, W. R. Watson, M. B. Tracy, and T. L. Parrott. "Comparison of Two Waveguide Methods for Educing Liner Impedance in Grazing Flow." *AIAA Journal*, **42(2)**, 232–240. 2004.
- [61] H. Ju and K.-Y. Fung. "Time-domain impedance boundary conditions with mean flow effects." *AIAA Journal*, **39(9)**, 1683–1690. 2001.
- [62] M. Jüschke and D. Ronneberger. "Akustische Beeinflussung des Druckabfalls im durchströmten Rohr." In "DAGA - 33rd German Annual Conference on Acoustics," Stuttgart, Germany. 2007.
- [63] S.-H. Ko. "Sound attenuation in lined rectangular ducts and its application to the reduction of aircraft engine noise." *Journal of the Acoustical Society of America*, **50(6, Part 1)**, 1418–1432. doi:10.1121/1.1912784. 1971.

- [64] W. Koch. "Radiation of sound from a two-dimensional acoustically lined duct." *Journal of Sound and Vibration*, **55(2)**, 255–274. doi:10.1016/0022-460X(77)90598-3. 1977.
- [65] J. W. Kooi and S. L. Sarin. "An Experimental Study of the Acoustic Impedance of Helmholtz Resonator Arrays Under a Turbulent Boundary Layer." AIAA Paper 1981–1998. 1981.
- [66] R. Lanoye, G. Vermeir, W. Lauriks, R. Kruse, and V. Mellert. "Measuring the free field acoustic impedance and absorption coefficient of sound absorbing materials with a combined particle velocity-pressure sensor." *Journal of the Acoustical Society of America*, **119(5)**, 2826–2831. doi:10.1121/1.2188821. 2006.
- [67] S. K. Lele. "Compact Finite Difference Schemes with Spectral-like Resolution." *Journal of Computational Physics*, **103**, 16–42. 1992.
- [68] H. C. Lester and T. L. Parrott. "Application of a finite element method for computing grazing incidence wave structure in an impedance tube - Comparison with experiment." AIAA Paper 1979–664. 1979.
- [69] H. C. Lester and T. L. Parrott. "Comparison of Measured and Predicted Impedance at Grazing Incidence." *AIAA Journal*, **18(5)**, 504–508. 1980.
- [70] M. Leyko, F. Nicoud, and T. Poinso. "Comparison of indirect and direct combustion noise in aircraft engines." In "11th CEAS-ASC Workshop, Experimental and Numerical Analysis and Prediction of Combustion Noise," Lisbon, Portugal. 2007.
- [71] X. D. Li, C. Richter, and F. Thiele. "Time-Domain Impedance Boundary Conditions for Subsonic Mean Flow." *Journal of the Acoustical Society of America*, **119(5)**, 2665–2676. 2006.
- [72] X. D. Li, C. Schemel, U. Michel, and F. Thiele. "On the Azimuthal Mode Propagation in Axisymmetric Duct Flows." AIAA Paper 2002–2521. 2002.
- [73] X. D. Li, C. Schemel, U. Michel, and F. Thiele. "Azimuthal Sound Mode Propagation in Axisymmetric Flow Ducts." *AIAA Journal*, **42(10)**, 2019–2027. 2004.
- [74] X. D. Li, N. Schönwald, J. Yan, and F. Thiele. "A Numerical Study on the Acoustic Radiation from a Scarfed Intake." AIAA Paper 2003–3245. 2003.
- [75] M. J. Lighthill. "On Sound Generated Aerodynamically. I. General Theory." *Proceedings of the Royal Society of London. Series A, Mathematical and Physical Sciences*, **211(1107)**, 564–587. 1952.
- [76] L. N. Long. "A Nonconservative Nonlinear Flowfield Splitting Method for 3-D Unsteady Fluid Dynamics." AIAA Paper 2000–1998. 2000.

-
- [77] F. C. de Metz and T. M. Farabee. "Laminar and Turbulent Shear Flow Induced Cavity Resonances." AIAA Paper 1977-1293. 1977.
- [78] A. Michalke. "Vortex Formulation in a Free Boundary Layer According to Stability Theory." *Journal of Fluid Mechanics*, **22(2)**, 371-383. 1965.
- [79] U. Michel. Private communication suggesting the possibility of a modal axisymmetric approach for CAA. 2002.
- [80] C. L. Morfey. "Acoustic Energy in Non-Uniform Flows." *Journal of Sound and Vibration*, **14(2)**, 159-170. 1971.
- [81] M. Möser. "Die Wirkung von zylindrischen Aufsätzen an Schallschirmen." *Acta Acoustica united with Acoustica*, **81**, 565-586. 1995.
- [82] B. Mühlbauer, B. Noll, and M. Aigner. "Numerical simulation of entropy noise and its acoustic sources in aero-engines." In "ASME Turbo Expo, GT2008-50321," Berlin, Germany. 2008.
- [83] I. Müller. *Grundzüge der Thermodynamik*. Springer, Berlin, Heidelberg, New York. ISBN 3-540-64703-1. 1998.
- [84] P. Murray, P. Ferrante, and A. Scofano. "Manufacturing Process and Boundary Layer Influences on Perforate Liner Impedance." AIAA Paper 2005-2849. 2005.
- [85] M. K. Myers. "On the acoustic boundary condition in the presence of flow." *Journal of Sound and Vibration*, **71(8)**, 429-434. 1980.
- [86] M. K. Myers. "Transport of energy by disturbances in arbitrary steady flows." *Journal of Fluid Mechanics*, **226**, 383-400. 1991.
- [87] D. Nürnberger, F. Eulitz, S. Schmidt, and A. Zachcial. "Recent progress in the Numerical Simulation of unsteady viscous multistage turbomachinery flow." ISABE 2001-1081, Bangalore. 2001.
- [88] Y. Özyörük and L. N. Long. "A time-domain implementation of surface acoustic impedance condition with and without flow." AIAA Paper 1996-1663. 1996.
- [89] Y. Özyörük and L. N. Long. "Time-domain calculation of sound propagation in lined ducts with sheared flows." *AIAA Journal*, **38(5)**, 768-773. 2001.
- [90] Y. Özyörük, L. N. Long, and M. G. Jones. "Time-domain numerical simulation of a flow-impedance tube." *Journal of Computational Physics*, **146(1)**, 29-57. 1998.

- [91] L. Panek. "Numerische Simulation der Störungsausbreitung in Düsenströmungen unter Berücksichtigung nichtlinearer Effekte." Diplomarbeit, Technische Universität Berlin. 2004.
- [92] L. Panek, N. Schönwald, C. Richter, and F. Thiele. "Simulation of the Rearward Propagation of Fan Noise through a Long Cowl Aero-engine." AIAA Paper 2008-2820. 2008.
- [93] A. T. Patera. "A spectral element method for fluid dynamics: Laminar flow in a channel expansion." *Journal of Computational Physics*, **54**(3), 468–488. doi: 10.1016/0021-9991(84)90128-1. 1984.
- [94] N. Peake. "On the behaviour of a fluid-loaded cylindrical shell with mean flow." *Journal of Fluid Mechanics*, **338**, 387–410. 1997.
- [95] A. D. Pierce. *Acoustics: An Introduction to Its Physical Principles and Applications*. Acoustical Society of America, Melville. ISBN 0-838318-612-8. 1989.
- [96] W. Polifke, C. Wall, and P. Moin. "Partially reflecting and non-reflecting boundary conditions for simulation of compressible viscous flow." *Journal of Computational Physics*, **213**(1), 437–449. 2006.
- [97] M. Pott-Pollenske, W. Dobrzynski, H. Buchholz, and D. Almoneit. "Characteristics of Noise from Aircraft Ground Operations." AIAA Paper 2007-3560. 2007.
- [98] W. H. Reed and T. R. Hill. "Triangular mesh methods for the neutron transport equation." LA-UR-73-479, Los Alamos Scientific Laboratory. 1973.
- [99] Y. Reymen, M. Baelmans, and W. Desmet. "Time-Domain Impedance Formulation suited for Broadband Simulations." AIAA Paper 2007-3519. 2007.
- [100] S. K. Richards, X. X. Chen, X. Huang, and X. Zhang. "Computation of fan noise radiation through an engine exhaust geometry with flow." *International Journal of Aeroacoustics*, **6**(3), 223–241. 2007.
- [101] C. Richter, D. Morgenweck, and F. Thiele. "CAA Simulation and Intensity Based Evaluation of a Model Experiment for Indirect Combustion Noise." *Acta Acustica united with Acoustica*, **95**(3), 479–492. 2009.
- [102] C. Richter, L. Panek, and F. Thiele. "On the Application of CAA-Methods for the Simulation of Indirect Combustion Noise." AIAA Paper 2005-2919. 2005.
- [103] C. Richter and F. Thiele. "CAA Tools for the simulation of indirect combustion noise from transonic nozzle flows." In "11th CEAS-ASC Workshop, Experimental and Numerical Analysis and Prediction of Combustion Noise," CEAS-ASC, Lisbon, Portugal. Paper 15. 2007.

-
- [104] C. Richter and F. Thiele. "The Stability of Time Explicit Impedance Models." AIAA Paper 2007-3538. 2007.
- [105] C. Richter, F. Thiele, X. D. Li, and M. Zhuang. "Comparison of Time-Domain Impedance Boundary Conditions by Lined Duct Flows." AIAA Paper 2006-2527. 2006.
- [106] C. Richter, F. Thiele, X. D. Li, and M. Zhuang. "Comparison of Time-Domain Impedance Boundary Conditions for Lined Duct Flows." *AIAA Journal*, **45**(6), 1333-1345. 2007.
- [107] S. W. Rienstra. "A classification of duct modes based on surface waves." *Wave Motion*, **37**, 119-135. 2003.
- [108] S. W. Rienstra. "Impedance Models in Time Domain, Including the Extended Helmholtz Resonator Model." AIAA Paper 2006-2686. 2006.
- [109] S. W. Rienstra and W. Eversman. "A numerical comparison between the multiple-scale and finite-element solution for sound propagation in lined flow ducts." *Journal of Fluid Mechanics*, **437**, 367-384. 2001.
- [110] S. W. Rienstra and A. Hirschberg. *An Introduction to Acoustics*. Eindhoven University of Technology press, <http://www.win.tue.nl/~sjoerdr/papers/boek.pdf>. Report IWDE 92-06. 2003.
- [111] S. W. Rienstra and G. G. Vilenski. "Spatial Instability of Boundary Layer Along Impedance Wall." AIAA Paper 2008-2932. 2008.
- [112] D. Ronneberger. "Theoretische und Experimentelle Untersuchung der Schallabstrahlung durch Querschnittssprünge und Lochplatten in Strömungskanälen." Ro 369/11, 12, 14. 1987.
- [113] C. Schemel. "Modellierung und numerische Simulation der Entstehung und Ausbreitung von Schall durch Entropiewellen in beschleunigten Rohrströmungen." Diplomarbeit, Technische Universität Berlin. 2003.
- [114] C. Schemel, F. Thiele, F. Bake, B. Lehmann, and U. Michel. "Sound Generation in the Outlet Section of Gas Turbine Combustion Chambers." AIAA Paper 2004-2929. 2004.
- [115] N. Schönwald, L. Panek, C. Richter, and F. Thiele. "Investigation of Sound Radiation from a Scarfed Intake by CAA-FWH Simulations Using Overset Grids." AIAA Paper 2007-3524. 2007.
- [116] T. Schwartzkopff, M. Dumbser, and C.-D. Munz. "CAA using Domain Decomposition and High Order Method on Structured and Unstructured Meshes." AIAA Paper 2004-2964. 2004.

- [117] A. Scofano, P. B. Murray, and P. Ferrante. "Back-Calculation of Liner impedance using Duct Insertion Loss Measurements and FEM Predictions." AIAA Paper 2007–3534. 2007.
- [118] J. H. Seo and Y. J. Moon. "Linearized perturbed compressible equations for low Mach number aeroacoustics." *Journal of Computational Physics*, **218**(2), 702–719. 2006.
- [119] I. J. Sharland. "Sources of Noise in Axial Flow Fans." *Journal of Sound and Vibration*, **1**(3), 302–322. 1964.
- [120] J. H. Spurk. *Strömungslehre*. Springer, Berlin, Heidelberg, New York. ISBN 3-540-51458-9. 1997.
- [121] D. Stanescu and W. G. Habashi. "2N-storage Low-dissipation and Low-dispersion Runge-Kutta Schemes for Computational Aeroacoustics." *Journal of Computational Physics*, **143**(2), 674–681. 1998.
- [122] C. K. Tam, H. Ju, and E. W. Chien. "Scattering of Acoustic Modes by Axial Liner Splices." AIAA Paper 2006–2459. 2006.
- [123] C. K. W. Tam. "Advances in Numerical Boundary Conditions for Computational Aeroacoustics." *Journal of Computational Acoustics*, **6**(4), 377–402. doi: 10.1142/S0218396X98000259. 1998.
- [124] C. K. W. Tam and L. Auriault. "Time-Domain Impedance Boundary Conditions for Computational Aeroacoustics." *AIAA Journal*, **34**(5), 917–923. 1996.
- [125] C. K. W. Tam, L. Auriault, and F. Cambuli. "Perfectly Matched Layer as an Absorbing Boundary Condition for the Linearized Euler Equations in Open and Ducted Domains." *Journal of Computational Physics*, **144**, 213–234. 1998.
- [126] C. K. W. Tam and T. Z. Dong. "Wall Boundary Conditions for High-Order Finite Difference Schemes in Computational Aeroacoustics." *Theoretical and Computational Fluid Dynamics*, **6**(6), 303–322. 1994.
- [127] C. K. W. Tam and C. Webb. "Dispersion-Relation-Preserving Finite Difference Schemes for Computational Aeroacoustics." *Journal of Computational Physics*, **107**(2), 262–281. 1993.
- [128] C. K. W. Tam, C. Webb, and T. Z. Dong. "A Study of Short Wave Components in Computational Aeroacoustics." *Journal of Computational Acoustics*, **1**, 1–30. 1993.
- [129] B. J. Tester. "The propagation and attenuation of sound in lined ducts containing uniform or plug flow." *Journal of Sound and Vibration*, **28**(2), 151–203. 1973.

-
- [130] The LAM/MPI Team. *LAM/MPI User's Guide*. Open Systems Laborator, Pervasive Technology Labs, Indiana University, Bloomington, IN. 7.0 edition. 2003.
- [131] K. W. Thompson. "Time dependent boundary conditions for hyperbolic systems." *Journal of Computational Physics*, **68(1)**, 1–24. doi:[http://dx.doi.org/10.1016/0021-9991\(87\)90041-6](http://dx.doi.org/10.1016/0021-9991(87)90041-6). 1987.
- [132] K. W. Thompson. "Time-dependent boundary conditions for hyperbolic systems, II." *Journal of Computational Physics*, **89(2)**, 439–461. doi:[http://dx.doi.org/10.1016/0021-9991\(90\)90152-Q](http://dx.doi.org/10.1016/0021-9991(90)90152-Q). 1990.
- [133] J. M. Tyler and T. G. Sofrin. "Axial Flow Compressor Noise Studies." *SAE Transactions*, **70**, 309–332. 1962.
- [134] W. R. Watson, M. G. Jones, and T. L. Parrott. "A Quasi-3-D Theory for Impedance Eduction in Uniform Grazing Flow." AIAA Paper 2005–2848. 2005.
- [135] C. Weckmüller, S. Guerin, and C. Richter. "Numerical Investigation of Geometry and Mean Flow Effects on Acoustic Radiation from a Duct Inlet." AIAA Paper 2007–3535. 2007.
- [136] Wikipedia the free encyclopedia. URL <http://www.wikipedia.com>, accessed February 2009.
- [137] C. Yu, Z. Zhou, and M. Zhuang. "An Acoustic Intensity-Based Inverse Method." *Journal of the Acoustical Society of America*, **123(4)**, 1892–1901. 2008.
- [138] C. Yu, Z. Zhou, M. Zhuang, X. Li, and F. Thiele. "A New Far-Field Acoustic Prediction Method and Its CAA Application." *AIAA Journal*, **47(2)**, 410–417. 2009.
- [139] F. Zhang and C. Bender. Private communication of base flow and microphone data. 2008.
- [140] F. Zhang, P. Habisreuter, H. Bockhorn, and H. Büchner. "LES of reactive flow in a strongly swirling combustor system." In "Int. Conf. on Jets, Wakes and Saperated Flows, ICJWSF-2008," 2008.
- [141] X. Zhang, X. X. Chen, C. L. Morfey, and P. A. Nelson. "Computation of Spinning Modal Radiation from an Unflanged Duct." AIAA Paper 2002–2475. 2002.
- [142] X. Zhang, X. X. Chen, C. L. Morfey, and P. A. Nelson. "Computation of Spinning Modal Radiation from an Unflanged Duct." *AIAA-Journal*, **42(9)**, 1795–1801. Originally published as AIAA Paper 2002–2475. 2004.

- [143] M. Zhaung. Private communication about the MATLAB optimization toolbox. 2004.
- [144] S. Zheng and M. Zhuang. “Application and verification of time domain impedance boundary conditions in multi-dimensional acoustic problems.” AIAA Paper 2002–2593. 2002.
- [145] S. Zheng and M. Zhuang. “Verification and Validation of Time-Domain Impedance Boundary Condition in Lined Ducts.” *AIAA Journal*, **43**, 306–313. 2005.
- [146] M. Zhuang. “Time Domain Impedance Boundary Conditions for a Slip Mean Flow Boundary.” *PAMM*, **4(1)**, 530–531. 2004.
- [147] M. Zhuang and C. Richter. *Computational Aeroacoustics and it's applications*. URL http://www.cfd.tu-berlin.de/Lehre/CAA/script/CAA_2008.pdf, script for the Lecture CAA (Numerische Methoden der Strömungsakustik). 2008.
- [148] J. Zierep. *Theoretische Gasdynamik*. G. Braun. 1976.